

# CARBOMETALATES

## Intermediate phases in the ternary systems *RE-T-C* (*RE* = Y, La, Gd-Er; *T* = Cr, Fe, Ru)

### DISSERTATION

for obtaining the academic degree of  
Doctor rerum naturalium  
(Dr. rer. nat.)

submitted to  
The Faculty of Mathematics and Natural Sciences  
of the University of Technology, Dresden

by  
Bambar Davaasuren  
born on 03.05.1979 in Ulaanbaatar

Approved by:

Prof. Dr. R. Kniep  
Prof. Dr. M. Ruck

This doctoral thesis was written at the Max Planck Institute for Chemical  
Physics of Solids from March 2007 to November 2010



## Acknowledgement

It is a pleasure to thank those people who made this thesis possible.

First of all, I would like to express my deepest gratitude with great sincerity to my Doctor father Prof. Dr. Rüdiger Kniep for offering me an interesting topic, continuous support and encouragement throughout my study. I remember our first meeting in Mongolia, when he made an interview with me and gave me the great opportunity to do my doctoral work in his group, which was a big investment in my life. It is an honor to be his student. I am deeply indebted to him.

I would like to thank my former teacher Prof. Dr. Dorj Daichaa from the National University of Mongolia for motivating and supporting me since my undergraduate studies.

I am heartily thankful to my co-supervisor, ScD. Dr. Enkhtsetseg Dashjav, whose encouragement, supervision and support from the preliminary to the concluding level enabled me to develop an understanding of the subject. Outside the institute she was like an elder sister to our family and helped us in all respect. On behalf of my family I want to express my appreciations to her. I would have been lost without her.

I owe my deepest gratitude to PD Dr. Guido Kreiner for his guidance, advices, productive and fruitful discussions and comments. Without him this work was not possible. I thank him for his detailed review, criticism and corrections during the preparation of articles and this thesis. On behalf of the young scientists of the National University of Mongolia, I want to thank Prof. Dr. R. Kniep, PD Dr. G. Kreiner and ScD. Dr. E. Dashjav for organizing workshops and providing a wholly equipped computer laboratory to our department.

I would like to thank Dr. Horst Borrmann for fruitful discussions on crystal chemistry and supporting with single crystal diffraction measurements. Dr. Yurii Prots, Dr. Raul Cardoso-Gil, Mr. Steffen Hückmann and Mr. Alexander Wölfel (University of Bayreuth) are acknowledged for providing X-ray diffraction measurement results. My special thanks to Dr. Frank R. Wagner, Dr. Marek Mihalkovic and Prof. PhD Michael Widom for quantum mechanical calculations. I am grateful to Dr. Walter Schnelle and Mr. Ralf Koban for physical property measurements and evaluations of the results. Dr. Gudrun Auffermann, Dr. Ulrich Burkhard, Dr. Stefan Hoffmann, Mr. Torsten Vogel, Ms. Ulrike Schmidt, Ms. Anya Völzke, Ms. Petra Scheppan, Ms. Monika Eckert and Ms. Susann Müller for the assistance in characterization methods.

I want to specially acknowledge Ms. Katrin Demian for her constant help and support to me and to our family. She was always there and ready to lend her hand whenever I needed her help. I am grateful to Ms. Susanne Zücker for helping me to do all the administrative work.

I also would like to make a special reference to Dr. Lev Akselrud for helping us to solve crystallographic problems. Special thanks to Dr. Daniel Grüner for his friendship and

detailed review and valuable corrections on my thesis. I am grateful to Dr. Peter Höhn and Dr. Alim Ormeci for their valuable advises, helpful discussions and encouragement. I would like to also thank Dr. Marcus Schmidt and Dr. Roman Gumeniuk for their assistance.

My sincere thanks to Prof. Dr. Michael Ruck and Prof. Dr. Sander van Smaalen for giving the opportunity to make single crystal diffraction measurements in their labs. It is my pleasure to thank PD Dr. Thomas Doert and PD Dr. Andreas Schönleber for fruitful discussions and advises about modulated structures.

I owe my deepest gratitude to Prof. Dr. Klaus Dieter Becker and Dr. Sven Ulf Weber for providing us with Mössbauer spectroscopic measurements and evaluation of the results.

I would like to thank all my friends for a friendly working atmosphere and making my stay enjoyable.

Finally, I take the opportunity to thank my family for their strong support, motivation and inspiration and always standing behind me. I am thankful to my wife for her encouragement and constant support and also being responsible for our children and me. Thanks to my uncle and his family and my parents-in-law who have been always a good back up for us. I want to dedicate this thesis to my grandmother Tsendjav Tsermaa and to my mother Sandag Davaasuren. They are the reason I am.



## List of publications, conference contributions and attended workshops

### Publication in peer-reviewed journals

1. B. Davaasuren, E. Dashjav, H. Borrmann, G. Kreiner, W. Schnelle, F. R. Wagner, M. Widom, R. Kniep, Planar Fe<sub>6</sub> cluster units in the crystal structure of RE<sub>15</sub>Fe<sub>8</sub>C<sub>25</sub> (RE = Y, Dy, Ho, Er), *Angew. Chem.* **2010**, *122*, 5824-5828, *Angew. Chem. Int. Ed.* **2010**, *49*, 5688-5692 .
2. B. Davaasuren, E. Dashjav, Th. Doert, G. Kreiner, W. Schnelle, F. R. Wagner, M. Mihalkovič, R. Kniep, Modulated La chains in the crystal structure of La<sub>3.65</sub>[Ru(C<sub>2</sub>)<sub>3</sub>], *Z. Anorg. Allg. Chem.* **2010**, *636*, 41-49.
3. B. Davaasuren, E. Dashjav, A. Kerkau, G. Kreiner, W. Schnelle, F. R. Wagner, R. Kniep, Synthesis, crystal and electronic structure of a samarium carbochromate(III), Sm<sub>2</sub>[Cr<sub>2</sub>C<sub>3</sub>], *Z. Anorg. Allg. Chem.* **2009**, *635*, 1741-1745.
4. B. Davaasuren, E. Dashjav, H. Borrmann, G. Kreiner, R. Kniep, Reinvestigation and superstructure of La<sub>3.67</sub>[Fe(C<sub>2</sub>)<sub>3</sub>], *J. Solid State Chem.* **2009**, *182*, 1331-1335.
5. B. Davaasuren, E. Dashjav, H. Borrmann, G. Kreiner, R. Kniep, Crystal structure of ytterbium lanthanum iron carbide, La<sub>3</sub>Yb<sub>0.63</sub>FeC<sub>6</sub>, *Z. Kristallogr., NCS*, **2009**, *224*, 13-14.
6. B. Davaasuren, E. Dashjav, H. Borrmann, G. Kreiner, R. Kniep, A new 1D-Modulated Crystal Structure of a Gd-Compound with Anionic Complexes [CFe(C<sub>2</sub>)<sub>2</sub>] and [Fe(C<sub>2</sub>)<sub>2</sub>], *Z. Anorg. Allg. Chem.* **2008**, *634*, 2019.
7. B. Davaasuren, E. Dashjav, L. Akselrud, G. Kreiner, W. Schnelle, R. Kniep, An incommensurate composite structure of a novel complex carbide: Dy<sub>5.64</sub>[Fe<sub>2</sub>C<sub>9</sub>], *J. Solid State Chem.* (in preparation)

### Oral presentation

1. B. Davaasuren, E. Dashjav, H. Borrmann, G. Kreiner, W. Schnelle, F. R. Wagner, R. Kniep  
Ternary rare-earth and transition metal carbides viewed as carbometalates  
*SCTE 2010*, Annecy, France, 09/2010
2. B. Davaasuren, R. Kniep  
New ternary intermediate phases in the system RE-Fe-C  
*VII. Mitteldeutsches Anorganiker-Nachwuchs Symposium (MANS 7)*, Technical University of Chemnitz, Germany, 09/2009

3. B. Davaasuren, E. Dashjav, H. Borrmann, G. Kreiner, F. R. Wagner, R. Kniep  
Intermediate ternary phases in the system  $RE$ -Fe-C  
*Hirschegg, Fachgruppe Festkörperchemie Seminar, Germany, 10/2009*
4. B. Davaasuren, E. Dashjav, H. Borrmann, G. Kreiner, R. Kniep  
A new 1D-modulated crystal structure of a Gd-compound with anionic complexes  
[CFe(C<sub>2</sub>)<sub>2</sub>] and [Fe(C<sub>2</sub>)<sub>2</sub>]  
*13. Vortragstagung der GDCh-Fachgruppe Festkörperchemie und Materialforschung, Bayreuth, Germany, 09/2008*

### Poster presentations

1. B. Davaasuren, E. Dashjav, H. Borrmann, G. Kreiner, W. Schnelle, F. R. Wagner, R. Kniep, S. U. Weber, K. D. Becker  
Crystal structure and properties of  $RE_{15}Fe_8C_{25}$  ( $RE = Y, Dy - Er$ )  
*Green Chemistry and Advanced Technology, Ulaanbaatar, Mongolia, 10/2010*
2. B. Davaasuren, E. Dashjav, H. Borrmann, G. Kreiner, W. Schnelle, F. R. Wagner, R. Kniep, S. U. Weber, K. D. Becker  
Crystal structure and properties of  $RE_{15}Fe_8C_{25}$  ( $RE = Y, Dy - Er$ )  
*First Mongolian-German Workshop on Advanced Materials, Ulaanbaatar, Mongolia, 09/2010*
3. B. Davaasuren, E. Dashjav, R. Kniep  
Crystal and electronic structures of the ternary iron carbides  
*International Symposium on Structure-property Relationship of solids, Stuttgart, Germany, 06/2010*
4. B. Davaasuren, E. Dashjav, Th. Doert, G. Kreiner, R. Kniep  
Modulated La chains in the crystal structure of  $La_{3.65}[Ru(C_2)_3]$   
*ECSSC XII - XIIIth European Conference on Solid State Chemistry Münster, Germany, 10/2009*
5. B. Davaasuren, E. Dashjav, H. Borrmann, G. Kreiner, W. Schnelle, F. R. Wagner, R. Kniep  
 $Dy_{15}Fe_8C_{26}$ : A new crystal structure containing  $Fe_6$  clusters  
*14. Vortragstagung der DGK, Hannover, Germany, 10/2009*
6. B. Davaasuren, E. Dashjav, H. Borrmann, G. Kreiner, F. R. Wagner, M. Michalkovic, R. Kniep  
The superstructure and homogeneity range of  $La(0.5 < x < 0.67)La_3[Fe(C_2)_3]$   
*16. International Conference on Solid Compounds of Transition Elements, Dresden, Germany, 07/2008*

7. B. Davaasuren, E. Dashjav, G. Kreiner, W. Schnelle, F. R. Wagner, R. Kniep  
Recent developments in ternary carbides: Carbometalates  
*ICCT MAS*, Ulaanbaatar, Mongolia, 06/2008
8. B. Davaasuren, E. Dashjav, Yu. Prots, G. Kreiner, W. Schnelle, F. R. Wagner, R. Kniep  
Synthesis and crystal structure of a samarium carbochromate(III),  $\text{Sm}_2[\text{Cr}_2\text{C}_3]$   
*16. Jahrestagung der Deutschen Gesellschaft für Kristallographie*, Erlangen, Germany, 03/2008
9. B. Davaasuren, E. Dashjav, H. Borrmann, G. Kreiner, R. Kniep  
Refinement of the superstructure of  $\text{La}_{0.67}(\text{La}_3[\text{Fe}(\text{C}_2)_3])$   
*16. Jahrestagung der Deutschen Gesellschaft für Kristallographie*, Erlangen, Germany, 03/2008

### **Workshop attendance**

1. Spektroskopische Methoden in der Festkörperchemie - vom Volumen zur Oberfläche  
MPI-CPfS, Dresden, Germany, 05/2010
2. Workshop on Preparation, Thermodynamics, Phase Equilibria, Solidification and Structures of Alloys and Intermetallic Compounds  
MPI-CPfS and NUM, Ulaanbaatar, Mongolia, 09/2009
3. CMA Euroschool "Mechanical Properties of Complex Metallic Alloys"  
Ljubljana, Slovenia, 05/2009
4. "6th Workshop on Structural Analysis of Aperiodic Crystals"  
University of Bayreuth, Germany, 03/2009
5. Zürich School of Crystallography  
University of Zürich, Switzerland, 07/2008



## Contents

<b>Acknowledgement</b>	<b>ii</b>
<b>List of publications, conference contributions and attended workshops</b>	<b>v</b>
<b>1 Introduction and motivation</b>	<b>1</b>
<b>2 Literature survey</b>	<b>7</b>
2.1 Overview of the binary subsystems of ternary systems $RE-T-C$ ( $T = Cr, Fe, Ru$ ) . . . . .	7
2.1.1 $RE-C$ ( $RE = rare-earth\ metals$ ) . . . . .	7
2.1.2 $T-C$ ( $T = Cr, Fe, Ru$ ) . . . . .	11
2.1.3 $RE-T$ . . . . .	19
2.2 Overview of the ternary systems . . . . .	24
2.2.1 $RE-Cr-C$ . . . . .	24
2.2.2 $RE-Fe-C$ . . . . .	26
2.2.3 $RE-Ru-C$ . . . . .	31
<b>3 Preparation and methods of characterization</b>	<b>39</b>
3.1 High temperature synthesis . . . . .	39
3.1.1 Arc melting . . . . .	39
3.1.2 High temperature reaction . . . . .	39
3.1.3 High frequency induction furnace . . . . .	40
3.2 Synthesis from metallic flux and melt centrifugation . . . . .	40
3.3 Spark Plasma Sintering (SPS) . . . . .	41
3.4 Starting materials . . . . .	42
3.5 X-ray diffraction . . . . .	42
3.5.1 Powder X-ray diffraction . . . . .	42
3.5.2 Single crystal X-ray diffraction . . . . .	43
3.5.3 Superspace approaches . . . . .	44
3.6 Metallographic investigations . . . . .	45
3.7 X-ray spectroscopic analysis . . . . .	45
3.7.1 Scanning electron microscopy and energy / wavelength dispersive X-ray analysis . . . . .	45
3.7.2 X-ray absorption spectroscopy (XAS) . . . . .	46
3.8 Mössbauer spectroscopy . . . . .	47
3.9 Thermal analysis . . . . .	48
3.10 ICP-OES and combustion technique . . . . .	49

3.11	Physical property measurements . . . . .	49
3.11.1	Magnetic susceptibility . . . . .	49
3.11.2	Electrical resistivity . . . . .	50
3.12	Chemical bonding analysis . . . . .	50
3.12.1	Density functional theory (DFT) . . . . .	50
3.12.2	LMTO-ASA method . . . . .	51
3.12.3	Crystal orbital Hamilton population (COHP) method . . . . .	51
3.12.4	Electron localization function (ELF) and Electron localizability indicator (ELI) . . . . .	51
<b>4</b>	<b><math>RE_{15}[Fe_8C_{25}]</math> (<math>RE = Y, Dy, Ho, Er</math>)</b>	<b>53</b>
4.1	Synthesis and phase analysis . . . . .	53
4.2	Crystal structure determination . . . . .	56
4.3	Crystal chemistry . . . . .	59
4.4	Phase stability . . . . .	68
4.5	Electronic structure and chemical bonding analysis . . . . .	68
4.6	Magnetic susceptibility . . . . .	75
4.7	Electrical resistivity . . . . .	77
4.8	Mössbauer spectroscopic studies . . . . .	77
4.9	X-ray absorption spectroscopic studies . . . . .	83
4.10	Summary . . . . .	85
<b>5</b>	<b><math>RE_{5,64}[Fe_2C_9]</math> (<math>RE = Y, Gd, Tb, Dy</math>)</b>	<b>87</b>
5.1	Synthesis and phase analysis . . . . .	87
5.2	Crystal structure determination . . . . .	89
5.3	Crystal chemistry . . . . .	95
5.4	Magnetic susceptibility . . . . .	102
5.5	Electrical resistivity . . . . .	103
5.6	Mössbauer spectroscopic studies . . . . .	104
5.7	X-ray absorption spectroscopic studies . . . . .	105
5.8	Summary . . . . .	107
<b>6</b>	<b><math>La_{3,67}[T(C_2)_3]</math> (<math>T = Fe, Ru</math>)</b>	<b>108</b>
6.1	Synthesis and phase analysis . . . . .	108
6.2	$La_{3,67}[Fe(C_2)_3]$ . . . . .	110
6.2.1	Crystal structure determination . . . . .	110
6.2.2	Crystal chemistry . . . . .	112
6.2.3	Phase stability and homogeneity range . . . . .	117
6.2.4	Electronic band structure and chemical bonding analysis . . . . .	118
6.2.5	Mössbauer spectroscopic studies . . . . .	121

6.2.6	X-ray absorption spectroscopic studies . . . . .	123
6.3	$\text{La}_{3.67}[\text{Ru}(\text{C}_2)_3]$ . . . . .	124
6.3.1	Crystal structure determination . . . . .	124
6.3.2	Crystal chemistry . . . . .	128
6.4	Phase stability . . . . .	131
6.5	Electronic structure and chemical bonding analysis . . . . .	132
6.6	Magnetic susceptibility . . . . .	135
6.7	Electrical resistivity . . . . .	136
6.8	Summary . . . . .	137
<b>7</b>	<b><math>\text{Sm}_2[\text{Cr}_2\text{C}_3]</math></b>	<b>138</b>
7.1	Synthesis and phase analysis . . . . .	138
7.2	Crystal structure determination . . . . .	139
7.3	Crystal chemistry . . . . .	140
7.4	Magnetic susceptibility . . . . .	144
7.5	Total energy calculations and phase stability . . . . .	144
7.6	Electronic structure and Chemical bonding analysis . . . . .	145
7.7	Summary . . . . .	148
<b>8</b>	<b>Summary</b>	<b>149</b>
<b>9</b>	<b>Appendix</b>	<b>152</b>
9.1	Unit cell parameters of related binary compounds . . . . .	152
9.2	Atomic coordinates, ADP, interatomic distances and bond angles for the crystal structure of $\text{RE}_{15}[\text{Fe}_8\text{C}_{25}]$ . . . . .	157
9.3	Modulation functions, ADP and interatomic distances in the crystal structure of $\text{Dy}_{5.64}[\text{Fe}_2\text{C}_9]$ . . . . .	163
9.4	ADP and interatomic distances for the crystal structure of $\text{La}_{3.67}[\text{Fe}(\text{C}_2)_3]$ . . . . .	168
9.5	Anisotropic displacement parameters (ADP) and interatomic distances for the crystal structure of $\text{La}_{3.67}[\text{Ru}(\text{C}_2)_3]$ . . . . .	169
9.6	Bond angles for the crystal structure of $\text{Sm}_2\text{Cr}_2\text{C}_3$ . . . . .	170
	<b>Bibliography</b>	<b>171</b>
	<b>List of Figures</b>	<b>188</b>
	<b>List of Tables</b>	<b>194</b>
	<b>Curriculum Vitae</b>	<b>198</b>
	<b>Versicherung</b>	<b>199</b>





# 1 Introduction and motivation

Carbides form an important family of compounds in research and industry due to fascinating chemical, mechanical, electrical, magnetic and optical properties. The most familiar examples are WC and carborundum (SiC). Tungsten carbide is used in cutting tools and coatings, as pure-material, sintered parts, or in Co/Mo/W/carbide sintered composites [1, 2]. SiC is the most promising material for high-powered semiconductor devices, substrate material for the manufacture of controlled graphene, and is widely used as an abrasive [3].

Carbides are defined as compounds of the element carbon with less electronegative partners like metals and non-metals [4–7]. Hydrogen is an exception. In this case, the compounds are called hydrocarbons. Most textbooks classify the family of carbides into three compound classes according to the classical bonding situation, physical properties and structural aspects [4–6]:

- 1) Ionic carbides are compounds of carbon with mainly group 1 and 2 elements and some strong electropositive elements like Al and La. Typical representatives are  $\text{CaC}_2$ ,  $\text{Al}_4\text{C}_3$ ,  $\text{La}_2\text{C}_3$ . Some textbooks in addition use the term salt-like carbides to point out the salt-like character (e.g. methanides and acetylides) according to their physical and chemical properties.
- 2) Metallic carbides are compounds of  $d$  elements with carbon. Other terms in use are interstitial or refractory carbides. Many metallic carbides show high temperature stability, high strength, wear resistance, and chemical inertness. They play an important role in industrial applications, e.g. as cutting tools, rocket nozzles and jet engine parts [1, 2]. Some metallic carbides with relative low melting point, e.g., TiC, ZrC are used to produce highly porous pure carbon materials, called Carbide-Derived Carbons (CDCs). In these compounds carbon atoms occupy parts of the octahedral voids of the metallic host structure. A general trend observed in interstitial carbides is that the cubic close packed (*ccp*) metal hosts have a higher filling degree of carbon atoms in interstices compared to the hexagonal close packed (*hcp*) arrangement of the metal host.
- 3) Covalent carbides are formed by  $p$  elements having similar size and electronegativity compared to carbon. The term metalloid carbides is also used in some textbooks. These compounds are characterized by strong covalent bonds. Thus, they are extremely hard, infusible and chemically inert. Examples are SiC and  $\text{B}_4\text{C}$ .

A drawback of this traditional classification is that it mixes up physical properties, chemical bonding, and structural aspects. Thus, it is useful only for binary carbides.

Composition, structural chemistry, chemical bonding and consequently the physical and chemical properties of ternary or higher carbides are more complex compared with the binary carbides. While the chemistry of binary carbides was well studied during the last century, the

higher carbides and nitrides, especially those of stoichiometric compositions, have been in focus only since the last three decades.

Nitridometalates emerged in the past two decades as a well established class of compounds by the intensive studies on nitrides and nitrido-compounds by Rüdiger Kniep and co-workers. Recently, they developed a similar concept for carbocompounds. They showed that carbometalates are stoichiometric carbides containing  $[T_yC_z]^{n-}$  complex anions in analogy to fluoro-, oxo- and nitridometalates. An understanding of the relationships between crystal structure, chemical bonding and physical properties would allow to predict novel functional materials and to tune their properties. In this respect, the systematic investigation of ternary and higher carbides has become very important from the academical and the practical point of view. Carbometalates are carbides which obey the following criteria [8, 9]:

- they are ternary or higher compounds without significant homogeneity ranges
- their well defined chemical formulae are charge balanced between cations and complex anions
- $C^{4-}$  ligands are covalently bonded to transition metal atoms resulting in complex anionic units or networks,  $[T_yC_z]^{n-}$
- because of the high polarizability of the  $C^{4-}$  ligand, a low oxidation state of the transition metal atom and small coordination number in the complex anions are expected
- the physical properties should be consistent with the structural and bonding characteristics.

A general tendency observed in anionic metalate complexes is that the oxidation state, and the coordination number of the transition metals, participating in the formation of the complex anions,  $[T_yL_z]^{n-}$  decrease with increasing polarizability of the ligands ( $L = F^- \rightarrow O^{2-} \rightarrow N^{3-} \rightarrow C^{4-}$ ) [8, 9]. The lowest oxidation states and coordination number of the transition metal elements are found in carbometalates with group 8-10 elements (*Figure 1.1*). The high negative charges of the complex anions, associated with the  $C^{4-}$ -ligands and the low valence state of the transition metal, are compensated by highly positive charges of the rare-earth (*RE*) cations.

A large number of investigations has been carried out on ternary carbides  $RE_xT_yC_z$  (*RE* = rare-earth, U or Th and *T* = transition metal) regarding synthesis, structural characterization and properties. Almost 60 structure types have been reported for this group of ternary carbides. Twenty of them contain monoatomic carbon ligands,  $C^{4-}$ , as structural units, together with the following 14 transition metals (V, Cr, Mn, Fe, Co, Ni, Mo, Ru, Rh, W, Re, Os, Ir, Pt). The remaining structure types contain carbon pairs  $C_2^{n-}$  and sometimes linear  $C_3^{m-}$  units or mixed ligands,  $C^{4-}$  and  $C_2^{n-}$  [10, 11]. Based on the metal to carbon ratio  $(x+y)/z$  the rare-earth transition metal ternary carbides containing monoatomic  $C^{4-}$  units, only, are classified as carbometalates or metal-rich carbides [9]. Those with  $(x+y)/z \leq 2$  are viewed as carbometalates, while in metal rich carbides the ratio is  $(x+y)/z \geq 4$ . So far, only 11 structure

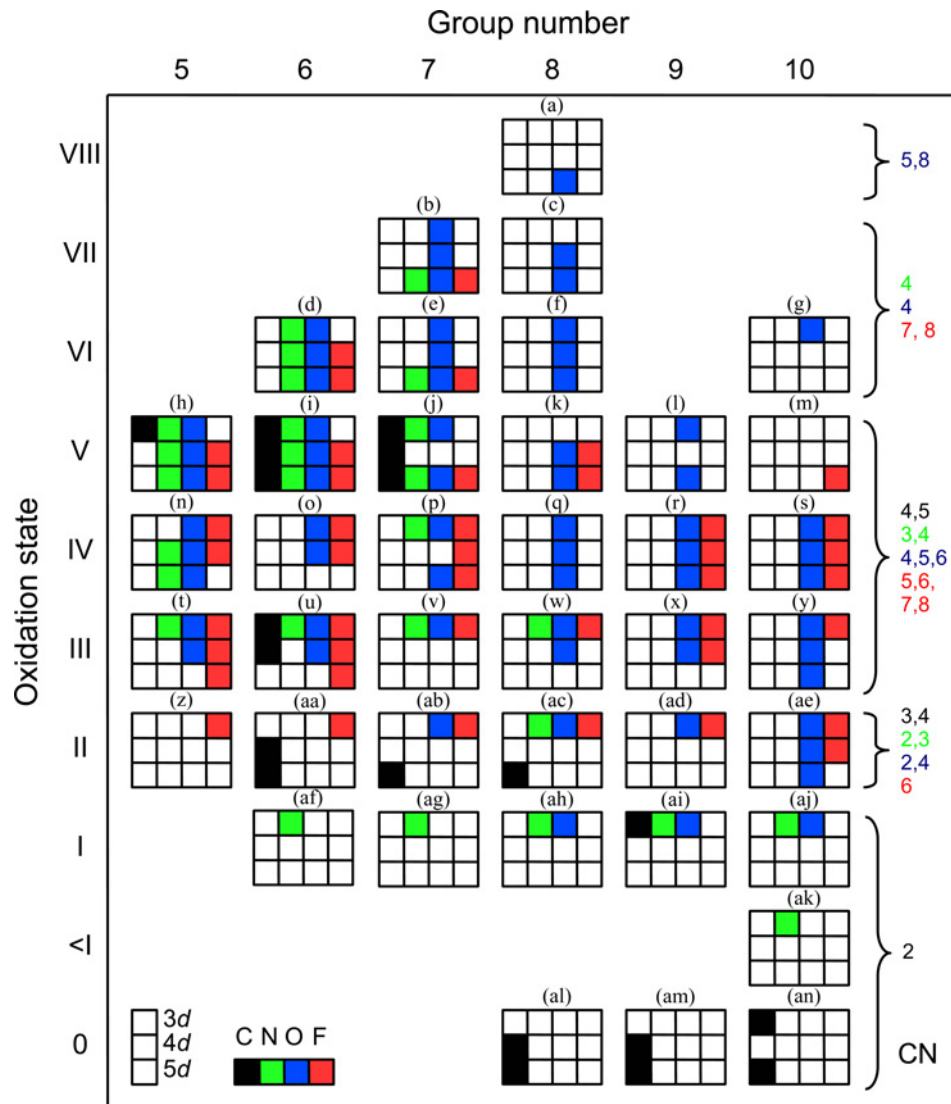


Figure 1.1: Oxidation states and coordination numbers of 3d, 4d, 5d-metals in carbo-, nitrido-, oxo-, and fluorometalates [9].

types of carbometalates are reported up to know. Carbometalates are clearly distinguished from metal-rich carbides, which are non-stoichiometric interstitial carbides whose chemical bonding situations are governed by metal–metal interactions. The following polyanions occur in carbometalates:

- discrete entities -  ${}^0_{\infty}[(T^0C^{-IV}_2)^{8-}]$  ( $T = Ru, Os, Rh, Ir, Ni, Pt$ ) [12, 13]
- anionic chains -  ${}^1_{\infty}[(Co^IC^{-IV})^3-]$  [14, 15],  ${}^1_{\infty}[(T^{II}C^{-IV}_2)^{6-}]$  ( $T = Re, Os$ ) [16, 17]
- layers -  ${}^2_{\infty}[(T^{II}C^{-IV}_2)^{6-}]$  ( $T = Mo, W$ ) [18, 19],  ${}^2_{\infty}[(T^{III}_2C^{-IV}_3)^{6-}]$  ( $T = Cr, Mo$ ) [20–23]
- frameworks -  ${}^3_{\infty}[(Mo^{III}_2C^{-IV}_3)^{6-}]$  [24],  ${}^3_{\infty}[(T^{III}_4C^{-IV}_4)^{4-}]$  ( $T = Cr, W$ ) [25, 26],  
 ${}^3_{\infty}[(Re^{IV}_3C^{-IV}_8)^{20-}]$  [27],  ${}^3_{\infty}[(T^VC^{-IV}_2)^{3-}]$  ( $T = V-Mn, Mo, W, Re$ ) [20, 28].

Figure 1.2 shows an overview of the structural units of the carbometalate anions together with the oxidation states of the central transition metal atoms. In contrast to nitridometalates,

carbometalates form a relatively unexplored class of compounds, and one of the main goals of this work is to synthesize and characterize new compounds of this type.

### Ionic formula and building units of the carbometalate anions

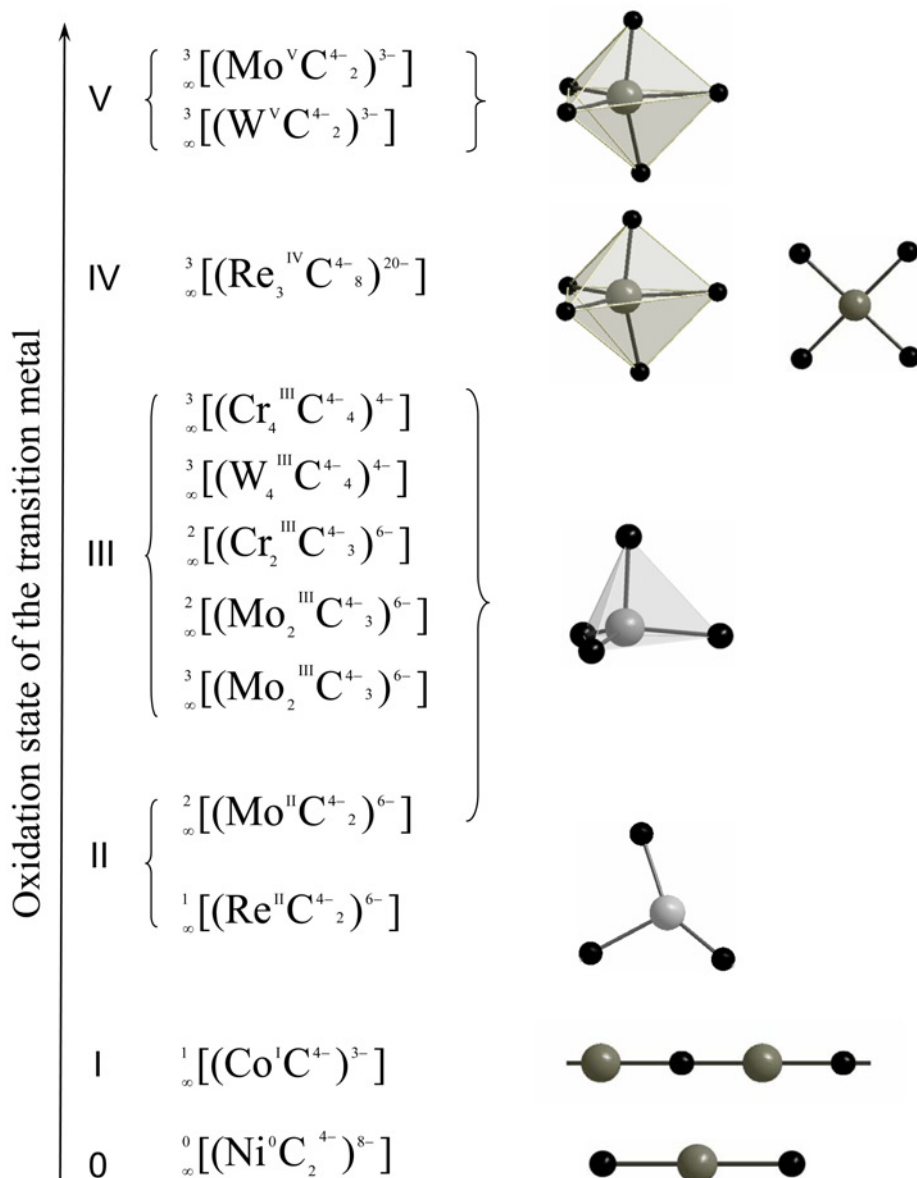


Figure 1.2: Ionic formulae and building units of complex carbometalate anions. Oxidation states of the transition metal atoms are indicated.

The remaining 40 structure types of ternary carbides  $RE_xT_yC_z$  contain  $C_2^{n-}$ ,  $C_3^{m-}$  units or mixed ligands,  $C^{4-}$  and  $C_2^{2-}$ . Examples are  $RE_2\text{FeC}_4$  [29],  $RE_{3.67}\text{FeC}_6$  [30],  $RETC_2$  ( $T = \text{Fe}, \text{Ni}, \text{Co}$ ) [31],  $RE_3\text{Ru}_2\text{C}_5$  [32],  $\text{GdRuC}_2$  [33],  $RE_7\text{Ru}_2\text{C}_{11}$  [34],  $RE_{10}\text{Ru}_{10}\text{C}_{19}$  [35],  $RE_4\text{Ni}_2\text{C}_5$  [36],  $RE_3\text{Mn}_2\text{C}_6$ -type [37],  $\text{La}_7\text{Os}_4\text{C}_9$  [38]. Their crystal structures can be described using complex polyanions and the metal to carbon ratio is in the same range as for the carbometalates,  $(x+y)/z \leq 2$ . However, according to the IUPAC nomenclature for polyanionic structures [39], the compounds containing  $C_2^{4-}$  or  $C_2^{2-}$  ligands, should be named

as dicarbo(4-) or dicarbo(2-) metalates. The situations gets more complicated for compounds containing mixed ligands such as monoatomic, diatomic or even triatomic carbon species. In general it is possible to name these polyanionic compounds as complex intermediate carbides. In reference [40] these types of carbides are also named as complex carbides. Now a question arises: Can we adopt the concept of complex anions to these compounds?

The main motivation of this work was the preparation and characterization of novel compounds in the ternary systems  $RE-T-C$  with  $T = Cr, Fe$  and  $Ru$  with a special focus on compounds containing  $C_2^{n-}$  and  $C_3^{m-}$  or mixed C and  $C_2^{n-}$  as structural units. This would allow to investigate the applicability of the concept of complex anions to this class of materials. The following tasks have been formulated to achieve this goal.

- To explore suitable phase diagrams for new intermediate ternary phases
- To optimize the synthesis conditions in order to grow single crystals suitable for crystal structure determinations, and to obtain single phase materials, which are essential for physical property measurements
- To investigate the electronic structures and the chemical bonding situations
- To shed light on the relationships between crystal chemistry, physical properties and chemical bonding
- To compare the chemical bonding situation, the crystal chemical aspects and the properties of real carbometalates with the ternary carbides containing  $C_2^{n-}$ ,  $C_3^{m-}$  units or some mixed ligands

This work is mainly focused on the ternary  $RE-Fe-C$  systems because there are no carboferrates known up to now. A large number of investigations were carried out and published in the literature on the binary rare-earth iron compounds in order to synthesize new magnetic materials by interstitial insertion of light elements such as H, C or N. About 200 entries can be found in the metals database [10] and in the database for inorganic compounds exclusively concerning the effect of carbon doping on the magnetic properties of phases  $RE_xFe_y$ . Due to their complex crystal structures and strong, dominating metal-metal interactions it is hard to unravel the origin of this effect. Thus, detailed information about the relationships between crystal structure, chemical bonding and properties of intermediate ternary carbides would also help to explain the regularities observed in metal rich carbides.

Favorable effects of rare-earth elements on the mechanical and other properties of steel have been widely mentioned in the literature. There are three main roles of rare-earth metals in steels: (i) modification of inclusions (shape control and modification of impurities such as MnS), (ii) deep purifying steel (deoxidation, desulfurization, and removing or depressing P, S, As, Sb, Bi, Pb, Sn), and (iii) alloying [41–43]. The largest part of the studies in this field is aimed on the modification of the mechanical properties of different kinds of steel. The properties of the steels can be modified by playing with the amount of rare-earth additions or the annealing temperature. However, the mechanism of the influence of the rare-earth ad-

ditions on the property of the steel is still not clear. Thus, systematic investigations of the  $RE-Fe-C$  systems would also have great practical importance for the steel industry. In this respect, the explorative synthesis of new ternary phases in the systems  $RE-Fe-C$  is essential to study the phase equilibria and phase stabilities for the construction of ternary  $RE-Fe-C$  phase diagrams.

**Scope of the thesis.** This thesis consists of 9 Sections. The theoretical and experimental background is first presented in *Sections 1 to 3* whereas the results are discussed in *Sections 4 to 8*. *Section 1* includes a brief introduction and motivation of the work followed by an overview of the binary and ternary systems that are important for this work. The preparation methods along with the starting materials are described in *Section 2*. A wide spectrum of techniques including X-ray diffraction methods, metallographic examinations, X-ray and Mössbauer spectroscopic studies, ICP-OES and combustion techniques, thermal analyses, electrical resistivity and magnetic susceptibility measurements and chemical bonding analyses were used to characterize the new compounds and are briefly mentioned in *Section 3*. In *Sections 4 to 7*, the syntheses, characterizations and crystal chemical aspects along with chemical bonding of the novel intermediate ternary phases  $RE_{15}[Fe_8C_{25}]$  ( $RE = Y, Dy, Ho, Er$ ),  $RE_{5.64}[Fe_2C_9]$  ( $RE = Y, Gd, Tb, Dy$ ),  $La_{3.67}[T(C_2)_3]$  ( $T = Fe, Ru$ ) and  $Sm_2[Cr_2C_3]$  are described. All experimental and theoretical results obtained within this work are then summarized in *Section 8*. Additional details on crystal structures, such as interatomic distances, anisotropic atomic displacement parameters and bond angles are listed in *Section 9* (Appendix).

## 2 Literature survey

### 2.1 Overview of the binary subsystems of ternary systems $RE-T-C$ ( $T = \text{Cr, Fe, Ru}$ )

The knowledge about related binary compounds is essential for the exploratory synthesis of novel ternary carbides. In contrast to the ternary rare-earth transition metal carbides, the binary phases of these systems have been well studied. However, a few systematic investigations of the ternary systems  $RE-T-C$  ( $T = \text{Cr, Fe, Ru}$ ) are already reported, which will be discussed in *Section 2.2*.

A certain amount of binary compounds were present as minority phases in most of the samples under investigation. Poor knowledge about binary compounds could lead to misinterpretations of chemical and physical properties of the new ternary phases. In the next section, a short overview on phase diagrams, crystal structures and chemical/physical properties of the binary phases of the systems,  $RE-C$ ,  $T-C$  and  $RE-T$  is given. The binary phase diagrams  $\text{Cr-C}$  and  $\text{Fe-C}$  are discussed in separate sections. The  $RE-C$  and  $RE-T$  systems contain a large number of stable and metastable binary compounds with a variety of structure types. Not every structure type is found for each  $RE$  element and the respective phase equilibria differ from one system to another. Thus, phase diagrams  $RE-C$  and  $RE-T$  are not discussed in this work, since it is hard to find representative data in literature.

#### 2.1.1 $RE-C$ ( $RE = \text{rare-earth metals}$ )

In the binary systems  $RE-C$ , more than 80 compounds, adopting 15 different structure types, were reported. The structural chemistry of binary rare-earth carbides is well investigated and intensive studies on the physical, especially the thermoelectrical properties of these compounds have been carried out. The reported binary rare-earth carbides, their crystal structure types and their properties are summarized in *Table 2.1* and will be discussed in detail in this section.

A critical evaluation of the systems  $RE-C$  revealed the existence of two related structures  $\beta-RE_3C$  and  $\alpha-RE_2C$ , each having a wide homogeneity range at high temperatures [44]. The unit cell constants of  $\beta-RE_3C$  and  $\alpha-RE_2C$  are given in *Table 9.1* in the appendix. The high temperature phase of the tri-rare-earth carbides,  $\beta-RE_3C$  or  $(RE_3C)$  crystallize with a C deficient NaCl-type structure, S.G.  $Fm\bar{3}m$  (225), commonly known as  $\text{Fe}_4\text{N}$ -type and exist with  $RE = \text{Y}$  and  $\text{Sm-Lu}$ . The  $RE$  atoms are arranged in a cubic close packed structure with the carbon atoms distributed randomly over the octahedral sites.  $\beta$  phase can also exist at room temperature in a metastable state. The low temperature phase  $\alpha-RE_2C$  crystallizes in the anti- $\text{CdCl}_2$  structure type, S.G.  $R\bar{3}m$  (166), with  $RE = \text{Y, Gd-Er, Yb}$ . Depending on the  $r_C/r_{RE}$  ratio, which is between 0.41 and 0.59 in *ccp* structures (Hägg's rule), these structure types do not form in the case of the early rare-earth elements. The crystal structure is

Table 2.1: Summary of binary rare-earth carbides.

Compound <sup>†</sup>	RE	Str. type, S.G.	C species	$d(\text{C-C})/\text{pm}$	Properties <sup>‡</sup> , References
$RE_3C$ ( $\beta$ )	Y, Sm–Lu	$Fe_4N$ , $Fm\bar{3}m$	C	-	High temp. modification. Wide homogeneity range. Gd–Tm $\rightarrow$ PM. FM ordering. Sm $\rightarrow$ VVP. Metallic. [44, 45]
$RE_2C$ ( $\alpha$ )	Y, Gd–Er, Yb	anti- $CdCl_2$ , $R\bar{3}m$	C	-	Low temp. modification. Wide homogeneity range. Metallic. [44, 45]
$RE_4C_3$	Y, Tb–Lu	$Sc_4C_3$ , $I\bar{4}3d$	C	-	HT-HP phases. [44]
$RE_3C_4$	Ho–Lu	$Sc_3C_4$ , $P4/mnc$	C, $C_2$ , $C_3$	125, 134	Ho–Yb $\rightarrow$ PM. Lu $\rightarrow$ Pauli PM. Ho and Er $\rightarrow$ AF ordering. [44, 46, 47]
$RE_2C_3$	Y, La–Yb	$Pu_2C_3$ , $I\bar{4}3d$	$C_2$	$\approx 127$	Wide homogeneity range. PM. Pr, Nd, Tb–Ho $\rightarrow$ AF ordering. Bad metals. Y, La phases SCs. [44, 47–49]
$REC_2$ ( $\alpha$ )	Y, La–Lu	$CaC_2$ , $I4/mmm$	$C_2$	127-129	Low temp. modification. PM except $\alpha$ - $SmC_2$ . Ce–Sm $\rightarrow$ AF ordering. Metals. Y, La, Lu phases SCs. [44, 45, 48–50]
$REC_2$ ( $\beta$ )	Y, La–Tm, Lu	KCN, $Fm\bar{3}m$	$C_2$	127-138	High temp. modification. PM. Ce–Sm $\rightarrow$ AF ordering. Metals. [44, 45, 50]
$RE_4C_7$ ( $\alpha$ )	Y, Ho	$Y_4C_7$ , $P2_1/n$	C, $C_3$	127-138	Low temp. modification. PM. Semiconductors. [51]
$RE_4C_7$ ( $\beta$ )	Ho–Tm, Lu	$Lu_4C_7$ , $P2_1/c$	C, $C_3$	130-135	High temp. modification. PM. Magnetic order below 20 K. [52]
$RE_4C_5$	Y, Gd–Ho	$Y_4C_5$ , $Pbam$	C, $C_2$	134	[53]

<sup>†</sup> Note: information about graphite intercalation compounds and fullerides are not included in this table

<sup>‡</sup> PM: Paramagnetic, Pauli PM: Pauli paramagnetic, FM: Ferromagnetic, AF: Antiferromagnetic, VVP: Van Vleck Paramagnetic, SCs: Superconductors, HT-HP: High temperature - High pressure

composed of hexagonal layers stacked along the  $c$  axis in sequence  $AcB\Box CaA\Box BbC\Box$  where  $A$ ,  $B$ ,  $C$  are RE layers,  $a$ ,  $b$ ,  $c$  are carbon layers and  $\Box$  are vacant layers (Figure 2.1). The crystal structure can be viewed as a cubic close packing of RE atoms alternately interleaved by filled and vacant carbon layers [45].

Some authors call these carbides nonstoichiometric monocarbides or hypocarbides (meaning under-carbide) [44], because microprobe analyses suggests homogeneity ranges from 4 to 2.5 RE per C atom ( $YC_{0.25}$  to  $YC_{0.4}$ ). The hypocarbides of RE = Gd–Tm show paramagnetic behavior and order ferromagnetically at low temperatures except for the Sm compound, which shows Van Vleck paramagnetism. All hypocarbides are metals and they can be described as methanides.



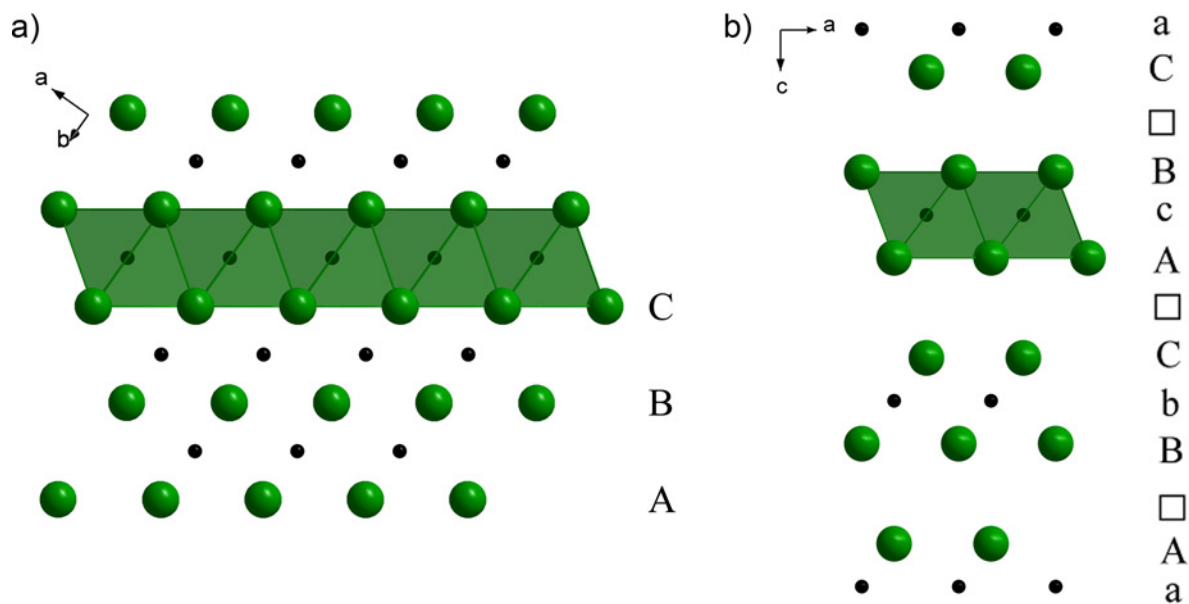


Figure 2.1: Sequence of close packed layers in the crystal structure of a)  $\beta$ - $RE_3C$  and b)  $\alpha$ - $RE_2C$ .

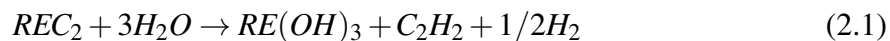
The compounds  $RE_4C_3$  with  $RE = Y, Tb-Lu$  were prepared by high temperature–high pressure methods. They are isotypic with  $Sc_4C_3$ , S.G.  $I\bar{4}3d$  (220), and contain monoatomic carbon species. The unit cell parameters and volume are listed in *Table 9.2*.

The  $Sc_3C_4$  (or earlier cited as  $Sc_{15}C_{19}$  [47]) structure type ( $P4/mnc$  (128)) forms with  $RE = Ho-Lu$  and was reported by Jeitschko *et al.* [46]. Unit cell parameters and volumes of the isotypic compounds  $RE_3C_4$  are summarized in *Table 9.3*. They are prepared by arc melting of mixtures of the elements in Ar atmosphere. The crystal structure contains  $C_3$ ,  $C_2$  and monoatomic carbon species. This fact is supported by analyzing the gaseous products formed by hydrolysis experiments. The C–C bond lengths for the  $C_3$  unit are ca. 134 pm, rather indicating a double bond, and each unit is located in a distorted bicapped quadratic antiprism (CN = 10) of  $RE$  atoms. The C–C distance for the  $C_2$  unit is 125.3 pm, which is closer to the triple bond length in ethyne of 120.3 pm. Both, isolated carbon atoms and the  $C_2$  units occupy octahedral holes. The magnetic susceptibilities of the isotypic  $Ho-Yb$  compounds obey the Curie-Weiss law while  $Lu_3C_4$  is a Pauli paramagnet. The Ho and Er compounds order antiferromagnetically at low temperatures, whereas, Tm and Yb compounds do not order down to 2 K. All  $RE_3C_4$  compounds are reported to be moisture sensitive.

The sesquicarbides  $RE_2C_3$  are synthesized by high temperature–high pressure methods. The phases with  $RE = La-Ho$  are stable while  $RE = Y, Er-Yb$  are metastable at ambient pressure. The unit cell parameters and unit cell volumes of the isotypic  $RE_2C_3$  phases are summarized in *Table 9.4*. The existence of a homogeneity range is observed for all  $RE_2C_3$  phases, except for  $Ce_2C_3$ , and extends to the metal rich side. The rare-earth sesquicarbides crystallize in the *bcc*  $Pu_2C_3$  structure type, S.G.  $I\bar{4}3d$  (220), which can be regarded as a variation of the anti  $Th_3P_4$  structure with carbon pairs replacing Th and rare earth replacing P, namely  $RE_4(C_2)_3$ , however with a higher coordination number for  $RE$ . No phase transition

was observed down to low temperatures. The C–C distances in all these isotopic compounds are slightly elongated (ca. 127 pm) compared to that of ethyne. There is a general agreement in the literature that  $C_2H_2$  and  $H_2$  are the primary gaseous reaction products by hydrolysis of  $RE_2C_3$ , which can therefore be classified as acetylides. It was argued that the instability of the  $Pu_2C_3$  structure type, which starts with  $Er_2C_3$  in the  $Lu_2C_3$  series, occurs when the non-bonding C–C distance becomes shorter than the van der Waals contact of 320 pm [44]. The paramagnetic scattering in these compounds gave effective magnetic moments in agreement with pure trivalent metal atoms, except for Ce. The Pr, Nd, Tb–Ho phases all exhibit antiferromagnetic ordering at low temperatures while Y, La and Lu members are superconducting over their entire homogeneity range [44, 48]. The rare-earth sesquicarbides are bad metals.

The golden yellow rare-earth dicarbides  $REC_2$  with  $RE = Y, La-Lu$  are prepared from the elements by high temperature reaction or by carbothermic reduction of metal oxides. They possess the tetragonal  $CaC_2$  structure type, S.G.  $I4/mmm$  (139), at room temperature ( $\alpha$ -modification) [45, 50]. The unit cell parameters and unit cell volumes of the isotopic  $REC_2$  phases are summarized in *Table 9.5*. The structure can be described as a distorted NaCl structure type composed of Ca atoms and  $C_2$  units. The C–C distances, 127 pm to 129 pm, in the  $C_2$  group are considerably larger than the 120 pm for the C–C triple bond in ionic alkaline earth dicarbides. The  $\alpha$ -phase transforms at high temperatures into a  $\beta$  modification, with face centered cubic KCN structure type, S.G.  $Fm\bar{3}m$  (225), which is observed for all  $RE_2C$  compounds, except for Yb. A Curie-Weiss law was observed by all  $REC_2$ , except  $\alpha$ - $SmC_2$ , well above 80 K. The  $RE = Ce-Sm, Tb-Er$  compounds become antiferromagnetic at low temperatures. The  $\mu_{\text{eff}}$  values are compatible with respective  $RE^{3+}$  ions. The tetragonal dicarbides with  $RE = Y, La-Er$  show metallic conductivity, whereas  $TmC_2$  behaves more like a semimetal. The Y, La and Lu compounds possess superconducting properties at low temperatures. The compounds  $REC_2$  are oxidized in air during heating to form the respective sesquioxides. They show catalytic activity for the para- $H_2 \leftrightarrow$  ortho- $H_2$  conversion. The overall hydrolysis reaction of lanthanide dicarbides takes place according to the following equation, similar to the sesquicarbides:



The rare-earth dicarbides are decomposed by inorganic acids and bases as well. Another feature of the rare-earth dicarbides is the formation of mixed dicarbides,  $RE_{1-x}RE'_x C_2$  [44].

Slightly more metal-rich  $RE$  carbides are formed at a nominal composition  $RE_4C_7$ . They have two different modifications with closely related crystal structures. The low temperature phase ( $\alpha$  modification) is known for  $RE = Y, Ho$  and crystallizes in S.G.  $P2_1/n$  (14) [51], whereas the high temperature modification ( $\beta$  phase) is reported for  $RE = Ho-Tm, Lu$  and their crystal structures were refined in S.G.  $P2_1/c$  (14) [52]. The unit cell parameters and unit cell volumes of the  $\alpha$ - and  $\beta$ -phases are given in *Table 9.6* (appendix). Both structures

contain two different carbon species:  $C^{4-}$  and linear  $C_3^{4-}$ . The monoatomic carbon atoms occupy the octahedral voids formed by rare-earth atoms. The  $RE$  octahedra form infinite puckered sheets which can be regarded as NaCl-type sheets. These sheets are separated by  $C_3$  units. The two structures can be viewed as stacking variants. In the  $\beta$  phase the stacking sequence is  $ABABAB\dots$  while it is  $AABBAABB\dots$  in the  $\alpha$  modification, where  $A$  and  $B$  represent the 2D infinite slabs running perpendicular to  $c$  and  $b$  of the unit cells of the  $\beta$  and  $\alpha$  modifications, respectively. The distances  $d(C-C)$  range from 126.8 pm to 137.7 pm and 130 pm to 135 pm in the  $\alpha$  and  $\beta$  modifications, respectively. The temperature-dependent magnetic susceptibilities of  $\alpha$ -,  $\beta$ - $Ho_4C_7$  and  $\beta$ - $Er_4C_7$  follow a Curie-Weiss law while the Y and Lu compounds are Pauli-paramagnets. The compounds show semiconducting behavior. The hydrolysis of the Lu compound mainly yields methane and propene.

Another type of binary carbides is represented by  $RE_4C_5$  ( $RE = Y, Gd-Ho$ ) [53], which was synthesized by arc melting of mixtures of the elements. The unit cell parameters and unit cell volumes of the compounds  $RE_4C_7$  are given in *Table 9.7* (appendix). The crystal structure of  $RE_4C_5$ , *oP18*, S.G. *Pbam* (55), contains 2  $RE$  and 3 C positions. One-fifth of the carbon atoms are isolated whereas the other carbon atoms form  $C_2$  dimers. The authors proposed a charge balanced formula,  $(RE^{3+})_4(C_2^{4-})_2C^{4-}$ . The hydrolysis of  $RE_4C_5$  results in a great variety of hydrocarbons [53].

Beside these types of binary carbides, the rare-earth elements form graphite intercalation compounds (GICs)  $REC_6$  [44] and fullerides –  $RE_2C_{60}$ ,  $RE_3C_{70}$  etc. [54, 55]. The GICs form by regular incorporation of additional atoms or compounds between the carbon layers of the graphite structure. They can be synthesized by reaction of graphite with metal vapor at temperatures below 873 K. The structure is described in the hexagonal S.G. *P6<sub>3</sub>/mmc* (194), with metal atoms on  $2h$  and carbon on  $12i$  sites, where the intercalated atoms are located above every third graphite hexagon in one layer. The intercalated phases show paramagnetic susceptibility and magnetic order at low temperatures. Many attempts to incorporate a wide variety of atoms or molecules into fullerenes have been made since the discovery of superconductivity in  $K_3C_{60}$  [56]. The rare-earth fullerides, e.g.,  $Yb_2C_{60}$ , are formed by exposing a film of empty fullerene molecules to a flux of Yb in ultrahigh vacuum. The thin-film electrical resistivity measurement indicate that  $Yb_2C_{60}$  is a superconductor.

### 2.1.2 $T - C$ ( $T = Cr, Fe, Ru$ )

#### Cr – C

The binary phase diagram of the Cr–C, system is well investigated [57] and three binary phases, namely  $Cr_7C_3$ ,  $Cr_3C_2$  and  $Cr_{23}C_6$  are reported.  $Cr_3C_2$  and  $Cr_{23}C_6$  form peritectically whereas the  $Cr_7C_3$  melts congruently, and all phases show homogeneity ranges up to several at.% (*Figure 2.2*) [58]. Technical applications of the chromium carbides include bearings, seals, valve seats and orifices. Chromium carbides are used as thermal spray materials for

protecting the underlying metal surface, and as additives to corrosion-resistant and wear-resistant materials. The reported chromium carbides and their modifications, their structure types, and their solidification behavior are given in *Table 2.2*.

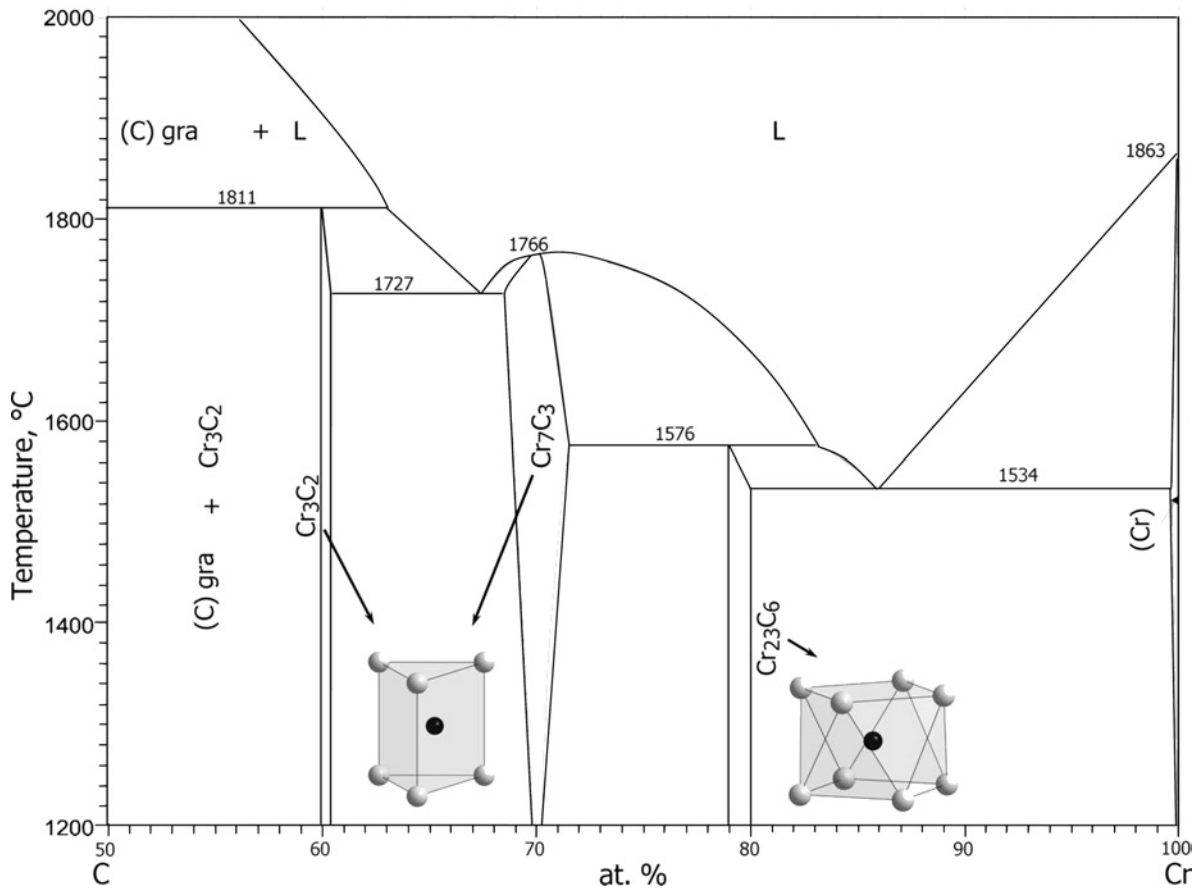


Figure 2.2: The binary phase diagram of the system Cr–C (50 to 100 at%). The local environments of the carbon atoms in the respective carbides are also shown. Redrawn from Pauling file [58].

The so-called  $\tau$ -carbide  $\text{Cr}_{23}\text{C}_6$  [59] is formed during heat treatment of many iron- and chromium-based alloys containing carbon. It can adversely affect the mechanical properties of such technologically important materials as ferritic and austenitic stainless steels. It can be prepared by high temperature synthesis methods, but preparation of single phase chromium carbide powders is a real challenge; they exhibit poor sinterability. Recently, Hirota *et al.* [60] succeeded to synthesize almost single-phase material by the pulsed electric-current pressure sintering method and the mechanical properties have been evaluated.  $\text{Cr}_{23}\text{C}_6$  crystallizes in the face-centered cubic lattice,  $cF92$ , S.G.  $Fm\bar{3}m$  (225), ( $a = 1065.0(2)$  pm,  $V = 1207.95(2) \cdot 10^6$  pm<sup>3</sup>) [61]. The structure may be viewed as a network of edge-sharing, non-interpenetrating Friauf polyhedra [62]. The Cr coordination around the carbon atom is a square anti-prism (CN = 8), with the carbon atom displaced slightly from the center. Electronic structure calculations of  $\text{Cr}_{23}\text{C}_6$  show that it is a metal with low magnetization associated with the Cr sites [63].

According to the phase diagram  $\text{Cr}_7\text{C}_3$  shows the widest homogeneity range among the

binary chromium carbides [58]. Some references reveal that  $Cr_7C_3$  exists in two different modifications, orthorhombic and hexagonal. However, in the phase diagrams reported up to now the information about HT-LT phase transition of  $Cr_7C_3$  is not included. As it was reported in [64–66], above 1200 °C, the orthorhombic structure of  $Mn_7C_3$ -type (S.G.  $Pm\bar{c}n$  (62),  $a = 701.49(12)$  pm,  $b = 1215.3(2)$  pm,  $c = 453.20(4)$  pm,  $V = 386.36(3) \cdot 10^6$  pm<sup>3</sup>) is formed, while the hexagonal modification with  $Ru_7B_3$ -type (S.G.  $P6_3mc$  (186),  $a = 1401(2)$  pm,  $c = 453(1)$  pm,  $V = 770.03(7) \cdot 10^6$  pm<sup>3</sup>), is stabilized below this temperature. First-principles calculations show that the hexagonal phase is energetically more stable than the orthorhombic one at 0 K, in agreement with the existence of the hexagonal phase at low temperatures. Furthermore, the Debye temperature of the orthorhombic phase is lower than that of the hexagonal one, indicating the stabilization of the orthorhombic phase at high temperatures by vibrational entropy [67]. The compound is synthesized by solid-state reaction of Cr/C mixtures or reduction of methane [68] and by the electric-current pressure sintering method [60]. In the hexagonal modification, the chromium atoms are forming octahedral and trigonal bipyramidal channels, running parallel to the  $c$  axis, oriented such that trigonal prismatic voids are formed between both types of columns available for accommodation of carbon atoms. Here, all the octahedral columns have the same orientation. Thus, the three prismatic voids positioned on the same half of the trigonal bipyramids are occupied and/or rectified. In the high temperature phase with  $Mn_7C_3$ -structure type, the confacial octahedral channels adopt two different orientations allowing for two crystallographically different carbon coordinations [69]. In this case, carbon fills two voids adjacent to one half and one void adjacent to the second half of the trigonal bipyramids.  $Cr_7C_3$  is non-magnetic and shows metallic behavior [70, 71].

$Cr_3C_2$  has the highest melting-point among the binary chromium carbides ( $T_m = 1800$  °C) and exhibits high-temperature oxidation resistance, good chemical stability and high hardness. Therefore, its electrical, thermal and mechanical properties have been investigated from the viewpoint of high-temperature materials.  $Cr_3C_2$  powder has been prepared by several methods: *i*) high temperature synthesis method [64], *ii*) solid-state reaction of Cr/C mixture under reductive atmosphere and *iii*) the electric-current pressure sintering method [60].  $Cr_3C_2$  crystallizes orthorhombic, S.G.  $Pnma$  (62),  $a = 553.99(6)$  pm,  $b = 283.27(4)$  pm,  $c = 1149.4(1)$  pm,  $V = 180.4(3) \cdot 10^6$  pm<sup>3</sup>. The chromium atoms form edge and face sharing bicapped trigonal prisms occupied by isolated carbon atoms. The temperature dependent magnetic susceptibility of  $Cr_3C_2$  follows the Curie-Weiss law, and the total density of states reveals a metallic character [64].

In addition to the stable chromium carbides, Inoue and Masumoto [72] have obtained metastable  $Cr_3C$  with  $Fe_3C$ -type structure ( $a = 458(1)$  pm,  $b = 512(1)$  pm,  $c = 680.0(1)$  pm,  $V = 159.46(3) \cdot 10^6$  pm<sup>3</sup>) by rapid quenching. Liu and Cheng [73] observed a metastable phase  $CrC$  ( $a = 403$  pm,  $V = 65.45 \cdot 10^6$  pm<sup>3</sup>) with rocksalt-type structure using carbon-ion implantation.  $CrC$  was found to be stable only up to  $\sim 250$  °C. In contrast,  $Cr_3C$  remains

unchanged until the temperature exceeds  $\sim 700$  °C. First principles calculations reveal that  $\text{Cr}_3\text{C}$  is a stable phase while  $\text{CrC}$  has a positive formation enthalpy and is thus unstable with respect to phase separation into pure Cr and C at 0 K [67].

Table 2.2: Summary of binary chromium carbides

Compound <sup>†</sup>	Str. type, S.G.	Reaction type	Properties, References
$\text{Cr}_{23}\text{C}_6$	$\text{Cr}_{23}\text{C}_6$ , $Fm\bar{3}m$	peritectic	metallic, low magnetization [58, 60–63]
$\text{Cr}_7\text{C}_3$	$\text{Mn}_7\text{C}_3$ , $Pm\bar{c}n$	congruent	high temp. phase, non magnetic, metallic. [58, 60, 64–71]
	$\text{Ru}_7\text{B}_3$ , $P6_3mc$		low temp. phase, non magnetic, metallic. [58, 60, 64–71]
$\text{Cr}_3\text{C}_2$	$\text{Cr}_3\text{C}_2$ , $Pnma$	peritectic	metallic, paramagnetic. [60, 64]

<sup>†</sup> Note: information about  $\text{CrC}$  and  $\text{Cr}_3\text{C}$  are not included in this table

## Fe – C

The binary system Fe–C is one of the technologically most important systems, and has a wide range of applications, in direction of steel production. Most of the important mechanical properties of high-strength steels develop during heat treatments that produce specific forms and distributions of carbide precipitates in austenitic or ferritic solid solution matrices [74]. Due to the existence of several metastable phases in this system, stable and metastable phase diagrams are reported. Because of its technological importance, the metastable Fe–C phase diagram in between Fe and  $\text{Fe}_3\text{C}$  is briefly discussed in this section (*Figure 2.3*).

The vast majority of steels rely on just two allotropes of iron: 1)  $\alpha$ -iron, body-centered cubic (*bcc*), solid solutions named ferrite, and 2)  $\gamma$ -iron, face-centered cubic (*fcc*), austenite. At ambient pressure, ferrite is stable at temperatures up to 911 °C, when it transforms into austenite. It reverts to high-temperature ferrite, labeled as  $\delta$ -iron, at 1392 °C.  $\delta$ -ferrite remains stable until it melts at 1536 °C. Ferrite ( $\alpha$ -iron) can dissolve up to 0.12 at.% (0.028 wt.%) C at 723 °C, while austenite ( $\gamma$ -iron) can dissolve 8.7 at.% (2.06 wt.%) C at 1147 °C (point **E** in *Figure 2.3*). The hardening of carbon steels, as well as many alloy steels, is based on this difference in the solubility of carbon in  $\alpha$ -iron and  $\gamma$ -iron. Various microstructures can be produced in steel alloys depending on the carbon content and the heat treatment. As a consequence of these different microstructures, the mechanical properties are changed. The eutectoid reaction  $\gamma$ -iron  $\rightarrow$   $\alpha$ -iron +  $\text{Fe}_3\text{C}$  (cementite) forms the pearlite microstructure (point **S**). The eutectic structure (eutectic point **C**) of the Fe–C system is called ledeburite I, constituting of austenite and cementite. At 723 °C ledeburite II, composed of primary cementite with recrystallized secondary cementite and of pearlite, is formed. So called bainite, another type of microstructure, consist of aggregates of plates of ferrite, separated by untransformed austenite, cementite or martensite [76]. Rapid cooling of austenite results in the formation of martensite (a body centered tetragonal phase).

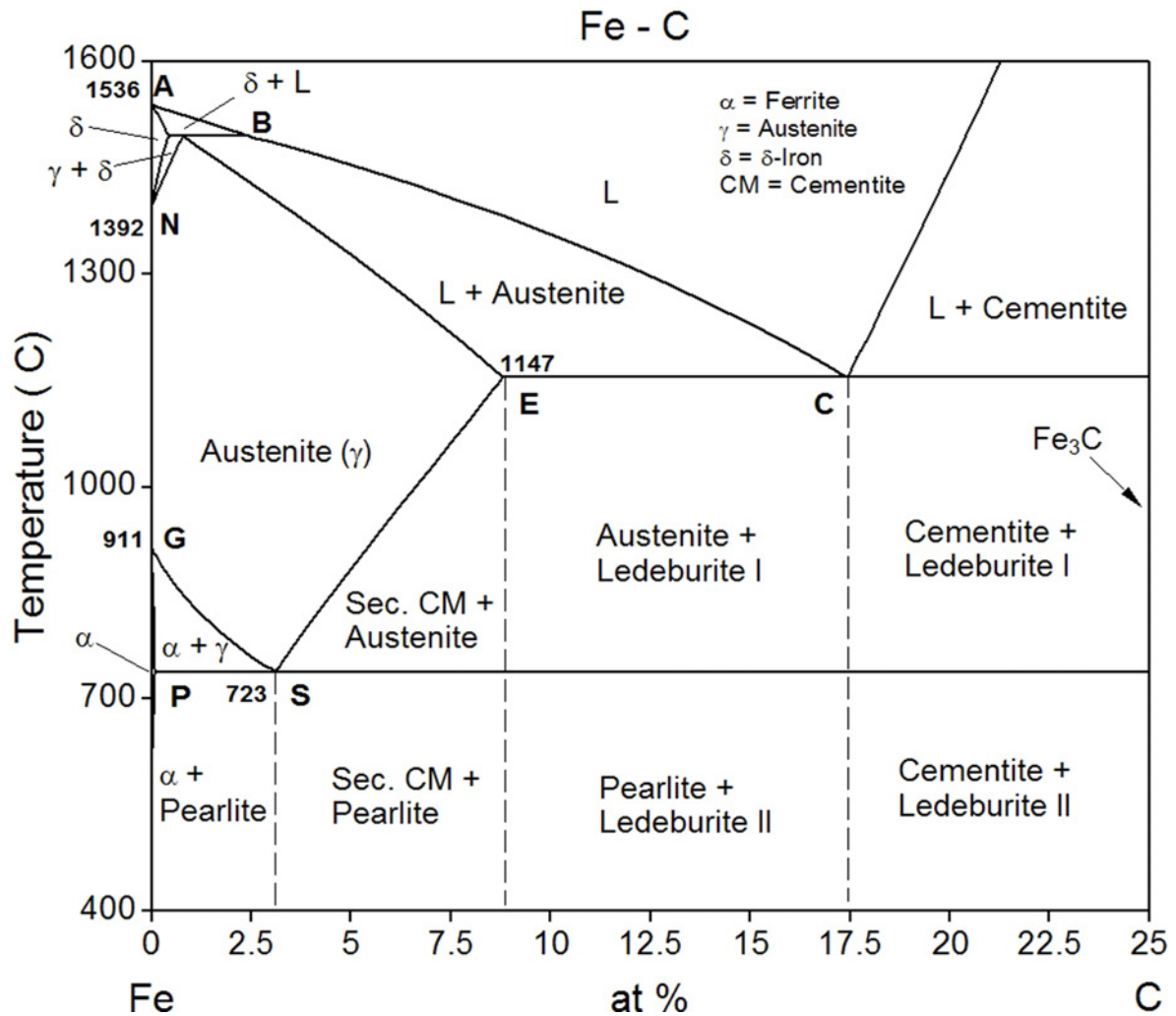


Figure 2.3: The Fe-rich part of the metastable Fe–C phase diagram. Drawn by the program Pandat [75].

In the Fe–C system, several binary phases such as  $\theta$ -Fe<sub>3</sub>C (cementite), the metastable Hägg- or  $\chi$  carbide, Fe<sub>5</sub>C<sub>2</sub> (in older references also named as iron percarbide [74]),  $\epsilon$ -Fe<sub>3</sub>C,  $\epsilon$ - and  $\eta$ -Fe<sub>2</sub>C and Fe<sub>7</sub>C<sub>3</sub> [74, 77] are known. The existing stable and metastable iron carbides and their polymorphous modifications, the respective structure types, the environment of the carbon atoms, Fe–C distances and selected properties are summarized in *Table 2.3*.

The  $\chi$ -carbide or Hägg carbide (Fe<sub>5</sub>C<sub>2</sub>) may form during the low temperature carburization of iron, iron oxide, or iron nitrides [74]. The crystal structure was determined from powder X-ray diffraction data by Rietveld methods [78] and adopts the Mn<sub>5</sub>C<sub>2</sub> structure type, S.G. C2/c (15),  $a = 1156.3(1)$  pm,  $b = 457.3(1)$  pm,  $c = 505.8(1)$  pm,  $\beta = 97.44^\circ$ . In this compound, each carbon atom is coordinated by 6 Fe atoms arranged in a trigonal prismatic manner. If one considers the network of iron-atom coordination polyhedra around the carbon atoms in cementite, one sees that they occur in single walls (each composed of a Fe–C–Fe sandwich) isolated from each other along [010]. In Fe<sub>5</sub>C<sub>2</sub> iron-atom coordination polyhedra around the carbon atoms occur in double-layered walls, each composed of an Fe–C–Fe–C–

Fe sandwich. One can also describe the arrangement of Fe atoms as pleated layers similar to cementite. The interatomic distances in  $\text{Fe}_5\text{C}_2$  range from  $d(\text{Fe-Fe}) = 247.1$  pm to 278.3 pm and  $d(\text{Fe-C}) = 169.6$  pm to 201.2 pm [78]. The total density of states shows that the  $\chi$ -carbide is a metal with a calculated mean magnetic moment of  $1.71 \mu_B/\text{Fe}$  [79] which is close to the measured value of  $1.78 \mu_B/\text{Fe}$  [80]. Due to its relatively high saturation magnetization (about 100 e.m.u./g)  $\chi\text{-Fe}_5\text{C}_2$  is a candidate for magnetic materials, which can be used for high quality video and cassette tapes [81].

Cementite is the most important metastable phase in the Fe–C system and is an essential constituent for hardening of many commercial steels. It can be synthesized or separated in different ways: i) high temperature synthesis from the elements followed by high temperature heat treatment at 800 °C, ii) heating of the Hägg carbide in  $\text{N}_2$  atmosphere or iii) separation from annealed carbon steel by anodic oxidation of the matrix.

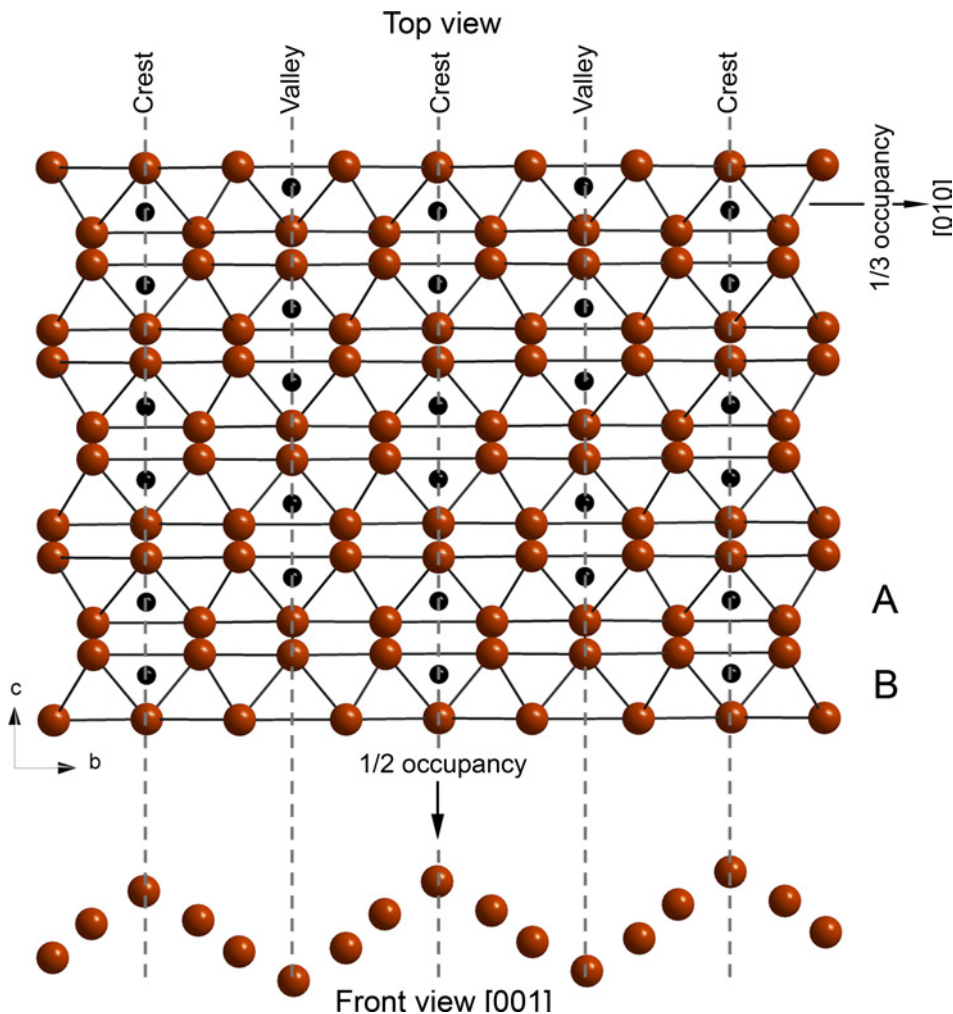


Figure 2.4: The pleated layers of  $\text{Fe}_3\text{C}$  viewed along [100]. The carbon atoms are arranged in different manner on the A and B pleated layers [82].

Single crystals can be grown by the Bridgman technique using graphite crucibles. The crystal structure was solved in S.G.  $Pnma$  (62),  $oP16$ , ( $a = 508.96(5)$  pm,  $b = 674.43(7)$  pm,  $c = 452.48(5)$  pm) [82]. As proposed by Fasiska [82], the arrangement of the Fe atoms of the ce-



mentite structure is best described by starting with the hexagonal close-packed arrangement. This arrangement is then compressed in  $[10\bar{1}0]$  direction so that the basal hexagonal layers fold at the lines of intersection of the  $(2\bar{1}\bar{1}0)$  planes to form regularly pleated layers stacked perpendicular to  $[100]$ . Carbon atoms occupy  $2/5$  ( $1/3$  along  $\langle 010 \rangle$  and  $1/2$  along  $\langle 001 \rangle$ ) of the all interstices that lie between the layers along the fold lines which are parallel to  $[001]$  (Figure 2.4). In other words, carbon atoms are surrounded by 6 Fe atoms forming trigonal prisms. It was concluded that the relative size of the interstitial non-metal atoms is the crucial factor in producing pleated or flat metal atom layers. Small non metal atoms, such as N, lead to flat layers ( $\epsilon\text{-Fe}_3\text{N}$ ), large ones, such as B, stabilize pleated layers, and interstitials of intermediate size, such as C, lead to both cementite and  $\epsilon\text{-Fe}_3\text{C}$  carbide [74, 82]. The interatomic distances in cementite range from  $d(\text{Fe-Fe}) = 244.3$  pm to 267.2 pm and vary between those in  $\alpha\text{-Fe}$  (248 pm),  $\gamma\text{-Fe}$  (260 pm) and  $\epsilon\text{-Fe}$  (250 pm to 253 pm);  $d(\text{Fe-C}) = 195.98$  pm to 201.11 pm [74, 83]. Electronic structure calculations showed that cementite is a ferromagnetic metal with an average magnetic moment for the iron atoms of  $1.95 \mu_B$  [83]. Cementite is the only superconducting phase in the Fe-C system with  $T_C$  of 1.3 K [48].

$\epsilon\text{-Fe}_3\text{C}$  may be produced by low temperature ( $170^\circ\text{C}$  to  $250^\circ\text{C}$ ) carburization of Fe or by tempering carbon-rich steels [74]. The composition of this phase seems to be variable between  $\text{Fe}_3\text{C}$  and  $\text{Fe}_2\text{C}$  [74, 79]. However, later in reference [77] it was reported that  $\epsilon\text{-Fe}_2\text{C}$  is a novel phase in the Fe-C system that crystallizes in the hexagonal S.G.  $P6_3mmc$  (194),  $a = 275.4(1)$  pm,  $c = 434.9(1)$  pm.  $\epsilon\text{-Fe}_3\text{C}$  adopts the  $\text{Fe}_3\text{N}$ -type structure, S.G.  $P6_322$  (182),  $a = 476.7(1)$  pm,  $c = 435.4(1)$  pm, where the Fe atoms are forming hexagonal close-packed layers. Carbon atoms are located in the octahedral interstices between the Fe atom layers in  $\epsilon\text{-Fe}_3\text{C}$  (Figure 2.5), while carbon has a trigonal prismatic coordination in cementite,  $\text{Fe}_5\text{C}_2$ , and  $\text{Fe}_7\text{C}_3$ .

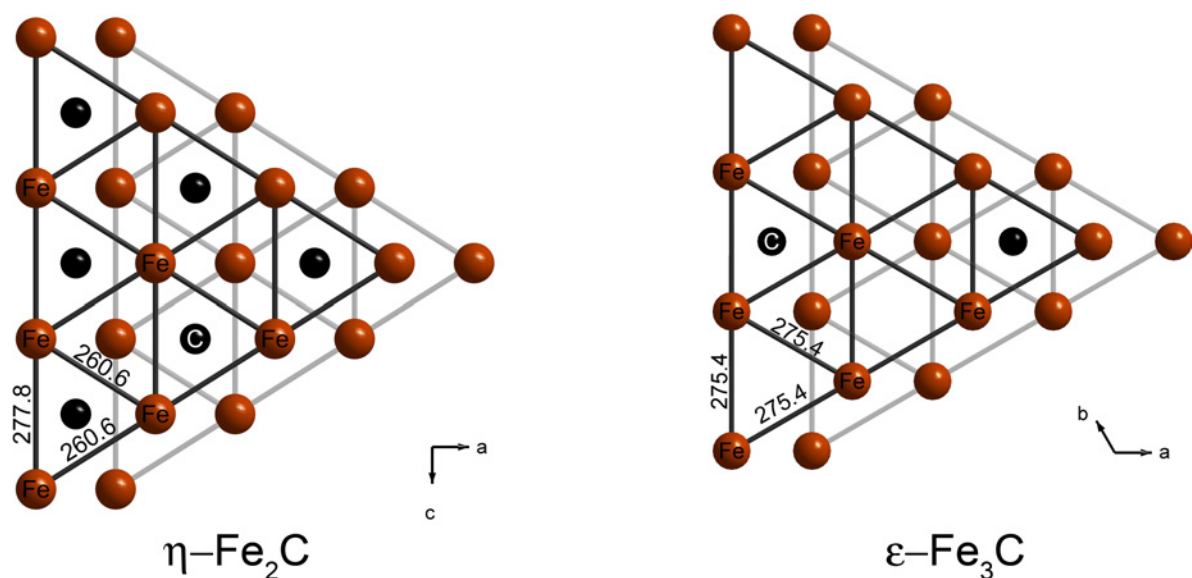


Figure 2.5: *hcp* layers of Fe atoms in the crystal structure of  $\eta\text{-Fe}_2\text{C}$  and  $\epsilon\text{-Fe}_3\text{C}$ . Carbon atoms occupy the octahedral voids; the lower layer is shaded.

There are as many octahedral voids as metal atoms. Both iron and carbon atoms form hexagonal close packed layers [84] with distances  $d(\text{Fe}-\text{C}) = 192.6$  pm and  $d(\text{Fe}-\text{Fe}) = 275.4$  pm. The calculated electronic structure indicates that  $\text{Fe}_3\text{C}$  exhibits a mixture of metallic, covalent, and ionic bonding. The average magnetic moment of  $\text{Fe}_3\text{C}$  is  $1.497 \mu_B/\text{Fe}$  atom [85].

$\eta\text{-Fe}_2\text{C}$  crystallizes in the  $\text{CaCl}_2$ -type structure (S.G.  $Pnmm$  (58)),  $a = 470.4(1)$  pm,  $b = 431.8(1)$  pm,  $c = 283.0(1)$  pm [79]. The Fe atoms again form a *hcp* arrangement containing octahedral voids available for carbon atoms. Distances  $d(\text{Fe}-\text{Fe})$  and  $d(\text{Fe}-\text{C})$  range from 259 pm to 278 pm and 181.6 pm to 189.9 pm, respectively [74, 82, 83]. First-principles total energy calculations show that  $\varepsilon\text{-Fe}_2\text{C}$  has no magnetic character while  $\eta\text{-Fe}_2\text{C}$  has a mean magnetic moment of  $1.66 \mu_B/\text{Fe-atom}$  [77, 79]. Both  $\varepsilon\text{-Fe}_3\text{C}$  and  $\varepsilon\text{-Fe}_2\text{C}$  are metallic carbides.

$\text{Fe}_7\text{C}_3$  is obtained by reacting of CO with Fe at 500 °C [86]. Two modifications with closely related crystal structures have been reported for  $\text{Fe}_7\text{C}_3$ : one with a hexagonal structure of  $\text{Ru}_7\text{B}_3$ -type,  $a = 688.2(1)$  pm,  $c = 454.0(1)$  pm [87, 88] and an orthorhombic phase of  $\text{Mn}_7\text{C}_3$ -type, S.G.  $Pm\bar{c}n$  (62),  $a = 687.9(1)$  pm,  $b = 1194.2(1)$  pm,  $c = 454.0(1)$  pm [89, 90]. The interatomic distances in both modifications of  $\text{Fe}_7\text{C}_3$  are very similar to those observed in cementite and the Hägg carbide. The iron-carbon distances in *hex*- $\text{Fe}_7\text{C}_3$  range from 193 pm to 206 pm and in the *orth*- $\text{Fe}_7\text{C}_3$  from 181 pm to 222 pm [86]. Both  $\text{Fe}_7\text{C}_3$  phases are ferromagnetic metals containing magnetic Fe species with mean magnetic moments of  $1.73 \mu_B/\text{Fe-atom}$ . Both materials have a high saturation magnetization and are also investigated for application in magnetic recording media [81, 86].

Table 2.3: Summary of binary iron carbides

Comp.	Str. type, S.G.	Coord. of C	$d(\text{Fe}-\text{C})/\text{pm}$	$\mu_B/\text{Fe}$	Properties
$\theta\text{-Fe}_3\text{C}$	$\text{Fe}_3\text{C}$ , $Pnma$	trigonal prism	196 to 201	1.95	FM, metallic. SC. [48, 74, 82, 83]
$\varepsilon\text{-Fe}_3\text{C}$	$\text{Fe}_3\text{N}$ , $P6_322$	octahedral	193	1.5	Metallic, magnetic. [74, 77, 79, 84, 85]
$\eta\text{-Fe}_2\text{C}$	$\text{CaCl}_2$ , $Pnmm$	octahedral	182 to 190	1.66	Metallic, magnetic. [74, 77, 79, 82, 83]
$\varepsilon\text{-Fe}_2\text{C}$	$\text{Fe}_3\text{N}$ , $P6_322$	octahedral	193	0	Metallic, non-magnetic. [74, 77, 79, 84, 85]
<i>orth.</i> - $\text{Fe}_7\text{C}_3$	$\text{Mn}_7\text{C}_3$ , $Pm\bar{c}n$	trigonal prism	181 to 222	1.74	FM, metallic. [81, 86–90]
<i>hex.</i> - $\text{Fe}_7\text{C}_3$	$\text{Ru}_7\text{B}_3$ , $P6_3mc$	trigonal prism	193 to 206	1.73	FM, metallic. [81, 86–90]
$\chi\text{-Fe}_5\text{C}_2$	$\text{Mn}_5\text{C}_2$ , $C2/c$	trigonal prism	167 to 201	1.71	Metallic, magnetic. [74, 78–81]

## Ru – C

No phase diagram or crystal structure data are available for the system C–Ru in the metals database [10], crystal structure database of inorganic compounds [11] and inorganic materials database [58].

### 2.1.3 $RE - T$

#### $RE - Fe$ systems

In the databases for intermetallic and inorganic compounds [10, 11, 58], more than 75 compounds adopting 17 structure types are reported for the binary systems  $RE-Fe$  up to now. The majority of them are Fe-rich compounds. Most of these compounds were produced by high temperature synthesis followed by high temperature heat treatments [91, 92]. Because of their interesting optical, electronic and magnetic properties and their structural variety, binary rare-earth iron phases were intensively studied by different authors. A lot of research was done on the influence of doping and substitution with elements such as H, B, N and C,  $RE$  or transition metals. For example the  $REFe_2$  compounds are good hydrogen absorbers. Hydrogenation of  $REFe_2$  or  $RE_2Fe_{17}$  alloys [93] and nitridation of  $Ce_2Fe_{17}$  and  $REFe_7$  change the magnetic properties dramatically [93–95]. The interstitial dissolution of H, C and N can expand the lattice of  $Nd_2Fe_{17}$ , leading to a significant increase of the Curie temperature [96]. The Curie temperature of the mixed rare-earth intermetallic compounds  $Sm_{2-x}Gd_xFe_{17}$  is unusually high compared to  $Sm_2Fe_{17}$  and  $Gd_2Fe_{17}$  [97]. In addition, it is well known that for compounds  $RE-Fe$  the Fe–Fe exchange interactions (a quantum mechanical effect which increases or decreases the expectation value of the energy or distance between two or more identical particles when their wave functions overlap) are dominant and essentially determine the value of  $T_C$ . The local environments of the Fe atoms are expected to influence the magnetic exchange interactions and the local moments on the Fe atoms.

The  $RE$  elements together with iron (except La and Eu) form Laves phases with both C15 ( $Fd\bar{3}m$  (227)) and C14 ( $P6_3/mmc$  (194)) structure. The unit cell parameters and unit cell volumes of the rare-earth iron Laves phases are listed in *Table 9.8*. In the C15 type the Fe atoms form a network of vertex-sharing tetrahedra, so that every Fe atom is linked with 6 other Fe atoms. The  $RE$  atoms have the same arrangement as the carbon atoms in diamond.  $RE$  atoms are coordinated by 4  $RE$  + 12 Fe (CN = 16), while Fe atoms have 6  $RE$  + 6 Fe (CN = 12) nearest neighbors, resulting in Frank-Kasper polyhedra around both atom types. The interatomic distances  $d(RE-RE)$  in these compounds are significantly shorter (by 20–40 pm) compared to those in the respective pure metals and the binary carbides [10, 11] whereas distances  $d(Fe-Fe)$  are similar compared with the Fe–Fe contacts in metallic iron, as well as binary and ternary iron carbides [29, 74]. The Y, Ce, Nd and Sm compounds show ferromagnetic behavior while the late rare-earth (Gd–Tm) compounds are ferrimagnetic. The magnetic moment of iron atoms in the  $REFe_2$  compounds is  $\approx 1.70 \mu_B$ , which is smaller

compared to that of pure iron ( $2.2 \mu_B$  for  $\alpha$ -Fe) [98–100].

The C14 rare-earth iron Laves phases were observed only at high pressure [101] and little is known about these phases.

The intermetallic compounds  $RE_2Fe_{17}$  crystallize with the rhombohedral  $Th_2Zn_{17}$  structure type (S.G.  $R\bar{3}m$  (166)) for the light rare-earth elements, and with the hexagonal  $Th_2Ni_{17}$  structure type (S.G.  $P6_3/mmc$  (194)) for the heavy rare-earth atoms smaller than Dy. For Gd, Tb and Y both structure types occur depending on the temperature. The unit cell parameters and unit cell volumes of the  $RE_2Fe_{17}$  compounds are listed in *Table 9.9*. Both structures are derivatives of the  $CaCu_5$ -type structure and can be constructed by replacement of one-third of the rare-earth atoms in  $CaCu_5$ -type  $REFe_5$  by dumbbells of Fe atoms in two different ordering modes. In the  $Th_2Zn_{17}$ -type structure, the substitution leads to an  $ABCABC\dots$  stacking sequence, whereas the stacking sequence in the  $Th_2Ni_{17}$  structure type is  $ABAB\dots$  [102]. Thus, the phase transition from the  $Th_2Zn_{17}$  structure type to the  $Th_2Ni_{17}$  structure type is a polytypic transformation [97].

The crystal structures of  $REFe_7$ ,  $R\bar{3}m$  (166), have been described as intergrowth structures of the  $CaCu_5$  and  $Th_2Zn_{17}$  structures. The structure is composed of  $REFe_5$  layers alternating with two  $RE_2Fe_{17}$  layers. To account for the rhombohedral symmetry,  $1/3$   $RE$  and  $4/3$  Fe atoms were statistically assigned to each of the substituted  $RE$  positions, and these were then arranged in a  $RE_2Fe_{17}$  layering sequence [102]. The unit cell parameters and unit cell volumes of the  $REFe_7$  phases are listed in *Table 9.10*.

$Nd_5Fe_{17}$ ,  $a = 2021.4(8)$  pm,  $c = 1232.9(8)$  pm,  $V = 4362.9(1) \cdot 10^6$  pm<sup>3</sup>, is a stable phase with potentially interesting magnetic properties. Unlike  $Nd_5Fe_{17}$ , the isotypic  $Sm_5Fe_{17}$ ,  $a = 2006.1(1)$  pm,  $c = 1228.2(2)$  pm,  $V = 4180.6(1) \cdot 10^6$  pm<sup>3</sup>, is found to be metastable and hard magnetic. The crystal structure of  $RE_5Fe_{17}$  was refined in S.G.  $P6_3mcm$  (193) and it contains 14 crystallographically distinct Fe sites and 7  $RE$  positions with a wide variety of environments. The unit cell contains 264 atoms and the very complex crystal structure is built up of layers which are the network/tessellation of triangles, pentagons, hexagons and heptagons. The stacking of layers leads to the formation of antiprisms [103]. The compounds order ferromagnetically with Curie temperatures above 500 K [104, 105].

The compounds  $RE_6Fe_{23}$  ( $Fm\bar{3}m$  (225)) are found for the late rare-earth elements,  $RE = Y, Sm-Lu$  [10, 11]. These compounds are characterized by  $fcc$  structures containing 116 atoms per unit cell. There is one crystallographic rare-earth site and four iron positions. All isotypic phases are ferromagnets ( $Er_6Fe_{23}$  is found to be ferrimagnetic [106]) with Curie temperatures  $\approx 500$  K [107]. The complex crystal structures of these compounds provide plenty of sites available for interstitial hydrogen and accordingly, these compounds were shown to have a strong affinity for hydrogen. Rhyne *et al.* observed that the absorption of 16 deuterium atoms per formula unit increases the Curie temperature of  $Ho_6Fe_{23}$  by  $\approx 200$  K and the absorption of the deuterium atoms leads to a structural phase transition from  $fcc$  to  $bct$  (body centered tetragonal) [108]. The magnetic properties were investigated for the

compositions  $RE_6(Fe_{1-x}Mn_x)_{23}$  [107, 109, 110], and, for instance, for the Y compounds it was found that the intermediate ternary phases have dramatically reduced Curie temperatures and magnetizations compared to the binaries [107]. *Table 9.11* shows the unit cell parameters and unit cell volumes of the isotypic compounds.

Compounds with  $CaCu_5$ -structure type, S.G.  $P6/mmm$  (191), are reported for Nd, Sm, Gd and Ho [111–113]. *Table 9.12* shows the unit cell parameters and unit cell volumes of the isotypic  $REFe_5$  compounds. They are reported to be metastable and the structure type was assigned on the basis of powder diffraction data. The crystal structure contains one rare-earth atomic position and two iron sites. The iron atoms form edge sharing bipyramidal chains running along the [001]. Around the sixfold axis these chains form channels occupied by rare-earth atoms. Formation and magnetic properties of the metastable ternary compounds  $Sm(Fe_{1-x}Co_x)_5$  were studied in detail [112]. It was established that the formation and the magnetization of  $Sm(Fe_{1-x}Co_x)_5$  ( $0.6 \leq x \leq 1.0$ ) strongly depends on the disc velocity of the melt spinning device or, in other words, on the formation of a fine-crystalline microstructure.

The rare-earth elements Y and Sm–Tm form intermetallic compounds with  $PuNi_3$  structure type, S.G.  $R\bar{3}m$  (166), with Fe, Co and Ni [10, 11, 110, 114]. The unit cell parameters and unit cell volumes of the  $PuNi_3$ -type rare-earth iron binary phases are given in *Table 9.13*. The  $PuNi_3$ -type structure can be derived from the  $CaCu_5$  and  $MgCu_2$  structures [115]. The structure is built up of alternating single layers of  $REFe_5$  and double layers of  $REFe_2$ . The third  $REFe_5$ -type layer, rather than being directly above the first, is displaced from it by  $1/3$ ,  $2/3$ ,  $2/3$ ; thus,  $REFe_3$  reveals a rhombohedral lattice. The reciprocal susceptibility of the Sm–Tm compounds are described by the Néel law for ferrimagnets with Curie temperatures of 540 K to 650 K [116]. The hydrogenation behavior and its effect on magnetic properties of the binary compounds as well as the magnetic anisotropy of Co-doped  $REFe_3$  compounds have also been investigated [116, 117]. For instance, hydrogenation of  $ErFe_3$  with  $3.42 \mu_B/f.u.$  at 21 kOe resulted in the formation of  $ErFe_3H_{3.5}$  with  $2.05 \mu_B/f.u.$

## ***RE – Ru***

In the crystal structure database of inorganic compounds [11] as well as in the metals database [10], more than 180 entries can be found for the systems  $RE-Ru$  concerning phase diagram studies and crystal structure determinations [10, 11, 58]. About 60 binary rare-earth ruthenium compounds crystallizing with 10 different crystal structure types are communicated up to now. No binary intermediate phase of Eu with Ru has been reported so far while in the case of Yb only a C14 type Laves phase was found. This might be related to the high vapor pressure of Eu and Yb which causes experimental difficulties. Even though Fe and Ru belong to same group of the periodic table, the binary rare-earth ruthenium compounds crystallize in completely different structure types, with the exception of C14 and C15 types, compared to  $RE-Fe$  compounds. Due to the different solidification behavior and individual structure types, a general discussion about the phase diagram of the  $RE-Ru$  systems is not given here.

Only the crystal structures and the reported physical properties of the binary compounds in the *RE*–Ru systems will be briefly reviewed.

Rare-earth elements form C14 (except La–Pr) and C15 (La–Gd) Laves phases together with ruthenium. The unit cell parameters and unit cell volumes of the rare earth ruthenium Laves phases are listed in *Table 9.14*. Pr–Gd form both C14 and C15 phases. It was proposed that the MgZn<sub>2</sub> Laves phase occurs as a low temperature phase on the Nd rich side of the phase diagram while the MgCu<sub>2</sub>-type is stable at the Ru rich side of the NdRu<sub>2</sub> at all temperatures [118]. The Y, La, Ce and Lu ruthenium Laves phases are reported to be superconductors with transition temperatures of 1.5 K, 1.6 K, 6.0 K and 0.9 K, respectively [48, 119]. Various investigations were carried out on these phases in order to tune their structural, electronic and magnetic properties. For instance, the superconducting transition temperatures of various compositions of the pseudo-binary LaRu<sub>2</sub>–CeRu<sub>2</sub> solid solutions were studied [119]. The partial replacement of Ce atoms by Tb (20 at.%) changed the superconducting transition temperature to 2.6 K and, in addition, short range ferromagnetic ordering was observed at 1.5 K [120]. It was established that hydrogenation causes strong structural modification as well as a decrease of the 4*d*(Ru)–5*d*(Ce,La) hybridization, which ultimately results in the loss of superconductivity in hydrogenated C15 phases [121].

All rare-earth elements, except Ce and Yb, form Mn<sub>5</sub>C<sub>2</sub>-type (*C2/c* (15)) compounds with ruthenium [10, 11, 58, 118]. The unit cell parameters and unit cell volumes of the Mn<sub>5</sub>C<sub>2</sub>-type rare-earth binaries are listed in *Table 9.15*. The *RE* atoms occupy the Mn sites and the Ru atoms accommodate the C positions in the crystal structure of the Mn<sub>5</sub>C<sub>2</sub>-type, resulting in the chemical formula *RE*<sub>5</sub>Ru<sub>2</sub>. The Ru atoms occupy the tricapped trigonal prismatic voids formed by *RE* atoms while the three independent *RE* atoms have 2×14 and 16 nearest neighbors forming Frank-Kasper polyhedra [122]. The Y compound is Pauli paramagnetic while the Gd and Dy compounds show paramagnetic behavior with effective magnetic moments corresponding to free rare-earth ions, *RE*<sup>3+</sup> [123].

The rare-earth elements Y, La–Tm, Lu form compounds with cementite,  $\theta$ -Fe<sub>3</sub>C structure type together with ruthenium, where the *RE* atoms sit on the Fe sites and the Ru atoms on the C sites. The unit cell parameters and unit cell volumes of cementite type phases in the *RE*–Ru systems are listed in *Table 9.16*. Analyzing the interatomic distances in these compounds, one can define the coordination number of Ru atoms to be 8 (cubic-antiprism) [10, 11, 58, 124].

A peculiar compound present only in the Ce–Ru binary system is Ce<sub>16</sub>Ru<sub>9</sub> [122], which represents its own structure type, (*hR150*), *R $\bar{3}m$*  (166), *a* = 1364.5(2) pm, *c* = 2274.2(3) pm, *V* = 3667.0(1)·10<sup>6</sup> pm<sup>3</sup>, containing 7 and 3 crystallographically independent *RE* and Fe positions, respectively. The coordination polyhedra around Ru are two tricapped trigonal prisms and a square antiprism, all formed by Ce atoms. Anomalously short Ce–Ce (331.2 pm to 387.1 pm) and Ce–Ru (255.7 pm to 320.6 pm) distances were found in this structure, which were assigned by the authors to the mixed valence state of Ce atoms. Ce<sub>16</sub>Ru<sub>9</sub> shows paramagnetic behavior with an effective magnetic moment of 1.84  $\mu_B$ , which is lower compared

to that of the  $Ce^{3+}$  ( $2.54 \mu_B$ ) and suggests a mixed valence for Ce. The electrical resistivity measurements show that the phase behaves as a Kondo system at low temperatures [125].

Another structure type which is found at present only in the Ce–Ru system is  $Ce_4Ru_3$ , which shows monoclinic symmetry,  $mS28$ , S.G.  $C2/m$  (12),  $a = 840.0(2)$  pm,  $b = 1383.7(4)$  pm,  $c = 598.5(2)$  pm,  $\beta = 117.90(2)^\circ$ ,  $V = 614.8(1) \cdot 10^6$  pm<sup>3</sup> [126]. The atoms are distributed on three Ce and two Ru sites. The crystal structure is characterized by columns of Ce antiprisms centered by Ru atoms running parallel to the [001]. Pairs of the remaining Ru atoms are inserted in between the columns.

A similar columnar motif of square antiprisms is also present in the crystal structure of  $Y_{44}Ru_{25}$ ,  $oP276$ , S.G.  $Pnna$  (52), which is observed in the systems  $RE-Ru$  ( $RE = Y, Sm-Er$ ) [10, 11, 58, 127]. In the  $Y_{44}Ru_{25}$  type, the square antiprisms form two different kinds of slabs located at different positions along [010]. Short Ce–Ru distances of 275 pm were attributed by the authors to the mixed valence state of the Ce species.

The  $Er_3Ru_2$ -type structure,  $hP10$ , S.G.  $P6_3/m$  (176), for rare-earth binary compounds were observed with Y, Dy–Tm and Lu [10, 11, 58, 128]. The unit cell parameters and unit cell volumes of the  $Er_3Ru_2$ -type compounds are given in *Table 9.17*. The structure contains two Ru and one Er position. The arrangement of the atoms in this structure type is characterized by a columnar arrangement of trigonal prisms formed by  $RE$  atoms around Ru. Along the edges parallel to the [001], the channels build up octahedra of  $RE$  atoms. The octahedral voids are occupied by additional Ru atoms forming chains. A very short Ru–Ru contact of 197 pm is found inside these channels. The trigonal prismatic arrangement of  $RE$  atoms is also found in  $RE_5Ru_2$  compounds [118, 122].

In the course of phase diagram studies of the binary systems La–, Pr– and Nd–Ru, phases with composition  $RE:Ru = 7:3$  were observed. Due to the similarity of their X-ray powder diffraction patterns the compounds were assumed to be isotypic with  $Sr_7Pt_3$  ( $oP16$ , S.G.  $Pnma$  (62)) and the lattice parameters were determined as follows:  $a = 742.2(1)$  pm,  $b = 2356.2(1)$  pm,  $c = 673.2(1)$  pm,  $V = 1177.3(1) \cdot 10^6$  pm<sup>3</sup> for  $La_7Ru_3$ ;  $a = 731.9(1)$  pm,  $b = 2296.1(1)$  pm,  $c = 655.8(1)$  pm,  $V = 1102.1(1) \cdot 10^6$  pm<sup>3</sup> for  $Pr_7Ru_3$  and  $a = 730.3(1)$  pm,  $b = 2283.0(1)$  pm,  $c = 653.2(1)$  pm,  $V = 1089.1(1) \cdot 10^6$  pm<sup>3</sup> for  $Nd_7Ru_3$  [129, 130]. The crystal structure contains monocapped trigonal prisms as well as square antiprisms of rare-earth atoms around Ru.

## **$RE - Cr$**

According to the metals database [10], crystal structure database of inorganic compounds [11] and inorganic materials database [58] there is no report on binary compounds in the  $RE-Cr$  system.

## 2.2 Overview of the ternary systems

### 2.2.1 RE – Cr – C

The phase equilibria of the ternary system Gd–Cr–C, for the isothermal section at 1173 K were systematically investigated by Jeitschko *et al.* [20]. This system contains the ternary compound  $\text{Gd}_2\text{Cr}_2\text{C}_3$ , which is an isotype of  $\text{Ho}_2\text{Cr}_2\text{C}_3$ , as the only ternary phase (Figure 2.6). The ternary phase diagrams of other RE–Cr–C systems have not been studied and there are no other ternary phases than those with the  $\text{Ho}_2\text{Cr}_2\text{C}_3$ -type structure reported up to now.

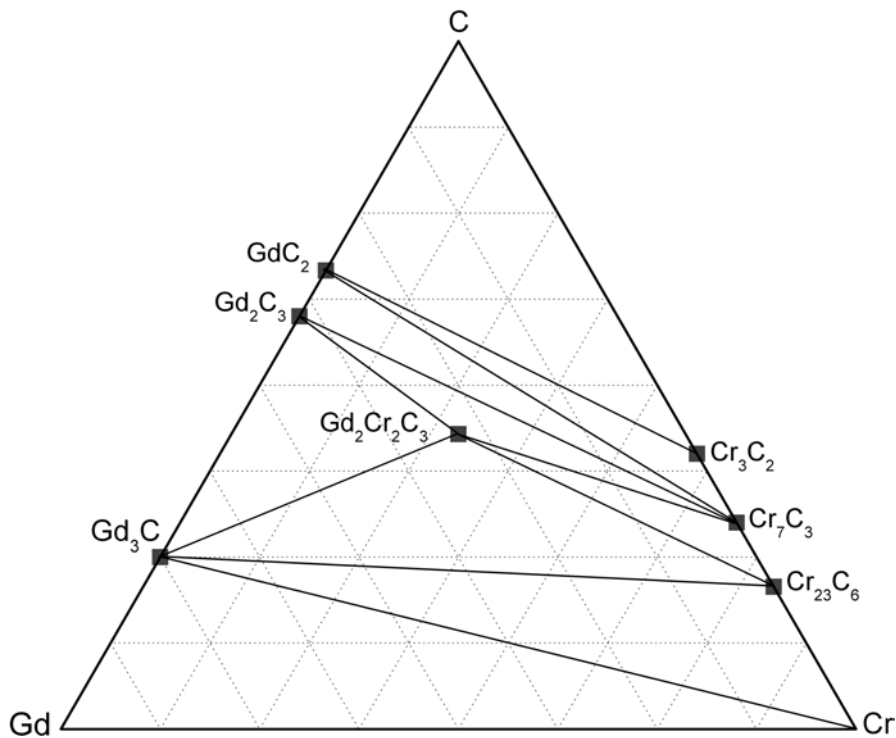


Figure 2.6: Isothermal section of the ternary phase diagram Gd–Cr–C at 1173 K [20].

The isotypic compounds  $\text{RE}_2\text{Cr}_2\text{C}_3$  ( $\text{RE} = \text{Y}, \text{Gd–Tm}$  and  $\text{Lu}$ ) were prepared by arc melting of mixtures of the elements in inert (Ar) atmosphere followed by heat treatment at 1173 K, followed by quenching in cold water. In the case of  $\text{Yb}_2\text{Cr}_2\text{C}_3$ , the authors report that the compound was synthesized by a metal flux method. A stoichiometric mixture of the elements was mixed with Li (as a metallic solvent) and sealed in an iron tube. The sample was heated to 1073 K and afterwards the Li matrix was dissolved in ethanol [131]. The crystal structure of  $\text{Ho}_2\text{Cr}_2\text{C}_3$  was solved from single crystal diffraction data and refined in  $\text{S.G. } C2/m$  (12). The unit cell parameters and unit cell volumes of the  $\text{RE}_2\text{Cr}_2\text{C}_3$  series are listed in Table 2.4 [20, 131, 132].

The crystal structure of  $\text{Ho}_2\text{Cr}_2\text{C}_3$  contains one Ho, one Cr and two C crystallographic positions. The metal atoms form a body centered distorted cubic arrangement with highly distorted octahedral voids. There are  $(6/2 =) 3$  voids located at the faces and  $(12/4 =) 3$  voids at the edges of the *bcc* cell. The octahedral voids at the faces and the neighboring



Table 2.4: Unit cell parameters and unit cell volumes of the ternary phases  $RE_2Cr_2C_3$ .

$RE_2Cr_2C_3$	$a / \text{pm}$	$b / \text{pm}$	$c / \text{pm}$	$\beta / ^\circ$	$V/10^6 \text{ pm}^3$
$Y_2Cr_2C_3$	1047.2(6)	339.2(2)	554.9(3)	106.3(1)	189.21(1)
$Sm_2Cr_2C_3$	1051.3(3)	347.1(1)	569.2(1)	105.6(1)	200.10(1)
$Gd_2Cr_2C_3$	1044.5(2)	343.7(1)	562.5(2)	105.8(1)	194.32(1)
$Tb_2Cr_2C_3$	1045.2(3)	340.3(1)	558.7(3)	105.9(1)	191.10(1)
$Dy_2Cr_2C_3$	1047.2(2)	337.6(1)	556.4(1)	106.2(1)	188.97(1)
$Ho_2Cr_2C_3$	1047.0(2)	336.5(1)	554.0(1)	106.3(1)	187.30(1)
$Er_2Cr_2C_3$	1046.4(3)	335.6(1)	550.7(2)	106.5(1)	185.42(1)
$Tm_2Cr_2C_3$	1050.0(4)	333.0(1)	548.2(2)	106.6(1)	183.65(1)
$Yb_2Cr_2C_3$	1049.3(8)	330.7(3)	548.3(4)	107.0(1)	182.00(1)
$Lu_2Cr_2C_3$	1049.2(2)	330.2(1)	545.2(2)	107.0(1)	180.62(1)

octahedral voids at the edges can not be simultaneously occupied. However, the voids at neighboring edges can be occupied at the same time. The structure exclusively contains discrete carbon species, occupying the octahedral voids. In the  $Ho_2Cr_2C_3$  structure type there are  $24(=4 \times 6)$  octahedral voids per unit cell and only one quarter of all octahedral voids is filled with carbon atoms. The chromium atoms are coordinated by 4 C atoms forming edge- and corner-sharing distorted tetrahedra resulting in 2D polyanionic layers  ${}^2_{\infty}[(Cr_2C_3)^{6-}]$  (Figure 2.7). The interatomic distances in  $Ho_2Cr_2C_3$  as discussed in reference [20] are:  $d(Ho-Ho) = 335.4 \text{ pm}$  and  $341.8 \text{ pm}$ ;  $d(Ho-Cr) = 310.2 \text{ pm}$ ,  $314.2 \text{ pm}$  and  $344.7 \text{ pm}$ ;  $d(Ho-C) = 242.1 \text{ pm}$  to  $262.9 \text{ pm}$ ;  $d(Cr-Cr) = 263.7 \text{ pm}$  and  $d(Cr-C) = 190.6 \text{ pm}$  to  $203.3 \text{ pm}$ . As reported in reference [131], the 2D infinite polyanionic chromium-carbon network does not carry magnetic moments as shown by the Pauli paramagnetism of the Y and Lu compounds.

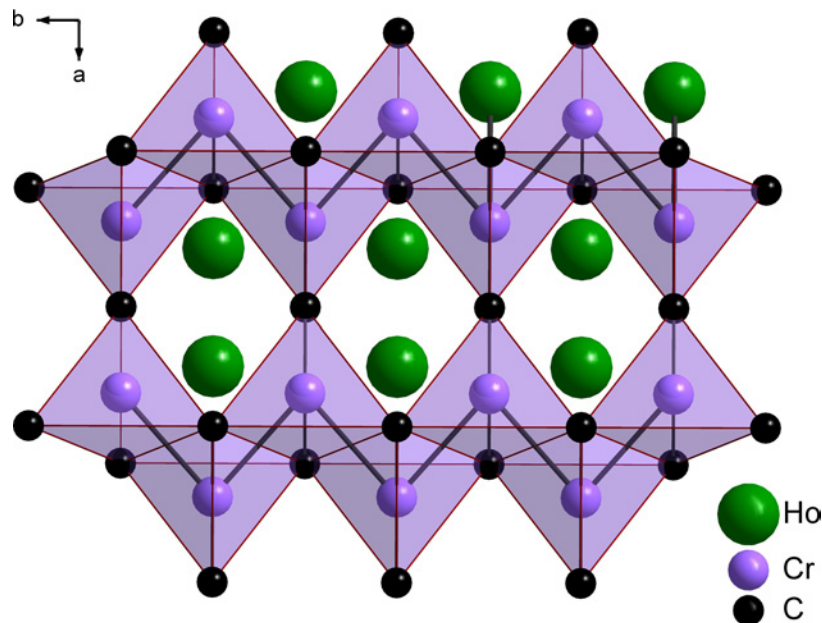


Figure 2.7:  $Ho_2Cr_2C_3$ : unit cell projection along  $[001]$ . The chromium atoms are forming zig-zag chains running along  $[010]$ . The overall interconnection of coordination tetrahedron results in  ${}^2_{\infty}[(Cr_2C_3)^{6-}]$ .

The magnetic behavior of the other isotypic carbides follows a Curie-Weiss law and the effective magnetic moments correspond to the respective free  $RE^{+3}$  ions. The experimental moments for all members of the isotypic series are slightly smaller than the theoretical ones, an observation which the authors ascribe to a crystal field effect.  $RE_2Cr_2C_3$  with  $RE = Tb-Er$  show antiferromagnetic ordering at low temperatures, and below  $T_N$ , the susceptibility becomes field dependent suggesting metamagnetic behavior. The magnetic phase transitions of the Tb, Ho and Er compounds were also investigated [21]. Later, the chemical bonding in the compounds with the  $Ho_2Cr_2C_3$  structure type were analyzed by orbital based COHP [133] and topological analysis of ELF and electron density [134, 135]. By them the ternary compounds were classified as rare-earth carbochromates (III) [9].

### 2.2.2 $RE - Fe - C$

A large amount of work has been done in these systems concerning the magnetic properties and the magnetic and structural phase transitions, which are of great technological importance. Especially the alloys of  $RE$ - together with  $3d$  metals (Co, Fe, Mn, Cr, or Cu) containing carbon atoms are very stable magnets with high remanence and high coercive field strengths, and they have already found applications in miniaturized equipments such as quartz watches, headphones, loudspeakers, magnetic storages, etc. Most of the investigations cover their microstructures, properties and compositions, aiming at modifications of materials. A part of these studies was devoted to the application of rare-earth metals in metallurgy and steel industry and has already been reviewed [136, 137]. Rare-earth metals react easily with water and light non-metallic elements (e. g. H, B, C, N, O, S) in molten steel, thus changing the properties of alloys and steel, such as strength, heat and vibration resistance, electrical conductivity and magnetic transition temperatures. They can also be used to clean steel [138, 139]. For example,  $RE$  elements in austenite segregate at grain boundaries, harden the steel and retard the formation of martensite [140]. A study of the electronic structure and the chemical bonding in such ternary phases is an important task nowadays for many research groups and this will help to deeper understanding of the relationships between structure, chemical bonding and properties.

During extended phase diagram studies of systems  $RE-Fe-C$  ( $RE = Y, Ce$  and  $Gd$ ) the following intermediate ternary phases have been reported:  $GdFeC$ ,  $RE_2Fe_2C_3$ ,  $RE_4Fe_4C_7$  ( $RE = Ce, Gd$ ),  $GdFe_2C_2$ ,  $Gd_3Fe_{20}C$ ,  $Gd_4Fe_{31}C_3$ ,  $YFeC_2$  and  $Y_2Fe_{17}C$  [139, 141, 142]. The ternary  $Gd-Fe-C$  compounds with an atomic ratio  $Gd : Fe = 1 : 1$  crystallize from the melt, although  $GdFeC$  is the only phase with congruent melting behaviour. The remaining  $Gd$ - and other  $RE-Fe-C$  compounds form peritectically. The chemical compositions of these compounds were determined by electron probe microanalysis, and the Bravais lattice and unit cell parameters were determined from X-ray powder diffraction data, which are listed in *Table 2.5*. However, no structural information can be found in the literature up to now. The crystal structures of  $RE_2FeC_4$  ( $RE = Y, Tb-Lu$ ) [29],  $RE_{3,67}FeC_6$  ( $RE = La-Nd, Sm$ ) [30] and

$REFeC_2$  ( $RE = Sm, Gd-Er, Lu$ ) [31] have been established and will be discussed in detail.

Table 2.5: Unit cell parameters and Bravais lattice types of intermediate ternary phases reported during phase diagram studies in systems  $RE-Fe-C$ .

Phases	Bravais lattice	$a$ / pm	$b$ / pm	$c$ / pm
$YFeC_2$	$tP$	1065.0(1)		860.0(1)
$GdFeC_2$	$hP$	912.0(1)		597.0(1)
$Gd_4Fe_4C_7$	$tP$	704.5(1)		1023.0(1)
$Gd_2Fe_2C_3$	$hP$	838.8(1)		1026.0(1)
$GdFe_2C_2$	$oP$	367.8(1)	299.5(1)	1450.0(1)
$Ce_4Fe_4C_7$	$tP$	722.0(1)		582.0(1)
$Ce_2Fe_2C_3$	$hP$	864.7(1)		1053.0(1)

$RE_2FeC_4$  ( $RE = Y, Tb-Lu$ ) [29] was reported to form by a peritectic reaction of  $REC_2$  with iron at 1173 K. The crystal structure was determined by both X-ray and neutron powder diffraction data.  $RE_2FeC_4$  crystallizes in the orthorhombic crystal system, S.G.  $Ibam$  (72) with  $Z = 4$ , and represents a new structure type. The unit cell parameters and volumes of the  $RE_2FeC_4$  series are listed in Table 2.6 [29]. The crystal structure of  $RE_2FeC_4$  will be explained using  $Er_2FeC_4$  as a representative example (Figure 2.8). The iron atoms are tetrahedrally coordinated by carbon atoms (Figure 2.8b) forming infinite chains running along [001].

Table 2.6: Unit cell parameters and unit cell volumes of ternary carbides  $RE_2FeC_4$ .

$RE_2FeC_4$	$a$ / pm	$b$ / pm	$c$ / pm	$V/10^6$ pm <sup>3</sup>
$Y_2FeC_4$	752.9(2)	956.5(1)	504.1(1)	363.0(1)
$Tb_2FeC_4$	752.6(1)	964.4(1)	506.8(1)	367.8(1)
$Dy_2FeC_4$	751.4(1)	959.4(2)	505.1(1)	364.1(1)
$Ho_2FeC_4$	751.4(1)	949.4(1)	502.2(1)	358.3(1)
$Er_2FeC_4$	750.6(1)	942.6(2)	500.6(1)	354.2(1)
$Tm_2FeC_4$	749.4(1)	936.7(1)	498.0(1)	349.5(1)
$Yb_2FeC_4$	748.0(1)	931.5(2)	495.8(1)	345.5(1)
$Lu_2FeC_4$	749.4(1)	924.9(1)	495.1(1)	343.1(1)

As assumed by the authors, the arrangement of the carbon atoms is halfway between square planar and tetrahedral coordination, with a pseudo  $\bar{4}$  axis running parallel to the  $b$  axis of the unit cell (Figure 2.8). This coordination is augmented by four  $RE$  atoms at 318 pm, which in turn form distorted tetrahedra (Figure 2.8a). The carbon atoms form pairs with a bond distance of 133.5 pm, which is almost the same as the double bond distance in olefines (134 pm). The  $C_2$  units have five rare-earth and two iron nearest neighbors. The distance  $d(Fe-C) = 196.8$  pm is close to the  $Fe-C$  contacts found in other binary or ternary carbides [30, 86]. The most interesting feature of this structure type is the presence of  $-Fe-Fe-$  infinite chains with  $d(Fe-Fe) = 250.3$  pm (Figure 2.8b), which is close to the contacts found in binary iron carbides (Section 2.1.2).

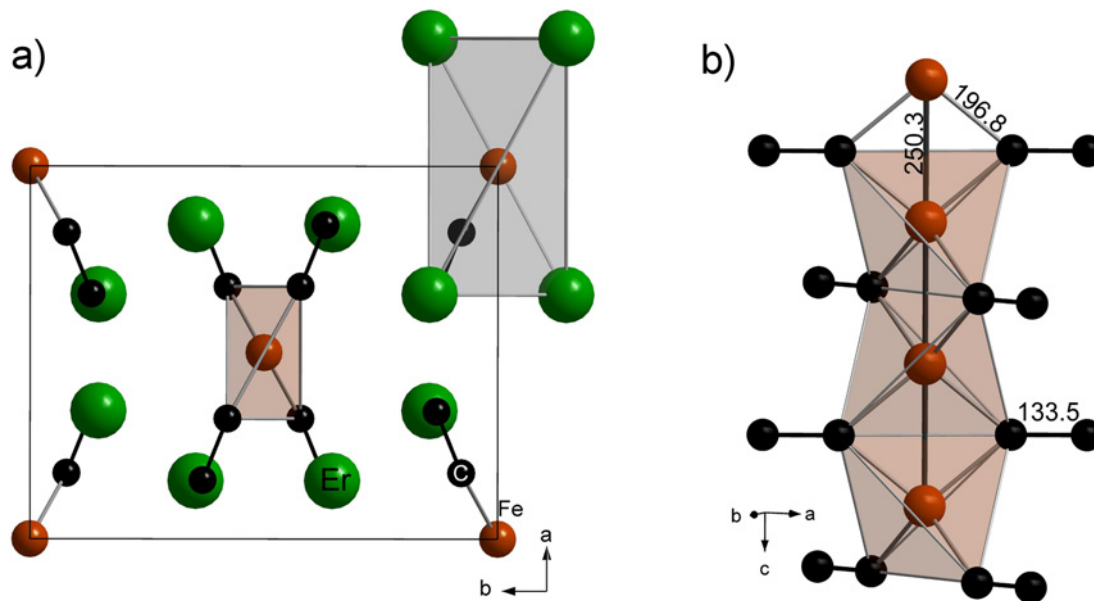


Figure 2.8: The crystal structure of  $RE_2FeC_4$  exemplarily shown for  $Er_2FeC_4$ . a) Unit cell projection viewed along [001] and coordination of Fe atoms by C and Er atoms, b) polyanionic part of the structure. Interatomic distances Fe–Fe, Fe–C and C–C are given in pm.

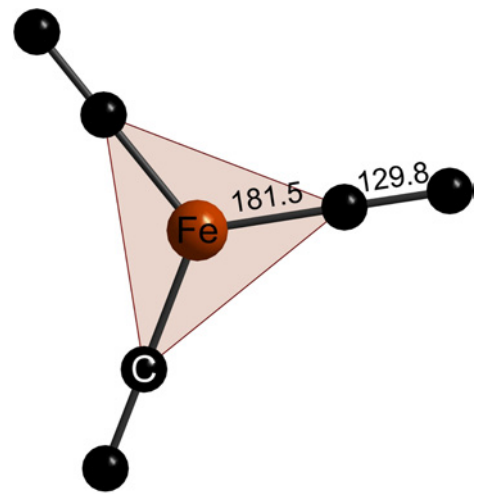
The physical properties were measured for the isotopic Y, Er and Tm compounds. All compounds show good electrical conductivity. The temperature and magnetic field dependent measurements show that the Er compound is paramagnetic with an effective magnetic moment corresponding to free  $Er^{3+}$  ions.  $Y_2FeC_4$  is essentially nonmagnetic. Mössbauer studies of the Y compound did not show magnetic splitting down to 4.2 K, indicating nonmagnetic Fe species. The authors rationalized the chemical formula as  $Er^{3+}_2Fe^{2+}(C_2^{-4})_2$ .  $Y_2FeC_4$  becomes superconducting at 3.6 K, while  $Lu_2FeC_4$  does not show a transition to a superconducting state down to 1.8 K. The crystal structure of  $RE_2FeC_4$  is closely related to  $CaC_2$ ,  $UCoC_2$  and  $ThCr_2Si_2$ . It can be seen that the structures of the ternary compounds are derived from that of  $CaC_2$  by gradual insertion of transition metal atoms. All compounds  $RE_2FeC_4$  are reported to be moisture and air sensitive and the hydrolysis products were identified as  $C_2H_6$ ,  $C_2H_4$  and  $CH_4$  and some higher hydrocarbons.

Jeitschko *et al.* [30] investigated the ternary system La–Fe–C and reported three ternary phases:  $La_2Fe_{14}C$ ,  $La_3FeC_5$  and  $La_{3.67-x}FeC_6$ .  $La_2Fe_{14}C$  seems to be isotopic with  $Nd_2Fe_{14}B$ .  $La_3FeC_5$ , with an unknown crystal structure, is formed after prolonged annealing at 1073 K. The crystal structure of  $La_{3.67-x}FeC_6$  was determined by single crystal X-ray diffraction and the powder diffraction data of the isotopic compounds were indexed. The isotopic compounds  $RE_{3.67-x}FeC_6$  ( $RE = La-Nd, Sm$ ) were synthesized by arc melting mixtures of the elements followed by heat treatment at 1073 K to 1273 K. The unit cell parameters and unit cell volumes of the ternary  $RE_{3.67-x}FeC_6$ -type phases are listed in Table 2.7 [30].  $RE_{3.67-x}FeC_6$  crystallizes hexagonal in S.G.  $P6_3/m$  (176) with two rare-earth, one iron and two carbon crystallographic sites.

Table 2.7: Unit cell parameters and unit cell volumes of ternary phases representing the  $RE_{3.67-x}FeC_6$ -type structure.

$RE_{3.67-x}FeC_6$	$a$ / pm	$c$ / pm	$V/10^6$ pm <sup>3</sup>
$La_{3.67-x}FeC_6$	878.7(2)	535.1(1)	357.8(1)
$Ce_{3.67-x}FeC_6$	868.6(1)	530.9(1)	346.9(1)
$Pr_{3.67-x}FeC_6$	863.4(2)	522.8(2)	337.5(1)
$Nd_{3.67-x}FeC_6$	858.5(2)	518.9(1)	331.2(1)
$Sm_{3.67-x}FeC_6$	849.7(2)	512.1(1)	320.2(1)

The structure of  $La_{3.67-x}FeC_6$  is closely related to  $Gd_3Mn_2C_6$  [37]. The main difference is the occupancy of the  $2b$  site (0, 0, 0), which is occupied by Mn in  $Gd_3Mn_2C_6$ . In the crystal structure of  $RE_{3.67-x}FeC_6$  this site was refined as a split position which reflects the structural disorder of  $RE$  atoms within the carbon channel. The structure contains carbon dumbbells with  $d(C-C) = 130$  pm connected end-on to the iron atoms to form trigonal planar  $Fe(C_2)_3$  groups, which represent the anionic part of the structure (Figure 2.9). The  $Fe(C_2)_3$  groups are surrounded by rare-earth ions in a tri-capped trigonal prismatic manner. No Fe–Fe contacts are present in this structure. The distances  $d(La-C)$  range from 262 pm to 297 pm, which compares well with those found in binary rare earth carbides (Section 2.1.1). The distances  $d(La-Fe)$  range from 321.6 pm to 358.6 pm corresponding to the La–Fe contacts in the crystal structure of  $La_2Fe_{14}C$  [143]. Comparing the La–Fe distances, the authors stated that there are only marginal La–Fe contacts in  $La_{3.67-x}FeC_6$ . The distance  $d(Fe-C) = 182$  pm is rather short compared to the Fe–C distances found in  $Er_2FeC_4$  (196.8 pm) and  $La_2Fe_{14}C$  (205 pm). Interestingly, the bond order of Fe–C was reported as 1.  $La_{3.67-x}FeC_6$  shows Pauli paramagnetism and metallic conductivity. It was concluded that the iron atoms in  $La_{3.67-x}FeC_6$  do not carry localized magnetic moments. No indication for superconductivity was observed down to 3 K. The isotypic phases are easily decomposed in air or moisture.

Figure 2.9: The  $Fe(C_2)_3$  anionic unit in the crystal structure of  $RE_{3.67-x}FeC_6$ .

Another structure type reported for ternary  $RE-Fe-C$  phases is the  $CeNiC_2$ -type, S.G.  $Amm2$  (38). Compounds with this structure type are obtained with  $RE = Sm, Gd-Er, Lu$ . The unit cell parameters and unit cell volumes of the  $CeNiC_2$ -type rare-earth iron carbides are listed in Table 2.8 [31]. The compounds were prepared by arc melting, followed by an annealing procedure at 1173 K. The crystal structure of  $DyNiC_2$  was solved from single crystal X-ray diffraction data. A series of  $RE-Fe-C$  compounds was assigned to be isotypic with  $DyNiC_2$  ( $CeNiC_2$ -type) and the lattice parameters were determined from powder diffraction

patterns.

Table 2.8: Unit cell parameters and unit cell volumes of the isotypic ternary carbides  $REFeC_2$ .

$REFeC_2$	$a / \text{pm}$	$b / \text{pm}$	$c / \text{pm}$	$V/10^6 \text{ pm}^3$
SmFeC <sub>2</sub>	376.1(1)	457.2(2)	601.0(2)	103.3(1)
GdFeC <sub>2</sub>	369.0(1)	455.9(2)	600.7(2)	101.1(1)
TbFeC <sub>2</sub>	363.7(1)	455.8(1)	599.7(1)	99.4(1)
DyFeC <sub>2</sub>	359.7(1)	455.3(1)	599.3(2)	98.2(1)
HoFeC <sub>2</sub>	356.1(1)	454.8(3)	598.2(3)	96.9(1)
ErFeC <sub>2</sub>	353.1(2)	454.3(2)	598.0(3)	95.9(1)
LuFeC <sub>2</sub>	345.0(3)	452.8(2)	596.5(1)	93.2(1)

The large lanthanoid atoms form a distorted hexagonal primitive lattice, while the transition metal atoms and carbon pairs fill the trigonal prismatic voids of this lattice. The structure can be derived from the hexagonal  $AlB_2$  structure and can be viewed as a layered structure with planar  ${}^2_{\infty}[(FeC_2)^{3-}]$  polyanionic layers stacked in the sequence ...AAA... with the  $RE$  atoms in between these layers.  $REFeC_2$  contains  $C_2$  units end-on connected to two Fe atoms and side-on to one Fe atom, and thus, occupy the center of the triangle formed by Fe atoms. The rare-earth atoms are surrounded by 8 carbon atoms forming square prisms. The Fe atoms are coordinated by 4 carbon atoms forming distorted square planar units. The atomic arrangement in the crystal structure of  $REFeC_2$  and the coordination polyhedra around the Fe atoms are shown in *Figure 2.10*. The distance  $d(C-C)$  in  $DyNiC_2$  of 137 pm, which can

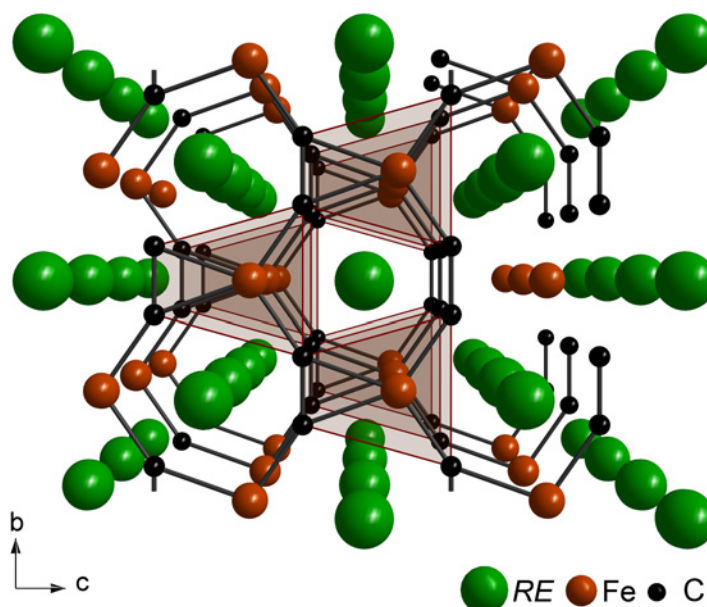


Figure 2.10: The crystal structure of  $REFeC_2$  viewed along  $[100]$ . The 2D planar polyanionic part of the structure is  ${}^2_{\infty}[(FeC_2)^{3-}]$ .

be expected for the isotypic Fe compounds as well, is close to the length of the C–C double bond in olefines. Simple electron counting rules can be used to assign the oxidation state

of the Fe atoms. Assuming  $RE^{3+}$  and  $C_2^{4-}$ , the oxidation state of Fe would become I in agreement with the tendency to form low oxidation states in carbometalates. The series of isotopic compounds were predicted to show metallic conductivity.

A large amount of work has been devoted to the synthesis of rare-earth iron ternary interstitial carbides because of their outstanding magnetic properties. In the metals database [10], 220 entries can be found that are related to the synthesis, crystal structure, magnetic properties and absorption of hydrogen in these compounds. Most of the interstitial ternary carbides crystallize in the  $Nd_2Fe_{14}B$ -type ( $P4_2mnm$  (136)), the  $Th_2Ni_{17}$ - ( $P6_3/mmc$  (194)) or the  $Th_2Zn_{17}$ -type ( $R\bar{3}m$  (166)) structures. These three structure types are closely related to the  $CaCu_5$ -type. In these interstitial carbides, the metal matrix of the intermetallic compounds remains the same. The carbon atoms occupy trigonal prismatic voids formed by 6 Fe atoms in the  $Nd_2Fe_{14}B$ -type and octahedral voids build up from  $(2 RE + 4 Fe)$  atoms in the  $Th_2Ni_{17}$ - or  $Th_2Zn_{17}$ -type structures. With increasing carbon content the crystal structure of  $RE_2Fe_{17}C_x$  changes from the hexagonal  $Th_2Ni_{17}$  to the rhombohedral  $Th_2Zn_{17}$ -type structure [144].

### 2.2.3 RE – Ru – C

In these systems 33 ternary phases adopting 6 structure types were reported up to now [10, 11, 58]. The structure types are:  $La_{3.67-x}FeC_6$  [30, 145],  $Gd_3Ru_2C_5$  [32],  $CaTiO_3$  (perovskite) [146, 147],  $GdRuC_2$  [33],  $Er_7Ru_2C_{11}$  [34] and  $Er_{10}Ru_{10}C_{19}$  [35]. Only for the system Ce–Ru–C informations on phase diagram studies can be found in the database [146]. It should be noted that the structure types found in the systems  $RE$ –Ru–C are completely different, except  $La_{3.67-x}FeC_6$  which is common in both the Fe and the Ru systems, compared to those reported in the systems  $RE$ –Fe–C. All compounds reported in the systems  $RE$ –Ru–C were synthesized by arc-melting, followed by high temperature annealing. The cooling rate has a clear influence on the formation of different phases:  $GdRuC_2$  was detected only with rapid quenching of the melt, while the competing phase  $Gd_{10}Ru_{10}C_{19}$  was formed by slow cooling.

During an exploratory synthesis of  $Gd_3Mn_2C_6$ -type compounds [37] in the  $RE$ – $T$ –C ( $T = Mn, Fe, Ru$ ) systems, the isotopic compounds  $RE_{3.67}TC_6$  ( $T = Fe, Ru$ ), with  $La_{3.67-x}FeC_6$  structure type, were found [30]. The lattice parameters of the isotopic ruthenium compounds, determined from their X-ray powder diffraction patterns, are listed in the left part of *Table 2.9*.

Rare-earth ruthenium carbides are found to crystallize with the perovskite-type structure,  $RERu_3C$ , S.G.  $Pm\bar{3}m$  (221), for  $RE = Ce, Dy - Lu$  [146, 147].  $CeRu_3C$  forms peritectically, whereas in the case of ytterbides except Dy,  $RERu_3C$  was already present in as-cast samples. The unit cell parameters and unit cell volumes of the perovskite type  $RERu_3C$  compounds are given on the right hand side of the *Table 2.9*. Various authors tried to develop empirical rules for the formation of perovskite-type phases  $RERu_3C$ . For instance, Haschke *et al.* [148] attempted to quantify the criteria in terms of the ratio of the radii of transition metals and



Table 2.9: Unit cell parameters and unit cell volumes of  $RE_{3.67-x}FeC_6$ -type compounds (left) and perovskite type ( $RERu_3C$ ) compounds (right).

$RE_{3.67-x}RuC_6$	$a / \text{pm}$	$c / \text{pm}$	$V/10^6 \text{ pm}^3$	$RERu_3C$	$a / \text{pm}$	$V/10^6 \text{ pm}^3$
$La_{3.67-x}RuC_6$	887.1(1)	536.1(1)	366.7(1)	$CeRu_3C$	415.2(1)	71.58(1)
$Ce_{3.67-x}RuC_6$	877.8(2)	528.3(1)	352.5(1)	$DyRu_3C$	412.4(6)	70.14(1)
$Pr_{3.67-x}RuC_6$	870.9(1)	524.9(1)	344.7(1)	$HoRu_3C$	412.4(3)	70.14(1)
$Nd_{3.67-x}RuC_6$	869.9(1)	521.8(1)	342.0(1)	$ErRu_3C$	411.7(2)	69.78(1)
$Sm_{3.67-x}RuC_6$	862.7(1)	514.7(1)	331.7(1)	$TmRu_3C$	411.5(1)	69.66(1)
				$YbRu_3C$	411.1(1)	69.48(1)
				$LuRu_3C$	410.6(2)	69.22(1)

carbon ( $r_C/r_T$ ). Stadelmaier reported that the  $r_C/r_T$  ratio should not exceed 0.62, as derived by considering octahedral coordination of carbon [149]. As noted in reference [146] some of the  $RERu_3C$  phases, e.g.  $URu_3C_{1-x}$ , can be regarded as a solid solutions of carbon in the binary compound  $URu_3$ . Other phases, however, such as  $CeRu_3C$ , form without the existence of a corresponding binary phase. This shows that carbon not only needs to fit in the octahedral voids, but also exerts influence on the formation of  $RERu_3C$ -type compounds. Single crystal X-ray diffraction studies of  $ThRu_3C$  showed that carbon occupies the octahedral holes formed by Ru atoms only [147]. Different authors confirm that there exist certain homogeneity ranges in perovskite-type  $RERu_3C$  phases, which can be immediately noticed by comparing the lattice parameters of the Dy and Ho compounds (*Table 2.9*).

$GdRuC_2$ , S.G. *Cmcm* (63),  $a = 436.5(1) \text{ pm}$ ,  $b = 927.7(1) \text{ pm}$ ,  $c = 520.2(1) \text{ pm}$ ,  $V = 210.7(1) \cdot 10^6 \text{ pm}^3$ , represents another structure type found in the systems  $RE-Ru-C$  [33]. Up to now, only the prototype  $GdRuC_2$  is known. The Gd atoms form a distorted hexagonal close packed arrangement (same as the As atoms in NiAs) with ruthenium atoms filling the octahedral voids (as Ni atoms in NiAs). The carbon atoms form dumbbells, which accommodate slightly distorted trigonal bipyramidal holes formed by Gd atoms. Together with ruthenium atoms, the carbon pairs form two-dimensional polyanionic layers  $\infty[(RuC_2)^{3-}]$  (*Figure 2.11*). The Ru atoms are tetrahedrally coordinated by  $C_2$  pairs ( $d(Ru-C) = 213.8(4) \text{ pm}$ ) and, if the short Ru-Ru contacts ( $d(Ru-Ru) = 260.1(1) \text{ pm}$ ) are considered to be a part of the first coordination shell, this results in an octahedral coordination formed by 4 C and 2 Ru atoms. Infinite linear chains formed by T atoms are also found in ternary rare-earth iron carbides such as  $RE_2FeC_4$  [29]. The C-C distance (137.9(6) pm) is slightly longer than the double bond distance in olefines. The carbon atoms occupy trigonal prismatic voids formed by 4 Gd + 2 Ru. The distances  $d(Gd-C) = 259.8(4) \text{ pm}$ ,  $260.5(4) \text{ pm}$  and  $283.4(2) \text{ pm}$  are similar to those in  $Gd_3Mn_2C_6$  ( $d(Gd-C) = 263.4(1) \text{ pm}$ ). In addition, the ruthenium atoms were reported to obey the 18-electron rule;  $8 e^-$  (4 C) +  $6 e^-$  (2 Ru) +  $4 e^-$  (2 lone pair). By assigning the Ru-C bonding electrons to C, thus fulfilling the octet rule for carbon, the Ru atoms form a so-called  $d^7$  system. The magnetic susceptibility shows Curie-Weiss behavior with an effective magnetic moment corresponding to free  $Gd^{3+}$  ions. Assuming  $C_2^{4-}$ , the chemical formula



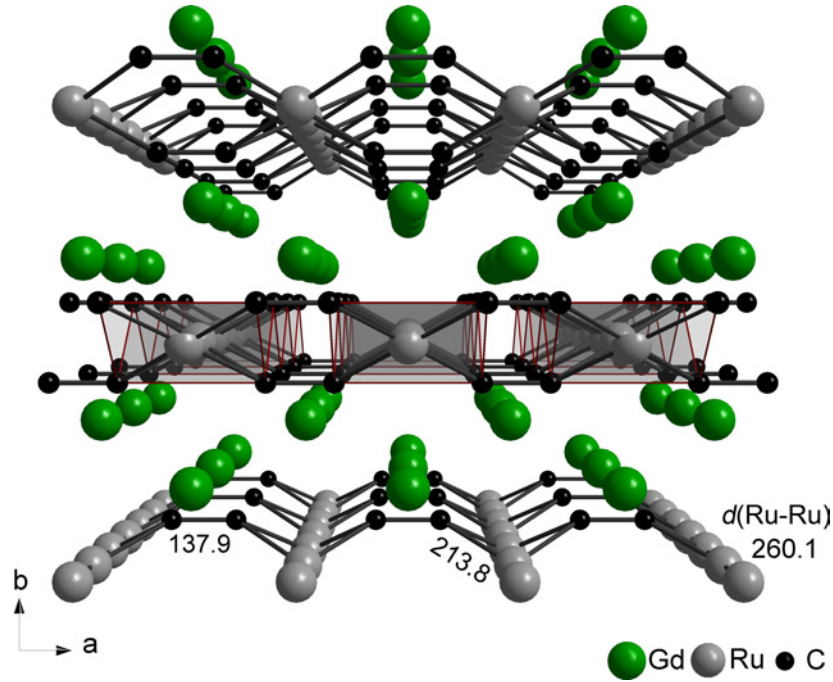


Figure 2.11: The crystal structure of  $\text{GdRuC}_2$  contains polyanionic layers  ${}_{\infty}^2[(\text{RuC}_2)^{3-}]$ , in which the ruthenium atoms are tetrahedrally coordinated by  $\text{C}_2$  units, and Gd atoms being sandwiched between the layers.

can be written as  $\text{Gd}^{+3}[\text{Ru}^{1+}(\text{C}_2)^{4-}]$ . The compound orders ferromagnetically below  $T_C = 45(3)$  K and is stable against air and moisture.

The  $\text{RE}_3\text{Ru}_2\text{C}_5$ -type compounds, S.G.  $P6_3/m$  (176), were reported with  $\text{RE} = \text{Y}$ , Gd–Er [32].  $\text{Gd}_3\text{Ru}_2\text{C}_5$  and  $\text{Tb}_3\text{Ru}_2\text{C}_5$  already exist in as-cast samples while the others were formed after high temperature annealing only. The crystal structure of this isotopic series will be discussed using  $\text{Gd}_3\text{Ru}_2\text{C}_5$  as an example. The lattice parameters of all the isotopic compounds, determined from their X-ray powder diffraction patterns, are listed in Table 2.10.

Table 2.10: Unit cell parameters and unit cell volumes of the isotopic carbides  $\text{RE}_3\text{Ru}_2\text{C}_5$ .

$\text{RE}_3\text{Ru}_2\text{C}_5$	$a$ / pm	$c$ / pm	$V/10^6$ pm <sup>3</sup>
$\text{Y}_3\text{Ru}_2\text{C}_5$	1138.4(3)	498.9(1)	559.9(1)
$\text{Gd}_3\text{Ru}_2\text{C}_5^\dagger$	1147.3(4)	502.4(2)	572.7(1)
$\text{Tb}_3\text{Ru}_2\text{C}_5^\dagger$	1143.4(5)	503.4(1)	569.9(1)
$\text{Dy}_3\text{Ru}_2\text{C}_5$	1139.6(3)	500.7(1)	563.2(1)
$\text{Ho}_3\text{Ru}_2\text{C}_5$	1136.5(2)	498.4(1)	557.5(1)
$\text{Er}_3\text{Ru}_2\text{C}_5$	1133.8(4)	495.3(2)	551.4(1)

<sup>†</sup> depending on the composition of the starting materials and the annealing temperatures the lattice parameters of these compounds may differ [32]. Here, those lattice parameters are presented which follow the lanthanoid contraction rule.

The crystal structure contains several partially occupied atomic positions, and is, thus, strongly disordered. Two of the carbon atoms form pairs with  $d(\text{C}-\text{C}) = 132.6(9)$  pm and the other two carbon atoms are isolated. The  $\text{C}_2$  units as well as the discrete carbon species

accommodate octahedral voids formed by metal atoms. The most interesting feature of the crystal structure is the presence of trigonal planar  $\text{Ru}_3$  clusters with  $d(\text{Ru}-\text{Ru}) = 296.2(1)$  pm. The  $\text{Ru}_3$  cluster is stabilized by 3  $\text{C}_2$  units and 4 monoatomic carbon species resulting in a  $\text{Ru}_3\text{C}_{10}$  unit (Figure 2.12a). All atoms within this cluster are coplanar except the only partially occupied monoatomic C species situated above or below the cluster. A physically reasonable chain model with linear  $\text{Ru}_3$  units ( $d(\text{Ru}-\text{Ru}) = 252$  pm) was proposed for the partially occupied Ru sites occupying the octahedral channels formed by the Gd atoms. The chemical bonding in  $\text{RE}_3\text{Ru}_2\text{C}_5$  was rationalized using the  $18e^-$ -rule which is widely used for organometallic compounds. Figure 2.12 shows a drawing from reference [32] showing the valence electron distribution in the trigonal  $\text{Ru}_3\text{C}_{10}$  cluster (Figure 2.12a) as well as in linear  $\text{Ru}_3$  units (Figure 2.12b) presented on the basis of the Lewis formalism. Assigning the Ru–C bonding electrons to the C atoms the cluster can be represented with the following formula:  $\{\text{Ru}^{5+}_3(\text{C}_2)^{4-}_3\text{C}^{4-}_4\}^{13-}$ . Presuming that there is no Ru–C bonding for partially occupied Ru atoms and assigning the RE–Ru bonding electrons to Ru atoms, the linear  $\text{Ru}_3$  units could have (18-) or (14-) formal charges. In this respect, the overall formula results in  $(\text{RE}_3)^{8.5+}(\text{Ru}_{0.33})^{2-}[(\text{Ru}_3\text{C}_{10})_{0.5}]^{6.5-}$  for  $\text{Ru}_3^{18-}$  and  $(\text{RE}_3)^{8.06+}(\text{Ru}_{0.33})^{1.56-}[(\text{Ru}_3\text{C}_{10})_{0.5}]^{6.5-}$  for  $\text{Ru}_3^{14-}$ , which already accounts for RE–RE bondings. The electrical conductivity of the isotypic Tb compound was measured and shows metallic behavior. The magnetic susceptibility of the RE = Gd–Ho compounds follow the Curie-Weiss law and show very soft ferromagnetism. The effective magnetic moments well agree with the theoretical values of respective  $\text{RE}^{3+}$  ions. The powders are stable in air.

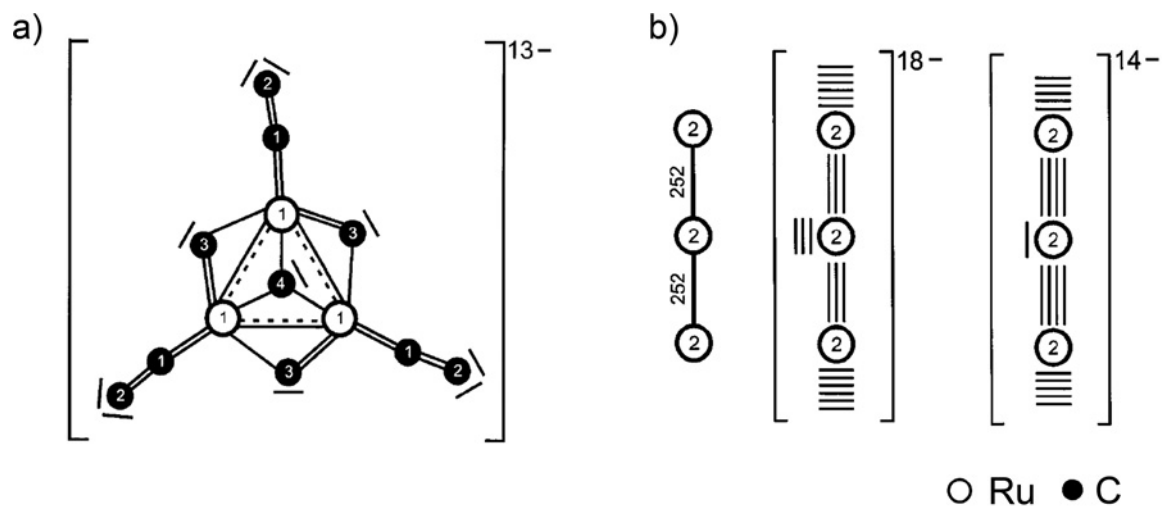


Figure 2.12: Electron counts for the representative units in the crystal structure of  $\text{RE}_3\text{Ru}_2\text{C}_5$  a) trigonal  $\text{Ru}_3\text{C}_{10}$  cluster and valence electron distribution using the Lewis formalism, b) Chain model consisting of linear  $\text{Ru}_3$  units. The open circle with number 2 in the center represents the partially occupied Ru atom ( $\text{Ru}_2$ ). The linear units carry large negative charges [32].

Another structure type of ternary compounds obtained in this system is presented by  $\text{RE}_7\text{Ru}_2\text{C}_{11}$  ( $\text{RE} = \text{Dy}-\text{Tm}$ ) [34]. The Er and Tm phases are already observed in as-cast samples while the Dy and Ho compounds were formed after heat treatment. Single crystals

of  $\text{Er}_7\text{Ru}_2\text{C}_{11}$ , grown in a high frequency furnace, were used for structure determination by X-ray diffraction. In the single crystal diffraction patterns of  $\text{Er}_7\text{Ru}_2\text{C}_{11}$  weak superstructure reflections were observed. The unit cell parameters of both, the sub- and the supercell are the same and are listed in *Table 2.11*. The structure of the subcell was refined in S.G. *Amma* (63), whereas in case of a superstructure the symmetry was reduced to the *klassengleiche* subgroup *Pnma* (62).

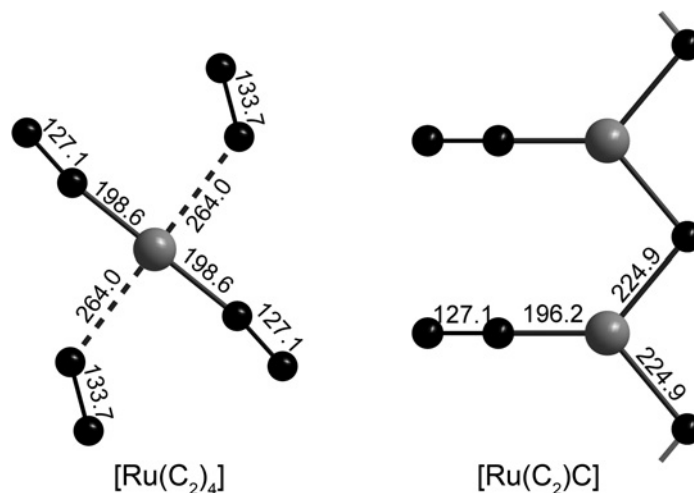
Table 2.11: Lattice parameters and unit cell volumes of the isotypic carbides  $RE_7\text{Ru}_2\text{C}_{11}$ . The lattice parameters correspond to the *Amma* and *Pnma* settings of the subcell and the superstructure, respectively.

$RE_7\text{Ru}_2\text{C}_{11}$	$a / \text{pm}$	$b / \text{pm}$	$c / \text{pm}$	$V/10^6 \text{ pm}^3$
$\text{Dy}_7\text{Ru}_2\text{C}_{11}$	1973.2(3)	352.2(1)	1659.5(3)	1153.0(1)
$\text{Ho}_7\text{Ru}_2\text{C}_{11}$	1961.8(4)	349.3(1)	1655.9(4)	1135.0(1)
$\text{Er}_7\text{Ru}_2\text{C}_{11}$	1950.6(2)	346.0(1)	1650.3(2)	1114.0(1)
$\text{Tm}_7\text{Ru}_2\text{C}_{11}$	1937.8(4)	343.7(1)	1643.7(3)	1095.0(1)

The striking feature of this structure type is the presence of two different isolated anions:  $[\text{Ru}(\text{C}_2)_4]$  and  $[\text{Ru}(\text{C}_2)\text{C}]$ . The left part of the *Figure 2.13* shows the planar 4-fold coordination around the Ru atom in the  $[\text{Ru}(\text{C}_2)_4]$  anionic part of the structure by  $\text{C}_2$  pairs with distances of 198.6 pm and 264 pm. The latter distance indicates an only marginal Ru–C bonding. In the  $[\text{Ru}(\text{C}_2)\text{C}]$  polyanion, the Ru atom is in trigonal planar coordination by two monoatomic carbon species and one  $\text{C}_2$  unit. These groups are linked to each other via the monoatomic C species resulting in one-dimensional infinite chains  $-\frac{1}{\infty}[\text{Ru}(\text{C}_2)\text{C}]$  (right part of *Figure 2.13*). The interatomic distances in the subcell are:  $d(\text{Er}-\text{Er}) = 334.6(1) \text{ pm}$  to  $370.3(1) \text{ pm}$ ,  $d(\text{Er}-\text{Ru}) = 302.6(1) \text{ pm}$  to  $339.5(1) \text{ pm}$ ,  $d(\text{Er}-\text{C}) = 234.0(1) \text{ pm}$  to  $274.0(1) \text{ pm}$ ,  $d(\text{Ru}-\text{C}) = 196.2(2) \text{ pm}$  to  $264.0(1) \text{ pm}$  and  $d(\text{C}-\text{C}) = 127.1(2) \text{ pm}$ ,  $133.7(1) \text{ pm}$ . The weak Ru–C interaction, with  $d(\text{Ru}-\text{C}) = 264 \text{ pm}$ , may cause the superstructure. In the superstructure one of the weak Ru–C bonds is opened (291 pm) and the other one gets stronger (237 pm). The authors call this situation an unusual Jahn-Teller distortion. As a result, the  $[\text{Ru}(\text{C}_2)_4]$  anionic part of the subcell breaks up to  $[\text{Ru}(\text{C}_2)_3]$  besides a  $\text{C}_2$  unit in the superstructure. The magnetic susceptibility of  $\text{Er}_7\text{Ru}_2\text{C}_{11}$  shows paramagnetic behavior with complex field-dependent antiferromagnetic ordering at low temperatures. The effective magnetic moment corresponds to free  $\text{Er}^{3+}$  ions and non-magnetic complex anions. The isotypic compounds are not sensitive against air and moisture.

The compounds of composition  $RE_{10}\text{Ru}_{10}\text{C}_{19}$  ( $RE = \text{Y}, \text{Gd}-\text{Lu}$ ) were synthesized by arc melting of mixtures of the elements followed by annealing at 1173 K [35]. Similar to  $RE_7\text{Ru}_2\text{C}_{11}$ , the Guinier X-ray powder diffraction patterns were showing only subcell reflections while single crystal diffraction data revealed two different superstructures, with monoclinic or orthorhombic symmetry. Both sub- and superstructures were solved by use of an  $\text{Er}_{10}\text{Ru}_{10}\text{C}_{19}$  single crystal. The lattice parameters obtained from Guinier X-ray powder

Figure 2.13: The two different, discrete polyanions in the crystal structure of  $\text{Er}_7\text{Ru}_2\text{C}_{11}$ ,  $[\text{Ru}(\text{C}_2)_4]$  (on the left) and  $[\text{Ru}(\text{C}_2)\text{C}]$  (on the right). All interatomic distances are shown on picture. The Ru–C bond with  $d(\text{Ru}-\text{C}) = 264$  pm is designated by dashed lines indicating only a marginal Ru–C bonding.



diffraction data are listed in *Table 2.12*. The substructure of  $\text{Er}_{10}\text{Ru}_{10}\text{C}_{19}$  was refined in the orthorhombic S.G. *Amm2* (38). The Er atoms in the subcell are situated in trigonal prisms of Ru atoms with  $d(\text{Er}-\text{Ru})$  vary from 287.3(1) pm to 328.1(1) pm. The Er–C contacts vary from  $d(\text{Er}-\text{C}) = 256(2)$  pm to 283(2) pm. The Ru atoms are located almost at the center of trigonal prisms formed by Er atoms and form trigonal planar  $\text{Ru}_3$  clusters, which were also observed in the crystal structure of  $\text{RE}_3\text{Ru}_2\text{C}_5$  [32]. The distances  $d(\text{Ru}-\text{Ru})$  vary from 272.0(1) pm to 281.9(1) pm and are very close to the metallic radius of Ru atoms with CN 12. The cluster-forming Ru atoms are coordinated by 6  $\text{C}_2$  units and isolated carbon atoms as well. These  $\text{C}_2$  units serve as bridging ligands between the  $\text{Ru}_3$  cluster and the remaining Ru atom which is bonded to 2  $\text{C}_2$  units in a side-on and one  $\text{C}_2$  unit in an end-on manner resulting in  $\text{Ru}(\text{C}_2)_{3/2}$  groups. The Ru–C and C–C contacts reveal interatomic distances  $d(\text{Ru}-\text{C})$  from 203(2) pm to 233(2) pm with  $d(\text{C}-\text{C}) = 136(4)$  pm and 138(4) pm, respectively. The Ru and C atoms form two dimensional polyanionic  ${}_{\infty}^2[\text{Ru}_{10}\text{C}_{19}]$  layers linked to each other by C and/or  $\text{C}_2$  units. The Er atoms are charge-balancing these polyanionic layers by sandwiching between them. Ordering of the C and  $\text{C}_2$  units causes different superstructures.

Table 2.12: Lattice parameters and unit cell volumes of the subcell of the isotopic carbides  $\text{RE}_{10}\text{Ru}_{10}\text{C}_{19}$ .

$\text{RE}_{10}\text{Ru}_{10}\text{C}_{19}$	$a$ / pm	$b$ / pm	$c$ / pm	$V/10^6$ pm <sup>3</sup>
$\text{Y}_{10}\text{Ru}_{10}\text{C}_{19}$	365.3(1)	1869.7(1)	730.1(1)	498.6(1)
$\text{Gd}_{10}\text{Ru}_{10}\text{C}_{19}$	374.0(1)	1868.4(4)	730.2(2)	510.2(7)
$\text{Tb}_{10}\text{Ru}_{10}\text{C}_{19}$	371.7(6)	1870.1(6)	729.7(6)	507.3(1)
$\text{Dy}_{10}\text{Ru}_{10}\text{C}_{19}$	366.8(2)	1868.5(2)	729.2(1)	499.8(4)
$\text{Ho}_{10}\text{Ru}_{10}\text{C}_{19}$	362.9(1)	1863.9(3)	728.5(2)	492.8(2)
$\text{Er}_{10}\text{Ru}_{10}\text{C}_{19}$	360.6(1)	1863.2(2)	728.6(1)	489.5(1)
$\text{Tm}_{10}\text{Ru}_{10}\text{C}_{19}$	358.5(1)	1858.6(2)	728.1(1)	485.1(1)
$\text{Yb}_{10}\text{Ru}_{10}\text{C}_{19}$	357.9(1)	1851.6(9)	728.4(1)	482.7(3)
$\text{Lu}_{10}\text{Ru}_{10}\text{C}_{19}$	354.8(2)	1854.6(8)	727.0(4)	478.4(3)

The isotopic phases show metallic behavior, and no superconducting transition was observed

down to 2 K. The susceptibility of  $\text{Lu}_{10}\text{Ru}_{10}\text{C}_{19}$  shows Pauli-paramagnetism indicating non magnetic Ru species in the structure. The other carbides show Curie-Weiss behavior with magnetic ordering temperatures all below 35 K and magnetic moments corresponding to free  $RE^{3+}$  ions. The ionic formula was rationalized by means of the  $18e^-$  rule:  $(RE^{3+}_{10})^{30+} [((\text{Ru}_3)_2^{10+}(\text{Ru}_4)^0(\text{C}_2^{4-})_9\text{C}^{4-})^{30-}]$ , which gives a formal charge of 1.67+ per Ru atom. The phases are not sensitive against air but react with  $\text{HCl}(\text{aq})$ , by formation of  $\text{CH}_4$ ,  $\text{C}_2\text{H}_4$  and  $\text{C}_2\text{H}_6$  supporting the double bonding character of the C–C.

All informations given on ternary rare-earth chromium, iron and ruthenium carbides are summarized in *Table 2.13*.

Table 2.13: Survey of ternary compounds reported in the ternary systems  $RE-T-C$  ( $T = Cr, Fe, Ru$ ).

Compound	Symmetry	C species	$d(C-C)/pm$	Complex anion	Properties
$RE_2Cr_2C_3$	$C2/m$	C	–	${}^2_{\infty}[Cr^{III}C_3]^{6-}$	Paramagnetic $RE^{3+}$ . Metallic. AF ordering at low temperature. Air and moisture sensitive.
$RE_2FeC_4$	$Ibam$	$C_2$	133.5	${}^1_{\infty}[Fe^{II}(C_2)_2]^{6-}$	Metallic. $Y_2FeC_4$ is SC at 3.6 K. Paramagnetic $RE^{3+}$ . AF ordering at low temperature. Air and moisture sensitive.
$RE_{3,67}FeC_6$	$P6_3/m$	$C_2$	129.8	$[Fe^I(C_2)_3]^{12-}$	Metallic. Non-magnetic iron. Air and moisture sensitive.
$REFeC_2$	$Amnm2$	$C_2$	ca.137	${}^2_{\infty}[Fe^I C_2]^{3-}$	Metallic. Air and moisture sensitive.
$RE_{3,67}RuC_6$	$P6_3/m$	$C_2$	ca. 130	$[Ru^I(C_2)_3]^{12-}$	Paramagnetic $RE^{3+}$ . AF at low temperatures. Not sensitive against air and moisture.
$GdRuC_2$	$Cmcm$	$C_2$	ca.138	${}^2_{\infty}[Ru^I C_2]^{3-}$	Paramagnetic $Gd^{3+}$ . FM at 45 K. Metallic. Not sensitive against air and moisture.
$RE_3Ru_2C_5$	$P6_3/m$	$C, C_2$	132.6	$[Ru_2C_5]^{9-}$	Paramagnetic $RE^{3+}$ . Very soft FM. Metallic. Stable in air.
$RE_7Ru_2C_{11}$	$Amma$	$C, C_2$	127.1, 133.7	$\{[Ru(C_2)_4][Ru(C_2)C]^{21-}\}$	Paramagnetic $RE^{3+}$ . AF at low temperatures. Metallic. Stable in air.
$RE_{10}Ru_{10}C_{19}$	$Amn2$	$C, C_2$	136.0, 138.0	$[(Ru_3)_2^{10+}(Ru_4)^0(C_2^4)_9(C_4^-)^{30-}]$	Paramagnetic $RE^{3+}$ . Magnetic ordering below 35 K. Metallic. Stable in air but reacts with $HCl(aq)$ .

FM: Ferromagnetic, AF: Antiferromagnetic

## 3 Preparation and methods of characterization

The formation of ternary carbides of rare-earth transition metals requires high temperatures due to the high melting points and low diffusion rates of the starting materials. Thus, for the synthesis of the ternary phases techniques such as arc melting, high frequency induction melting and high temperature reaction were mainly used. Since the formation rate of the ternary phases in these systems is controlled by solid state diffusion, subsequent heat treatment was required to obtain phase pure materials. SPS (Spark Plasma Sintering) and metal flux methods were used in special cases for synthesis and sintering purposes. Most intermediate ternary carbides are air and moisture sensitive, and so are the starting materials. Therefore, all preparations and sample handling were carried out in argon filled glove boxes (MBraun). A broad spectrum of methods, such as chemical analyses, diffraction techniques, spectroscopic methods and theoretical calculations were applied for sample characterization. This chapter gives an overview of the characterization techniques and methods used in this work.

### 3.1 High temperature synthesis

#### 3.1.1 Arc melting

An arc melting furnace (CENTORR vacuum industries 5S/A38042-A) with water cooling system, copper hearth and non-consumable tungsten electrode is fully integrated inside an argon filled glove box. In order to purify the atmosphere in the recipient, a titanium ingot was melted prior to melting the samples. A cold pressed pellet of the reaction mixture was placed on a copper hearth and subsequently transferred to the furnace. The starting material is melted by an electric arc created between a tungsten electrode and the copper hearth. The specimen was melted several times in order to ensure compositional homogeneity. The electric current was adjusted between 16 A and 32 A, considering the vapor pressure of the starting materials. Weight losses of  $\sim 1-2\%$  were considered to be acceptable. The arc melting furnace was also used for weld-sealing of Nb, Mo and Ta ampoules. X-ray powder diffraction was carried out on as-cast samples, which usually comprise various different phases. The arc melted samples were weld-sealed in Nb, Mo or Ta ampoules, subsequently encapsulated in fused silica tubes and heat treated at different temperatures (1173 K to 1573 K) using chamber furnaces (Nabertherm). After annealing, the samples were quenched in ice-water and further characterized.

#### 3.1.2 High temperature reaction

For syntheses involving elements with high vapor pressure, such as Sm and Yb, the starting materials were cold-pressed into pellets, weld-sealed in Mo or Ta ampoules and transferred

into a furnace. The synthesis was carried out in a horizontal corundum tube furnace (Lora 1800, HTM Reetz GmbH, Berlin, Germany) under continuous argon flow. An exemplary temperature program is shown in *Figure 3.1*.

The reaction temperature was chosen between the melting points of the rare-earth elements and the transition metal. The starting mixture was heated with a constant rate (ca. 4 K/min) to the reaction temperature and kept at this temperature for 72 hours to ensure homogeneity of the reaction mixture.

Then, the sample was slowly cooled to 1173 K to accomplish seed formation, diffusion, and crystal growth. The reaction products were analyzed by X-ray powder diffraction methods. Single crystals of the respective targeted phases frequently grew on the surface of the sample and could be easily separated for crystal structure determinations. In order to obtain single phase materials, the samples were further annealed at different temperatures (1173 K to 1473 K) using chamber furnaces (Nabertherm) for the long term heat treatments. Grinding of the samples and annealing at different temperatures were repeated until nearly single phase materials were obtained.

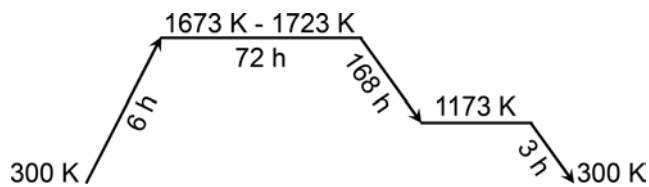


Figure 3.1: A typical temperature program for high temperature reactions.

### 3.1.3 High frequency induction furnace

A high frequency furnace (TIG 5/300, Hüttinger, Germany) fully integrated inside an argon filled glove box was used for either synthesis or annealing purposes. The furnace was connected to both, gas and vacuum lines, which gives the possibility to conduct the reactions along with annealing under vacuum as well as in argon atmosphere at temperatures up to 1473 K. Cold-pressed pellets from the elements or prereacted samples were weld-sealed in metal crucibles (Nb, Mo, Ta) and placed on top of an inverted corundum crucible at the bottom of the quartz glass tube. The latter was closed with a quartz glass cap connected to vacuum and gas lines. The quartz glass tube was positioned such that the crucible containing the sample is centered within the copper coil without contacting the quartz glass tube. Before and after reactions the system was evacuated and flushed with argon. During the experiments, the temperature of the metal crucible was continuously controlled by an IR pyrometer (Dr. George Maurer; Kohlberg, Germany) with a detection range between 973 K and 1873 K.

## 3.2 Synthesis from metallic flux and melt centrifugation

Liquid metals or metallic fluxes are commonly used for the synthesis of new compounds and the growth of single crystals of known phases. The metal should have the following characteristics to be an applicable flux: *i*) it should form a melt at reasonably low temperatures



so that normal heating equipments and containers can be used, *ii*) the metal should have a large difference between its melting point and the boiling point, *iii*) it should be possible to separate the metal from the products, by chemical dissolution, filtration, or if necessary, mechanical removal, and *iv*) the metal flux should not form highly stable binary compounds with any of the reactants [150]. In addition, no solubility of the flux in the growing crystal.

Pre-melted alloys or mixtures of the starting materials with stoichiometric atomic ratio were pressed into pellets and placed in Ta crucibles fitted with a Ta-sieve together with the flux metal in the volume ratio 1 : 3 and then put into fused evacuated quartz glass tubes. The sealed quartz glass tube together with quartz wool insulation was then put into cylindrical container made of stainless steel. This assembly was heated to 1373 K for 6 hours and kept at this temperature for 24 hours. Afterwards, the system was cooled to 873 K for 100 hours and quenched in cold water. In order to separate the flux from the grown crystal the sample was placed into a steel container and heated to 873 K. After keeping at 873 K for 2 hours the steel container was turned around and transferred into a high-temperature centrifuge [151, 152]. By this, the metal flux-melt was forced through the Ta-sieve (*Figure 3.2*).

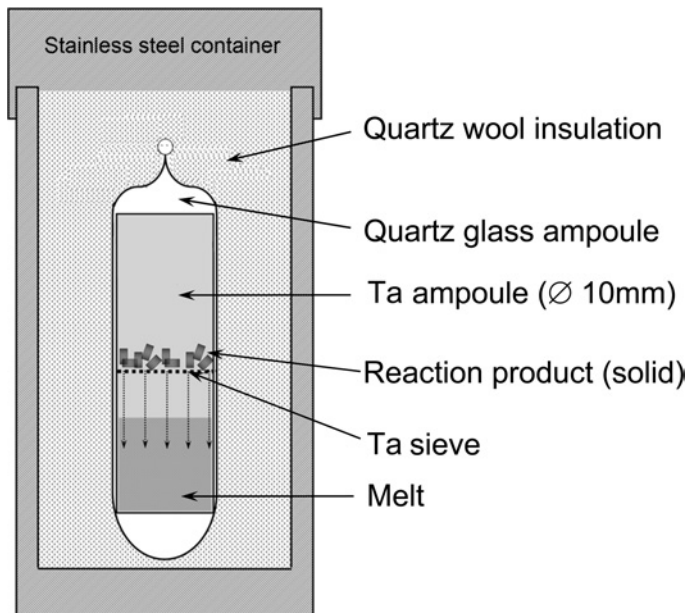


Figure 3.2: Schematic representation of the equipment used for reactions and crystal growth supported by the flux method.

### 3.3 Spark Plasma Sintering (SPS)

In the SPS process high energy, low voltage current pulses momentarily generate a spark plasma and high local temperatures up to ten thousand degrees between the particles resulting in optimum thermal and electrolytic diffusion of the components [153]. SPS sintering temperatures range between 1273 K and 2773 K. In this work, the SPS method was used for annealing the arc melted multiphase samples in order to obtain phase pure material. The earlier synthesized multiphase materials were ground and sieved with a 20  $\mu\text{m}$  sieve, followed by transfer into graphite dies with a diameter of 8 mm. They were then placed in the reaction chamber of an SPS system based on a SPS Dr. Sinter 515 machine, which is integrated in an argon glove box [154]. The pulse sequence was 12 pulses (each 3.3 ms) followed by a

pause (6.6 ms), which is the standard operating regime. Temperature control during the SPS process was carried out using a K-type thermocouple.

### 3.4 Starting materials

Table 3.1 gives an overview of the elements and materials used in this work.

Table 3.1: Chemicals and materials used for synthesis and crucible/ampoule materials.

Chemicals	Company	Comment	Purity
La	AMES	pieces	99.99%
Sm	AMES	pieces	99.99%
Gd	DR. LAMPRECHT	pieces	99.9%
Tb	DR. LAMPRECHT	pieces	99.9%
Dy	AMES	pieces	99.99%
Ho	AMES	pieces	99.99%
Er	AMES	pieces	99.99%
Yb	AMES	pieces	99.99%
Y	AMES	pieces	99.99%
Cr	ALDRICH	powder	99.99%
Fe	ALFA-AESAR	pieces	99.99%
Ru	ALFA-AESAR	powder	99.99%
Graphitic Carbon	CHEMPUR	powder	99.9%
Nb-crucible	PLANSEE	⊘ 8mm tube	99.9%
Mo-crucible	PLANSEE	⊘ 12mm tube	99.9%
Ta-crucible	PLANSEE	⊘ 8mm tube	99.9%
Quartz glass	HERAEUS QUARZSCHMELZE	tube	

### 3.5 X-ray diffraction

#### 3.5.1 Powder X-ray diffraction

Powder X-ray diffraction (PXRD) was used as a primary tool for phase identification by comparing the experimental powder patterns with the data from crystallographic databases (PDF or ICSD) or with simulated diffraction patterns of known compounds using the program package WINXPOW [155]. The crushed and finely ground polycrystalline materials were placed between vaseline-coated mylar foils on a flat sample holder. Diffraction patterns were recorded on a Huber-Guinier-camera G670, equipped with a Ge (111) monochromator (Cu  $K\alpha_1$  radiation,  $\lambda = 154.059$  pm) or Quartz ( $10\bar{1}\bar{1}$ ) monochromator (Co  $K\alpha_1$  radiation,  $\lambda = 178.896$  pm) in transmission geometry in the range  $4^\circ < 2\theta < 90^\circ$ . Powder X-ray diffraction was also applied for the precise determination of the unit cell parameters. The unit cell parameters were determined at room temperature using LaB<sub>6</sub> as internal standard (SRM660a,  $a = 415.6916$  pm, 295.5 K) and refined by least squares refinements of the Bragg reflection

positions using the PPLP [156] and WinCSD [157–159] programs. Powder XRD was also used for crystal structure determinations and refinements of single phase materials, for which good quality single crystals could not be obtained. For the Rietveld refinements the programs GSAS [160] and JANA 2006 [161] were used.

### 3.5.2 Single crystal X-ray diffraction

Single crystals were mounted on glass fibers and sealed in Lindemann glass capillaries ( $\varnothing$  0.2 mm). Intensity data were collected at room temperature on one of the following diffractometers: *i*) Rigaku AFC7 diffractometer with Mercury CCD detector and graphite-monochromatized Mo K $\alpha$  ( $\lambda = 71.069$  pm) radiation, *ii*) image plate diffractometer IPDS-2 (Stoe Cie, Darmstadt, Germany) with Mo K $\alpha_1$  ( $\lambda = 71.069$  pm) radiation; *iii*) Rigaku AFC8 diffractometer equipped with curved R-axis rapid imaging plate detector and graphite-monochromatized Ag K $\alpha$  ( $\lambda = 56.088$  pm) radiation, and *iv*) image plate diffractometer MAR 345dtb with Mo K $\alpha$  ( $\lambda = 71.069$  pm) radiation. The data reduction including corrections for Lorentz and polarisation factor were carried out using the programs CRYSTALCLEAR [162], X-AREA [163] or EVAL15 [164] depending on the type of diffractometer. Absorption corrections were performed by multi-scan and/or numerical methods. The crystal structures were solved by either direct methods SHELXS97 or Patterson synthesis and then refined using the program package and SHELXL97 [165]. Modulated and composite structures were solved by a charge-flipping algorithm using the program SUPERFLIP [166], which is implemented in JANA 2006 [161]. For standardizing crystallographic data the program STRUCTURE TIDY [167], implemented in the PLATON software [168] package, was used. The structure models were assessed by convergence of the *R*-values (*R*1; *wR*2 and *Goof*), indicating the fit of the structure model to the observed data. *R*1 is given by:

$$R1 = \frac{\sum_{hkl} \|F_o\| - |F_c|}{\sum_{hkl} |F_o|} \quad (3.1)$$

Weighted *wR*2 is based on  $F^2$  and defined as:

$$wR2 = \sqrt{\frac{\sum_{hkl} w(F_o^2 - F_c^2)^2}{\sum_{hkl} w(F_o^2)^2}} \quad (3.2)$$

Weighting is done according to (for SHELXL97):

$$w = \frac{1}{\sigma^2(F_o^2) + (w1 \cdot P)^2 + w2 \cdot P} \quad (3.3)$$

where

$$P = \frac{(2F_c^2 + F_o^2)}{3} \quad (3.4)$$

Another important factor for assessment of a structure model is given by the goodness of fit *Goof*.

$$GooF = S = \sqrt{\frac{\sum_{hkl} w(F_o^2 - F_c^2)^2}{n - p}} \quad (3.5)$$

where  $n$  is the number of independent reflections and  $p$  is the total number of refined parameters. For a very good structure model,  $GooF$  is close to 1.

### 3.5.3 Superspace approaches

Incommensurately modulated structures, composite structures and quasicrystals constitute the category of aperiodic crystals. Modulated structures are derived from the 3D periodic structures, where the atoms, groups of atoms or molecules are shifted or rotated with respect to their neighbors in a such a way that the 3D translational symmetry is broken. To restore the periodicity, the concept of higher dimensional superspace was developed by De Wolff, Janssen and Janner [169–175]. They proposed that the shifts in modulated structures are not arbitrary, but follow distinct rules: within these distortions, additional periodicity is present which can be mathematically described by so-called *atomic modulation functions* (AMF) (Equation 3.7). Thus, modulation can be considered as a periodic deformation of the original crystal structure. When the periodicity of the modulation is in phase with the periodicity of the average structure, the modulation is called *commensurate* modulation or *superstructure*. In this case, translational periodicity can be preserved by enlarging the unit cell of the average structure. When the periodicity of the modulation and the average structure are related by an irrational number they can be in phase accidentally once, but there is no translational symmetry between points where the short and the long period are in phase, and this kind of modulated crystal structures are called *incommensurate* or *aperiodic*. Due to the periodic character of the modulation, additional weak reflections appear in the diffraction pattern. These peaks are called *satellite reflections* of the *main* reflections, which belong to the average structure, and appear at equal distances  $\pm \mathbf{q}$  from all main reflections. The vector  $\mathbf{q}$  is called modulation wave vector. The stronger the modulation, the stronger the intensity of satellite reflections [176]. The modulation wave vector  $\mathbf{q}$  can be defined with respect to the reciprocal lattice of the 3D periodic structure (average structure) as presented in equation 3.6.

$$\mathbf{q} = \sum_{i=1}^3 \sigma_i \cdot \mathbf{a}_i^* \quad (3.6)$$

where one of the  $\sigma_i$  must be an irrational number for incommensurately modulated crystals. The atomic modulation functions ( $\mathbf{u}(\bar{x}_4)$ ) describe the atomic parameters along a fourth superspace coordinate,  $\bar{x}_4$ . It is defined as  $\bar{x}_4 = t + \mathbf{q} \cdot \mathbf{r}^\circ$ , where  $\mathbf{r}^\circ$  is the average position of the atoms and  $t$  is the phase of the modulation. One can distinguish *i*) occupational, *ii*) displacive and *iii*) thermal modulations. The modulation functions can be harmonic (continuous) or non-harmonic (discontinuous). The harmonic modulation can be expressed by truncated

Fourier series, of the following form (*Equation 3.7*):

$$\mathbf{u}(\bar{x}_4) = \sum_{n=1}^m \mathbf{A}^n \sin(\bar{x}_4) + \mathbf{B}^n \cos(\bar{x}_4) \quad (3.7)$$

where  $\mathbf{A}^n = (A_1^n, A_2^n, A_3^n)$  and  $\mathbf{B}^n = (B_1^n, B_2^n, B_3^n)$  are the six independent coefficients for each harmonic component of the modulation [177, 178]. In case of discontinuous modulations, special functions such as Crenel [179] or saw-tooth (combination of positional and occupational modulation) functions [180] are used.

Incommensurate composite structures are based on two interpenetrating periodic structures, or subsystems, that are mutually incommensurate. The three basis vectors of the reciprocal lattice and the modulation wave vector of each of the subsystems are derived from the set of  $(3+d)$  reciprocal lattice basis vectors by so-called  $W$ -matrices. The  $W$ -matrices are  $(3+d) \times (3+d)$  square matrices with integer components [178].

For solving and refining modulated and incommensurate composite structures as well as for calculation of the  $t$  – plots (which shows variation of a certain geometric parameter with modulation phase  $t$  and provides all values for this parameter occurring anywhere in the three-dimensional crystal structure [176]) as well as the Fourier maps the program JANA 2006 [161] and for structure visualizations the program DIAMOND [181] were used.

### 3.6 Metallographic investigations

Metallographic examinations were done on bulk specimen of about 5 mm diameter. As the materials are air and moisture sensitive, they were handled and prepared in a glove box. A piece of the specimen was embedded in two-component epoxy resin and ground using fixed abrasive papers (SiC, grit sizes 40, 24 and 15  $\mu\text{m}$ ). The ground samples were polished in four steps using a slurry of 6, 3, 1 and 1/4  $\mu\text{m}$  diamond powders with  $n$ -hexane as lubricant on polishing cloth (MD-Dur, Struers). After each step, the specimens were cleaned with a rubber cleaning tool. The microstructures were examined by optical microscopy (Axioplan 2, Zeiss) using bright field, dark field, differential interference contrast (DIC) and polarised light.

### 3.7 X-ray spectroscopic analysis

#### 3.7.1 Scanning electron microscopy and energy / wavelength dispersive X-ray analysis

A focused high-energy electron beam interacts with the atoms of a material and several signals are produced containing information about the sample's surface topography and composition. The types of signals produced by a scanning electron microscopy (SEM) include secondary electrons (SE), back-scattered electrons (BSE), characteristic X-rays, light (cathodoluminescence), specimen current and transmitted electrons (in the case of thin samples).

Microstructure and composition of the material under investigation were examined using a Philips XL 30 SEM with an integrated energy-dispersive X-ray (EDX) spectrometer. The characteristic X-ray signals were analyzed using the software package EDAX Genesis. The EDX analyses in this work were performed without using standards. The standardless EDX is in general only reliable for elements with  $Z > 10$ , which means that the carbon content can not be determined quantitatively. Quantitative analyses were done using a wavelength-dispersive X-ray (WDX) spectrometer (Cameca SX 100) using the pure elements as standards. In this work, the C content was calculated from WDX results by the difference method, i.e.  $\tilde{X}(C) = 1 - \sum \tilde{X}_i(\text{metal})$ , (sum over *RE* and *T* metal).

### 3.7.2 X-ray absorption spectroscopy (XAS)

When X-rays hit a sample, the oscillating electric field of the electromagnetic radiation interacts with the electrons bound in an atom. Either the radiation will be scattered by these electrons, or absorbed and excite the electrons. At certain energies, the absorption increases drastically and gives rise to an *absorption edge* corresponding to the binding energy of electrons in the *K, L, M, etc.*, shell of the absorbing element. This absorption process is exploited in XAS. XAS gives details about the electronic structure of an element, such as density of unoccupied states and oxidation state. In this work, the Fe *K*-threshold of the samples was measured at the synchrotron beamline *E4* at HASYLAB/DESY in Hamburg. Airtight stainless steel containers were charged with

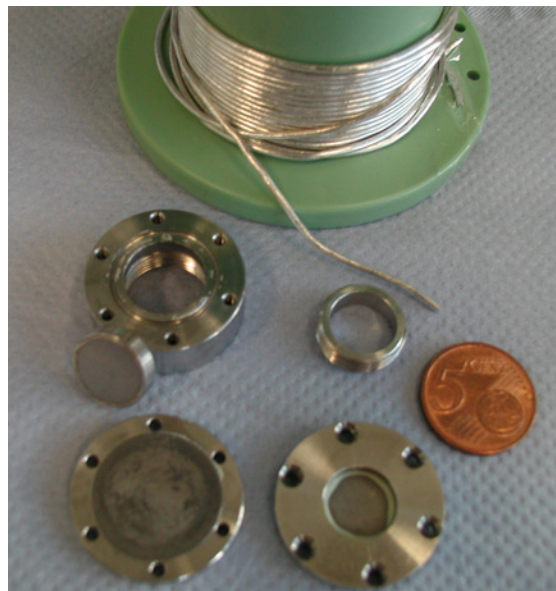


Figure 3.3: Beryllium cells used for the XAS measurements of air and moisture sensitive polycrystalline samples.

air/moisture sensitive polycrystalline materials, diluted with  $B_4C$  powder in the volume ratio 1 : 3, sealed by indium metal wire gaskets and afterwards closed by Be windows of 0.5 mm thickness (*Figure 3.3*). The monochromatic (Si(111) double-crystal monochromator) X-ray passes through the sample and a reference material, which is used for calibration of the energy scale. The intensity of the X-ray is measured with gas-filled ionization chambers in front of and behind the sample and behind the reference material. The absorption of the sample and the reference material follows the Lambert-Beer law. The weights of the sample and reference materials were calculated using the program XAFSMASS [182], depending on the energy of the absorption edge of the element under investigation, in order to have optimal absorption. The spectra were evaluated by use of the programs ATHENA and ARTEMIS [183].

### 3.8 Mössbauer spectroscopy

Mössbauer spectroscopy is based on the recoilless nuclear  $\gamma$ -ray resonance absorption referred to as *Mössbauer Effect*. Nuclei in atoms undergo a variety of energy level transitions, often associated with the emission or absorption of a  $\gamma$ -ray. These energy levels are influenced by their environment, both electronic and magnetic, which can split these energy levels. The interaction between the nucleus and its environment is called *hyperfine* interaction. However, there are two major obstacles to observe the resonance: 1) the hyperfine interactions are extremely small and 2) the recoil of the nucleus [184, 185].

Let's consider a very simple model, in which the vibrational state of the crystal is described by a single frequency  $\omega$ , the so-called Einstein frequency. It is instructive to consider the two limiting cases, in which the mean recoil energy is either larger or smaller than the transition energy of the Einstein oscillator [186]:

$$\Delta E > \hbar \cdot \omega \quad \text{case1} \quad (3.8)$$

$$\Delta E < \hbar \cdot \omega \quad \text{case2} \quad (3.9)$$

In case 1, the probability of a nuclear transition taking place without any oscillator transition - that is, the probability of a recoilless process - is correspondingly small. The situation is entirely different in case 2. Here it is immediately evident that a nuclear transition which is accompanied by an oscillator transition occurs relatively seldom, leading under these circumstances to a high probability for recoilless processes *Figure 3.4* [187].

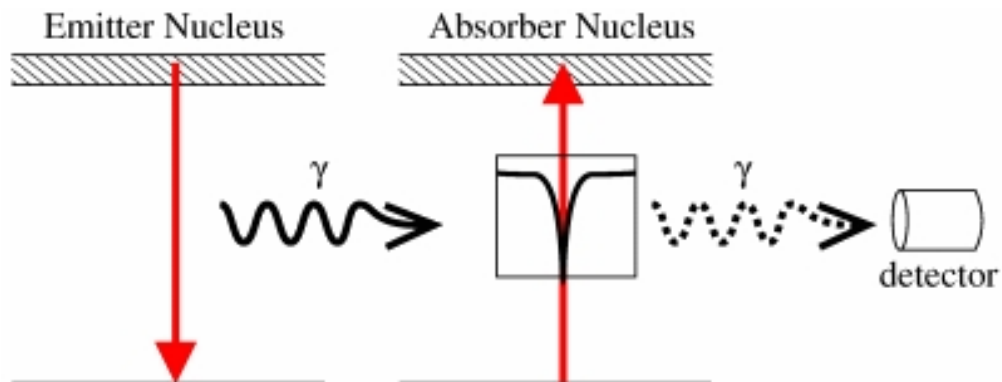


Figure 3.4: Mössbauer spectrum of resonance absorption.

Resonance only occurs when the transition energy of the emitting and absorbing nucleus match exactly. The effect is isotope specific. The relative number of recoil-free events is strongly dependent upon the  $\gamma$ -ray energy and so the *Mössbauer Effect* is only detected in isotopes with very low lying excited nuclear states. In addition, the resolution is dependent upon the lifetime of the excited state. These two factors limit the number of isotopes that can be used successfully for Mössbauer spectroscopy. The most common is  $^{57}\text{Fe}$ , which has

both a sufficiently low energy and long-lived excited state. As the environment of the nuclei in a system under investigation will almost certainly be different from that of the source, the hyperfine interactions between the nucleus and its environment will change the energy of the nuclear transition. To detect this, the energy of probing  $\gamma$ -rays must be changed. This is commonly achieved by oscillating a radioactive source with a velocity of a few mm/s and recording the spectrum in discrete velocity steps. The energy levels in the absorbing nuclei are influenced by their environment in three main ways: *i) Isomer Shift*, *ii) Quadrupole Splitting* and *iii) Magnetic Splitting*. These three interactions depend on the oxidation state, local environment and local magnetic properties of the nuclei and alone or in combination are the primary characteristics of Mössbauer spectra.

For the measurements, very finely ground air/moisture sensitive samples ( $< 20\mu\text{m}$ ), containing 5-10 mg of Fe, were put into an air tight polyethylene (PE) sample holder with O-ring gaskets and set screw. Mössbauer spectroscopic measurements were made using a conventional microcomputer controlled spectrometer (Halder) in sinusoidal mode and in vertical transmission arrangement. Measurements were performed with an area density of 5  $\text{mg}/\text{cm}^2$  iron using a  $^{57}\text{Co}/\text{Rh}$  radiation source. The transmitted intensities were stored in a 1024 multichannel analyzer (Halder). The velocity range was  $\pm 4$  mm/s and isomer shifts are reported relative to  $\alpha$ -Fe. The Mössbauer spectrum was folded to 510 channels and fitted with the Recoil Mössbauer analysis software [188] using Lorentzian lineshapes. Spectra were decomposed into subspectra with following parameters: isomer-shift (IS) (mm/s), half width  $\Gamma$  of the lines (mm/s), quadrupole splitting QS (mm/s), internal magnetic field H(T), and area  $A(\%)$  of the individual subspectra. The convergence of the iteration and the  $\chi^2$ -value of the final fit served as an indication of the quality of the refinement (*Equation 3.10*).

$$\chi^2 = \sum_{i=1}^N \frac{(Y_{i,calc} - Y_{i,obs})^2}{Y_{i,obs}^2} \cdot \frac{1}{N - K} \quad (3.10)$$

Here  $Y_{i,calc}$  and  $Y_{i,obs}$  are calculated and observed intensities per channel  $i$ , respectively;  $N$  is the total number of measured intensities and  $K$  is the number of refined parameters. The measurements as well as data fitting were performed in Prof. K. D. Becker's laboratory at Technical University of Braunschweig. Before and after the Mössbauer spectroscopic measurements the compounds were analyzed by XRD to ensure the stability of the compounds against  $\gamma$ -rays and to check the tightness of the sample holder.

### 3.9 Thermal analysis

Thermal analysis comprises a group of techniques where the properties of materials are studied as they change with temperature. In this work we used differential thermal analysis (DTA) and differential scanning calorimetry (DSC). A DTA diagram is a curve of the temperature difference between a sample and a reference material plotted against time or tem-



perature, whereas a DSC curve indicates the heat flux versus time or temperature. The measurements were carried out in argon atmosphere (Netzsch STA 409 EP). A Ta-crucible was charged with about 50-100 mg of the ground sample and weld-sealed in a glove box. The sample was heated to 1773 K and cooled to room temperature with constant heating and cooling rate of 5 K/min. Heating and cooling cycles were repeated three times in order to clearly identify the thermal effects. The thermal effects on DTA/DSC curves contain information about chemical or physical changes of the sample, i.e., melting, decomposition, phase transitions, recrystallization and so on. The measured data were evaluated by the program PROTEUS 4.0 BETA (Netzsch-Gerätebau) implemented in the NETZSCH software package [189].

### 3.10 ICP-OES and combustion technique

The chemical composition of the starting materials as well as of the synthesized materials were quantitatively analyzed by ICP-OES (Inductively Coupled Plasma Optical Emission Spectrometry). About 10-50 mg of the materials were dissolved in *aqua regia* (1  $V_{(\text{HNO}_3)}$  : 3  $V_{(\text{HCl})}$ ) and injected into the argon plasma chamber of the ICP-OES apparatus (Vista RL, Varian, Darmstadt). The ICP-OES method allows to conduct multi-element analyses by detecting their characteristic optical emission lines. For determination of the non-metallic components the combustion method (C and N) or the hot gas extraction method (O, Leco CHLN-932) were used. For this, the samples are encapsulated in a tin capsule and combusted or pyrolyzed in an oxygen stream together with an accelerator to determine the content of carbon and nitrogen. The gases  $\text{CO}_2$  or  $\text{NO}_x$  pass through a hot copper metal wire mesh where  $\text{NO}_x$  is reduced to  $\text{N}_2$  and excess  $\text{O}_2$  is removed.  $\text{CO}_2$  is detected by infrared absorption while  $\text{N}_2$  is detected by measuring the heat conductivity. By use of the carrier gas hot extraction, the sample is molten in a graphite crucible under a helium flow. Carbon is dissolved from the crucible and reacts with the oxygen in the sample to form CO and sometimes partly  $\text{CO}_2$ . Both gases are detected by infrared absorption.

### 3.11 Physical property measurements

#### 3.11.1 Magnetic susceptibility

Bulk pieces of the polycrystalline samples of about 40-100 mg mass were sealed in pre-calibrated quartz tubes (diameter = 4 mm, wall thickness = 1 mm) under 400 mbar He-atmosphere. The magnetic susceptibility was measured on a SQUID magnetometer (MPMS XL-7, Quantum Design). The magnetometer contains a high-precision temperature control system that allows measurements between 1.8 K to 400 K with an accuracy of 0.01 K (valid at low temperatures). A superconducting magnet provides magnetic fields up to  $B_{ext} = 7$  T, with a field accuracy of 10  $\mu\text{T}$  (for small fields).

### 3.11.2 Electrical resistivity

The dc (direct-current) electrical resistance of the samples was determined by a conventional four-point setup on roughly bar-shaped pieces. The measurements were carried out in temperature ranges between 4 K and 320 K. All handling of the samples were carried out under inert gas. The equipments using the four-point method are based on the following principle: two outer contacts comprise a two-wire current source that circulates current through the sample; two inner contacts provide a two-wire voltage measurement circuit that measures the voltage drop across the sample. The value of resistance is computed from the measured values of current and voltage according to Ohm's law.

## 3.12 Chemical bonding analysis

### 3.12.1 Density functional theory (DFT)

Modern quantum chemistry relies on two distinct domains of theoretical approaches, the ab-initio Hartree-Fock Self-Consistent-Field (HF-SCF) method (and its extensions) and the density functional theory (DFT). In the last decades DFT was developed as the mainstream in quantum chemistry of solids, which had been introduced in the mid-1960s by Hohenberg, Kohn and Sham [190]. The fundamental quantity of DFT is the electron density, from which according to Hohenberg and Kohn all of the ground state properties of a system may be derived. DFT can account for correlation effects. Furthermore, Kohn and Sham formulated mathematical solutions for density functional problems in many-body systems by solving a set of Schrödinger equations of the form:

$$\hat{H}_{KS}\Psi_i(\vec{r}) = \varepsilon_i\Psi_i(\vec{r}) \quad (3.11)$$

$$\hat{H}_{KS} = \hat{T}_\rho + \hat{V}_H + \hat{V}_{xc} + \hat{V}_{ext} \quad (3.12)$$

$$\hat{F}[\rho] = \hat{T}_\rho + \hat{V}_H + \hat{V}_{xc} \quad (3.13)$$

where the  $\hat{F}[\rho]$  defines the electron part only, and the problem can only be solved iteratively using the self-consistent field (SCF) method until input and output electron densities differ by less than a selected convergence criterion. Coupling of the electron density  $\rho$  with the ground state properties of a system, such as energy, is the most important idea of DFT. In a crystal, the Kohn-Sham equations can be solved independently for each  $k$ -point once the density has been calculated. Therefore, the size of the secular determinant only depends on the number of basis functions in the unit cell. However, to obtain accurate densities and wave functions, the calculations have to be carried out for a sufficiently large number of  $k$ -points.

### 3.12.2 LMTO-ASA method

The LMTO-ASA (linear muffin-tin orbital – atomic sphere approximation) method is widely used for DFT electronic structure calculations in solid state chemistry and physics, when a fast yet accurate calculation of the band structure and related properties is more important than an accurate total energy [191]. For this method the electrostatic potential of a crystal is approximated by a so-called muffin-tin potential which is spherically symmetric within a sphere with definite radius  $r_{MT}$  centered around each nucleus (MT sphere), and constant outside the spheres. The basis functions are the atom-centered muffin-tin orbitals (MTO) that have a different functional form inside and outside the spheres, but are continuous and differentiable at  $r_{MT}$ . The MTOs represent a minimum basis set and are obtained by solving the Schrödinger equation within the MT spheres. In the ASA, the domains of the atoms are replaced by spheres of equal volume, the so-called Wigner-Seitz spheres, which are touching each other or overlapping up to ca. 10%. The spaces between these MT spheres are filled by so called empty spheres, which are wave functions without nuclei. The calculations presented in this thesis were carried out using the program TB-LMTO47 on an IBM RS/6000 running AIX and on PCs running Linux. The ASA sphere radii and positions of empty spheres were determined automatically according to the method described in [191, 192]. Starting from atomic Hartree potentials, the calculations were iterated to self-consistency. For integrations in  $k$ -space, the tetrahedron method was used.

### 3.12.3 Crystal orbital Hamilton population (COHP) method

The crystal orbital Hamilton population (COHP) method was developed as an indicator for chemical bonding in solids and molecules by analyzing the orbital interactions in momentum space within density-functional electronic structure calculations [133]. The COHP was calculated in this work on the basis of LMTO-ASA calculations using a supplement to the TB-LMTO47 program [191]. COHP indicates whether an orbital interaction is bonding, nonbonding or antibonding within an energy range. Bonding states are characterized by a positive overlap integral, but a negative Hamiltonian matrix element, thus negative COHP values corresponds to bonding states. By integrating COHP values of the interactions up to the Fermi level,  $\text{ICOHP}(E_F)$ , the bond strength can be quantitatively characterized: the ICOHP represents the contribution of a given two-center interaction to the band-structure energy.

### 3.12.4 Electron localization function (ELF) and Electron localizability indicator (ELI)

In addition to COHP analysis, the electron localizability indicator (ELI) was used for chemical bonding analysis of the investigated compounds [134, 135]. Topological analysis of ELI allows the chemical bonding analysis of solids in real space by looking for local maxima and the zero-flux surfaces of its gradient field. The ELI is defined in terms of a novel space par-

tioning scheme and has the following advantages compared to the well-established electron localization function (ELF), *i*) ELI does not require scaling by a reference system which has to be chosen somewhat arbitrary; *ii*) ELI can be defined at a correlated level of theory; *iii*) a variant of ELI, called ELI-D, allows for charge decomposition analysis, i.e., the contributions of individual (atomic or molecular) orbitals to ELI can be calculated. In the case of ELI-D, the space is divided into so-called microcells each of which containing the same, infinitesimal fraction of a same-spin electron pair.  $ELI(r)$  is then proportional to the charge contained in a microcell at position  $r$  [8].

The analysis of the ELF or ELI topology can be coupled with Bader's quantum theory of atoms in molecules (QTAIM) [193], which is based on the topological analysis of the charge density. According to his definition, a QTAIM atom comprises a volume that: *i*) contains a nucleus and *ii*) is limited by zero-flux surfaces of the electron density gradient. This volume is frequently called atomic basin. Two kinds of information that can be extracted from QTAIM analysis are the volume of an atom and the charge of an atom.

QTAIM analysis is coupled with ELF/ELI analysis as follows. The zero-flux surface of the ELF/ELI gradient is used to define basins, which may represent a bond, a lone pair, or an inner shell of an atom, and the electron density is then integrated within this basin [194]. This combination allows to assign the number of electrons that participate in an individual bond in the ELF/ELI picture.

## 4 $RE_{15}[Fe_8C_{25}]$ ( $RE = Y, Dy, Ho, Er$ )

### 4.1 Synthesis and phase analysis

A series of isotypic compounds  $RE_{15}[Fe_8C_{25}]$  was synthesized from mixtures of Y, Dy, Ho or Er (Ames, 99.99%), Fe (Alfa Aesar, 99.99%) and graphitic carbon (Chempur, 99.9%) in the molar ratio  $RE : Fe : C = 15 : 8 : 25$ . The cold-pressed pellets were arc-melted several times to improve the homogeneity of the samples. For heat treatment the samples were put into Ta ampoules, which were sealed by arc-welding. The Ta-ampoules containing the samples were then sealed in evacuated fused silica ampoules, annealed at five different temperatures for 21 days (between 1173 K and 1573 K with steps of 100 K) in a horizontal tube furnace and finally quenched in water. The optimal annealing temperature, with highest yield of the main phase, was determined to be 1173 K for the Y, Ho and Er phases while nearly single phase  $Dy_{15}[Fe_8C_{25}]$  was obtained only at 1573 K. The grey reaction products were obtained with good crystallinity. All the compounds were already formed in the as-cast samples as the majority phase. In the case of the Y and Dy compounds, the formation of the  $RE_{15}[Fe_8C_{25}]$  type compounds seems to depend on the cooling rate. Slow cooling of  $Dy_{15}[Fe_8C_{25}]$  containing samples results in the formation of another ternary phase,  $Dy_{5.64}[Fe_2C_9]$  (see *Section 5.1*), whereas  $Y_{5.64}[Fe_2C_9]$  was always present as a minority phase in all  $Y_{15}[Fe_8C_{25}]$  containing samples annealed between 973 K and 1573 K. In order to prepare single phase  $Y_{15}[Fe_8C_{25}]$  and  $Y_{5.64}[Fe_2C_9]$  materials, systematic investigations of the Y–Fe–C ternary phase diagram should be conducted.

Powder X-ray diffraction patterns were recorded on a Huber-Guinier camera G670 in the range  $10^\circ < 2\theta < 85^\circ$  with a step width of  $0.005^\circ$  using monochromatic  $Co\ K\alpha_1$  radiation ( $\lambda = 178.896(1)$  pm).  $LaB_6$  was used as an internal standard (SRM660a,  $a = 415.6916$  pm). The lattice parameters, determined by least-squares refinement of the peak positions obtained from powder diffraction patterns using the program WinCSD [157–159] are listed in *Table 4.1*. The unit cell parameters of  $RE_{15}[Fe_8C_{25}]$  phases follow the lanthanoid contraction rule. In all samples, a tiny amount of metallic Fe ( $< 5\%$  of max. intensity) and a few very weak reflections ( $< 5\%$  vol.) originating from an unidentified minority phase (*Figure 4.1*) were always present.

The thermal behavior of the nearly single phase  $Dy_{15}[Fe_8C_{25}]$  sample was examined by DTA (*Section 3.9*). The bulk material (85 mg) was sealed in a Ta-crucible by arc-melting. The samples were heated to 1723 K with a heating rate of 10 K/min, which is the operating limit of the device in an Ar-filled glove box, and cooled down to room temperature with a cooling rate of 10 K/min. The DTA measurements were performed on two different specimens, with one and three heating/cooling cycles, respectively. *Figure 4.2* shows the first heating/cooling cycle of the DTA investigation.

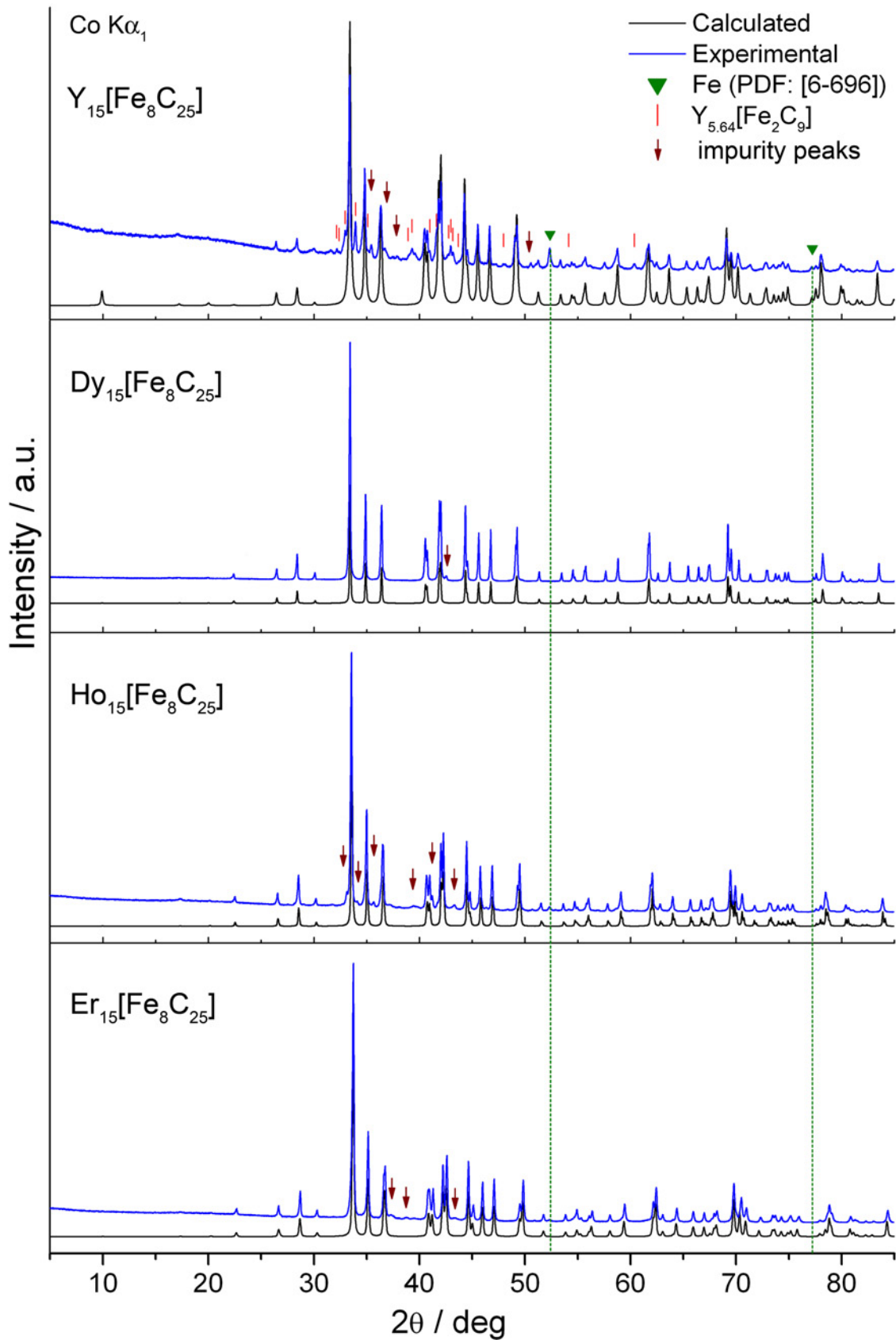


Figure 4.1: Experimental and calculated powder X-ray diffraction patterns for compounds  $RE_{15}[Fe_8C_{25}]$ . The peaks corresponding to  $\alpha$ -Fe are marked by solid green triangles, the Bragg peak positions of  $Y_{5.64}[Fe_2C_9]$  phase are marked with red vertical bars and the dark-red arrows represent the peaks of an unidentified impurity/trace phase, respectively.

A strong endothermic effect,  $\approx 0.4 \mu\text{V}/\text{mg}$ , with the peak maximum at 1682 K is observed during heating process (plus a small additional effect at  $\sim 1640$  K). After the DTA measurement the sample looked as if it was molten. X-ray phase analysis after the first cycle reveals the presence of  $\text{Dy}_{15}[\text{Fe}_8\text{C}_{25}]$ ,  $\text{Dy}_{5.64}[\text{Fe}_2\text{C}_9]$ ,  $\text{Dy}_2\text{C}_3$ ,  $\alpha\text{-Fe}$  and TaC. Thus, the endothermic effect at 1682 K corresponds to the peritectic decomposition of  $\text{Dy}_{15}[\text{Fe}_8\text{C}_{25}]$ . XRD also shows that the sample had reacted with the Ta-crucible at higher temperatures, thus additional effects were observed during cooling and repeated heating which could not be assigned. This means that  $\text{Dy}_{15}[\text{Fe}_8\text{C}_{25}]$  is stable up to  $\sim 1640$  K and for single crystal growth samples should be annealed below this temperature. A similar thermal behavior can be expected for isotypic compounds.

Based on the DTA results, single crystals of all isotypic phases, except  $\text{Y}_{15}[\text{Fe}_8\text{C}_{25}]$ , were successfully grown by a high temperature heat treatment procedure (Section 3.1.2). As-cast samples of the Ho and Er compounds were sealed in Ta-ampoules and heated to 1823 K, gently cooled down to 1173 K with a cooling rate of about 4 K/min and further cooled to room temperature within 3 hours. After heat treatment prismatic crystals, suitable for single crystal diffraction studies were grown. Single crystals of  $\text{Dy}_{15}[\text{Fe}_8\text{C}_{25}]$  were grown during a 30 days annealing process at 1573 K.

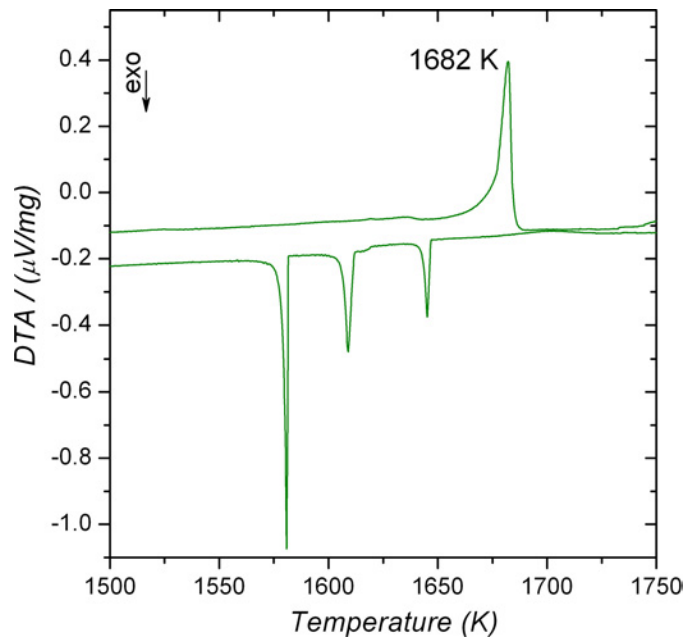


Figure 4.2: DTA curves (heating and cooling) of nearly single phase  $\text{Dy}_{15}[\text{Fe}_8\text{C}_{25}]$ .

Table 4.1: Unit cell parameters and the Bravais lattice types of compounds  $\text{RE}_{15}[\text{Fe}_8\text{C}_{25}]$  ( $\text{RE} = \text{Y}, \text{Dy}, \text{Ho}$  and  $\text{Er}$ ).

Compound	Bravais lattice	$a / \text{pm}$	$c / \text{pm}$	$V/10^6 \text{ pm}^3$
$\text{Y}_{15}[\text{Fe}_8\text{C}_{25}]$	$hP$	1194.92(4)	513.83(3)	636.37(5)
$\text{Dy}_{15}[\text{Fe}_8\text{C}_{25}]$	$hP$	1192.63(2)	514.36(2)	633.59(3)
$\text{Ho}_{15}[\text{Fe}_8\text{C}_{25}]$	$hP$	1189.11(7)	511.26(5)	626.06(8)
$\text{Er}_{15}[\text{Fe}_8\text{C}_{25}]$	$hP$	1185.29(4)	508.46(4)	618.64(1)

In order to obtain single phase materials for physical property measurements, the SPS method was used for sintering of the pre-reacted samples as described in Section 3.3. The sintering procedure was carried out at 923 K, 1123 K, 1423 K and 1523 K for 1 hour for the  $\text{Dy}_{15}[\text{Fe}_8\text{C}_{25}]$  samples. Up to the sintering temperature of 1423 K, the X-ray phase ana-

lysis did not reveal any significant change while after treatment at 1523 K the main phase  $Dy_{15}[Fe_8C_{25}]$  decomposed to  $DyC_2$  and  $\alpha$ -Fe. Some additional X-ray reflections were observed which belong to an unknown phase. Thus, in order to achieve the optimal conditions further investigations should be carried out.

The atomic ratio of the elements of  $Dy_{15}[Fe_8C_{25}]$  was semi-quantitatively determined by metallographic examination combined with WDX analyses as described in *Section 3.7.1* on polished samples (*Section 3.6*). WDX (Cameca SX 100) analyses using metallic Fe and  $DyF_3$  as standards by analyzing 10 different points revealed an averaged composition of the majority phase (98 vol.%) corresponding to the atomic ratio of Dy : Fe : C = 30.0(4) : 16.4(3) : 53.6  $\approx$  15.0 : 8.2 : 26.8; the carbon content was determined by the difference method. The EDX analysis on a single crystal of the isotypic phase  $Er_{15}Fe_8C_{25}$  resulted in the atomic ratio Er : Fe = 65.4(6) : 34.6(9)  $\approx$  15.09 : 8.0 (*Figure 4.3*). No perceptible homogeneity range was observed by using variable carbon contents ( $\pm 10$  at.%) during preparation. The  $RE_{15}[Fe_8C_{25}]$  phases are stable in air and moisture.

## 4.2 Crystal structure determination

Prismatic shaped single crystals were isolated from bulk  $RE_{15}[Fe_8C_{25}]$  ( $RE = Dy, Ho$  and  $Er$ ) under liquid paraffin in an Ar-filled glove box. Crystals with sizes of about  $50 \times 50 \times 100 \mu\text{m}$  were mounted on glass fibres and sealed in Lindemann glass capillaries of  $\varnothing 0.2$  mm diameter. Single crystal diffraction investigations were carried out on a Rigaku AFC8 diffractometer equipped with curved R-axis rapid imaging plate detector and graphite monochromatized Ag  $K\alpha$  ( $\lambda = 56.088$  pm) radiation for  $Er_{15}[Fe_8C_{25}]$ . An image plate diffractometer IPDS-2 (Stoe Cie, Darmstadt, Germany) with Mo  $K\alpha$  ( $\lambda = 71.069$  pm) radiation was used for data collection of  $Ho_{15}[Fe_8C_{25}]$  and a Rigaku AFC7 diffractometer with Mercury CCD detector and graphite monochromatized Mo  $K\alpha$  ( $\lambda = 71.069$  pm) radiation for  $Dy_{15}[Fe_8C_{25}]$ . All measurements were performed at ambient temperature. Crystallographic data and further details of data collection and crystal structure refinements are listed in *Table 4.3*.

The structure solution and refinement procedure will exemplarily be discussed for  $Er_{15}[Fe_8C_{25}]$ . *Figure 4.3* shows a BSE image of a single crystal of  $Er_{15}[Fe_8C_{25}]$  and a diffraction pattern for the  $hk2$ -layer. The diffraction pattern appeared to be trigonal but the space group could not be unambiguously determined since no systematic absences were observed after processing the data; the extinction symbol is  $P- - -$ . Thus, the  $R_{int}$  values of the merged data set were carefully analyzed. Excluding triclinic symmetry, the Laue classes  $\bar{3}m$  (hex.) and  $\bar{3}$  (hex.) had the lowest  $R_{int}$  value of 0.03 whereas the apparent Laue group  $6/m$  and  $6/mmm$  showed  $R_{int}$  values of 0.08. The mean value for Sheldrick's criterion  $|E^2 - 1|$  of 0.681 is much lower than the expected value of 0.736 for the non-centrosymmetric case. These facts indicate that the specimen under investigation was merohedrally twinned [195]. In the next step, as recommended in reference [195], the  $R_{int}$  values for candidate space groups with



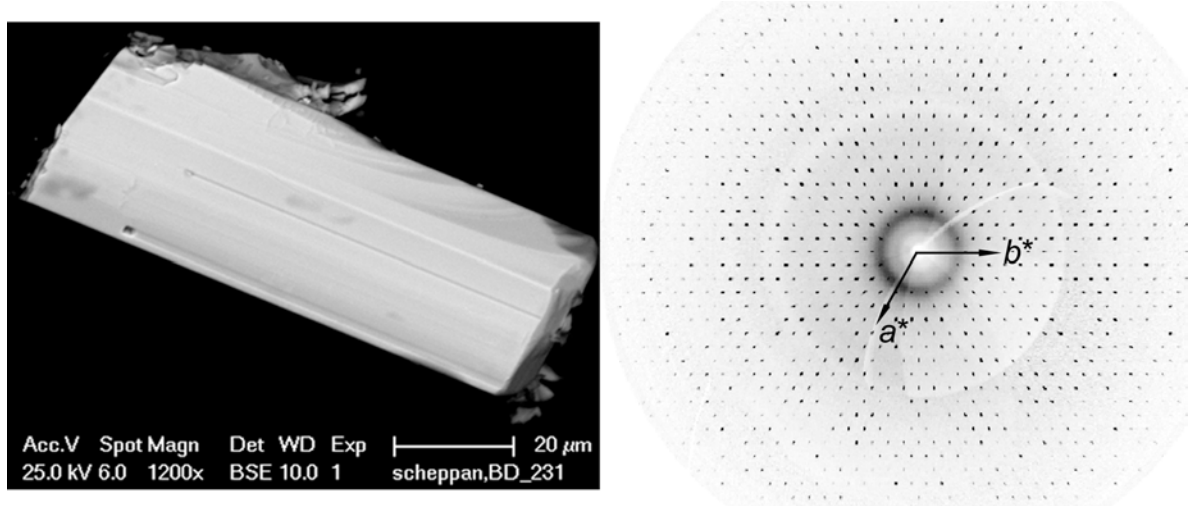


Figure 4.3: Back scattered electron (BSE) image of a  $\text{Er}_{15}[\text{Fe}_8\text{C}_{25}]$  single crystal and its diffraction pattern (reconstructed Laue image,  $hk2$ -layer).

extinction symbol  $P$  - - were analyzed (Table 4.2).

Table 4.2: Possible space groups with extinction symbol  $P$  - - for Laue classes  $\bar{3}m$ ,  $\bar{3}$ ,  $6/m$  and  $6/mmm$ .

H-M symbol	No.	Laue class	$R_{int}$	H-M symbol	No.	Laue class	$R_{int}$
$P\bar{3}m1$	164	$\bar{3}m$	0.051	$P6/mmm$	191	$6/mmm$	0.081
$P3m1$	156	$\bar{3}m$	0.051	$P\bar{6}2m$	189	$6/mmm$	0.081
$P321$	150	$\bar{3}m$	0.051	$P\bar{6}m2$	187	$6/mmm$	0.081
$P\bar{3}$	147	$\bar{3}$	0.046	$P622$	177	$6/mmm$	0.081
$P3$	143	$\bar{3}$	0.046	$P6mm$	183	$6/mmm$	0.081
$P\bar{3}1m$	162	$\bar{3}m$	0.088	$P\bar{6}$	174	$6/m$	0.079
$P31m$	157	$\bar{3}m$	0.088	$P6$	168	$6/m$	0.079
$P312$	149	$\bar{3}m$	0.088	$P6/m$	175	$6/m$	0.079

On the basis of these  $R_{int}$  values one can conclude that the true Laue symmetry is  $\bar{3}m$  or  $\bar{3}$  and the possible space groups are the ones with  $R_{int} \leq 0.051$ . The three space groups belonging to Laue class  $\bar{3}m$  were chosen and the crystal structure was solved by direct methods using the program package WinGX [196]. A structure model with reasonable CFOM (combined figure of merit) of 0.03 was found in space group  $P321$  (150). The structure refinement using this model with anisotropic ADPs of the metal atoms converged to residuals of  $R1 = 0.11$  and  $wR2 = 0.29$ . The possible merohedral twin matrix and the mass fractions of the twin components were determined using the program TWINROTMAT implemented in the program package PLATON [168]. The basic idea behind the algorithm in TWINROTMAT is to statistically analyze the possible twin axes using the reflections with  $F_{obs} \gg F_{calc}$ . All crystals under investigation were twinned with the same twin law,  $010\ 100\ 001$ . After applying the twin law, for example in the case of  $\text{Er}_{15}[\text{Fe}_8\text{C}_{25}]$ , the refinement converged to residuals  $R1 = 0.02$  and  $wR2 = 0.03$  for 6330 unique reflections and 78 variables with residual electron density of  $\approx 2e^- / \text{\AA}^3$ , indicating a good fit of the observed electron density. An examination

for missing symmetries did not suggest a new space group for the structure. The atomic displacement parameters for the metal atoms were refined in anisotropic approximation. Only for  $Er_{15}[Fe_8C_{25}]$  the carbon atoms were anisotropically refined.

Table 4.3: Crystallographic data and details on data collection and structure refinements for compounds  $RE_{15}[Fe_8C_{25}]$  ( $RE = Dy, Ho, Er$ )<sup>†</sup>.

Chemical formula, $Z$	$Dy_{15}[Fe_8C_{25}], 1$	$Ho_{15}[Fe_8C_{25}], 1$	$Er_{15}[Fe_8C_{25}], 1$
Crystal system	trigonal		
Space group	$P321$ (no. 150)		
Temperature [K]	295		
Radiation, $\lambda$ [pm]	Mo $K\alpha$ , 71.069		Ag $K\alpha$ , 56.088
Twin matrix	010 100 001 -100 0-10 00-1		010 100 001
Twin fractions	0.20 : 0.45 : 0.16	0.57 : 0.43	0.67 : 0.33
Formula mass [g·mol <sup>-1</sup> ]	3184.55	3220.71	3255.66
$a$ [pm]	1192.63(3)	1190.38(3)	1186.02(2)
$b$ [pm]	514.36(2)	510.80(1)	508.85(1)
$V$ [pm <sup>3</sup> ·10 <sup>6</sup> ]	633.59(3)	626.83(2)	619.87(2)
$\rho_{calc}$ [g·cm <sup>3</sup> ]	8.346	8.533	8.722
Crystal size [ $\mu\text{m}^3$ ]	50 × 50 × 100	40 × 50 × 90	20 × 20 × 80
$T_{min}, T_{max}$	0.5897, 1.0	0.585, 1.0	0.5897, 1.0
$R_{int.}$	0.0296	0.046	0.0255
$\theta$ -range [°]	1.97 – 32.20	1.98 – 43.38	1.97 – 32.20
Scan		$\phi, \omega$	
$hkl$ -range	-9 ≤ $h$ ≤ 16 -17 ≤ $k$ ≤ 10 -7 ≤ $l$ ≤ 7	-23 ≤ $h$ ≤ 23 -23 ≤ $k$ ≤ 23 -9 ≤ $l$ ≤ 4	-28 ≤ $h$ ≤ 29 -29 ≤ $k$ ≤ 29 -11 ≤ $l$ ≤ 12
Extinction coefficient $\chi$ <sup>(a)</sup>	0.000585(3)	0.000777(2)	0.003875(5)
Absorption correction		Multiscan	
Absorption coefficient, $\mu$ [mm <sup>-1</sup> ]	48.01	51.163	29.214
Unique reflections / parameters	1345 / 65	3029 / 73	6330 / 78
$R(F_o) / wR(F_o^2) / GooF$ (all data)	0.026 / 0.052 / 1.13	0.022 / 0.041 / 1.02	0.016 / 0.031 / 1.12
max. / min. $\Delta\rho$ [ $\bar{e} / (10^6 \cdot \text{pm}^3)$ ]	2.36 / -2.46	3.23 / -2.44	3.70 / -4.04
$w1 / w2$ <sup>(b)</sup>	0.0202 / 0.6651	0.0173 / 2.299	0.0091 / 0.6248

<sup>†</sup> Supplementary data are available from the FIZ, D-76344 Eggenstein-Leopoldshafen, Germany, e-mail [crysdata@FIZ-karlsruhe.de](mailto:crysdata@FIZ-karlsruhe.de), by quoting the depository number CSD-420018, CSD-421364 and CSD-421467

<sup>(a)</sup>  $F_c$  is multiplied by  $k[1 + 0.001 \cdot x F_c^2 \cdot \lambda^3 / \sin(2\theta)]^{-1/4}$

<sup>(b)</sup>  $R = \Sigma(|F_o| - |F_c|) / \Sigma |F_o|$ ,  $wR = (\Sigma w(F_o^2 - F_c^2)^2 / (\Sigma w(F_o^2)^2))^{1/2}$  with  $w = 1/[\sigma^2(F_o^2) + (w1 \cdot P)^2 + w2 \cdot P]$  with  $P = (F_o^2 + 2F_c^2)/3$

As  $P321$  is a non-centrosymmetric space group, the presence of racemic twinning was confirmed too. Only in the case of  $Dy_{15}[Fe_8C_{25}]$  the Flack parameter was significant, and

was taken into account during the refinement. The atoms are distributed on 3 *RE*, 3 Fe and 5 C positions and the atomic sites are fully occupied within the standard deviations except one carbon site *2c* (C5), which corresponds to the monoatomic carbon species in the crystal structure. Exemplarily, atomic coordinates in the asymmetric unit, equivalent atomic displacement parameters and site occupancies of the Wyckoff positions for  $\text{Er}_{15}[\text{Fe}_8\text{C}_{25}]$  are given in Table 4.4. The anisotropic displacement parameters of the atoms and atomic coordinates for all isotopic  $\text{RE}_{15}[\text{Fe}_8\text{C}_{25}]$  compounds are listed in Table 9.18 and Table 9.19, respectively. After several refinements checking the correlation between occupancy and atomic displacement parameters the occupancy parameter for the C5 site was fixed to 50%. However, the ordering of C5 atoms is possible in the *translationengleiche* subgroup *P3* (143). By the transformation of index 2,  $P321 \xrightarrow{t^2} P3$ , the *2c* site in space group *P321* splits into  $2 \times 1a$  sites in *P3* (143) with the same unit cell. The refinement in *P3* yields the same half occupancy for these carbon sites. Therefore, there is no reason to reduce the symmetry to *P3* for the refinement. However, the lower symmetry space group was chosen as an ordered model for the crystal structure description and for electronic structure calculations, since it allows removing one of two carbon atoms at a *1a* site. Investigations of a series of samples with varying carbon content (during preparation) by powder X-ray diffraction analysis did not evidence any homogeneity range. Furthermore, no weak reflections indicating a superstructure could be observed.

Table 4.4:  $\text{Er}_{15}[\text{Fe}_8\text{C}_{25}]$ : Fractional atomic coordinates, equivalent isotropic displacement parameters [ $10^4 \text{ pm}^2$ ] and site occupancies; estimated standard deviations are given in parentheses.

Atom	Site	<i>Occ.</i>	<i>x</i>	<i>y</i>	<i>z</i>	<i>U<sub>eq.</sub></i>
Er1	6 <i>g</i>	1	0.2885(1)	0.4046(1)	0.2535(1)	0.0047(1)
Er2	6 <i>g</i>	1	0.5118(1)	0.1445(1)	0.2454(1)	0.0048(1)
Er3	3 <i>f</i>	1	0.1689(1)	0	1/2	0.0069(1)
Fe1	3 <i>e</i>	1	0.2488(1)	0	0	0.0083(1)
Fe2	3 <i>e</i>	1	0.8682(1)	0	0	0.0055(1)
Fe3	2 <i>d</i>	1	1/3	2/3	0.2615(2)	0.0050(1)
C1	6 <i>g</i>	1	0.0776(2)	0.3962(2)	0.2426(6)	0.0075(2)
C2	6 <i>g</i>	1	0.1643(2)	0.5244(2)	0.2597(5)	0.0054(2)
C3	6 <i>g</i>	1	0.2995(2)	0.1895(2)	0.1933(5)	0.0086(3)
C4	6 <i>g</i>	1	0.4197(2)	0.2973(2)	0.2395(5)	0.0057(2)
C5	2 <i>c</i>	0.5	0	0	0.240(2)	0.0068(8)

### 4.3 Crystal chemistry

The crystal structures of the isotopic series  $\text{RE}_{15}[\text{Fe}_8\text{C}_{25}]$  represents a new structure type with Pearson symbol *hP48* and will be described exemplarily for  $\text{Er}_{15}[\text{Fe}_8\text{C}_{25}]$ .

The striking feature of this crystal structure is a planar group of six Fe atoms in form

of a slightly distorted triangle with the Fe atoms taking positions at the vertices and at the midpoints of the triangle. Such planar  $Fe_6$ -structural units have not been observed in carbides so far. Each  $Fe_6$ -cluster is surrounded only by carbon atoms within the nearest neighbor distances to the Fe atoms; twelve  $C_2$ -pairs are end-on connected to the Fe atoms at the vertices and at the midpoints of the triangle and one monatomic C carbon ligand caps this  $Fe_6$ -cluster from top or bottom, forming an even bigger cluster unit  $[Fe_6(C)(C_2)_6(C_2)_{6/2}]$  (Figure 4.4).

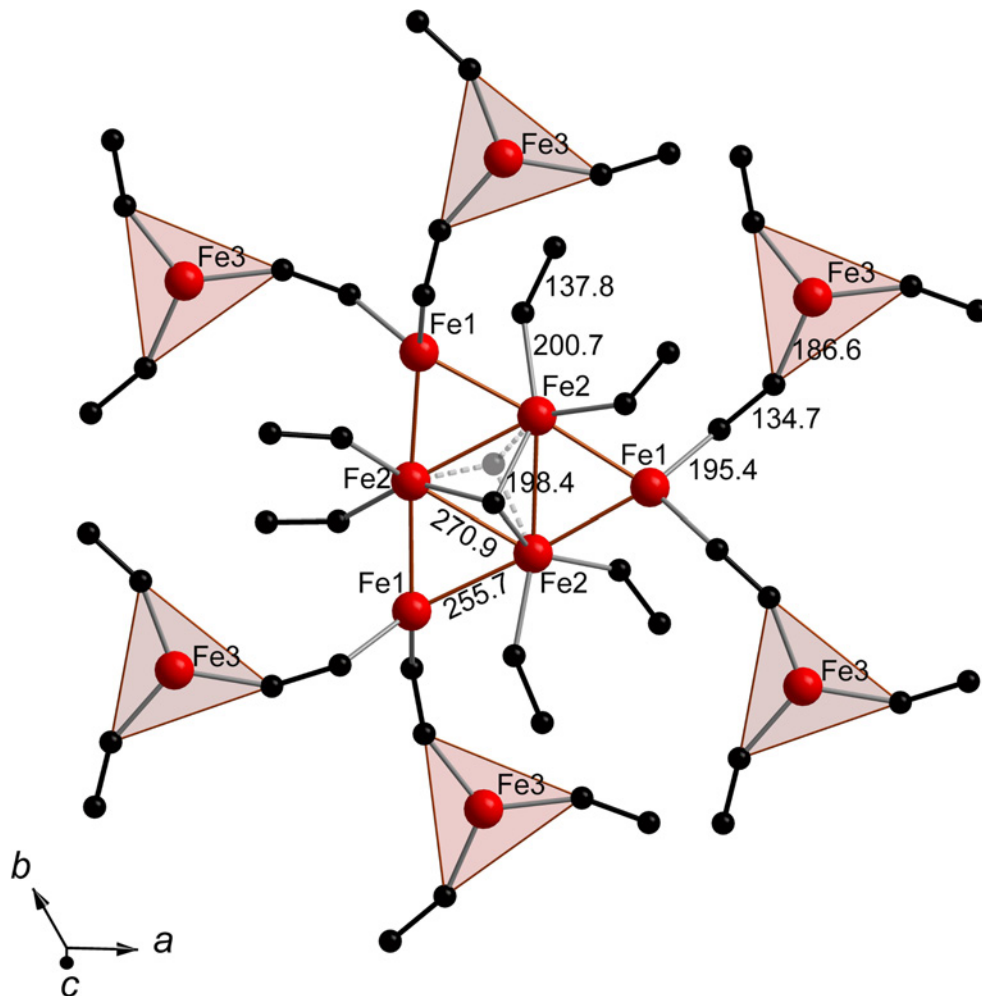


Figure 4.4: Planar  $Fe_6$ -clusters surrounded by twelve  $C_2$ -pairs, six of them serving as bridging ligands to trigonal planar  $[Fe(C_2)_3]$ -units. A monoatomic carbon ligand takes a position either above or below the  $Fe_2$  triangle.

Each cluster has six nearest neighbor clusters in the  $ab$ -plane at a distance of  $\sim 1190$  pm (between the centers of the clusters) and is connected to neighboring clusters via trigonal planar  $Fe_3(C_2)_3$  groups, thereby forming infinite 2D layers. Figure 4.5a shows the layer-motifs viewed along  $[010]$ . The primitive stacking of the polyanionic layers can easily be recognized. Er cations are positioned between the layers. The arrangement of Er atoms can also be described in the following way: 9 Er atoms (Er1, Er2) build up a trigonal tricapped prism embedding a  $Fe_3(C_2)_3$  trigonal planar group. The prisms share their common basal faces to form one dimensional chains running along  $[001]$  (Figure 4.5b).

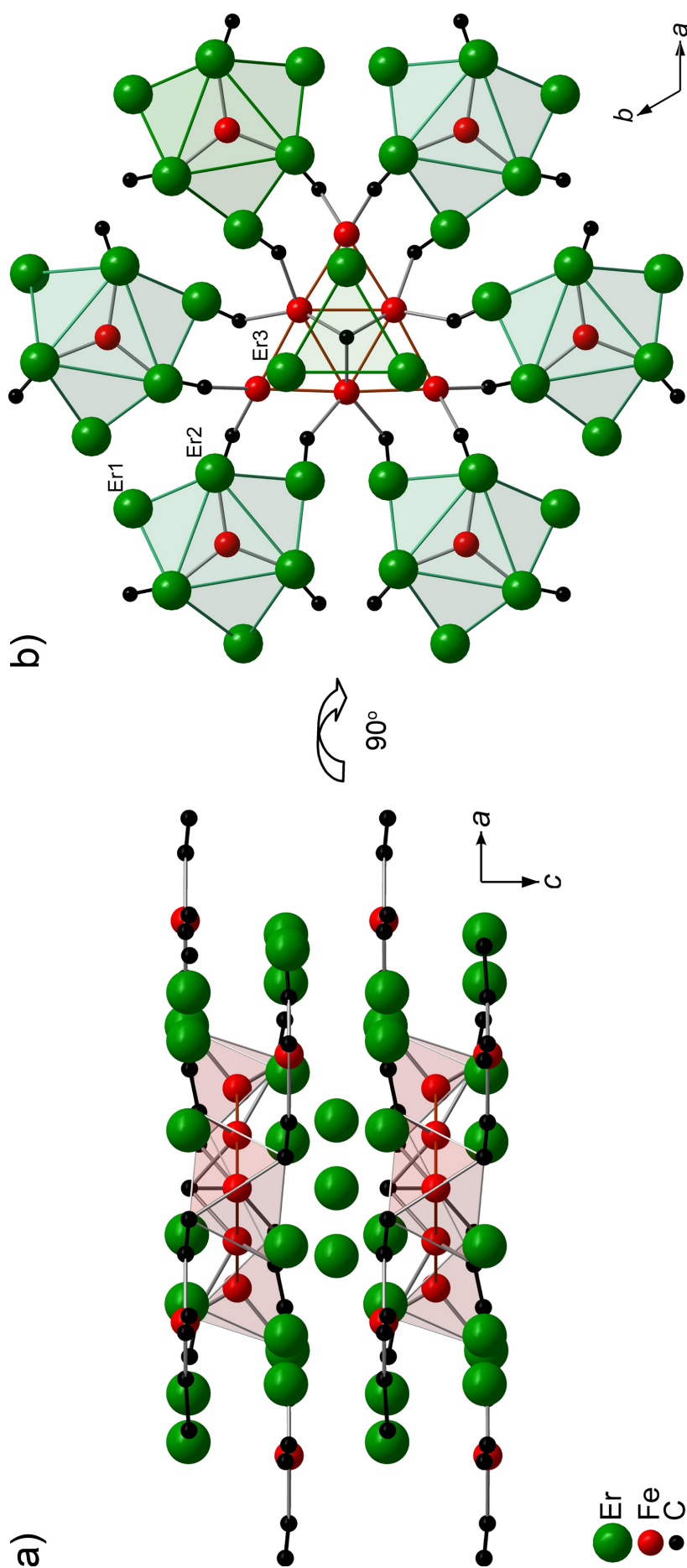


Figure 4.5: Crystal structure of  $\text{Er}_{15}[\text{Fe}_8\text{C}_{25}]$ : a) Primitive stacking of layers in the crystal structure viewed along  $[010]$  and b) Crystal structure viewed along  $[001]$ .

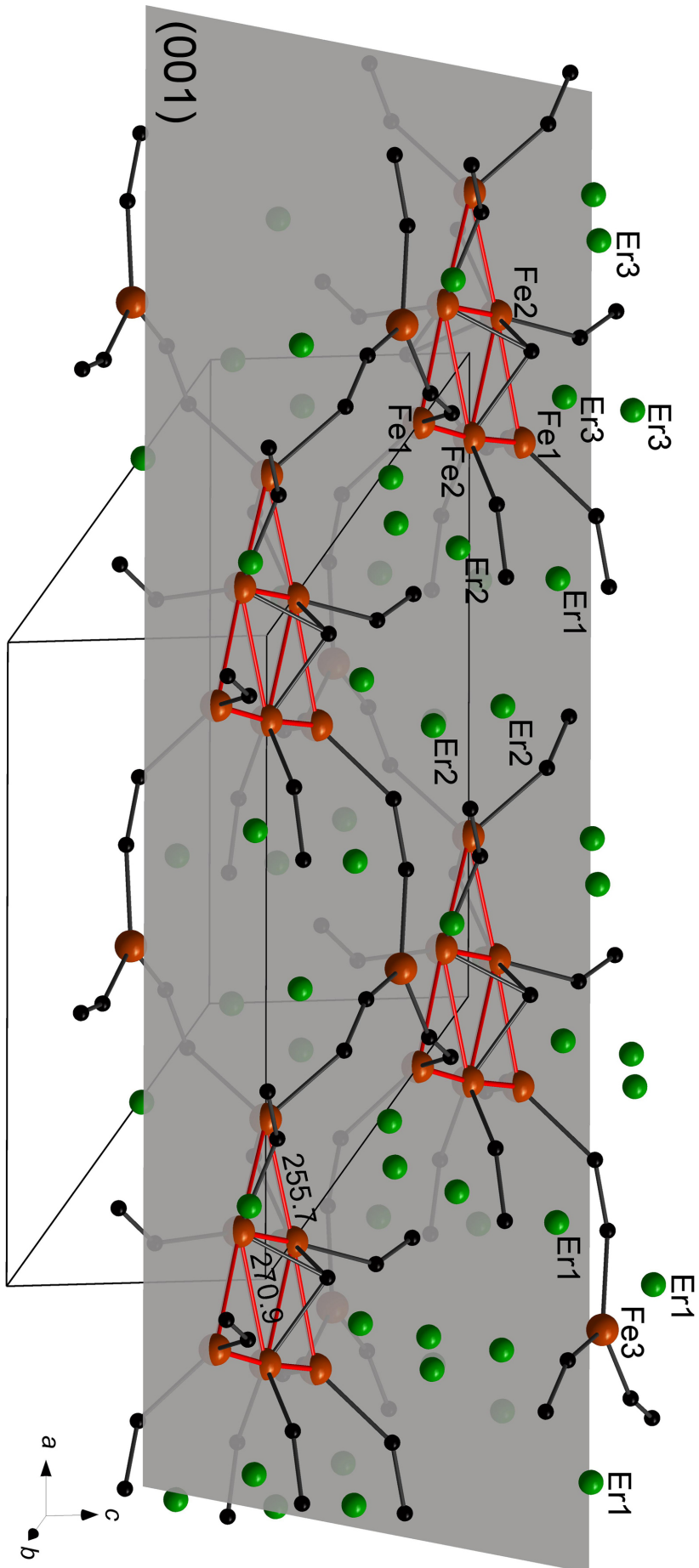


Figure 4.6: Crystal structure of  $Er_{15}[Fe_8C_{25}]$ :  $Fe_6$ -clusters lying on a common (001) plane (grey), and interconnected via trigonal planar  $[Fe(C_2)_3]$ -units.

Tricapped trigonal prismatic columnar chains containing  $\text{Fe}_3(\text{C}_2)_3$  groups in the crystal structure of  $\text{Er}_{15}[\text{Fe}_8\text{C}_{25}]$  are also present in the crystal structure of  $\text{La}_{3.67}[\text{Fe}(\text{C}_2)_3]$  (*Section 6.2.2*) as well as in nitridoferrates like  $\text{Ba}_3[\text{FeN}_3]$  [197]. In these crystal structures the chains are formed around the 6- or 3-fold axes running along [001]. In  $\text{La}_{3.67}[\text{Fe}(\text{C}_2)_3]$  the chains share common edges caused by a  $6_3$  symmetry element and form a host framework structure (*Figure 6.5*), whereas in  $\text{Er}_{15}[\text{Fe}_8\text{C}_{25}]$ , due to the point group symmetry (321), these building blocks are isolated from each other and form a honey-comb like arrangement (*Figure 4.5b*). Inside the honey-comb arrangement the  $\text{Er}_3$  atoms form trigonal prismatic chains containing the  $\text{Fe}_6$ -clusters.  $\text{Er}_3$  atoms together with the  $\text{Fe}_2$  atoms form octahedral channels running [001], which are stuffed by monoatomic carbon species. Because of the space-consuming ligands surrounding the clusters and their linking via isolated structural units, the distance between neighboring clusters within polyanionic layer becomes very large. The connection of clusters is visualized in *Figure 4.6*. The clusters on the (001) plane are connected to each other by  $\text{Fe}_3(\text{C}_2)_3$  groups which are located above and below the plane. Six out of twelve  $\text{C}_2$  units serve as bridging ligands between the  $\text{Fe}_6$ -clusters and the  $\text{Fe}_3(\text{C}_2)_{3/2}$  groups. The random distribution of the monoatomic carbon ligands is indicated in *Figure 4.6* by their positions above or below the  $\text{Fe}_6$  cluster-plane.

The structural relationship between the  $\text{Fe}_6$  cluster unit in this ternary compound and binary iron carbides can be considered in the following way. In the crystal structure of  $\gamma\text{-Fe}$  or the binary iron carbides  $\varepsilon\text{-Fe}_3\text{C}$  and  $\eta\text{-Fe}_2\text{C}$ , infinite hexagonal nets are formed by the Fe atoms as shown in *Figure 4.7*, all having comparable Fe–Fe distances. The short Fe–Fe distances in the crystal structure of  $\text{RE}_{15}[\text{Fe}_8\text{C}_{25}]$  ( $d(\text{Fe}_1\text{–}\text{Fe}_2) = 255.7$  pm and  $d(\text{Fe}_2\text{–}\text{Fe}_2) = 270.9$  pm) are just between the respective distances in  $\gamma\text{-Fe}$  (242.5 pm),  $\varepsilon\text{-Fe}_3\text{C}$  (275.4 pm) and  $\eta\text{-Fe}_2\text{C}$  (260.6 pm and 277.8 pm) (*Figure 4.7*). Comparing the Fe–Fe interatomic distances, the planar  $\text{Fe}_6$  triangular units can be regarded as *homonuclear  $\text{Fe}_6$  clusters*. From a structural point of view, the planar isolated  $\text{Fe}_6$ -clusters in the crystal structure of  $\text{RE}_{15}[\text{Fe}_8\text{C}_{25}]$  can be regarded as fragments of the binary iron carbides or elemental iron. Indeed, it is possible to define the trigonal unit cell of  $\text{RE}_{15}[\text{Fe}_8\text{C}_{25}]$ , with the  $\text{Fe}_6$  clusters at the vertices of the unit cell, also on the hexagonal lattice of  $\gamma\text{-Fe}$ . *Figure 4.8* shows a comparison of the arrangement of the Fe atoms in the hexagonal lattice of  $\gamma\text{-Fe}$  with the arrangement of  $\text{Fe}_6$  clusters in  $\text{RE}_{15}[\text{Fe}_8\text{C}_{25}]$ . The trigonal unit cell resulting for  $\gamma\text{-Fe}$  reveals an only slightly elongated lattice parameter ( $a \approx 1199$  pm) compared with  $\text{RE}_{15}[\text{Fe}_8\text{C}_{25}]$ . The amazing thing is that the arrangement (distance and orientation) of the  $\text{Fe}_6$  units in the crystal structure of  $\gamma\text{-Fe}$  and  $\text{RE}_{15}[\text{Fe}_8\text{C}_{25}]$  are almost matching. One may assume that the replacement of the Fe atoms in the crystal structure of  $\gamma\text{-Fe}$  (which do not participate in the formation of the  $\text{Fe}_6$  units) by RE and carbon atoms results in the formation of the  $\text{RE}_{15}[\text{Fe}_8\text{C}_{25}]$  crystal structure. In addition, only very few examples of more or less isolated Fe–Fe bonds have been reported. The crystal structure of  $\text{Er}_2\text{FeC}_4$  [29] contains one dimensional iron chains with Fe–Fe distances of 250 pm.  $\text{Fe}_2$  dimers with bond lengths between 269 pm and 314 pm have been

reported in metal organic compounds [198–202].

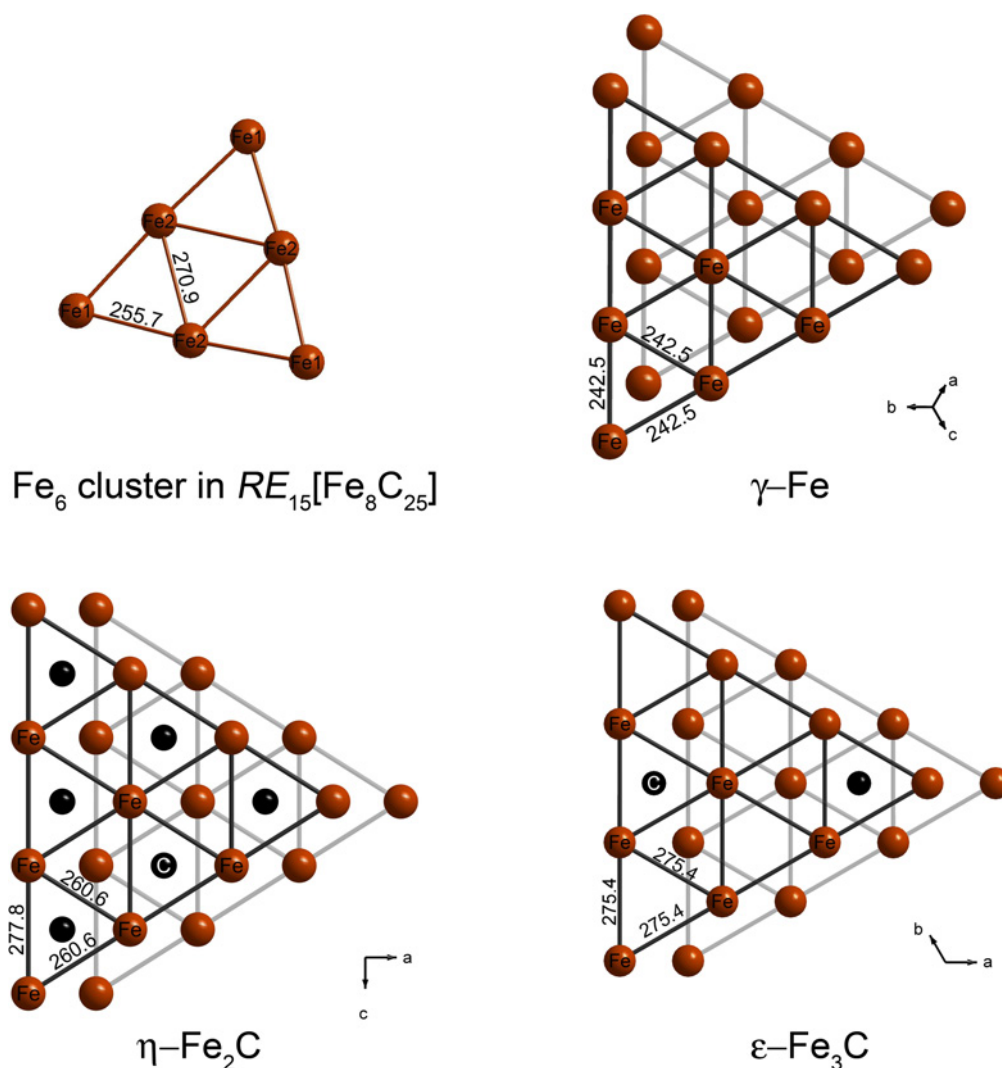


Figure 4.7: Structural fragments in the crystal structures of  $RE_{15}[Fe_8C_{25}]$ ,  $\gamma$ -Fe,  $\eta$ - $Fe_2C$  and  $\epsilon$ - $Fe_3C$ . The  $Fe_6$  cluster can be formally considered as part of the crystal structure of iron and binary carbides.

Coordination polyhedra and interatomic distances are described below, in more detail. The crystal structure of  $Er_{15}[Fe_8C_{25}]$  contains three crystallographically different Er atoms, two of them occupying the general position  $6g$  and another one on the position of a two-fold axis, thus having a multiplicity of three ( $3f$  site). The coordination of all atom types on the different crystallographic sites in the crystal structure of  $Er_{15}[Fe_8C_{25}]$  is shown with the respective interatomic distances in *Figure 4.9*. Both Er1 and Er2 atoms have three Fe nearest neighbors at an average distance of 306.9 pm and 317.9 pm, respectively. These distances are similar to the Er–Fe contacts in  $Er_2FeC_4$  ( $d(\text{Er–Fe}) = 317$  pm) [29] and in binary intermetallic phases such as  $ErFe_2$  ( $d(\text{Er–Fe}) = 310$  pm) [101] and  $Er_6Fe_{23}$  ( $d(\text{Er–Fe}) = 305$  pm) [203]. Because the sum of the covalent radii of Er and Fe atoms equals 297 pm [165], the Er–Fe contacts at distances higher than 300 pm can be considered as only marginal contacts having a low contribution to the effective coordination number (ECoN) of Er1 and Er2 [204]. Besides Fe atoms, the Er1 and Er2 atoms each have eight Er nearest neighbors at average distances of



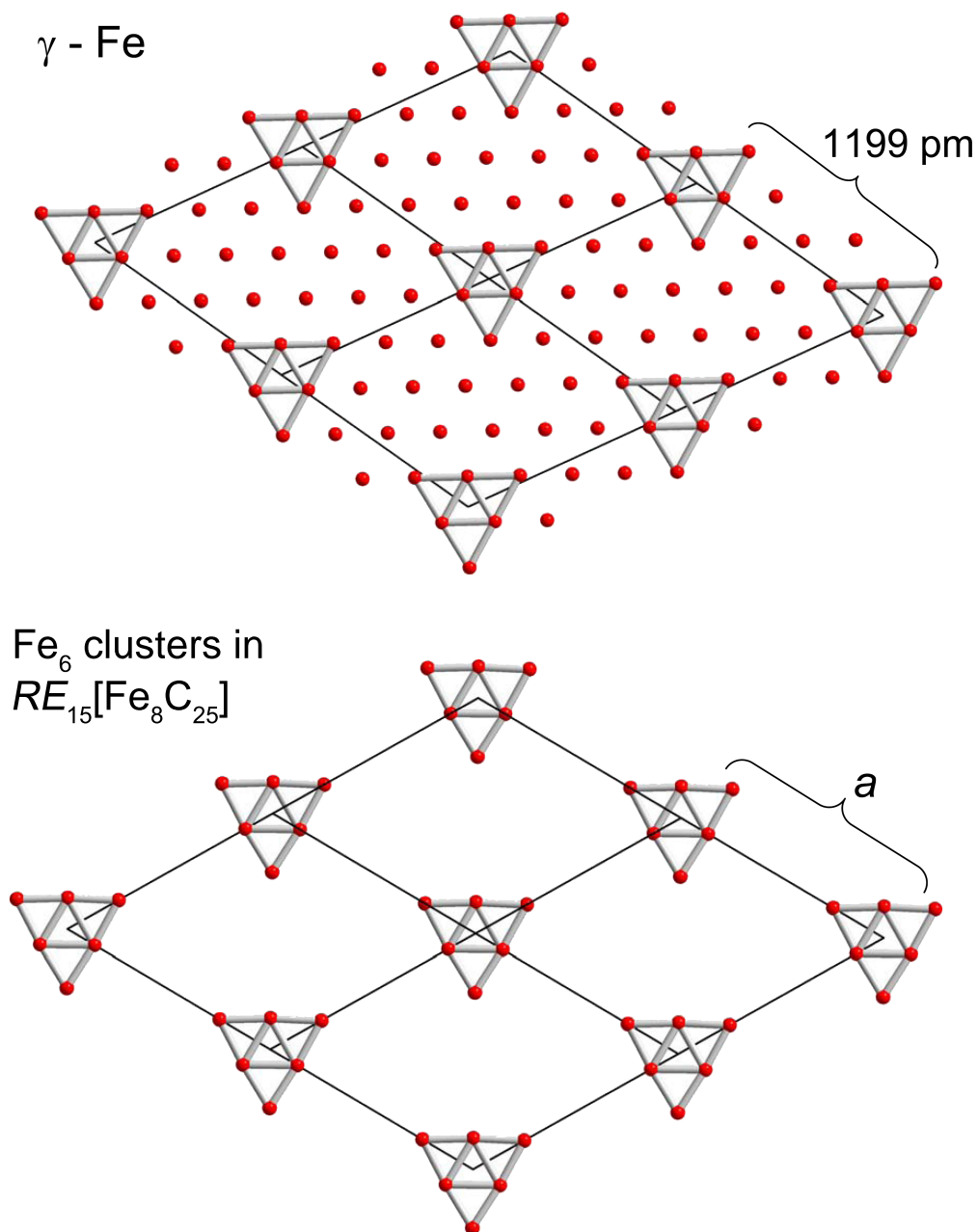


Figure 4.8: Comparison of the structural arrangements of Fe atoms in the hexagonal structure of  $\gamma$ -Fe (top) with the arrangement of  $Fe_6$  clusters in the crystal structure of  $RE_{15}[Fe_8C_{25}]$  (bottom).

356.6 pm and 363.6 pm, respectively. Similar distances are observed in the crystal structure of  $Er_2FeC_4$  ( $d(Er-Er) = 343$  to  $372$  pm) and in CeNiC<sub>2</sub>-type  $ErFeC_2$  ( $d(Er-Er) = 353$  to  $375$  pm) [31]. In addition, the Er<sub>2</sub> atoms have two more Er–Er contacts at distances of 387.9 pm and 394.0 pm which are more than 40 pm longer than the covalent diameter of Er atoms (346 pm) [165]. These contacts can probably be excluded from the first coordination shell (Figure 4.9a). Thus, the coordination number of Er1 and Er2 by metal atoms can be counted as 11. The coordination shells of Er1 and Er2 atoms are completed by eight carbon atoms at distance between 245.5 to 263.6 pm and 240.6 to 286.5 pm, respectively (Figure 4.9b).

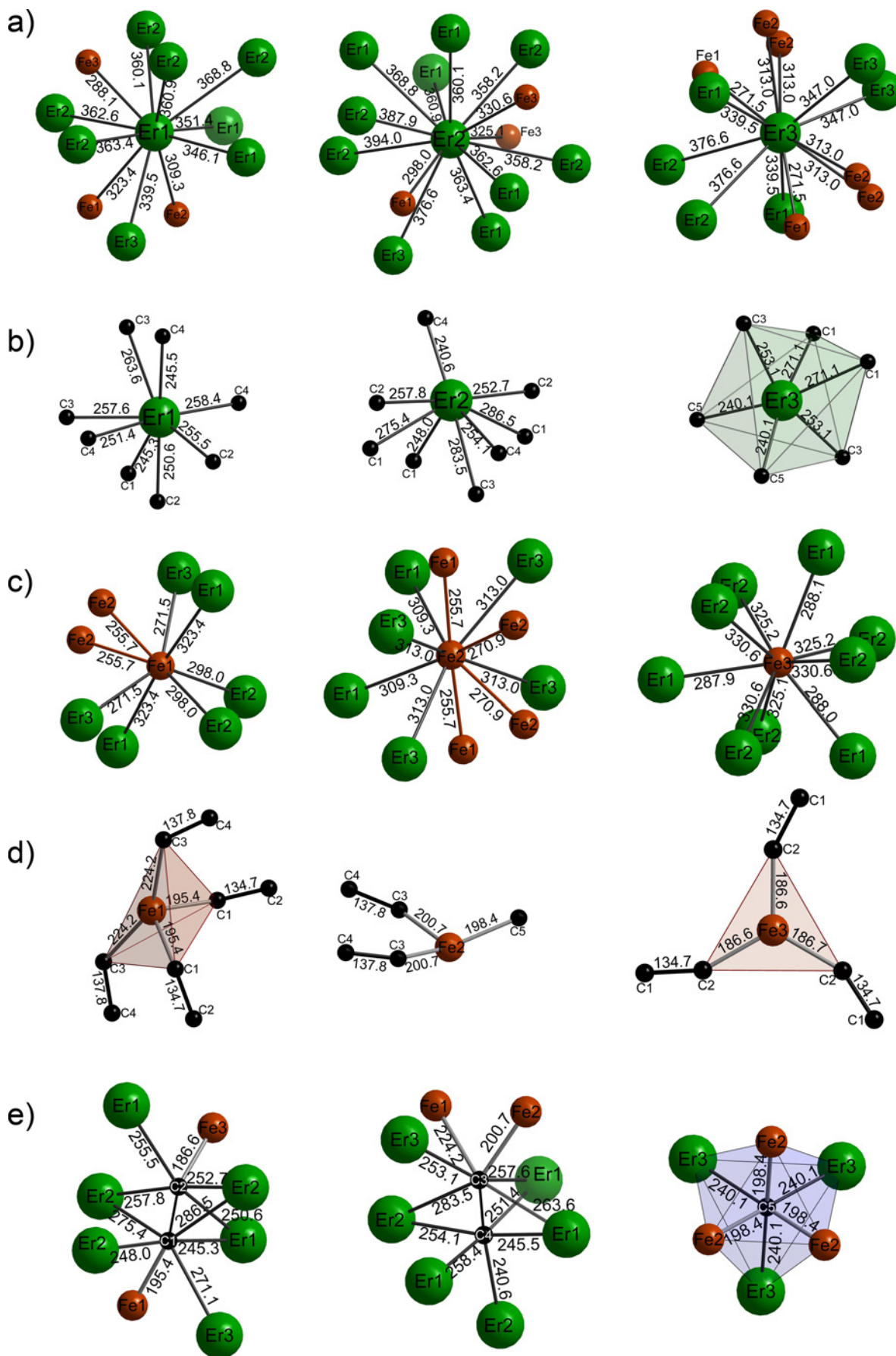


Figure 4.9: Coordination shells of all atomic types in the crystal structure of  $Er_{15}[Fe_8C_{25}]$ . Coordination around a) Er atoms, c) Fe atoms and e) carbon atoms by metal atoms. Nearest carbon neighbors for b) Er atoms, and d) the Fe atoms, respectively.

Similar distances can be also found in  $\text{Er}_2\text{FeC}_4$ ,  $\text{ErFeC}_2$  or in binary carbides such as  $\text{ErC}_2$  ( $d(\text{Er}-\text{C}) = 240$  to  $264$  pm) [205]. As differing in site symmetry, the Er3 atoms differ from the other Er atoms in their coordination as well.

Er3 is coordinated by six Fe atoms ( $2 \times 271.5$  pm and  $4 \times 313.0$  pm) and 6 Er atoms ( $2 \times 339.5$  pm,  $2 \times 347.0$  pm and  $2 \times 376.6$  pm) resulting in the coordination number 12 (*Figure 4.9a*). In Pearson's Crystal Database [11], the shortest Er–Fe distances of 280.5 pm is found in the intermetallic phase  $\text{Er}_2\text{Fe}_{17}$  [206]. This means that the short Er–Fe contacts of 271.5 pm in the crystal structure of  $\text{Er}_{15}[\text{Fe}_8\text{C}_{25}]$  could indicate a bonding interaction which will be analyzed using the COHP method in *Section 4.5*. The Er3 atoms are in contact with six carbon atoms arranged in a distorted octahedral manner (*Figure 4.9b*) with interatomic distances between 240.1 pm and 271.1 pm. These values are almost in the same range of distances  $d(\text{Er}-\text{C})$  as observed in  $\text{Er}_2\text{FeC}_4$  (236.1 pm to 287.2 pm) [29].

The Fe1 and Fe3 sites both are eight-fold metal coordinated while Fe2 has ten metal neighbors, (2 Fe2 + 6 Er), (8 Er) and (2 Fe1 + 2 Fe2 + 6 Er), respectively (*Figure 4.9c*). There are two different Fe–Fe distances (255.7 pm and 270.9 pm) which are slightly longer than the distances found in  $\gamma$ -Fe (245.5 pm) [207] and comparable with those found in binary iron carbides such as  $\epsilon$ - $\text{Fe}_3\text{C}$  (275.4 pm) [84], and  $\eta$ - $\text{Fe}_2\text{C}$  (260.6 pm and 277.8 pm) [79] or  $\text{Er}_2\text{FeC}_4$  (250.3 pm). This indicates that there are considerable Fe–Fe bonding interactions in the compounds  $\text{RE}_{15}[\text{Fe}_8\text{C}_{25}]$ , as also confirmed by electronic structure calculations (*Section 4.5*). The Fe1 bind to monodentate  $\text{C}_2$  ligands which are arranged in a distorted tetrahedral manner (*Figure 4.9d*) with Fe–C distances of 195.4 pm and 224.2 pm. The position of the Fe1 atom in this tetrahedron is strongly shifted towards the Fe2 and Er3 atoms, indicating considerable metal–metal interactions. If one accounts for the partial occupancy of the C5 position, the Fe2 atom has two monodentate  $\text{C}_2$  ligands and one isolated carbon species at distances 198.4 pm and 200.7 pm and, thus, a non-coplanar trigonal carbon coordination, which is also observed in  $\text{U}_2\text{NiC}_3$  [31]. The Fe3 atoms are coordinated by three  $\text{C}_2$  units forming distorted trigonal planar  $\text{Fe}3(\text{C}_2)_3$  groups with  $d(\text{Fe}-\text{C}) = 186.7$  pm. All iron atoms in the crystal structure occupy special positions: Fe1 and Fe2 are sitting on the two-fold axes while Fe3 atom has the site symmetry  $3..$ . The Fe–C interatomic distances are very close to the sum of the covalent radii of Fe and C atoms (201 pm) similar to the respective distances observed in binary iron carbides,  $\epsilon$ - $\text{Fe}_3\text{C}$  (193 pm) and  $\eta$ - $\text{Fe}_2\text{C}$  (182 to 190 pm), and in ternary compounds such as  $\text{La}_{3.67}[\text{Fe}(\text{C}_2)_3]$  (182 pm) and  $\text{Er}_2\text{FeC}_4$  (197 pm). The coordination number of the three crystallographically independent Fe atoms with respect to the carbon ligands is 4, 3 and 3.

Four of the crystallographically five different carbon atoms form  $\text{C}_2$  pairs, with C–C distances of  $d(\text{C}1-\text{C}2) = 134.7$  pm and  $d(\text{C}3-\text{C}4) = 137.8$  pm, while the remaining one is a monoatomic carbon (C5). The C–C distances are slightly longer than the C–C double bond found in olefins (134 pm). Each of the  $\text{C}_2$  pairs have 2 Fe and 6 Er neighbors, whereas the monoatomic carbon atoms occupy voids of the octahedral channels, running along [001], and

formed by Fe<sub>2</sub> and Er<sub>3</sub> atoms. There are 2 ( $= 8 \times 1/4$ ) octahedral voids per unit cell from which every second is occupied by the monoatomic carbon atoms (C<sub>5</sub>). Thus, the chemical formula including vacancies ( $\square$ ) can be written as  $Er_{15}[Fe_8C_{25}]\square$ . It should be noted that the accommodation of monoatomic carbon atoms in the octahedral voids of a structure is also preferred in binary iron carbides with hexagonal close packed layers, such as  $\epsilon$ -Fe<sub>3</sub>C and  $\eta$ -Fe<sub>2</sub>C (see *Section 2.1.2*), and in rare-earth carbometalates [9]. The general tendency observed in binary carbides is the following: when the metal atoms are arranged in a cubic close packing (*ccp*), the filling of octahedral voids is essentially higher compared to a hexagonal close packed (*hcp*) arrangement. This may also explain the half or one sided occupation of C<sub>5</sub> atoms (with respect to the planar Fe<sub>2</sub> triangle) in the crystal structure of  $Er_{15}[Fe_8C_{25}]$ . The distribution of the vacancies and monoatomic carbon atoms was investigated by means of total energy calculations using various superstructure models and is discussed in *Section 4.4*. The isotypic phases  $RE_{15}[Fe_8C_{25}]$  represent the first example of compounds in ternary systems  $RE$ -Fe-C with mixed ligands (C<sub>2</sub>, and monoatomic carbon atoms).

#### 4.4 Phase stability

DFT calculations were carried out on Y-Fe-C model structures,  $Y_{15}[Fe_8C_{25}]$ , using the VASP code [208, 209]. The 5*s*, 5*p*, 5*d*, and 6*s* orbitals for Y, the 4*s*, 4*p* and 3*d* orbitals for Fe, and the 2*s* and 2*p* orbitals for C were treated as valence orbitals. All calculations were scalar relativistic with the plane wave cut-off energy set to 400 eV. For all model structures, the atomic positions and lattice parameters were relaxed until the maximal force acting on each atom was less than 0.05 eV/Å. Several structure models were considered by doubling the unit cell along the *a*-axis: alternating occupation of the monoatomic carbon atom on the 2*c* site; alternating spin direction of the Fe<sub>6</sub>-clusters; altering the stacking sequences of Fe<sub>6</sub>-cluster along [001] from AA . . . to ABAB . . ., by shifting the Fe<sub>6</sub>-cluster together with the associated Y and C atoms by *c*/2. Remarkably, the total energies for placing carbon above or below the Fe<sub>6</sub>-cluster were identical within 0.5 meV per atom (below the level of significance of the calculations). Also, the spin-polarized calculations reveal that magnetic phases with an ordered moment of about 6  $\mu_B$ /f.u. are energetically favorable, lowering the total energy by about 0.2 eV/f.u. with respect to the non-magnetic one. The results further indicate the preference of one-sided occupation of the monoatomic carbon above or below the Fe<sub>6</sub>-cluster compared to a two-sided occupancy. This strongly supports the results of the crystal structure refinements. Shifting of Fe<sub>6</sub>-clusters is unfavorable due to strong coupling along the *c*-axis, and is consistent with the observed primitive stacking of the polyanionic layers.

#### 4.5 Electronic structure and chemical bonding analysis

The electronic band structure was calculated for  $Y_{15}[Fe_8C_{25}]$  with the structure model in space group *P3* (143), which allows one-sided occupation of monoatomic carbon above

or below the Fe<sub>6</sub>-clusters. Electronic structure calculations were performed using the self-consistent scalar relativistic TB-LMTO-ASA method [210] within the local (spin) density approximation (L(S)DA) [211] to the DFT. Complementary chemical bonding analysis with the focus on metal–metal interactions was performed employing the COHP method [133] on the one hand, and the electron localizability indicator (ELI-D) [134, 135] as well as the QTAIM (Quantum Theory of Atoms in Molecules) method [193] on the other hand.

The total DOS show metallic character with 212 states/eV at the Fermi level  $E_F$ . Both, non-spin polarized and spin polarized calculations, were carried out and the converged total energy was lower in the magnetic case. The spin-polarized calculation with ferromagnetic ordering yields a total magnetic moment of about  $5 \mu_B/\text{f.u.}$ , which is consistent with the magnetic moments obtained from total energy calculations using the VASP code. In spin-polarized calculations, the  $\alpha$  and  $\beta$  spin channels become inequivalent, which results in different populations of  $\alpha$  and  $\beta$  spin channels. The DOS curves of the minority ( $\alpha$ ) and majority ( $\beta$ ) spin channels are rather similar, which means spin polarization has no significant effect on the shape of the DOS but merely cause shifts in energy. *Figure 4.10* shows the total and the partial DOS curves for both  $\alpha$ - and  $\beta$ -spin channels. The energy shift results in a larger population of the majority  $\beta$ -channel, corresponding to three electrons in total. The states of lowest energy between -15 eV and -13 eV (range **A**) and the narrow peak at around -10.5 eV (range **B**) originate from the 2s orbitals of C<sub>2</sub> pairs and the monoatomic carbon atoms, respectively. The next two regions between -9 eV and -3 eV (ranges **C** and **D**) are dominated by C 2p orbitals with considerable Y 4d and Fe 3d contributions. The part below the  $E_F$  (between -2.8 eV up to  $E_F$ , range **E**) is derived from Fe 3d states, and Y 4d contributions.

The COHP indicates strong covalent Fe–C and C–C bonds as well as considerable Fe–Fe interactions, which are all exhausted below  $E_F$  (*Figure 4.11*). The averaged ICOHP value of -0.935 eV/Y–C bond is approximately one half of that of the Fe–C bonds (-2.078 eV/Fe–C bond) and bonding states are still available above  $E_F$ . The averaged Y–Y and Y–Fe interactions are the weakest ones in the crystal structure with ICOHP values of -0.154 eV/bond and -0.276 eV/bond, respectively. In contrast, Fe–Fe interactions are considerably stronger and the ICOHP values amount -0.602 eV/bond. In most cases (Y–Y, Y–C, Y–Fe), the  $\alpha$  and  $\beta$  spin channels contribute similarly to the COHP; the differences between their ICOHP values range from 0.001 to 0.01 eV/bond. Exceptions are the Fe–Fe and Fe–C bonds with a difference  $> 0.6$  eV/bond. The strong antibonding Fe–Fe peak is below  $E_F$  for the  $\beta$  spin channel, whereas this peak is above the Fermi level for the  $\alpha$  channel. By spin polarized splitting, the presence of an antibonding peak at  $E_F$  is avoided, which explains the enhanced stability of the magnetic structure [212]. For Y<sub>15</sub>[Fe<sub>8</sub>C<sub>25</sub>], the ratios of ICOHP(metal–C) / ICOHP(metal–metal)  $\approx 3$  and ICOHP(Fe–C)  $\gg$  ICOHP(Y–C) are closely related to the respective values observed for carbometalates [9]. The isotopic series of compounds RE<sub>15</sub>[Fe<sub>8</sub>C<sub>25</sub>] justifies the criteria of a bonding situation for a complex anionic structure except for the ligand type, which is a monoatomic C in the original concept [9]. Thus, according to the bonding situation, the

compound represents a rare-earth carbo-dicarboferrate [39].

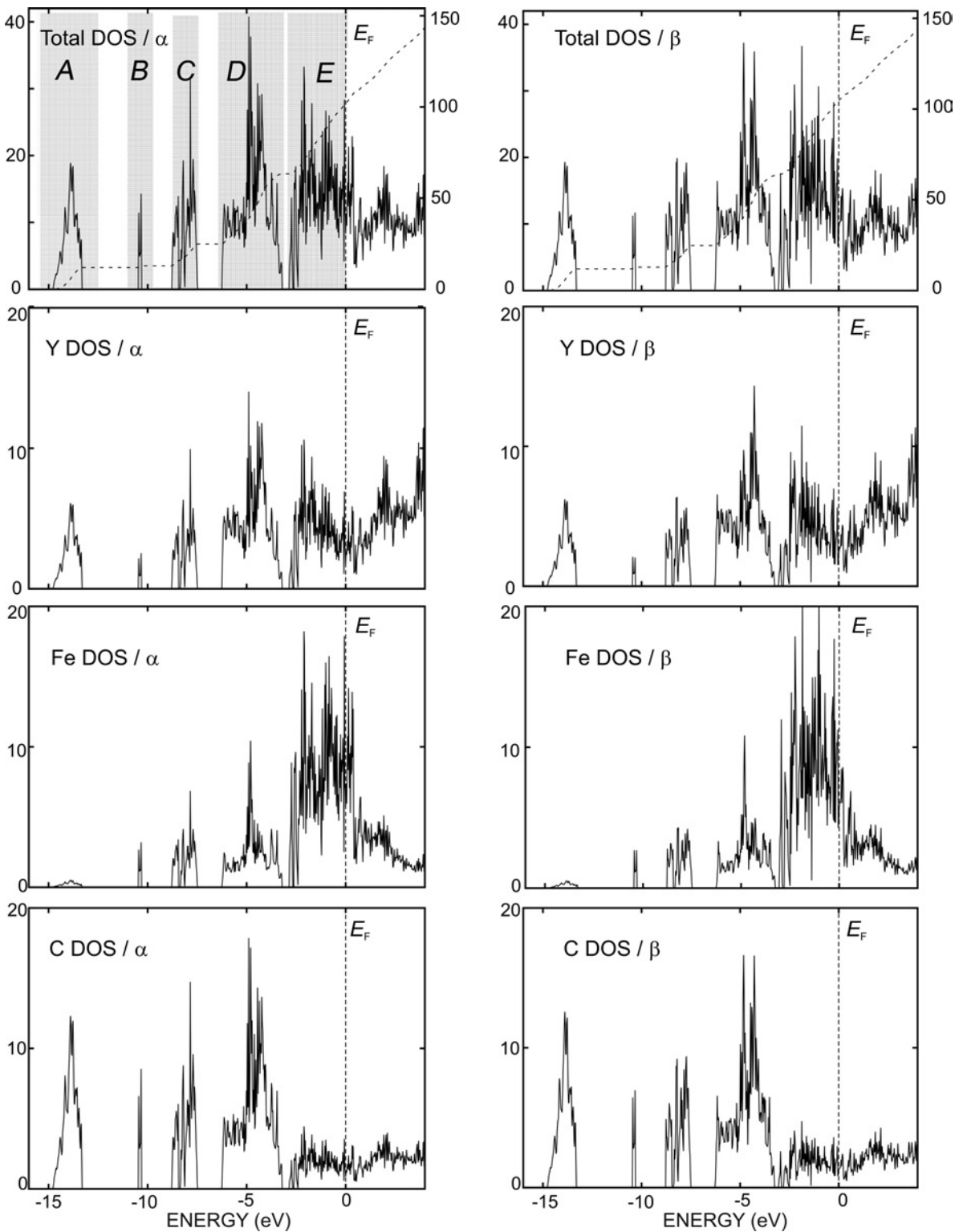


Figure 4.10: Total and projected DOS for the majority ( $\beta$ ) and minority ( $\alpha$ ) spin channels of  $Y_{15}[Fe_8C_{25}]$ . The total DOS of the valence electrons displays five different structures denoted **A**, **B**, **C**, **D** and **E** ranges.



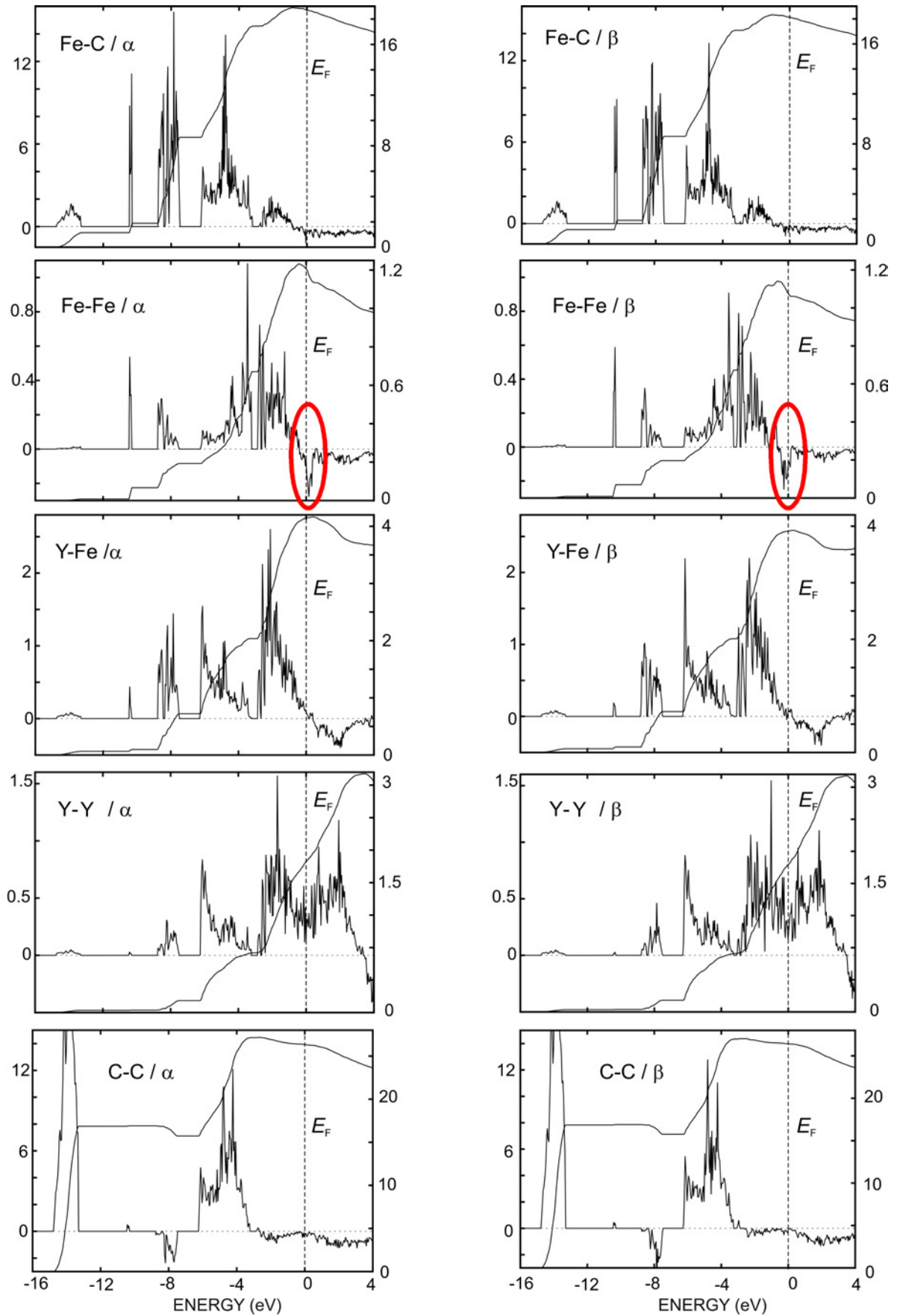


Figure 4.11: COHP diagrams of selected interatomic interactions for the majority and minority spin channels of  $Y_{15}[Fe_8C_{25}]$ . The energy shift in the  $\beta$ -channel with respect to the  $\alpha$ -channel is highlighted with red ellipses.

Electron counting on  $Y_{15}[Fe_8C_{25}]$  was performed in the following way. The charge of the  $C_2$  units in  $Y_{15}[Fe_8C_{25}]$  directly influences the assignment of the oxidation state for the Fe atoms. The partial DOS of the six  $C_2$  units in the primitive unit cell together with their COHP diagrams are depicted in *Figure 4.12* (only for the  $\alpha$  channel). The five regions from *A* to *E* on the DOS can be assigned to  $\sigma_s$ ,  $\sigma_p$ ,  $\sigma_s^*$ ,  $\pi$  and  $\pi^*$  states, respectively. The  $\sigma_s$ ,  $\sigma_p$ ,  $\sigma_s^*$  and  $\pi$  states are fully filled and the  $\pi^*$  states (*E*-region) in the vicinity of Fermi level are partially filled. From the integrated DOS we can count 59  $e^-$  in the regions from *A* to *D* and 11  $e^-$  in the  $\pi^*$  state, which results in 70  $e^-$  up to  $E_F$ . In an isolated  $C_2^{2-}$  unit (isoelectronic to  $N_2$ ) no antibonding  $\pi^*$  orbitals are occupied, while in an isolated  $C_2^{4-}$  (isoelectronic to  $O_2$ ) half of the antibonding  $\pi^*$  orbitals are occupied. In both molecules the  $\sigma_p$  orbitals, are fully occupied, yielding formal bond orders of 3 and 2 for  $C_2^{2-}$  and  $C_2^{4-}$ , respectively [38]. In terms of a simple ionic picture, e.g.,  $CaC_2$  ( $Ca^{2+}(C_2)^{2-}$ ), the filled bonding  $\pi$  states and the empty antibonding  $\pi^*$  and  $\sigma_p^*$  states induce a short C–C bond distance of  $\approx 120$  pm.

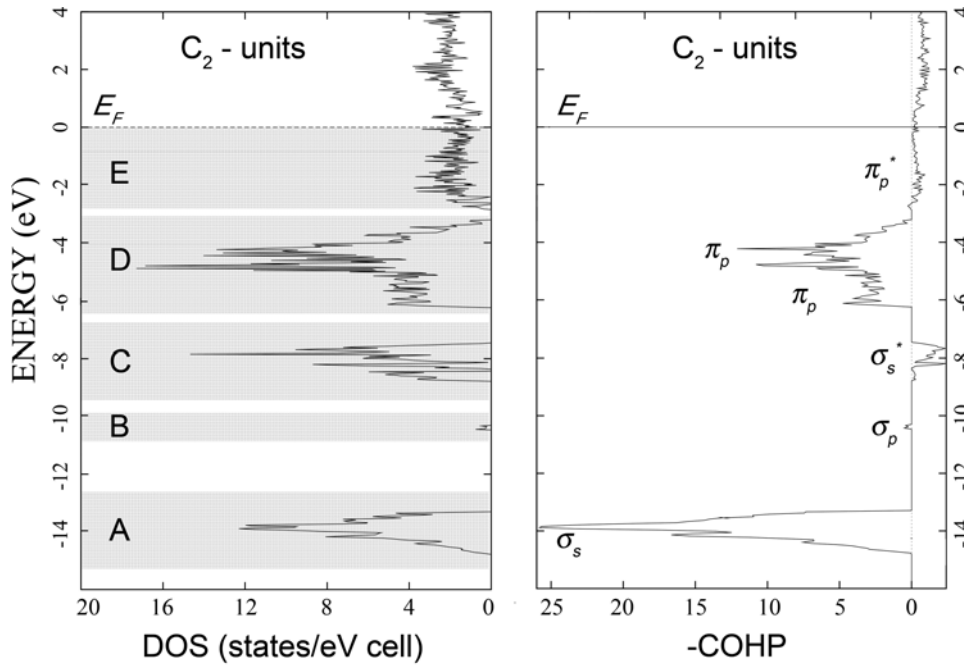


Figure 4.12: Partial DOS and COHP diagrams for the  $C_2$  units of  $Y_{15}[Fe_8C_{25}]$  (in the  $\alpha$ -channel). The types of the two center interactions are shown on the respective peak maxima (right). COHP clearly reveal a partially filled  $\pi^*$  states near the  $E_F$  indicating the  $C_2^{4-}$  character of the  $C_2$  units.

With increasing number of electrons in the  $C_2$  unit, e.g., in  $UC_2$  ( $U^{4+}(C_2)^{4-}$ ), the C–C bond distance increases to  $\approx 135$  pm because the antibonding  $\pi^*$  states are gradually filled [213]. The C–C distances in the crystal structure of  $Y_{15}[Fe_8C_{25}]$  are  $\sim 135$  pm and  $\sim 138$  pm. On the basis of these considerations and the electron number from IDOS (70  $e^-$ ) the  $C_2$  units in the crystal structure of  $RE_{15}[Fe_8C_{25}]$  have definitely no  $C_2^{2-}$  but rather a  $C_2^{4-}$  character ( $6 \times C_2^{2-}$  ( $\sigma_s^2 \sigma_s^{*2} \sigma_p^2 \pi^4$ ) = 60  $e^-$ ;  $6 \times C_2^{4-}$  ( $\sigma_s^2 \sigma_s^{*2} \sigma_p^2 \pi^4 \pi^{*2}$ ) = 72  $e^-$ ). A similar situation was observed for  $La_7Os_4C_9$  with mixed carbon ligands, however, it was stated that the satisfactory classification of  $C_2$  is impossible due to the lack of an established classification scheme [38].



To charge balance the chemical formula of  $RE_{15}[Fe_8C_{25}]$ , simple electron counting rules based on ionic concepts can be used with the following strategy: the polymeric complex anion carries a total charge of 45- counting the  $RE$  species (in agreement with susceptibility data; see *Section 4.6*) as  $RE^{3+}$  (resulting in  $RE_{15} = 45+$ ). Further assumptions concerning the charges of the mono- and diatomic carbon ligands are based on the crystal-chemical concept of carbometalates [9] as well as on experimental values of C–C distances in the  $C_2$ -pairs. For the present compounds these data allow to count the monoatomic carbon as  $C^{4-}$ , and the diatomic species as  $C_2^{4-}$ . The iron clusters (Fe1, Fe2) in the crystal structure are interconnected by Fe3 in trigonal-planar coordination by  $C_2$ -pairs. Trigonal-planar  $[Fe(C_2)_3]$  groups are also observed in the crystal structure of  $RE_{3.67}[Fe(C_2)_3]$  (*Section 2.2.2* and *6.2.2*) contains  $Fe^{1+}$  species. Altogether, the (ionic) chemical formula of the cluster compounds can be written as  $(RE^{3+})_{15}[(Fe_6)^{5+}(Fe^{1+})_2(C_2^{4-})_{12}C^{4-}]^{45-}$ , resulting in a mean valence state of the six iron atoms of the cluster unit of 0.83+ (= (5+) / 6), which, in general, would be consistent with homoatomic bonding interactions within the clusters.

Another point which should be discussed for the  $RE_{15}[Fe_8C_{25}]$  phases is the metal–metal interactions. Further aspects of metal–metal bonding can be extracted from the topological analysis of ELI-D and the electron density. The  $Fe_6$ -cluster bonding is characterized by a number of local maxima of ELI-D in the valence shells (i.e., 4<sup>th</sup> shell) of the Fe1 and Fe2 atoms. Owing to the high, but unsymmetrical coordination of the Fe atoms (*Figure 4.13a*) there is no clear-cut distinction between intra-cluster and external bonding basins. As a characteristic, all of these basins possess attractors located inside the Fe atomic basins of the electron density, i.e., within the QTAIM [193] Fe1 and Fe2 atoms. As an adequate procedure, all of these  $Fe_6$ -cluster ELI-D basins were united into one cluster superbasis. The lone pair type basins of the carbon ligands establishing dative bonds to the Fe atoms are clearly separated from the cluster superbasis. The  $Fe_6$ -cluster superbasis is depicted in grey color in *Figure 4.13b*. The red color marks the separated Fe 3rd shell ELI-D basins, which are completely located inside the corresponding QTAIM Fe atom and which are touching the cluster superbasis (*Figure 4.13b*). From integration of the electron density within the ELI-D cluster superbasis a sizable electronic population of  $8.2e^-$  is obtained. Integration of the spin density within the ELI-D basins reveals only a small degree of spin polarization ( $0.1e^-$ ) within the cluster superbasis. As to be expected, the highest spin polarization is found in the 3rd shell regions of the Fe atoms of the cluster ( $3.9e^-$  in total). All these results give rise to the notion of a covalently bonded, magnetic  $Fe_6$ -cluster stabilized by dative ligand-to-metal bonds. However, this is not yet the complete picture. Recent investigations of novel organometallic complexes with unsupported  $RE-T$  bonds (e.g.  $Cp_2Y-ReCp_2$  [214]) and exemplary analysis of  $RE-T$  interactions in  $La_7Os_4C_9$  [38], revealed the presence of polar covalent  $RE-T$  interactions. The picture is that of a dative bond between an electron-rich  $T$  and a coordinatively unsaturated  $RE$  atom involving a  $T$  "lone pair" created by the specific arrangement of strongly interacting electron-donor ligands.

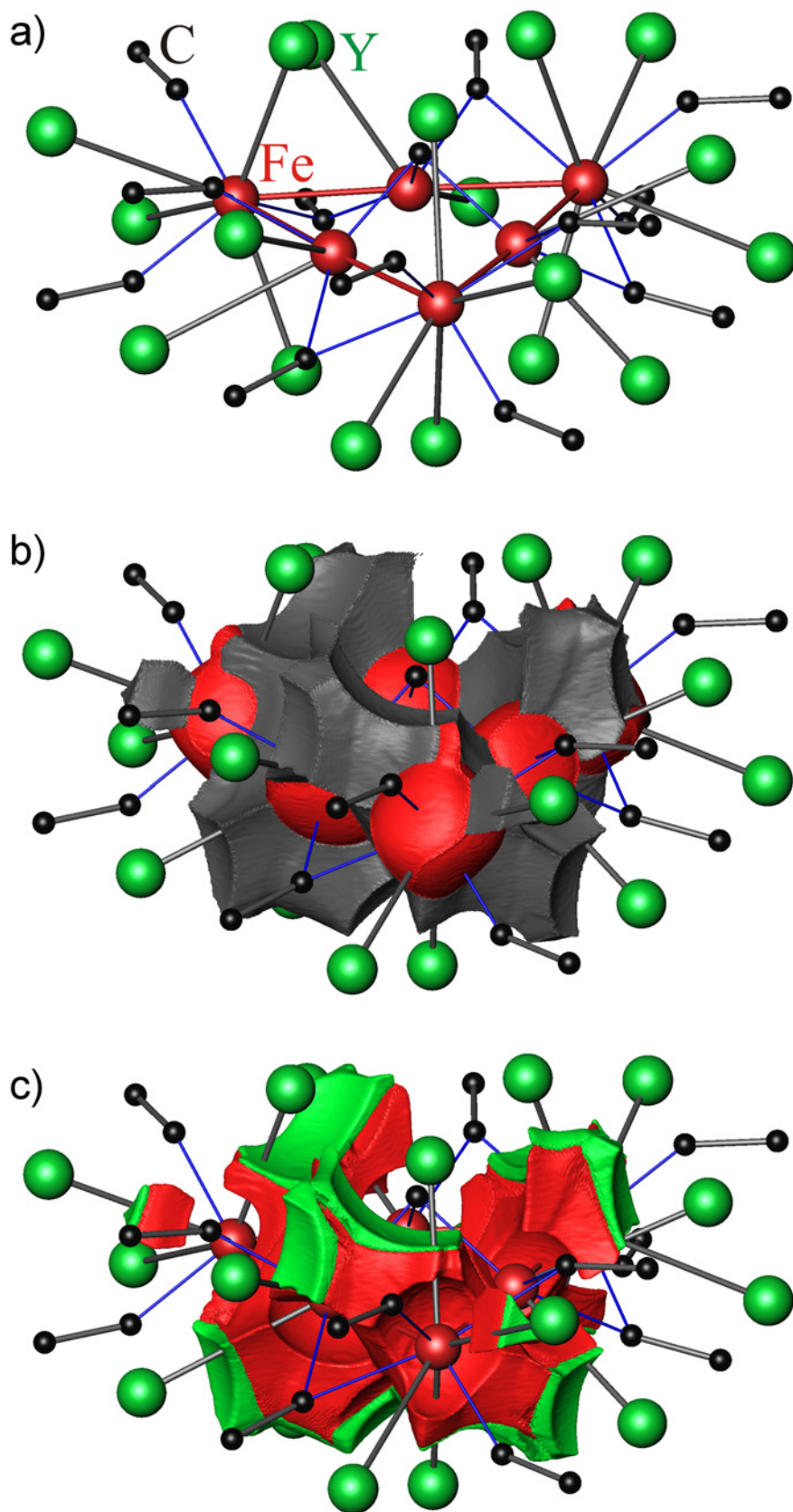


Figure 4.13:  $Y_{15}[Fe_8C_{25}]$ : a)  $Fe_6$ -cluster and nearest neighbors, b)  $Fe_6$ -cluster superbasis of ELI-D (grey) and Fe 3rd shell basins (red), c)  $Fe_6$ -cluster superbasis of ELI-D intersected by QTAIM atoms: red parts belong to Fe, green parts to Y atoms.

The present case can be considered as an extension of this picture. The Fe atoms are rather electron-rich with effective QTAIM charges of -0.1 and +0.2 for Fe1 and Fe2 cluster atoms, respectively. They are not only strongly interacting with the carbon ligands but also among each other, which gives rise to a sizable number of electrons ( $1.37e^-$  per cluster Fe atom) in the valence region of the  $3d$   $T$  metal. The formation of electron localizability maxima in the valence region of a  $T$  element forming a pure  $d$ - $d$  covalent interaction in a  $T_2$ -dimer has been already exemplarily demonstrated [215]. Here, the  $Fe_6$  cluster superbasis also contains such regions. The whole superbasis serves as an electron donor region for the attached  $RE$  atoms. The polarity of the interactions can be investigated applying the method of ELI-D/QTAIM basin intersection in analogy to the corresponding ELF/QTAIM intersection procedure [194]. The intersection of the ELI-D cluster superbasis with the QTAIM atomic basins of Fe and Y is shown in *Figure 4.13c*, with most volume parts of the superbasis belonging to the QTAIM Fe atoms (red color) and only a minor part (green color) to the Y atoms. Integration of the electron density in the intersection parts reveals that  $7.2e^-$  (88%) out of the total  $8.2e^-$  belong to the  $Fe_6$  cluster atoms and only 11% to the attached Y atoms. The largest populations for the Y atom intersections are found above and below the  $Fe_6$ -cluster plane, corresponding to the shortest Fe–Y contacts ( $d(Fe1-Y3) = 274$  pm). Although this distance is the same above and below the plane, the intersections are not. The reason is the missing monoatomic carbon ligand below the plane leading to more extended superbasis regions on the opposed side of the bond and to twice as large populations of the intersecting Y regions. From this point of view the only one-sided coordination of the  $Fe_6$ -cluster by monoatomic carbon enhances the Fe–Y bonding compared to a two-sided coordination.

#### 4.6 Magnetic susceptibility

Magnetic susceptibility measurements were performed on a SQUID magnetometer (MPMS XL-7, Quantum Design) in the temperature range of  $T = 1.8$  K to 400 K and in magnetic fields  $\mu_0 H = 10$  mT to 7 T as described in *Section 3.11.1*.

The magnetic susceptibilities  $\chi = M/H$  for  $\mu_0 H > 1$  T were corrected for ferromagnetic impurities with  $T_C \gg 400$  K (Fe-metal) by the Honda-Owen method. The corrected inverse magnetic susceptibility of  $RE_{15}[Fe_8C_{25}]$  ( $RE = Dy, Ho, Er$ ) phases are plotted in *Figure 4.14*. For  $T > 100$  K the corrected data  $\chi_{corr}(T)$  are well described by the Curie-Weiss law with effective magnetic moments  $\mu_{eff} = 10.0 \mu_B$  / Dy-atom ( $\theta_P = +12$  K),  $\mu_{eff} = 10.7 \mu_B$  / Ho-atom ( $\theta_P = +51$  K), and  $\mu_{eff} = 9.7 \mu_B$  / Er-atom ( $\theta_P = +64$  K), respectively, in agreement with the values expected for the ground multiplets of the trivalent  $RE$  ions. Broad anomalies in  $T < 20$  K originate probably from the magnetic ordering of the  $RE$  moments. In  $Y_{15}[Fe_8C_{25}]$  the  $Y^{3+}$  ion carries no magnetic moment, but, as in the samples of the other isotopic phases, the high-field susceptibility data show the presence of metallic Fe. From powder XRD it is known that the sample contains  $\sim 5$  wt.% metallic Fe. Thus, assigning all ferromagnetism to the Fe

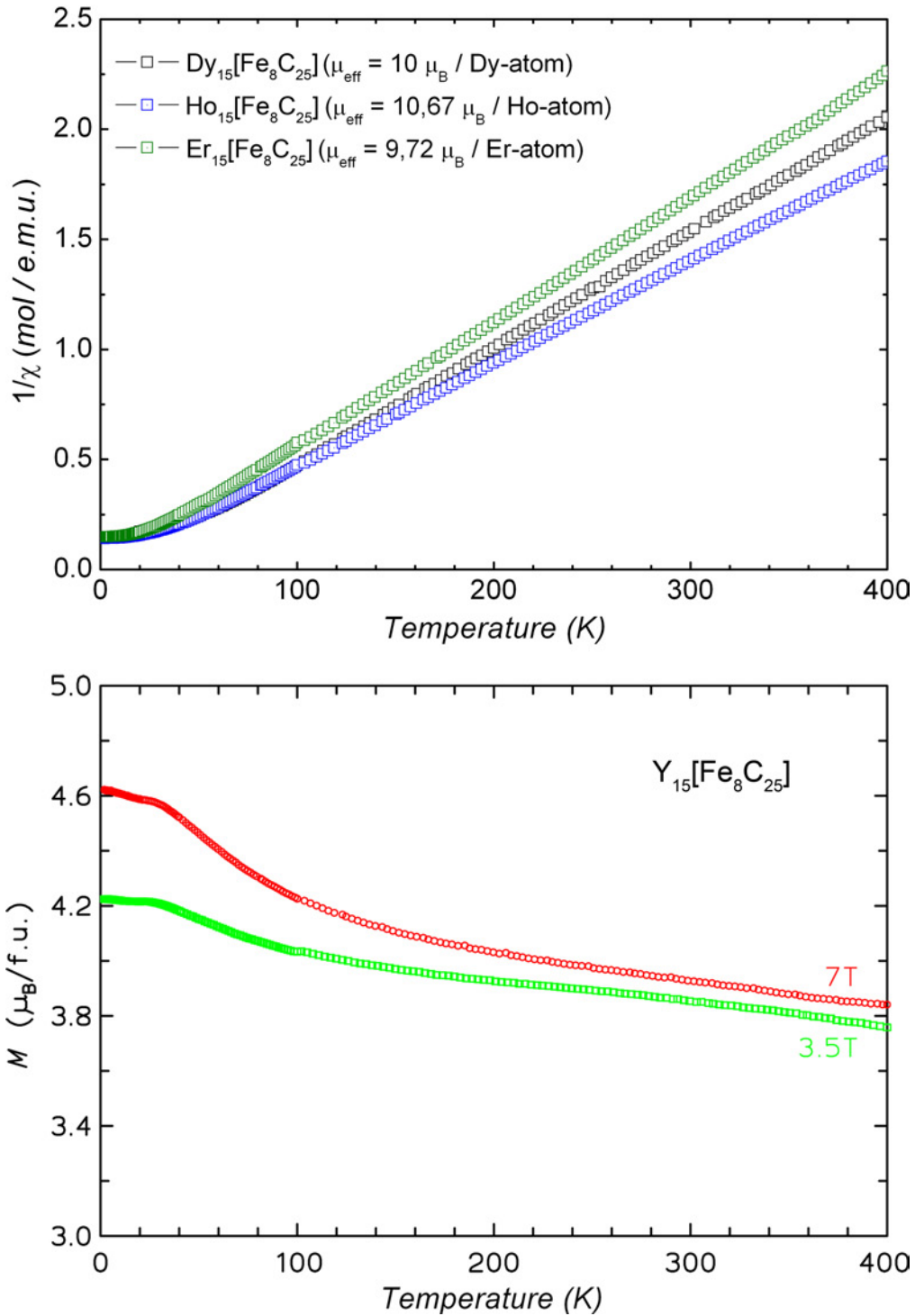


Figure 4.14: Corrected inverse magnetic susceptibility of  $RE_{15}[Fe_8C_{25}]$  ( $RE = Dy, Ho, Er$ ) (top) and magnetization curve of  $Y_{15}[Fe_8C_{25}]$  at different magnetic fields (bottom).

metal impurities (saturated specific magnetization  $M_{sat} = 222 \text{ emu g}^{-1}$ ) results in a Fe-content of about 4.6 wt.% and a small intrinsic paramagnetic susceptibility  $\chi_{corr}$  for  $Y_{15}[Fe_8C_{25}]$ . The temperature dependence of the corrected susceptibility  $\chi_{corr}$  of  $Y_{15}[Fe_8C_{25}]$  resembles a Curie-Weiss law and a fit results in  $\mu_{eff} = 6 \pm 1 \mu_B$ /f.u. A broad shoulder visible at  $\approx 30$  K in  $\chi_{corr}(T)$  might be interpreted as a ferromagnetic ordering transition. In this case the ordered

magnetization would be  $0.8 \mu_B/\text{f.u.}$ . Because the free  $\text{Y}^{3+}$  ion is non-magnetic, this magnetic moment could be assigned to the local ordering of magnetic Fe atoms. In order to determine the local magnetic behavior of Fe atoms, Mössbauer spectroscopy was carried out at liquid He temperatures (see *Section 4.8*).

#### 4.7 Electrical resistivity

The electrical resistivity  $\rho(T)$  measured on compact pieces of the sample shows a metal-like temperature dependence above 50 K (*Figure 4.15*). The resistivities at 300 K are 0.33 m $\Omega\text{cm}$ , 0.63 m $\Omega\text{cm}$ , 0.65 m $\Omega\text{cm}$  and 0.48 m $\Omega\text{cm}$  for  $\text{Y}_{15}[\text{Fe}_8\text{C}_{25}]$ ,  $\text{Dy}_{15}[\text{Fe}_8\text{C}_{25}]$ ,  $\text{Ho}_{15}[\text{Fe}_8\text{C}_{25}]$ , and  $\text{Er}_{15}[\text{Fe}_8\text{C}_{25}]$ , respectively. Only for  $\text{Dy}_{15}[\text{Fe}_8\text{C}_{25}]$  a broad hump at 25 K and a strong decrease of  $\rho(T)$  below this temperature clearly indicates the magnetic ordering of the  $\text{Dy}^{3+}$  species. The  $\rho(T)$  curves of the Y, Ho, and Er compounds show minima around 38 K, 31 K, and 38 K, respectively, rising slightly towards 4 K. The origin of this common behavior is unknown, but the temperature of the minimum in  $\rho(T)$  ( $\text{Y}_{15}[\text{Fe}_8\text{C}_{25}]$ ) roughly coincides with the hump observed in the corrected magnetic susceptibility. These features might be due to magnetic ordering of the  $\text{Fe}_6$ -clusters.

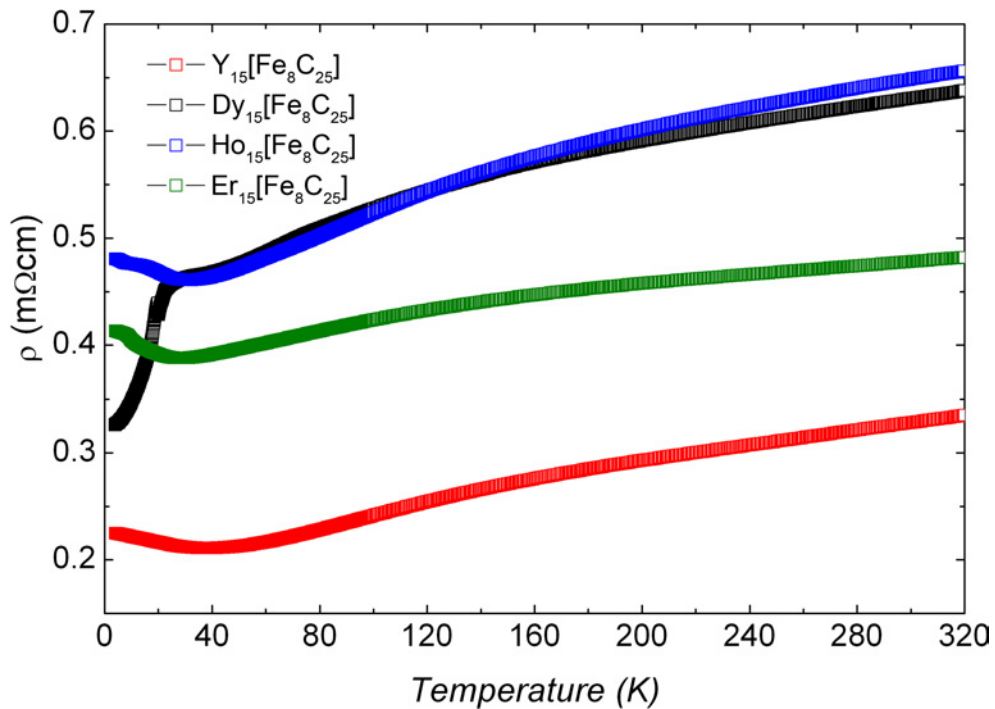


Figure 4.15: Electrical resistivity  $\rho(T)$  of the isotypic phases  $\text{RE}_{15}[\text{Fe}_8\text{C}_{25}]$  ( $\text{RE} = \text{Dy}, \text{Ho}, \text{Er}$ ).

#### 4.8 Mössbauer spectroscopic studies

Mössbauer spectroscopy was carried out on  $\text{Y}_{15}[\text{Fe}_8\text{C}_{25}]$  and  $\text{Dy}_{15}[\text{Fe}_8\text{C}_{25}]$  at room and low temperatures down to 5 K, as shown in *Figure 4.16* and *4.17*, respectively. The samples

were prepared and measured according to the procedure described in *Section 3.8*. Because  $Dy_{15}[Fe_8C_{25}]$  contains heavy Dy atoms the intensity of the transmitted  $\gamma$ -rays is weaker compared to  $Y_{15}[Fe_8C_{25}]$ .

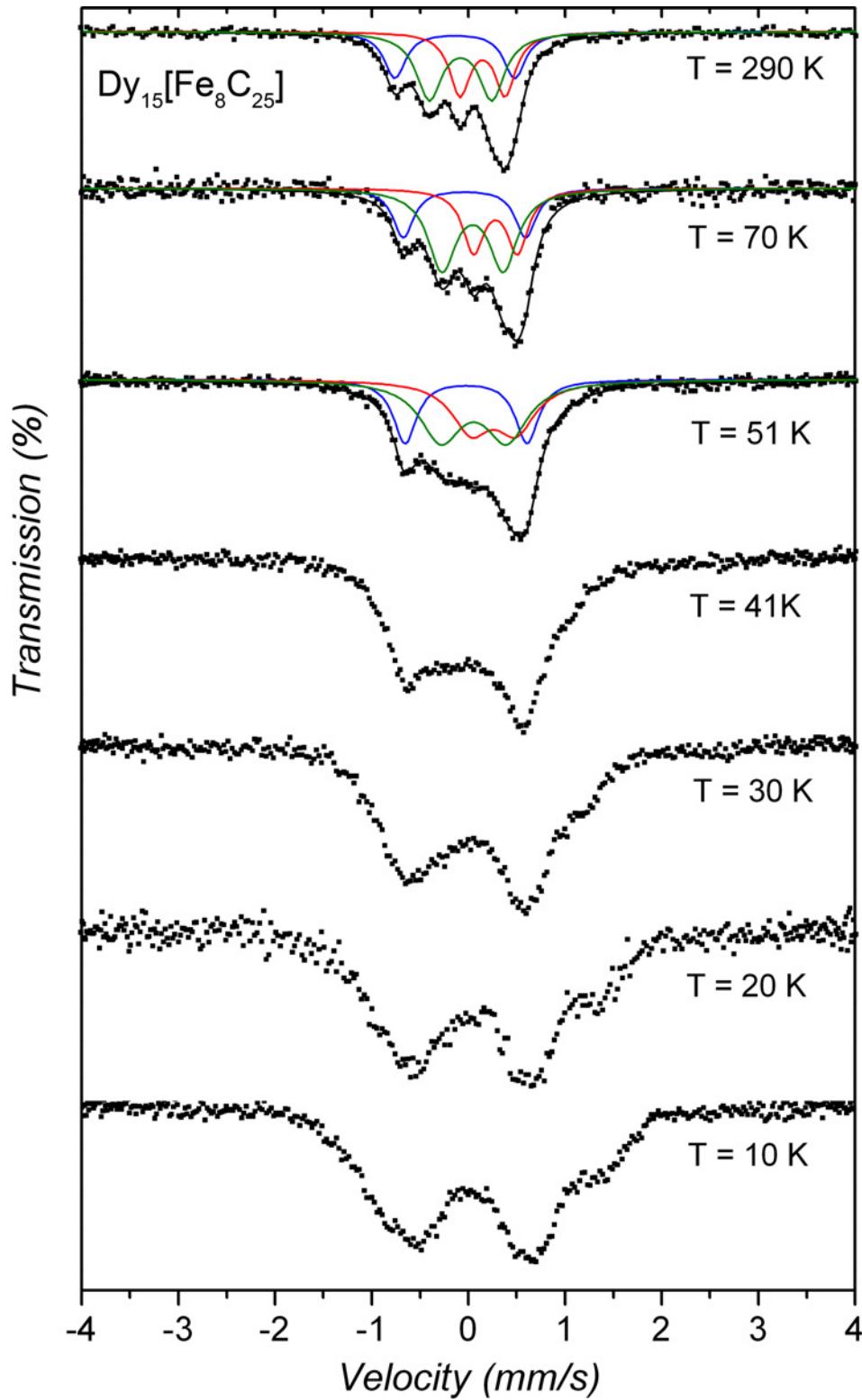


Figure 4.16: The Mössbauer spectrum of  $Dy_{15}[Fe_8C_{25}]$  measured at temperatures between 10 K and 290 K. The measured spectra (dots) are fitted (black) with three subspectrum (red, green and blue) between 290 K and 50 K.

Considering the shape and the relative intensity of the peaks, the observed spectrum was best fitted with three quadrupole doublets. This shows the existence of three crystallographically different iron species, Fe1, Fe2 and Fe3, which is in agreement with the results from the crystal structure refinement. According to the crystal structure, the atomic ratio of iron atoms is Fe1 : Fe2 : Fe3 = 3 : 3 : 2, which is directly proportional to the intensity (integrated area) of the peaks. Based on the above information on signal intensities, the following strategy was chosen to identify the corresponding left and right part of the quadrupole doublets: first the spectrum was fitted with six Lorentzian distribution functions and then two peaks with similar intensities were taken as one pair. The hyperfine parameters obtained from the fit are listed in *Table 4.5*. In this way one pair of lines with lowest intensity (area) was assigned to Fe3 (blue subspectrum in *Figure 4.16*, 290 K).

Table 4.5: Fitted hyperfine parameters of  $\text{Dy}_{15}[\text{Fe}_8\text{C}_{25}]$ : Temperature [K], Isomer shift (IS) [mm/s] relative to  $\alpha$ -Fe, half width ( $\Gamma/2$ ) [mm/s], quadrupole splitting ( $\Delta E_Q$ ) [mm/s], hyperfine field H[T], and relative area (A) [%] of the subspectra, estimated standard deviations are given in brackets.

T	Subspectra	Species	IS <sup>†</sup>	$\Delta E_Q$	H	$\Gamma/2$	A
290	1 (red)	Fe1	0.257(7)	0.468(13)		0.128(13)	32(3)
	2 (green)	Fe2	0.029(8)	0.647(17)		0.162(15)	43(5)
	3 (blue)	Fe3	-0.031(9)	1.239(20)		0.131(16)	25(3)
70	1 (red)	Fe1	0.391(12)	0.453(25)		0.134(22)	29(5)
	2 (green)	Fe2	0.154(12)	0.634(23)		0.175(22)	48(7)
	3 (blue)	Fe3	0.070(14)	1.266(30)		0.131(24)	22(4)
51	1 (red)	Fe1	0.371(30)	0.465(82)		0.247(38)	33(11)
	2 (green)	Fe2	0.166(39)	0.681(59)		0.260(45)	42(14)
	3 (blue)	Fe3	0.086(8)	1.262(20)		0.144(18)	25(4)
41	1 (red)	Fe1	0.371	-0.319(20)	1.66(18)	0.264(11)	42(4)
	2 (green)	Fe2	0.166	0.409(43)	2.04	0.236(55)	23(7)
	3 (blue)	Fe3	0.067	-0.617(11)	0.29(2)	0.199(35)	35(6)
30	1 (red)	Fe1	0.331(50)	-0.302(34)	5.15(30)	0.2050	21.8
	2 (green)	Fe2	0.289(23)	0.134(30)	5.77(18)	0.189	24.4
	3 (blue)	Fe3	0.136(15)	-0.523(18)	1.32(16)	0.253(30)	54(23)
20	1 (red)	Fe1	0.330(80)	-0.371(88)	5.69(71)	0.233(73)	25(11)
	2 (green)	Fe2	0.275(32)	0.255(45)	6.03(15)	0.188(42)	33(9)
	3 (blue)	Fe3	0.136(46)	-0.616(46)	1.50(24)	0.231(70)	43(18)
10	1 (red)	Fe1	0.369	-0.329(18)	4.88(13)	0.183(23)	32.7
	2 (green)	Fe2	0.283	0.271(27)	6.04(12)	0.233(22)	43.1
	3 (blue)	Fe3	0.650	-0.685(25)	2.14	0.174(22)	24.1

<sup>†</sup> Note: the numbers given without e.s.d. were fixed during the fit

In order to assign the remaining two doublets (red and green) to Fe1 and Fe2, quantum mechanical calculations were carried out on  $\text{Y}_{15}[\text{Fe}_8\text{C}_{25}]$  compound avoiding strong correlations of  $f$ -electrons. For the calculations we used a full potential linearized augmented plane waves (FLAPW) method implemented in the program package WIEN2k [216]. Due to the



partial occupancy of the C5 site (*Section 4.3*) the calculations were done in space group  $P3$  (143), where the Fe3 site splits into two independent iron positions, Fe3a and Fe3b. The calculated hyperfine parameters are listed in *Table 4.6*.

Table 4.6: Calculated electric field gradient  $V_{zz}$  [ $V/m^2$ ], asymmetry parameter  $\eta$ , quadrupole splitting ( $\Delta E_Q$ ) [mm/s], hyperfine field H[T] and electron density at the Fe nucleus  $\rho(0)$  [ $au^{-3}$ ] for  $Y_{15}[Fe_8C_{25}]$ .

Site	$V_{zz}$	$\eta$	$\Delta E_Q$	H	$\rho(0)$
Fe1	$3.5 \cdot 10^{21}$	0.58	0.614	10.7	15308.96
Fe2	$-3.5 \cdot 10^{21}$	0.93	0.661	10.0	15309.20
Fe3a	$4.8 \cdot 10^{21}$	0.00	0.800	2.0	15309.51
Fe3b	$5.6 \cdot 10^{21}$	0.00	0.933	1.9	15309.63

Experimentally observed and calculated values for quadrupole splittings are in reasonable agreement. However, the spin state and local symmetry of the Fe atoms in  $Dy_{15}[Fe_8C_{25}]$  can not be determined by quadrupole splitting values, because of the lack of systematic Mössbauer spectroscopic studies of carbides. The isomer shift is given by the distance of the barycenter of the quadrupole doublet from the zero Doppler velocity [217]. It directly depends on the  $s$  electron density at the nucleus of the absorber atom (as sum of contributions from all  $s$ -electron shells),  $\rho(0)$ , but maybe influenced indirectly via shielding/screening effects of  $p$ ,  $d$  and  $f$  electrons [184]. This means that with increasing number of  $d$  electrons, or in other words with decreasing valence state of Fe, the electron density at the nucleus of Fe will decrease. Consequently, the Mössbauer spectrum of a Fe atom with lower oxidation state will show more positive isomer shift compared to one with a higher oxidation state. In this respect, the subspectra 1 (red) with IS = 0.257 at 290 K can be assigned to Fe1 and the subspectra 2 (green) with IS = 0.029 to Fe2, respectively. Thus, the valence states of Fe atoms in  $Dy_{15}[Fe_8C_{25}]$  have the following decreasing sequence: Fe3 > Fe2 > Fe1 (see *Table 4.5*).

The spectra of  $Dy_{15}[Fe_8C_{25}]$  can be fitted with three doublet subspectra at temperatures 290 K, 70 K and 51 K. Due to the temperature dependence of the second order Doppler shift, the centers of the spectra are shifted with temperature. Below 51 K, the spectra start to broaden and the shapes of the spectra change compared to the spectra taken at higher temperatures. This indicates the presence of a magnetic hyperfine interaction with fields ranging between 1 and 7 T for the individual subspectra (see *Table 4.5*). A consistent fit to all low temperature spectra is not yet available. The reason is probably a distribution of fields and/or the presence of angles between magnetic hyperfine fields and electric field gradients at the different sites.

In order to clarify the origin of the internal magnetic field, we have recorded spectra of  $Y_{15}[Fe_8C_{25}]$  down to 5 K (*Figure 4.17*). The hyperfine parameters for  $Y_{15}[Fe_8C_{25}]$  are given in *Table 4.7*. These spectra can also be fitted with three quadrupole doublets in accordance with the Dy compound. However in addition there is a strong contribution from a sextet with



hyperfine parameters typical for  $\alpha$ -Fe. Furthermore, there is still a yet weaker sextet with a slightly smaller hyperfine field which is probably induced by an iron containing intermetallic compound.

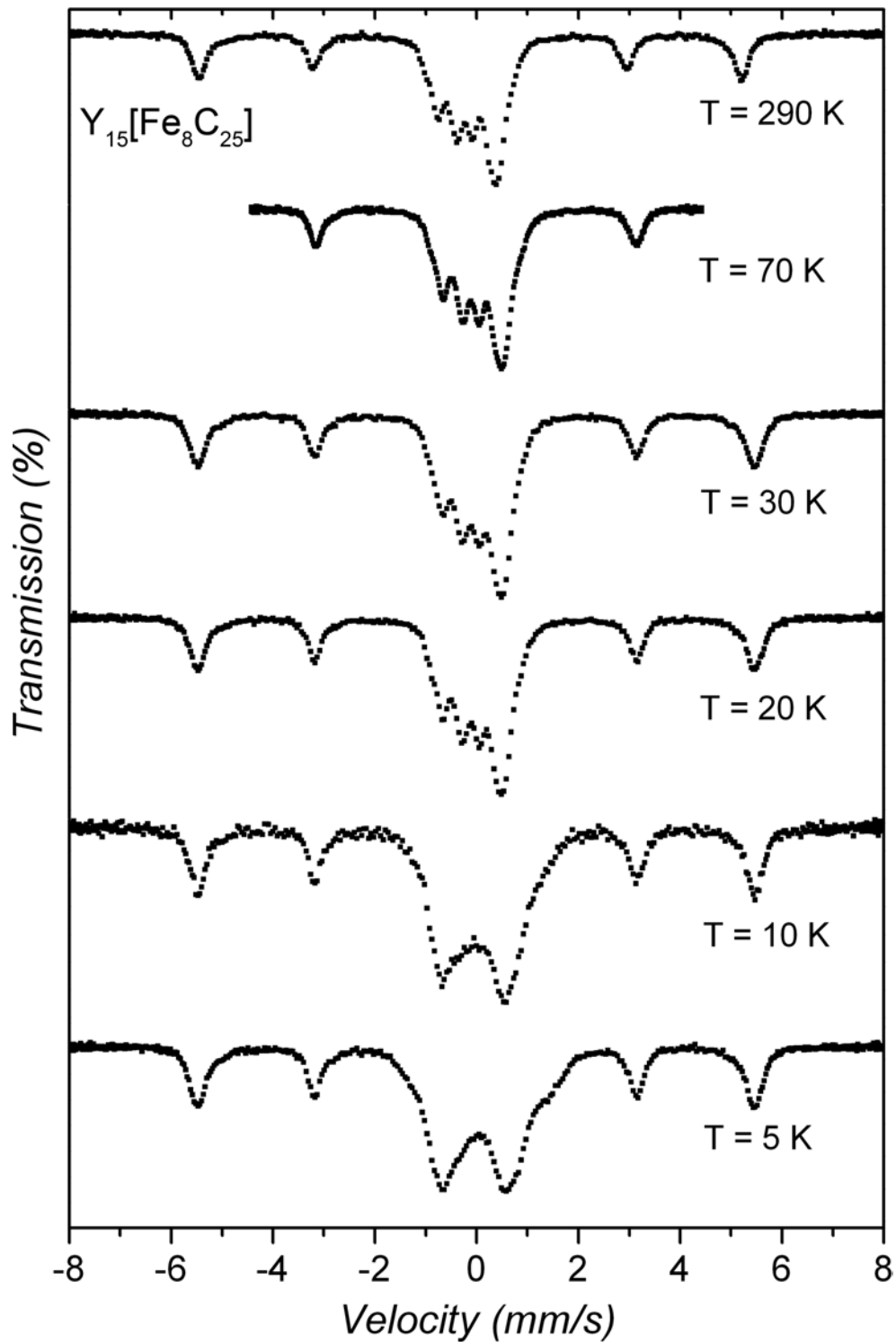


Figure 4.17: The Mössbauer spectrum of  $Y_{15}[Fe_8C_{25}]$  measured at temperatures between 5 K and 290 K. Due to the presence of trace phase signals the fit is not shown.

Table 4.7: Fitted hyperfine parameters of  $Y_{15}[Fe_8C_{25}]$ : Temperature [K], Isomer shift (IS) [mm/s] relative to  $\alpha$ -Fe, half width ( $\Gamma/2$ ) [mm/s], quadrupole splitting ( $\Delta E_Q$ ) [mm/s], hyperfine field H[T], and relative area (A) [%] of the subspectra, estimated standard deviations are given in brackets.

T	Subspectra <sup>†</sup>	Species	IS <sup>‡</sup>	$\Delta E_Q$	H	$\Gamma/2$	A
290	1	Fe1	0.319(2)	0.588(6)	–	0.108(6)	12(1)
	2	Fe2	0.050(4)	0.652(6)	–	0.209(6)	38(1)
	3	Fe3	-0.078(3)	1.150(6)	–	0.120(6)	14(5)
	S1	$\alpha$ -Fe	-0.013(3)		33.01(2)	0.169(4)	35(7)
70	1	Fe1	0.088(2)	1.280(4)		0.127(4)	15.7(6)
	2	Fe2	0.381(2)	0.456(4)		0.103(4)	12.3(5)
	3	Fe3	0.157(3)	0.626(5)		0.195(5)	35.0(9)
	S1	$\alpha$ -Fe	0.106(3)		33.64(3)	0.160(5)	37.0(9)
30	1	Fe1	0.801(3)	1.289(6)		0.145(5)	16.2(7)
	2	Fe2	0.379(3)	0.460(5)		0.122(5)	13.2(6)
	3	Fe3	0.147(3)	0.632(6)		0.204(6)	34(1)
	S1	$\alpha$ -Fe	0.101(2)		33.96(2)	0.171(4)	31.9(6)
	S2	IM	0.142(2)		32.00(2)	0.249(32)	4.9
20	1	Fe1	0.083(3)	1.289(6)		0.134(6)	16.1(8)
	2	Fe2	0.381(3)	0.448(6)		0.110(5)	12.3(7)
	3	Fe3	0.152	0.631(7)		0.203(7)	35(1)
	S1	$\alpha$ -Fe	0.103(3)	0.005(3)	33.95(2)	0.168(5)	33(1)
	S2	IM	0.184(32)		31.3(3)	0.18(6)	3(1)
10	1	Fe1	0.48(16)	1.66(30)		0.275(53)	10.5(2)
	2	Fe2	0.390(38)	0.429(67)		0.142(33)	6.6(24)
	3	Fe3	0.167	0.57(26)		0.242(87)	19(16)
	4		0.100(9)	1.356(89)		0.346(34)	32(16)
	S1	$\alpha$ -Fe	0.1081	0.0044(62)	33.95	0.170(1)	30(1)
	S2	IM	0.238(41)	0.029(40)	31.77(36)	0.106(61)	2.0(1)
5	1	Fe1	0.105(12)	-1.54(2)	3.22(8)	0.155(11)	6.4(2)
	2	Fe2	0.3252(60)	-0.411	4.28(4)	0.194	17.4(2)
	3	Fe3	0.1558(56)	0.522	6.1	0.271(5)	27.3(3)
	4		0.058(7)	-1.160(1)	1.47(5)	0.221(7)	16.0(2)
	S1	$\alpha$ -Fe	0.100(2)	0.009(5)	33.94(2)	0.172(2)	30.0(3)
	S2	IM	0.20(3)	-0.116(51)	31.6 2)	0.160(1)	2.8(1)

<sup>†</sup> S1: sextet 1 related to  $\alpha$ -Fe, S2: sextet 2 related to a trace compound containing Fe, IM: iron intermetallic

<sup>‡</sup> Note: the numbers given without e.s.d. were fixed during the fit.

The spectra down to about 20 K reveal little changes (i.e., the sites associated with the doublets stay non-magnetic). However, the spectral shapes at 10 K and 5 K are clearly different indicating the onset of a magnetic hyperfine fields at these sites. Only the spectra at 10 K and 5 K are fitted with four subspectra and two sextets (Table 4.7). The appearance of a fourth subspectrum is probably related with the magnetic ordering of Fe atoms, giving rise to a magnetic structure of the compound. That presumption should be checked by low temperature Neutron diffraction experiments in the future.

In conclusion, both compounds reveal magnetic hyperfine fields at iron: for the Dy com-

pound below 51 K, for the Y compound below 20 K. The higher onset temperature in the Dy case could be explained by Dy induced effects. The magnetic hyperfine fields of only a few Tesla could correspond to an ordered magnetic moments at iron atoms in the order of only some tenths of  $\mu_B$ , which is in agreement with magnetization measurement results (*Section 4.6*). Since Y carries no magnetic moment, the magnetic ordering found in the  $Y_{15}[Fe_8C_{25}]$  at low temperatures provides convincing evidence for magnetic coupling between iron species.

Calculated and experimental values for the average quadrupole splittings  $\Delta E_Q$  match marginally, while the hyperfine field values are clearly divergent (see *Table 4.5 to 4.7*). This might be explained by the structure model and by the magnetic ordering type used for calculation. Thus, further detailed studies should clarify whether a low temperature magnetic structure exists and what kind of magnetic ordering occurs.

#### 4.9 X-ray absorption spectroscopic studies

The Fe *K*-threshold of the compounds  $RE_{15}[Fe_8C_{25}]$  was measured at the synchrotron beamline *E4* at HASYLAB/DESY in Hamburg. We have focused on the XANES (X-ray absorption near edge structure) part of the X-ray absorption spectra due to its sensitivity on oxidation states. The samples were prepared and measured according to the procedure described in *Section 3.7.2*. The standard procedure is to compare the absorption edge of the sample with the reference materials and to assign the oxidation state of the absorbing atom with respect to the references. Due to the polarizability, various ligands show different ligand field effects on the central atom/transition metal. As a consequence, the X-ray absorption edge of the transition metal will have some energy shift, even if the oxidation state of the transition metal is the same. Thus, in order to get reliable results, the reference material should contain same kind of ligand similar to the sample under investigation. Unfortunately, the binary and ternary iron carbides were rarely investigated by XAS. Due to the lack of reference materials for the carbide systems, we have chosen metallic iron as a standard. The high purity iron powder was prepared in the same way as other samples for the XAS measurement. *Figure 4.18* shows the XAS spectra of the isotopic compounds  $RE_{15}[Fe_8C_{25}]$  ( $RE = Y, Dy, Ho, Er$ ).

The energy scale was calibrated using the spectrum of metallic Fe and the obtained energy shift was applied to the other spectra. The background was corrected for both, pre-edge and post-edge regions, and finally the spectra were normalized to one. All XAS spectra exhibit a similar shape indicating the isotypism of the investigated compounds. The XANES spectra reveal pre-edge peaks. Similar to nitrides [218], the pre-edge peak is observed as a shoulder of the main absorption edge. From the crystal structure refinements we know that Fe has three different atomic environments: distorted tetrahedral, non-coplanar trigonal and trigonal planar. The lack of centrosymmetry in these coordinations could explain the appearance of the pre-edge peak. On the other hand, the  $RE_{15}[Fe_8C_{25}]$  compounds show metallic behavior, which means that there is some *d-p* hybridization at the Fermi level. This

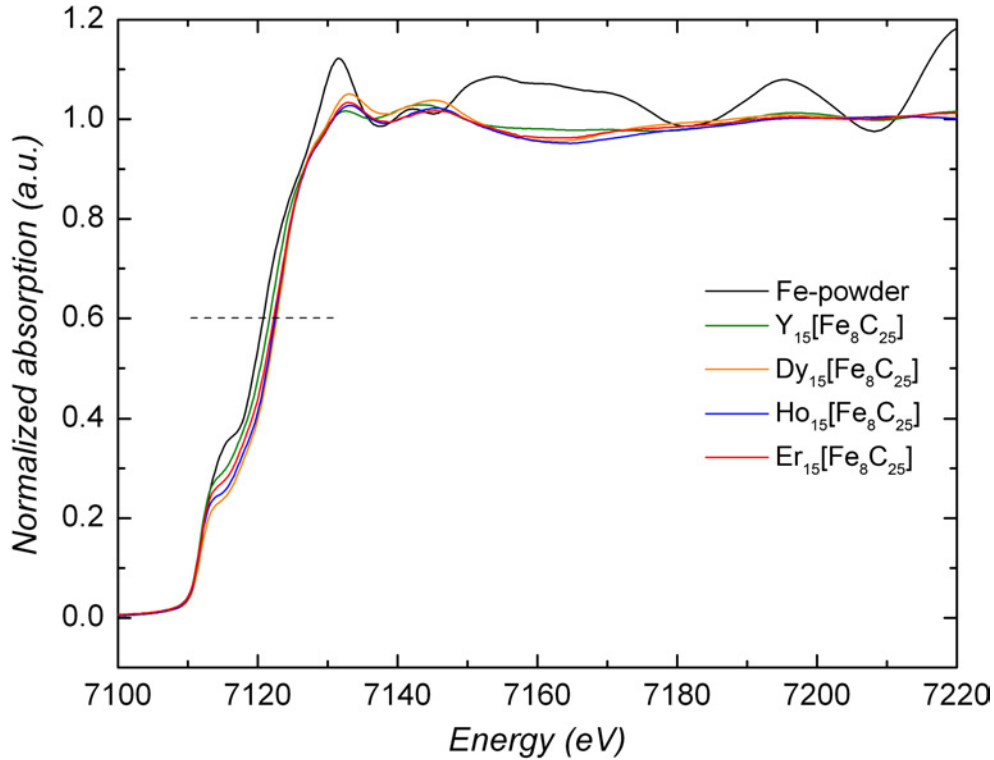


Figure 4.18: Normalized XAS spectra of the isotypic phases  $RE_{15}[Fe_8C_{25}]$  ( $RE = Y, Dy, Ho, Er$ ) and of pure Fe as a reference material.

would allow a forbidden  $1s \rightarrow 3d$  transition, which can be assigned to the pre-edge peak [218–220]. Meitzner *et al.* [221] studied the XAS spectra of  $5d$  metals and concluded that the white line intensity of the  $K$ -edge absorption depends on the number of free  $5d$  states. If we assume that this statement is also true for  $3d$  metals, the XAS spectrum of  $RE_{15}[Fe_8C_{25}]$  shows that the Fe atom has less free  $3d$  states, thus indicating a low valence state for Fe. As described in reference [218], the main absorption edge is defined at about 0.6 of the full edge jump. Thus, we determined the Fe  $K$ -edge threshold (7112 eV), reflecting the  $1s \rightarrow 4p$  transition, of  $RE_{15}[Fe_8C_{25}]$  at 0.6 of the normalized  $K$ -edge. All  $RE_{15}[Fe_8C_{25}]$  compounds showed a positive energy shift with respect to the Fe-powder reference and their values are listed in *Table 4.8*.

Table 4.8: X-ray absorption threshold of Fe  $K$ -edge and energy shift ( $\Delta E$ ) of Fe observed for the isotypic phases  $RE_{15}[Fe_8C_{25}]$  ( $RE = Y, Dy, Ho, Er$ ).

Compound	Energy at 0.6 (eV)	$\Delta E$ (eV)
Fe	7112.0	
$Y_{15}Fe_8C_{25}$	7121.7	9.7
$Dy_{15}Fe_8C_{25}$	7122.7	10.7
$Ho_{15}Fe_8C_{25}$	7122.5	10.5
$Er_{15}Fe_8C_{25}$	7122.3	10.3

For the Dy, Ho and Er compounds the energy shift values are the same within the accuracy

of the measurements, which is about 0.5 eV. The significant difference for  $Y_{15}[Fe_8C_{25}]$  might be related with the presence of a minority phase,  $Y_{5.64}[Fe_2C_9]$ . Since the oxidation state of Fe in metallic iron is zero, the positive energy shift of the Fe *K*-edges suggests a positive oxidation state of Fe in the compounds  $RE_{15}[Fe_8C_{25}]$ .

#### 4.10 Summary

Nearly single phase materials of the isotypic compounds  $RE_{15}[Fe_8C_{25}]$  ( $RE = Y, Dy, Ho, Er$ ) were successfully prepared by a high temperature synthesis route and the crystal structures of  $Dy_{15}[Fe_8C_{25}]$ ,  $Ho_{15}[Fe_8C_{25}]$ , and  $Er_{15}[Fe_8C_{25}]$  were determined from single crystal X-ray diffraction data. The crystal structures contain planar (magnetic)  $Fe_6$ -clusters stabilized by mixed monoatomic and diatomic carbon ligands, with considerable Fe–Fe interactions. The homonuclear  $Fe_6$  clusters represent a new structural motif in the crystal chemistry of iron compounds. Besides one monoatomic carbon atom a total of 12 diatomic carbon ligands are attached to the clusters resulting in  $[Fe_6(C)(C_2)_6(C_2)_{6/2}]$  units, which are interlinked via  $Fe_3(C_2)_{3/2}$  groups forming two dimensional polyanionic  ${}^2_{\infty}[Fe_6(C)(C_2)_6(C_2)_{6/2}Fe_2(C_2)_{6/2}]$  slabs which are stacked along [010]. The *RE* species are sandwiched between the layers and reveal significant contributions to chemical bondings  $Fe \rightarrow RE$  in the sense of polar dative interactions. The only partial occupancy of the monoatomic carbon position was supported by total energy calculations and arguments for the preference of half occupancy were given on the basis of the chemical bonding analysis. *RE*-species are assigned the oxidation state  $RE^{3+}$ . The bond order and the effective charge on the  $C_2$  units is a complex phenomenon and must be systematically investigated in order to develop a clear classification scheme. In the frame of our present knowledge, the  $C_2$  units in the crystal structure of  $RE_{15}[Fe_8C_{25}]$  are concluded to be definitely not  $C_2^{2-}$ , but have rather a  $C_2^{4-}$  character. Trigonal-planar  $[Fe(C_2)_3]$  groups are also known from the crystal structure of  $RE_{3,67}[Fe(C_2)_3]$  (Section 2.2.2 and 6.2.2) with Fe atoms in the valence state  $Fe^{1+}$ . Altogether, the (ionic) chemical formula of the cluster compounds can be written as  $(RE^{+3})_{15}[(Fe_6)^{5+}(Fe^{1+})_2(C_2^{4-})_{12}C^{4-}]^{45-}$ , resulting in 0.83+ (= (5+)/6) as a mean valence state of the six iron atoms of the cluster unit. This is, in general, consistent with homoatomic bonding interactions within the clusters. Quantum mechanical calculations show that the Fe atoms are present in low valence states with only small effective charges (QTAIM method) of -0.1 and +0.2 for the cluster (Fe1, Fe2) and +0.15 for iron in trigonal planar coordination (Fe3). Thus, a rough estimation of the valence states of iron by simple electron counting is significantly different from the effective charges, but reflecting the general trend to low valence states. Mössbauer investigations of  $Dy_{15}[Fe_8C_{25}]$  show the existence of three crystallographically different iron species, Fe1, Fe2 and Fe3, which is in accordance with the crystal structure refinement results. By considering the calculated electron density at the nuclei of the Fe atoms, the valence state of iron follows the decreasing sequence:  $Fe3 > Fe2 > Fe1$ . Low temperature Mössbauer studies confirmed

local magnetic ordering of the Fe atoms. The XAS investigations show that the oxidation state of Fe atoms in  $RE_{15}[Fe_8C_{25}]$  is greater than zero. The chemical bonding situations of the compounds  $RE_{15}[Fe_8C_{25}]$  fulfill the criteria for polyanionic structures, known from carbometalates. Thus, they can be classified as rare-earth carbo-dicarbo(4-)ferrates according to the IUPAC nomenclature for polyanionic structures [39]. Indeed, there are many other similar compounds such as  $La_7Os_4C_9$  [38],  $La_5Os_3C_{4-x}$  [222],  $Gd_3Ru_2C_5$  [32],  $Er_7Ru_2C_{11}$  [34] and  $Er_{10}Ru_{10}C_{19}$  [35]. Because all of the compounds contain polyanions formed by the transition metals and carbon ligands, they should be classified and named as metalates. Therefore, the complex anionic entities should be written in square brackets, e.g.  $RE_{15}[Fe_8C_{25}]$ . Further work should be focused on the stabilization of even larger clusters in the systems  $RE-Fe-C$ .

## 5 $RE_{5.64}[Fe_2C_9]$ ( $RE = Y, Gd, Tb, Dy$ )

### 5.1 Synthesis and phase analysis

The isotypic compounds  $RE_{5.64}[Fe_2C_9]$  were synthesized by arc-melting of cold-pressed pellets of elemental mixtures of Y, Gd, Tb or Dy (Ames, 99.99%), Fe (Alfa Aesar, 99.99%) and graphitic carbon (Chempur, 99.9%) in the molar ratio  $RE : Fe : C = 5.7 : 2 : 9$ . For heat treatment the samples were sealed in arc-welded Ta crucibles finally sealed in evacuated fused silica ampoules. The samples were annealed at five different temperatures (between 1173 K and 1573 K with steps of 100 K) for 21 days in a horizontal tube furnace and finally quenched in water. The optimal annealing temperature (concerning the highest yield of the main phase) was determined to be 1373 K. The reaction products were ground and annealed (at 1373 K) several times in order to improve the homogeneity of the samples. The reaction products were grey and of good crystallinity. The respective compounds were already present as the majority phase in as-cast samples. Small amounts of elemental Fe (< 5 vol.%) and an unidentified phase (< 5 vol.%) were always present in the samples even after repeated long-time annealing (*Figure 5.1*).

Powder X-ray diffraction patterns were recorded on a Huber-Guinier camera G670 in the range  $10^\circ < 2\theta < 85^\circ$  with a step width of  $0.005^\circ$  using monochromatic Co  $K\alpha_1$  radiation ( $\lambda = 178.896(1)$  pm).  $LaB_6$  (SRM660a,  $a = 415.6916$  pm) was used as an internal standard. The lattice parameters, determined by least-squares refinement of the peak positions in the powder diffraction patterns using the program WinCSD [157–159] are listed in *Table 5.1*.

Table 5.1: Unit cell parameters of the isotypic phases  $RE_{5.64}[Fe_2C_9]$  ( $RE = Y, Gd, Tb$  and  $Dy$ ) determined from X-ray powder data.

Compound	$a$ / pm	$b$ / pm	$c$ / pm	$V/10^6$ (pm <sup>3</sup> )
$Y_{5.64}[Fe_2C_9]$	2929.8(1)	1260.9(5)	502.8(3)	1857.4(2)
$Gd_{5.64}[Fe_2C_9]$	2946.8(1)	1276.2(1)	510.4(1)	1919.1(2)
$Tb_{5.64}[Fe_2C_9]$	2935.5(7)	1267.5(3)	506.1(1)	1883.0(1)
$Dy_{5.64}[Fe_2C_9]$	2929.8(2)	1261.2(7)	502.6(4)	1857.2(3)

By varying the molar ratio of the starting materials (5.7 : 2 : 9, 6 : 2 : 9, 2 : 2 : 3, 15 : 8 : 25 etc.) we did not observe any lattice parameter shifts greater than 1 pm in the powder diffraction patterns. The unit cell volumes of the compounds  $RE_{5.64}[Fe_2C_9]$  follow the lanthanoid contraction rule.

After annealing, the chemical composition of the ternary phase was determined by WDX analysis of polished samples of  $Gd_{5.64}[Fe_2C_9]$  (*Section 3.6*). WDX (Cameca SX 100) analysis using  $FeSb_2$  and  $GdPd_3$  as standards and analyzing 10 different points revealed an average composition of the majority phase (95 vol.%) corresponding to the atomic ratio  $Gd : Fe : C$

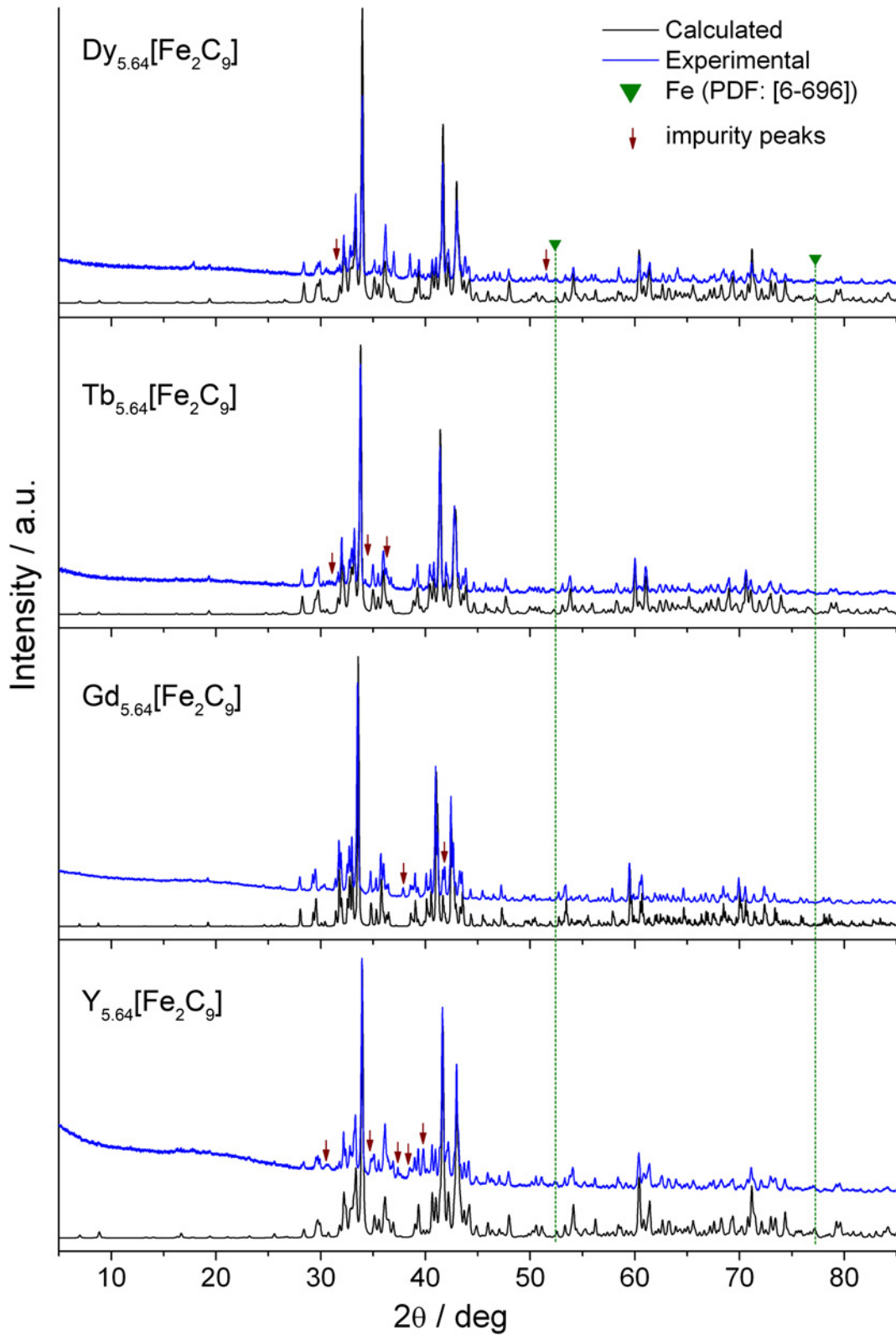


Figure 5.1: Experimental and calculated X-ray powder diffraction patterns of  $RE_{5.64}[Fe_2C_9]$  ( $RE = Y, Gd, Tb$  and  $Dy$ ). The peaks corresponding to  $\alpha$ -Fe are denoted by solid green triangles and the dark red arrows represent unidentified peaks.

$\approx 5.7 : 2.0 : 11.4$ . The carbon content was determined by the difference method. The EDX analysis on single crystals of the isotypic compound  $Dy_{5.64}[Fe_2C_9]$  resulted in the atomic



ratio Dy : Fe  $\approx$  5.7 : 2.0 (Figure 5.2). The atomic ratio Dy : Fe obtained from microprobe analyses is in good agreement with that obtained from the crystal structure refinements, Dy : Fe : C = 5.64 : 2 : 9. The same chemical composition was taken for the refinements of all the isotopic compounds. The compounds  $RE_{5.64}[Fe_2C_9]$  are air and moisture sensitive.

Single crystals of the isotopic compounds were successfully grown by high temperature heat treatment procedures (Section 3.1.2). A single crystal of  $Gd_{5.64}[Fe_2C_9]$  was grown by long-term annealing at 1373 K. As-cast samples of the Y, Tb and Dy compounds were sealed in Ta-ampoules and heated to 1823 K, slowly cooled down to 1173 K with a cooling rate of ca. 4 K/min and then further cooled to ambient temperature within 3 hours. After heat treatment prismatic crystals, suitable for single crystal diffraction studies were grown on the sample surface (Figure 5.2).

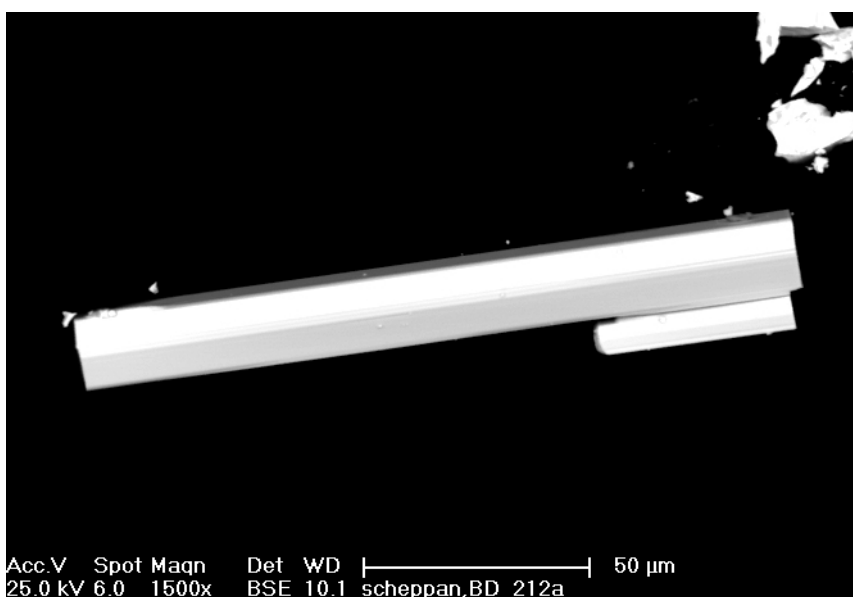


Figure 5.2: Back scattering electron (BSE) image of a crystal  $Dy_{5.64}[Fe_2C_9]$ .

## 5.2 Crystal structure determination

Single crystals were separated from the surface of annealed samples under liquid paraffin in an Ar-filled glove box. Specimens with average dimensions of about  $20 \times 25 \times 40 \mu\text{m}$  were selected and mounted on glass fibres. Single crystal X-ray diffraction investigations of  $Dy_{5.64}[Fe_2C_9]$  were carried out at the Laboratory of Crystallography, University of Bayreuth, on an image plate diffractometer MAR 345dtb with Mo  $K\alpha$  ( $\lambda = 71.069 \text{ pm}$ ) radiation at ambient temperature. Data reduction including Lorentz and polarization factor correction as well as numerical absorption corrections was performed using the program EVAL15 [164]. Relevant crystallographic data and further details of the data collection are listed in Table 5.3.

The single crystal X-ray diffraction patterns clearly revealed an orthorhombic symmetry. Satellite reflections were observed between the main reflections only along  $c^*$ . The diffraction

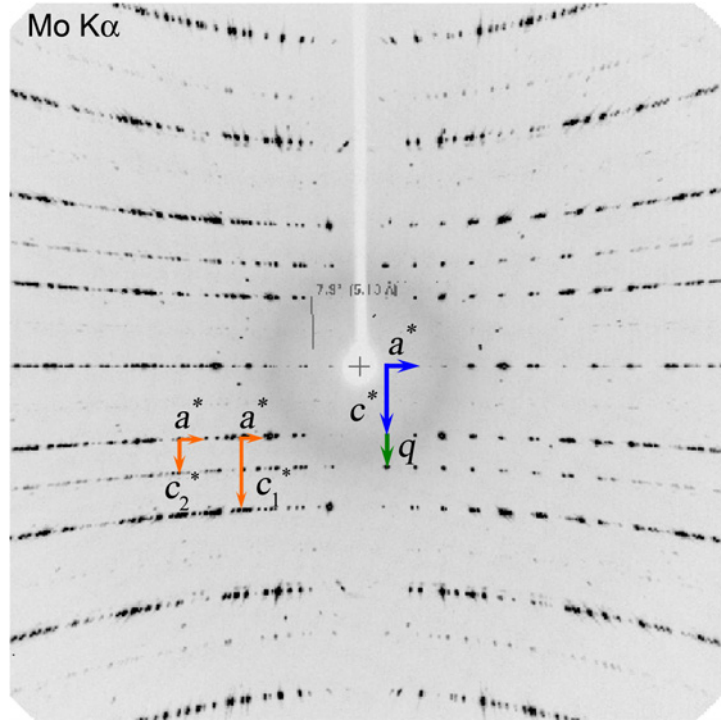


Figure 5.3: Oscillation photograph of a single crystal  $Dy_{5.64}[Fe_2C_9]$  along  $b^*$ . Two possible choices for indexing the diffraction pattern are shown. The first choice corresponds to a modulated structure (blue), and the second choice corresponds to a composite with two sets of reciprocal basis vectors (orange).

patterns could be indexed in two different ways. The first choice was to index the reflections with an orthorhombic unit cell ( $a = 2934.63(9)$  pm,  $b = 1263.63(5)$ ,  $c = 504.14(3)$  pm) and a modulation wave vector  $q = 0.4775c^*$  (Figure 5.3, blue). Satellite reflections up to the second order were taken for integration. The diffraction symmetry of the main reflections belong to the Laue class  $mmm$ . The data analysis showed that only Bragg peaks compatible with the reflection conditions listed in Table 5.2 were present.

Table 5.2: Reflection conditions for the average crystal structure of  $Dy_{5.64}[Fe_2C_9]$ .

Group	Reflection condition	Group	Reflection condition
$hkl$	any	$h00$	$h = 2n$ ( $2_1$ -screw axes along $x$ )
$hk0$	$h = 2n$ (glide plane $a \perp z$ )	$0k0$	$k = 2n$ ( $2_1$ -screw axes along $y$ )
$h0l$	any	$00l$	$l = 2n$ ( $2_1$ -screw axes along $z$ )
$0kl$	$k + l = 2n$ (glide plane $n \perp x$ )		

The integral extinction conditions suggests a primitive lattice type, while the set of zonal and serial extinction conditions is in agreement with two possible space groups:  $Pn2_1a$  (No. 33) and  $Pnma$  (No. 62). In the first step, the average structure was solved by direct methods (SHELX97 [165]) using only the main reflections. As the Sheldrick criterion  $|E^2 - 1| = 1.04$  is in favor for centrosymmetry, the space group  $Pnma$  (No. 62) was chosen for structure refinements. The refinement with anisotropic displacement parameters for all atoms converged to residuals  $R1 = 0.045$  and  $wR2 = 0.086$ . In this model, all atoms of the crystal structure are distributed on 13 Dy, 3 Fe and 18 C positions and the sites are fully occupied except for three crystallographic positions of the Dy atoms. Each of these 3 atomic sites is occupied

by about 30%. Full occupation would result in unphysically short Dy–Dy distances smaller than 253 pm. All fully occupied atomic sites are forming a framework structure with empty channels. The partially occupied Dy positions fill these empty channels. As disorder would cause streaks or diffuse reflections on the diffraction pattern, the satellite reflections point to an ordering of the Dy atoms within these channels. In the next step, the satellite reflections were taken into account. Several commensurately and incommensurately modulated structure models in suitable superspace groups were checked in order to find a physically reasonable model. The refinements were done using the software packages JANA2006 [161] and WinCSD [157–159]. However, the  $R$  factors for the satellite reflections were about 0.25 for the first order and 0.35 for the second order satellites, respectively, indicating that neither the commensurate nor the incommensurate model can properly describe the real crystal structure.

The second choice was to index the observed reflections corresponding to a composite structure. Composite structures consist of two or more periodic substructures, each with their own space group and with mismatch in at least one dimension. Such kind of structures cannot be forced into a single unit cell and their misfit lattices give rise to mutual modulations. In this case, the composite structure consists of two orthorhombic subsystems with common  $a$ ,  $b$  parameters but different in their  $c$  axes:  $a = 2934.63(9)$  pm,  $b = 1263.63(5)$ ,  $c_1 = 504.14(3)$  pm and  $c_2 = 1056.01(5)$ , which are mutually incommensurate (*Figure 5.3, orange*). The high data/parameter ratio by using this approach usually improves the numerical stability of the refinements compared with refinements involving superstructures with large unit cells [223]. Integer indexing of the Bragg reflections is defined by a set of reciprocal basis vectors  $\mathbf{M} = \{\mathbf{a}^*, \mathbf{b}^*, \mathbf{c}_1^*, \mathbf{c}_2^*\}$ . The set of basis vectors of the reciprocal lattice of the basic structure of the each subsystem is related to the vector set  $\mathbf{M}$  through the non-singular  $(3+1) \times (3+1)$  integer matrix  $W$ . In our case, the  $W$  matrices for the first and second subsystems are:

$$W_1 = \begin{pmatrix} 1 & 0 & 0 & 0 \\ 0 & 1 & 0 & 0 \\ 0 & 0 & 1 & 0 \\ 0 & 0 & 0 & 1 \end{pmatrix} \quad \text{and} \quad W_2 = \begin{pmatrix} 1 & 0 & 0 & 0 \\ 0 & 1 & 0 & 0 \\ 0 & 0 & 0 & 1 \\ 0 & 0 & 1 & 0 \end{pmatrix}$$

The main reflections of the first subsystem will have indexes  $(hkl0)$ , whereas  $(hk0m)$  define the main reflections of the second subsystem. The  $(hklm)$  reflections belong to both subsystems and represent the  $m^{\text{th}}$  order satellite for the first and  $l^{\text{th}}$  order satellite for the second subsystem.

The crystal structure of  $\text{Dy}_{5.64}[\text{Fe}_2\text{C}_9]$  was successfully refined as a composite structure using the program WinCSD [157–159]. The framework part of the average structure was taken as the first subsystem, whereas the guest Dy atoms within the channels were treated as the second subsystem. Thus, the complete structure can be described as a host-guest assembly: the host structure contains most of the atoms (10 Dy, 3 Fe and 18 C positions)

Table 5.3: Crystallographic data and details on data collection and crystal structure refinements for the composite structure  $Dy_{5.64}[Fe_2C_9]^\dagger$ .

Chemical formula, $Z$	$\{Dy_{0.64}\}\{Dy_5[Fe_2C_9]\}$ , 8
Crystal system	orthorhombic
Superspace group	$Pnma(00g)$
Formula mass [ $g \cdot mol^{-1}$ ]	1145.23
Radiation, $\lambda$ [pm]	Mo $K\alpha$ , 71.069
Temperature [K]	295
$a$ [pm]	2934.63(9)
$b$ [pm]	1263.63(5)
$c_1 = c_H$ [pm]	504.14(3)
$c_2 = c_G$ [pm]	1056.01(5)
Modulation vectors, $q_H$ or $q_G$	0.4775 or 2.0942
$\rho_{calc}$ [ $g \cdot cm^3$ ]	9.067
Crystal size [ $\mu m$ ]	$20 \times 25 \times 40$
Crystal color	silvery metallic
$\phi$ -range [ $^\circ$ ]	0 – 276
$\theta$ -range [ $^\circ$ ]	1.4 – 27.6
$hklm$ -range	$-20 \leq h \leq 38$ $-3 \leq k \leq 6$ $-16 \leq l \leq 16$ $-2 \leq m \leq 2$
Absorption correction	numerical from crystal shape
Absorption coefficient, $\mu$ [ $mm^{-1}$ ]	56.08
$T_{min}, T_{max}$	0.520, 0.746
No. of measured reflections	26733
Criterion for observed reflections	$F \geq 4\sigma$
$R(all), wR(all)$	0.055, 0.059
$R_F, wR_F(hkl0)$	0.035, 0.036
$R_F, wR_F(hk0m)$	0.058, 0.062
$R_F, wR_F(hkl1)$	0.134, 0.136
$R_F, wR_F(hkl2)$	0.139, 0.142
Goof	1.01

<sup>†</sup> Supplementary data are available from the FIZ, D-76344 Eggenstein-Leopoldshafen, Germany, e-mail [crysdata@FIZ-karlsruhe.de](mailto:crysdata@FIZ-karlsruhe.de), by quoting the depository number CSD-422082

and the guest structure (2 Dy) fills the channels in the host structure. The two substructures share the  $ab$  plane, but have different translational periods and are thus modulated along [001] (Figure 5.5a). The unit cell parameters, the modulation vectors and the  $W$  matrixes of host and guest structures are given in Table 5.4. Braces<sup>1</sup> are used to denote the subsystems of the composite structure.

The reflection conditions are in agreement with the possible space groups  $Pnam$  (62) and  $Pna2_1$  (33) (see Table 5.2) for the host structure and  $Pbam$  (55) and  $Pba2$  (32) ( $h = 2n$  for  $h00m$ ,  $k = 2n$  for  $0k0m$ ,  $h = 2n$  for  $h000$  and  $k = 2n$  for  $0k00$ ) for the guest structure. Here,

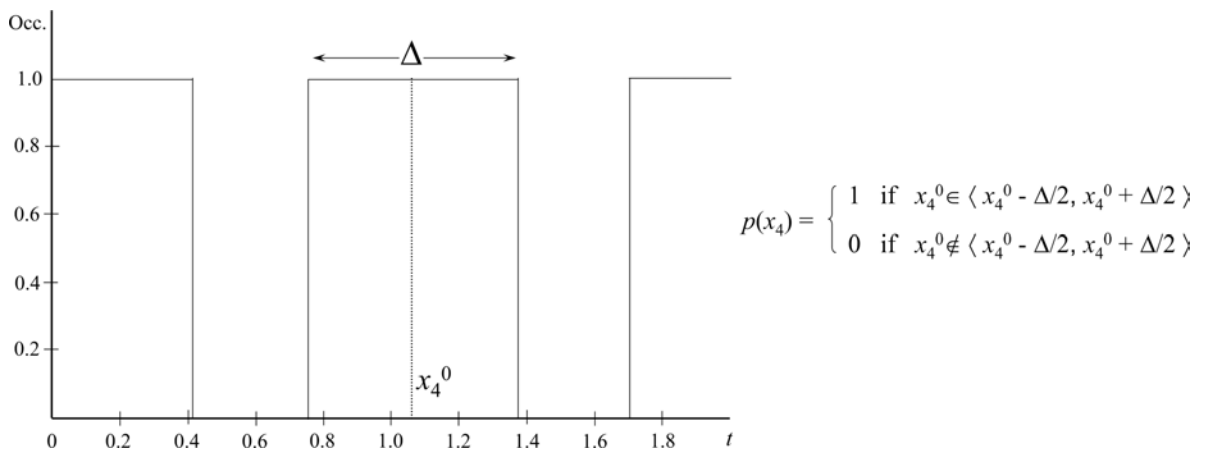
<sup>1</sup>Commonly, brackets are used to denote the subsystems. Throughout this thesis brackets are only used to consistently indicate complex anions in a chemical formula.

Table 5.4: Unit cell parameters, modulation vectors and  $W$  matrixes of host and guest structures of the composite structure  $\text{Dy}_{5.64}[\text{Fe}_2\text{C}_9]$ .

	Host structure $\{\text{Dy}_5[\text{Fe}_2\text{C}_9]\}$	Guest structure $\{\text{Dy}_{0.64}\}$
$a$ (pm)		2934.63(9)
$b$ (pm)		1263.63(5)
$c$ (pm)	504.14(3)	1056.01(5)
$q$	$0.4775c_H^* = c_G^*$	$2.0942c_G^* = c_H^*$
$W^\dagger$	$W_1$	$W_2$

<sup>†</sup> see text

the crystallographic settings were chosen in a way that the sublattices have common  $a$  and  $b$  axes and mismatch is given along the  $c$  axis direction. Refinements were carried out for the centrosymmetric as well as the non-centrosymmetric space groups. The refinement converged to almost similar residuals for the centrosymmetric ( $R(\text{all})$ ,  $wR(\text{all})$  0.055, 0.059) and the non-centrosymmetric ( $R(\text{all})$ ,  $wR(\text{all})$  0.05, 0.07) space groups. However, in the non-centrosymmetric case short Dy–Dy contacts of ca. 180 pm are observed. The attempt to treat the short Dy–Dy contacts with Crenel function failed. Therefore, the centrosymmetric space groups  $Pnam$  and  $Pbam$  were chosen, since they provide physically meaningful interatomic distances. The combination of the space group pair results in the superspace group  $Pnam(00g)$  for the composite structure. Satellites up to the second order were included in the refinements, which finally converged to  $R_F(hkl0) = 0.035$ ,  $R_F(hk0m) = 0.058$ ,  $R_F(hkl1) = 0.134$  and  $R_F(hkl2) = 0.139$  for reflections with  $F > 4\sigma(F)$ . Further details on the crystal structure refinements are summarized in *Table 5.3*. The fractional atomic coordinates and equivalent atomic displacement parameters of the average structure are listed in *Table 5.5*. All atomic positions are fully occupied except Dy12, which belongs to the guest structure. The occupational modulation of the Dy12 site was modeled with a Crenel function, which describes a periodic distribution of atoms and vacancies as a square wave. The shape and the formula of the Crenel function is shown in *Figure 5.4*.

Figure 5.4: Crenel function of width  $\Delta$  and center  $x_4^0$ .

The parameter  $p(x_4)$  presents the occupational probability,  $x_4^0$  and  $\Delta$  are the parameters of

the Crenel function. The parameter  $\Delta$  defines the  $t$ -range (phase of the modulation) and  $x_4^0$  defines the center of this range.

Table 5.5:  $\{Dy_{0.64}\}\{Dy_5[Fe_2C_9]\}$ : Fractional atomic coordinates, equivalent isotropic displacement parameters [ $10^4 \text{ pm}^2$ ] of the atoms in the host-guest crystal structure; estimated standard deviations are given in parentheses.

Atom	Site	$x$	$y$	$z$	$U_{eq.}$
Subsystem 1: Host structure - $\{Dy_5[Fe_2C_9]\}$					
Dy1	4c	0.37276(1)	0.26055(3)	1/4	0.0086(2)
Dy2	4c	0.46831(2)	0.91673(4)	1/4	0.0085(2)
Dy3	4c	0.10825(1)	0.56368(4)	1/4	0.0084(2)
Dy4	4c	0.04675(1)	0.80218(3)	1/4	0.0081(2)
Dy5	4c	0.25201(2)	0.31067(4)	1/4	0.0093(2)
Dy6	4c	0.28153(1)	0.61154(3)	1/4	0.0084(2)
Dy7	4c	0.67163(2)	0.57283(4)	1/4	0.0101(2)
Dy8	4c	0.45564(1)	0.49531(3)	1/4	0.0081(2)
Dy9	4c	0.03683(1)	0.20275(3)	1/4	0.0076(2)
Dy10	4c	0.29492(1)	0.02431(4)	1/4	0.0089(2)
Fe1	4c	0.18899(4)	0.6995(1)	1/4	0.0065(4)
Fe2	4c	0.46127(4)	0.1493(1)	1/4	0.0049(4)
Fe3	8d	0.12413(3)	0.10524(8)	0.5000(2)	0.0083(3)
C1	4c	0.4617(3)	0.7132(8)	1/4	0.012(3)
C2	4c	0.0664(4)	0.3909(9)	1/4	0.016(3)
C3	4c	0.5392(3)	0.5032(8)	1/4	0.013(3)
C4	4c	0.1294(3)	0.7573(8)	1/4	0.011(3)
C5	4c	0.2212(3)	0.1084(8)	1/4	0.013(3)
C6	4c	0.4531(3)	0.3010(8)	1/4	0.012(3)
C7	4c	0.3170(3)	0.4249(8)	1/4	0.013(3)
C8	4c	0.2398(3)	0.7852(8)	1/4	0.013(3)
C9	4c	0.0821(3)	0.0338(8)	1/4	0.013(3)
C10	4c	0.4100(3)	0.0670(8)	1/4	0.014(3)
C11	4c	0.1941(3)	0.5560(8)	1/4	0.013(3)
C12	4c	0.3506(3)	0.4979(8)	1/4	0.013(3)
C13	4c	0.1766(3)	0.1348(8)	1/4	0.013(3)
C14	4c	0.0218(4)	0.3936(9)	1/4	0.014(3)
C15	4c	0.4195(3)	0.6823(9)	1/4	0.015(3)
C16	4c	0.8806(4)	0.5139(11)	1/4	0.019(3)
C17	4c	0.2817(4)	0.8224(8)	1/4	0.017(3)
C18	4c	0.1901(4)	0.4531(10)	1/4	0.021(3)
Subsystem 2: Guest structure - $\{Dy_{0.64}\}$					
Dy11	8i	0.13902(2)	0.31816(5)	0.3155(1)	0.0038(3)
Dy12 <sup>†</sup>	4g	0.13972(6)	0.3237(2)	0	0.0034(4)

<sup>†</sup> parameters of the Crenel function:  $x_4^0 = 0.09$  and  $\Delta = 0.64$

Outside the  $\Delta$  range there are no atoms (vacancies only) and inside the range there are atoms. The average occupancy of the Dy12 site is defined by  $\Delta$ , which in our case is 0.64. The Crenel function can be expressed by a Fourier series  $p(\bar{x}_4)$ , with  $\bar{x}_4 = t + q \cdot r$  (see *Section*

3.5.3) because it is a periodic function. The chemical formula of the host structure is given by  $\{\text{Dy}_{40}[\text{Fe}_{16}\text{C}_{72}]\}$  or  $\{\text{Dy}_5[\text{Fe}_2\text{C}_9]\}$  with  $Z = 8$  formula units per unit cell, whereas the guest structure contains 10.68 ( $= 8 + 0.67 \times 4$ ) atoms per unit cell.  $5.10 = 10.68 \times 0.4775$  atoms of the guest structure corresponds to one unit cell of the host structure, i.e.  $5.1/8 = 0.64$  guest atoms per formula unit of the host structure. The chemical formula for the composite structure is given by  $\{\text{Dy}_{0.64}\}\{\text{Dy}_5[\text{Fe}_2\text{C}_9]\}$ . The displacement modulation of all atomic positions was modeled with harmonic functions up to the second order for the host structure and with fourth order harmonic functions for the guest structure, respectively. Thus,  $\text{Dy}_{5.64}[\text{Fe}_2\text{C}_9]$  shows positional modulations for all atoms and occupational modulation only for the Dy<sub>12</sub> atom. The modulation functions are given in *Table 9.26*. Anisotropic displacement parameters are listed in *Table 9.24*.

### 5.3 Crystal chemistry

$\text{Dy}_{5.64}[\text{Fe}_2\text{C}_9]$  is described as a composite structure composed of host and guest structures, which are mutually incommensurate in  $z$  direction. Projections of the host structure along [001] and guest structure along [100] are shown in *Figure 5.5a*.

The characteristic feature of the host structure  $\{\text{Dy}_5[\text{Fe}_2\text{C}_9]\}$  is the coexistence of two different complex anions with iron as the central atoms and carbon species as the ligands:  $[\text{FeC}(\text{C}_2)_2]$  trigonal planar units and  $[\text{Fe}(\text{C}_2)_4]$  edge sharing tetrahedral chains (*Figure 5.6*).

One of the complex anions is a distorted trigonal planar group  $[\text{FeC}(\text{C}_2)_2]$ . A similar unit is observed in the anionic partial structure of  $\text{La}_{3.67}[\text{Fe}(\text{C}_2)_3]$  [145] (see also *Section 6.2.2*), but instead of three  $\text{C}_2$  ligands there are one monoatomic and two monodentate diatomic carbon ligands connected to the Fe atom. Each trigonal unit  $[\text{FeC}(\text{C}_2)_2]$  is surrounded by large tricapped trigonal prisms (formed by nine Dy atoms) which are fused to columns along [001] via common basal planes resulting in one of the main building blocks of the host structure. Here, we name this building block as **A**. The crystal structure of  $\text{La}_{3.67}[\text{T}(\text{C}_2)_3]$  ( $T = \text{Fe}, \text{Ru}$ ) represents a framework structure which also contains such kind of **A** units (for details see *Section 6*). In addition, the crystal structure of  $\text{RE}_{15}[\text{Fe}_8\text{C}_{25}]$  [224] (*Section 4*) also contains **A** units as the main building block. Thus, **A** can be considered as one of the principal building elements participating in the formation of ternary compounds in  $\text{RE-T-C}$  systems.

The other complex anion is a distorted tetrahedra  $[\text{Fe}(\text{C}_2)_4]$ , which is also present in the anionic partial structure of  $\text{Y}_2[\text{Fe}(\text{C}_2)_2]$  [29]. The distorted  $\text{Fe}(\text{C}_2)_4$  tetrahedra form  $\text{SiS}_2$ -analogous chains running along [001] by sharing common edges (*Figure 5.6*). Each  $\text{Fe}(\text{C}_2)_4$  group is surrounded by four Dy atoms also arranged in a distorted tetrahedral manner and forming large edge sharing tetrahedral chains running along [001]. This is the second main building block of the host structure and will be designated as **B**. This building unit is also present in the crystal structure of  $\text{Y}_2[\text{Fe}(\text{C}_2)_2]$ . In this way, the host structure  $\{\text{Dy}_5[\text{Fe}_2\text{C}_9]\}$  of the composite  $\text{Dy}_{5.64}[\text{Fe}_2\text{C}_9]$  is built up from the building blocks already known from the

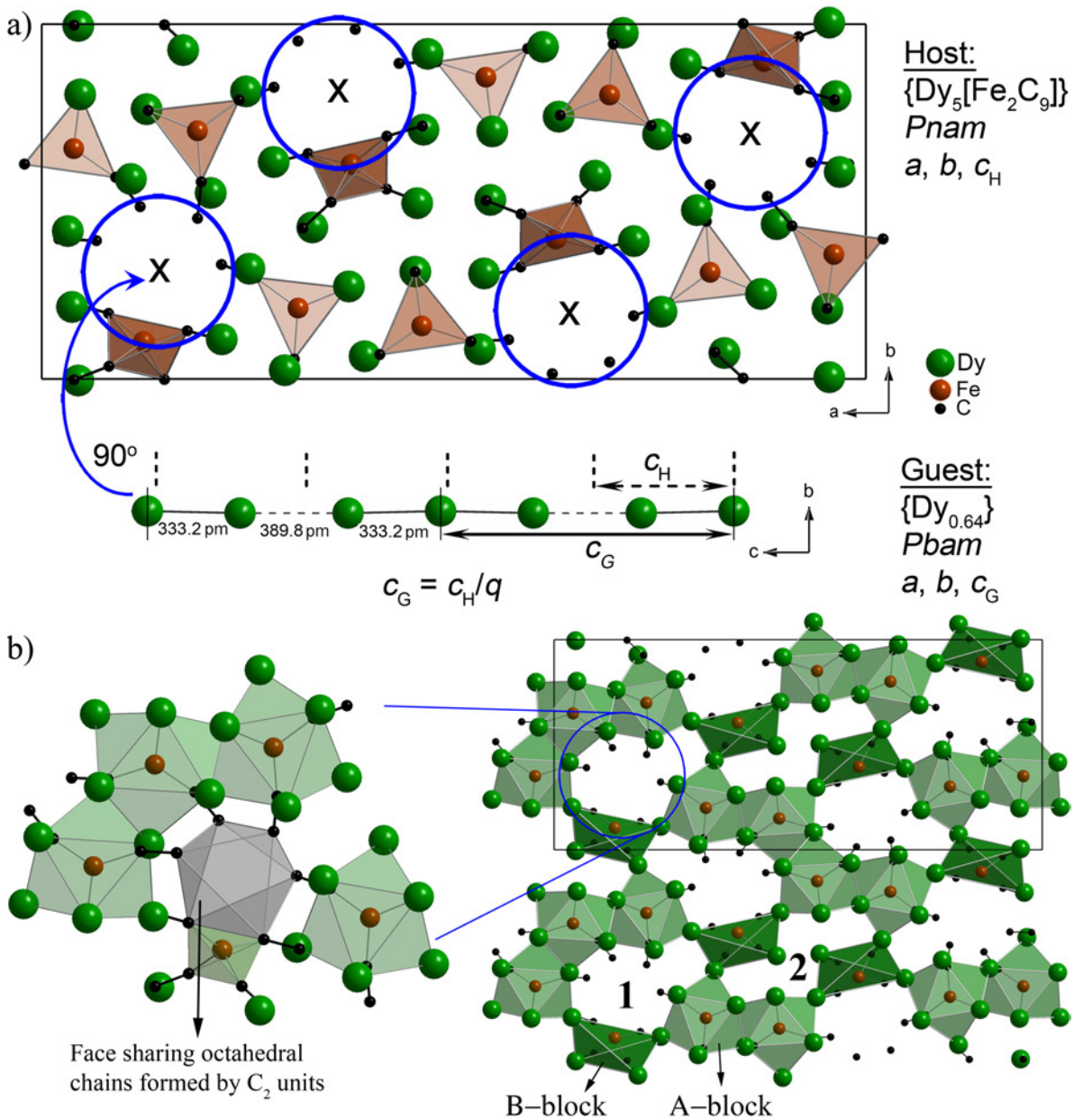


Figure 5.5: a) Host structure  $\{Dy_5[Fe_2C_9]\}$  viewed along  $[001]$ ,  $Pnam$ ,  $a = 2934.63(9)$  pm,  $b = 1263.63(5)$  pm,  $c_H = 504.14(3)$  pm; the blue circles mark the empty channels and black crosses the positions of the guest atoms in the host substructure, i.e., the guest chain  $\{Dy_{0.64}\}$  running along  $[100]$ ,  $Pbam$ ,  $a = 2934.63(9)$  pm,  $b = 1263.63(5)$  pm,  $c_G = 1056.01(5)$  pm; the dashed lines mark the length  $c_H$  of the first subcell indicating the misfit of two subcells; b) the host structure  $\{Dy_5[Fe_2C_9]\}$  viewed along  $[001]$ . Building blocks **A** and **B** are shown. Linkage of **A** and **B** creates two different kinds of irregular shaped channels, labeled **1** and **2**. Zoom of channel **1** (left). The face sharing octahedral chain is depicted by grey polyhedra.

crystal structures of  $La_{3.67}[Fe(C_2)_3]$  and  $Y_2[Fe(C_2)_2]$ . The unit cell projection of the host structure along  $[010]$ , shows that **B** is linked to three **A** units via common vertices, whereas **A** is connected to  $1A + 2B$  or  $2A + 1B$ . Condensation between **A** units along  $[001]$  is achieved by face sharing. The linkages between neighboring blocks create two different kinds of channels running along  $[001]$ , **1** and **2**, in the host structure as shown in *Figure 5.5b*.



Channel **1** is inside the cyclic arrangement of  $A-A-A-B-A-B$  and their extension along  $[001]$  (Figure 5.5b). Channel **2** is much smaller (formed by  $4A + 2B$  in the sequence  $A-A-B-A-A-B$ ) and does not contain any atoms due to space restrictions. All composite framework structures reported up to now accommodate other kind of chemical element inside the empty channel.  $Dy_{5.64}[Fe_2C_9]$  is, to our knowledge, the first example containing the same chemical element (Dy) in, both, host and guest substructures.

Inside the channel **1** the  $C_2$  units form face sharing octahedral chains running along  $[001]$  (Figure 5.5b). Figure 5.7b shows a cut-out of the modulated chain of Dy atoms occupying the channels of the composite structure and an adjacent polyanionic tetrahedral string as well as trigonal planar groups, taken from a  $23 \times 11$  supercell. The tetrahedral strings give rise to the formation of a linear Fe–Fe chain with an average distance of 250.4 pm, which probably makes the host framework rigid. The channel for the guest atoms is formed by the carbon ligands of the tetrahedral and trigonal planar groups. Due to the limited amount of space for the guest atoms, some of the Dy atoms within the channels are located inside the carbon octahedra, others, however, are pushed in direction of the octahedral faces, thereby changing the coordination of the guest atoms by carbon from octahedral to tetrahedral or even to a trigonal planar environment (Figure 5.7b). The guest La atoms in  $La_{3.67}[Fe(C_2)_3]$  occupy positions displaced from the centers of two neighboring carbon octahedra (Figure 5.7a). Two filled octahedra alternate with one empty octahedron. Thus,  $2/3$  ( $= 0.67$ ) of the octahedra are occupied by La atoms. Higher La contents would result in too short La–La distances. For  $Dy_{5.64}[Fe_2C_9]$ , the amount of guest Dy atoms in the channels is calculated in the following way. The unit cell of the host structure as well as the unit cell of the guest structure contain an integral number of formula units:  $\{Dy_5[Fe_2C_9]\}$  ( $Z = 8$ ) and  $\{Dy_{10.68}\}$  ( $Z = 1$ ), respectively. Because the volume of the unit cell of the host structure is somewhat smaller than the unit cell volume of the guest structure by an irrational factor, only a fraction of a formula unit of  $\{Dy_{10.68}\}$  fits into one unit cell of  $\{Dy_5[Fe_2C_9]\}$ . This fraction is defined by the ratio of the  $c$ -axes of the two subsystems, which is in the present case 0.4775. The number of formula units of the guest structure for each formula unit of  $\{Dy_5[Fe_2C_9]\}$  is calculated to be 0.06 ( $= 0.4775 \cdot 1/8$ ). In other words, 0.64 ( $= 0.06 \times 10.68$ ) Dy guest atoms

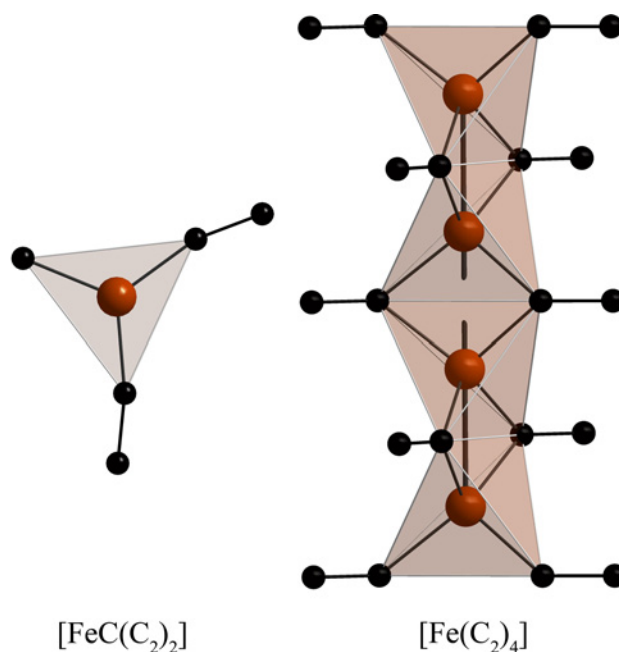


Figure 5.6: Polyanionic partial structures in the host structure  $\{Dy_5[Fe_2C_9]\}$ .

are located inside the carbon octahedra, others, however, are pushed in direction of the octahedral faces, thereby changing the coordination of the guest atoms by carbon from octahedral to tetrahedral or even to a trigonal planar environment (Figure 5.7b). The guest La atoms in  $La_{3.67}[Fe(C_2)_3]$  occupy positions displaced from the centers of two neighboring carbon octahedra (Figure 5.7a). Two filled octahedra alternate with one empty octahedron. Thus,  $2/3$  ( $= 0.67$ ) of the octahedra are occupied by La atoms. Higher La contents would result in too short La–La distances. For  $Dy_{5.64}[Fe_2C_9]$ , the amount of guest Dy atoms in the channels is calculated in the following way. The unit cell of the host structure as well as the unit cell of the guest structure contain an integral number of formula units:  $\{Dy_5[Fe_2C_9]\}$  ( $Z = 8$ ) and  $\{Dy_{10.68}\}$  ( $Z = 1$ ), respectively. Because the volume of the unit cell of the host structure is somewhat smaller than the unit cell volume of the guest structure by an irrational factor, only a fraction of a formula unit of  $\{Dy_{10.68}\}$  fits into one unit cell of  $\{Dy_5[Fe_2C_9]\}$ . This fraction is defined by the ratio of the  $c$ -axes of the two subsystems, which is in the present case 0.4775. The number of formula units of the guest structure for each formula unit of  $\{Dy_5[Fe_2C_9]\}$  is calculated to be 0.06 ( $= 0.4775 \cdot 1/8$ ). In other words, 0.64 ( $= 0.06 \times 10.68$ ) Dy guest atoms

correspond to one formula unit  $\{Dy_5[Fe_2C_9]\}$ . Thus, the chemical formula for the composite structure is  $\{Dy_{0.64}\}\{Dy_5[Fe_2C_9]\}$ . By this, it becomes clear that the Dy content within the channel of  $Dy_{5.64}[Fe_2C_9]$  is lower than that in the commensurately modulated (often called lock-in phase)  $La_{3.67}[Fe(C_2)_3]$  *Figure 5.7b*. This may be one of the reasons for the formation of an incommensurately modulated composite structure. Another consideration for the formation of the composite structure can be the charge compensation of the octahedral carbon channels by Dy atoms. Due to the partial occupancy of the Dy atoms within the channels a narrow homogeneity range may exist.

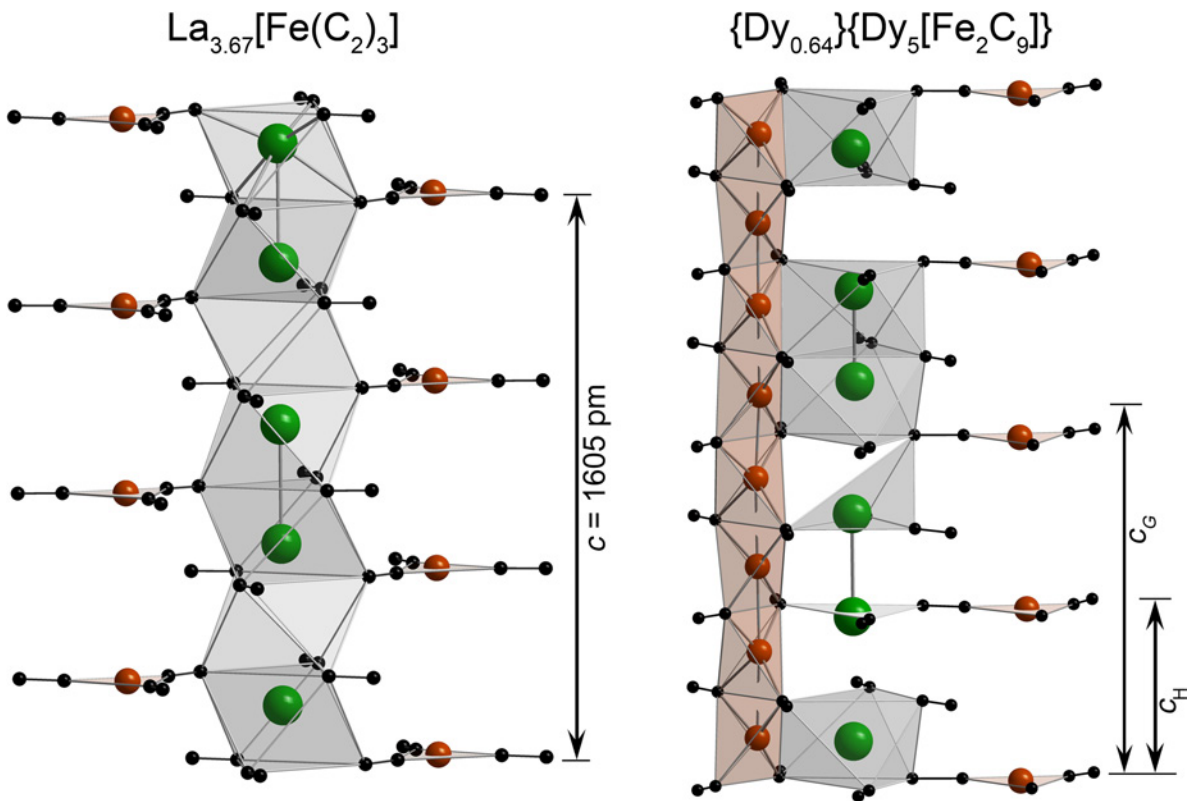


Figure 5.7: a) La atoms inside a channel of face-sharing octahedra together with trigonal planar  $Fe(C_2)_3$  groups in the crystal structure of  $La_{3.67}[Fe(C_2)_3]$ ; La atoms occupy pairs of neighboring carbon octahedra. This pair alternates with one empty octahedron; b) Dy atoms within an octahedral channel of the modulated composite structure together with a tetrahedral string of  $Fe(C_2)_{4/2}$  and trigonal planar  $FeC(C_2)_2$  groups.

In the composite both substructures are modulated due to their mutual interactions. The guest Dy atoms within the channel (Dy11, Dy12) exhibit large displacement modulation amplitudes  $A_z$  along  $z$ , ranging from 0.0107 to 0.0985, while  $A_x$  and  $A_y$  are smaller than 0.006. The modulation amplitudes for all atoms in the host structure are less than 0.02, thus indicating a fairly rigid host substructure. The Fourier coefficients of the modulation functions for all atoms are listed in *Table 9.27*. *Figure 5.8* shows the modulations of selected interatomic distances as a function of the modulation phase  $t$ . Average interatomic distances for host and guest structures are given in *Table 9.25*. It is remarkable that all interatomic distances in the crystal structure of  $Dy_{5.64}[Fe_2C_9]$  exhibit relatively small variations except

Dy11–Dy12.

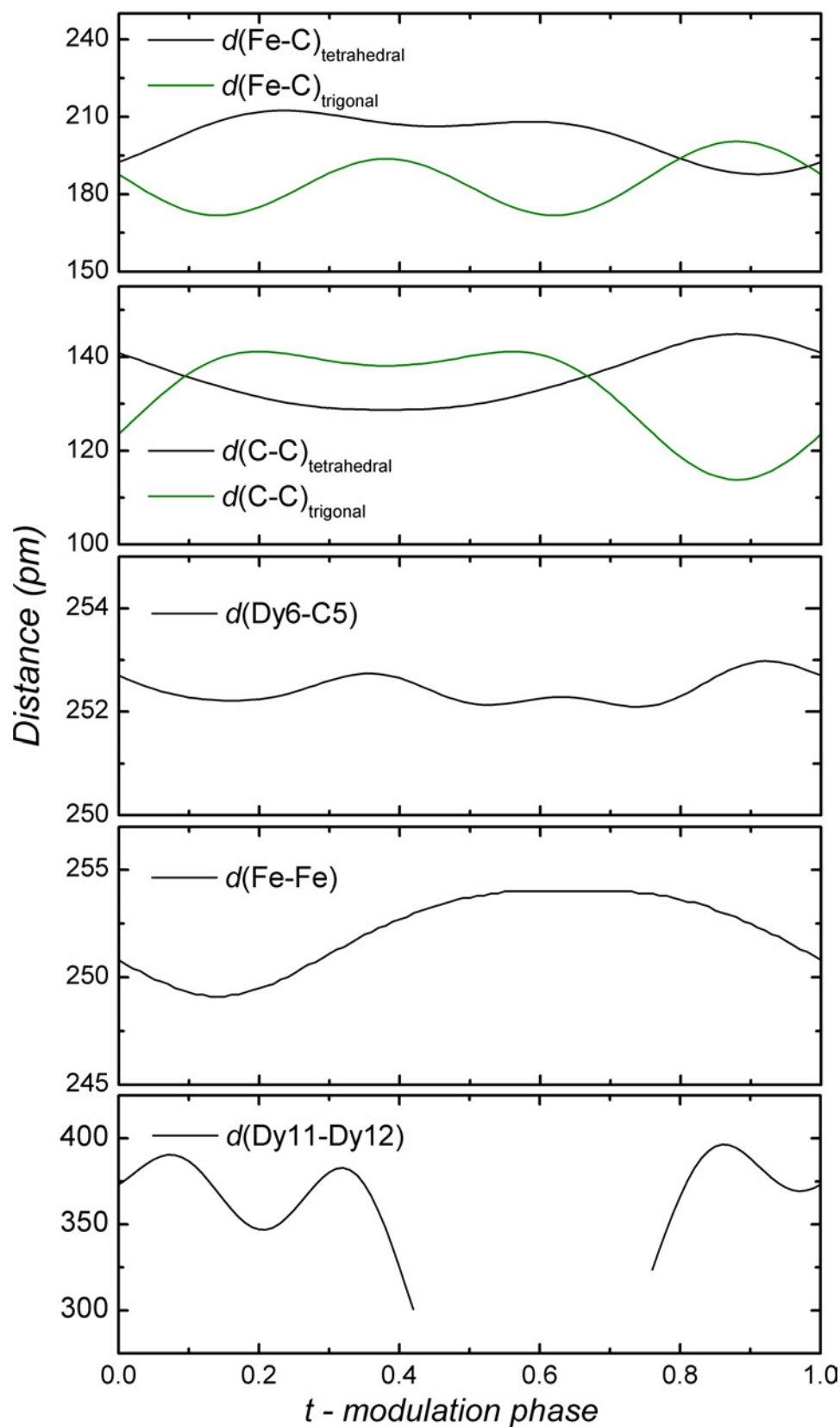


Figure 5.8:  $\text{Dy}_{5.64}[\text{Fe}_2\text{C}_9]$ :  $t$ -plots of the modulation for selected distances: a-b) Fe–C and C–C in the tetrahedral chains as well as in trigonal planar units, c) Dy–C connected to trigonal planar Fe–C units and d) Dy–Dy distances within the guest chain.

The distances in these  $t$ -plots are selected so that all chosen atoms connected to each other. The Fe–C distances are typical for covalent bonds. The bond lengths in the tetrahedral chains are slightly longer than those in the trigonal units. The changes in C–C distances are rather large with  $\Delta d \simeq 20$  pm, however they remain constant in a wide range of  $t = 0.1$  to  $0.8$ . The Dy5–C6 bonds are linked to the Fe–C bonds of the  $FeC(C_2)_2$  trigonal planar group, thus their modulation periods are similar. The distance  $d(Fe-Fe)$  of ca. 252 pm lies in a range of weak bonding interactions and its deviations from the average value are less than  $\Delta d = 2$  pm in the range of  $t = 0.3$  to  $0.9$ . The Dy11–Dy12 distances in the channels reveal a moderate change, with  $\Delta d \simeq 80$  pm. Because of the occupational modulation of Dy12 with a Crenel function the distances in the range of  $t = 0.4$  to  $0.8$  in the plot are missing. In other words, for  $t = 0.43$  to  $0.76$  there are no atoms.

The Dy atoms in the host structure are 10-, 11- and 12-fold coordinated by metal atoms forming bi-, tri- and fourcapped square prismatic arrangements. Exemplarily, the metal environment of Dy1, Dy2 and Dy3 are shown in *Figure 5.9 (1 to 3)*. The average  $d(Dy-Dy)$  and  $d(Dy-Fe)$  distances are 368.18(1) pm and 315.09(1) pm, respectively. Similar distances are also observed in other ternary compounds such as  $Dy_{15}[Fe_8C_{25}]$  ( $d(Dy-Dy) = 340.6$  to  $370.2$  pm,  $d(Dy-Fe) = 274.4$  to  $334.2$  pm) [224] and binary phases, e.g.,  $DyFe_2$  ( $d(Dy-Dy) = 330$  pm,  $d(Dy-Fe) = 314.7$  pm) [101]. The coordination number of the Dy atoms regarding to the carbon ligands are 5, 7, 8 and 9. For instance, Dy1 is 5-fold coordinated by carbon ligands forming distorted square pyramids (*Figure 5.9 (4)*). Dy2 has 8 nearest neighbor carbon atoms arranged in a tricapped distorted square pyramid (*Figure 5.9 (5)*). Dy5 is embedded in a bi-capped square pyramid formed by carbon atoms, thus resulting in  $CN = 7$  (*Figure 5.9 (6)*), whereas the local environment of Dy6 is defined by a monocapped square prismatic arrangement of carbon atoms (*Figure 5.9 (7)*). The average  $d(Dy-C)$  contact is 260.16(2) pm, which is slightly longer than the sum of the covalent radii of Dy and C atoms (ca. 240 pm). Similar distances are also observed in ternary or in binary carbides such as  $Dy_{15}[Fe_8C_{25}]$  ( $d(Dy-C) = 244.9$  to  $276.5$  pm) [224],  $Er_2FeC_4$  ( $d(Dy-C) = 236.4$  to  $265.7$  pm) [29] or in  $DyC_2$  ( $d(Dy-C) = 251.2$  to  $266.2$  pm) [225].

In the host structure there are three crystallographically independent Fe positions. Fe1 and Fe2 have the same local environment formed by metal atoms and carbon ligands. They are surrounded by 9 Dy atoms forming a tricapped trigonal prism (*Figure 5.9 (8)*). As mentioned before, this kind of metal atomic arrangement is very often observed in ternary rare-earth iron carbides, e.g.,  $Dy_{15}[Fe_8C_{25}]$  [224] and  $La_{3.67}[Fe(C_2)_3]$  [145]. Fe3 is linked to 4 Dy and 2 other Fe3 atoms (*Figure 5.9 (9)*). The average  $d(Fe-Fe)$  distance of 252.07(2) pm is comparable with the respective values found in  $Dy_{15}[Fe_8C_{25}]$  [224] (255.7 pm and 270.9 pm),  $Er_2FeC_4$  (250.3 pm) and binary iron carbides such as  $\epsilon$ - $Fe_3C$  (275.4 pm) [84] and  $\eta$ - $Fe_2C$  (260.6 pm and 277.8 pm) [79], and is slightly longer than the distances observed in  $\gamma$ -Fe (245.5 pm) [207]. Iron atoms in the crystal structure of  $Dy_{5.64}[Fe_2C_9]$  serve as central atoms of the anionic partial structure.

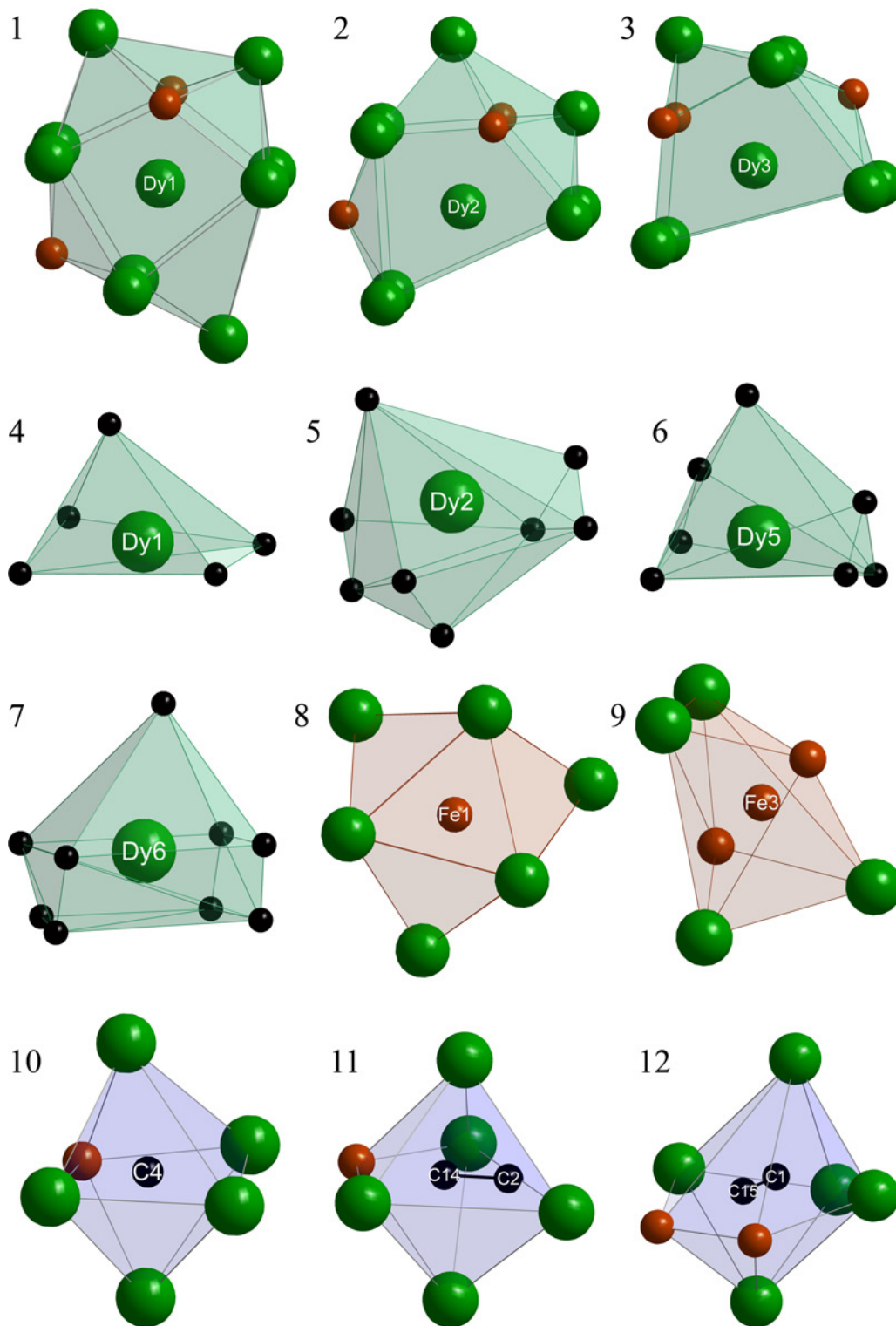


Figure 5.9: Coordination polyhedra of all atomic sites in the host structure  $\{\text{Dy}_5[\text{Fe}_2\text{C}_9]\}$ . Local coordination of Dy by metal atoms: Dy1 - fourcapped square prism (1), Dy2 - tricapped square prism (2) and Dy3 - bicapped square prism (3). Coordination of Dy by carbon ligands: Dy1 - distorted square pyramid (4), Dy2 - tricapped distorted square pyramid (5), Dy5 - bicapped square pyramid (6), Dy6 - monocapped square prism (7). Metal coordination of Fe atoms: Fe1 - tricapped trigonal prism (8), Fe3 - unusual coordination polyhedra formed by 4 Dy and 2 Fe3 atoms (9). Coordination polyhedra around carbon atoms: monoatomic carbon C4 - occupies the octahedral void (10); C<sub>2</sub> pairs have two different local environments: octahedral (11) and distorted pentagonal bipyramidal (12).

Fe1 and Fe2 atoms are coordinated by one monoatomic carbon and two dicarbo ligands (end-on) forming distorted trigonal planar  $FeC(C_2)_2$  groups. The local carbon environment of Fe3 is formed by a tetrahedral arrangement of carbon pairs. The average Fe–C distances are  $d(Fe-C) = 185.3$  to  $201.1$  pm, and are closely related to those found in binary iron carbides,  $\epsilon$ - $Fe_3C$  (193 pm) and  $\eta$ - $Fe_2C$  (182 to 190 pm) and ternary compounds such as  $Dy_{15}[Fe_8C_{25}]$  (186.3 to 227.7 pm),  $La_{3.67}[Fe(C_2)_3]$  (182 pm) and  $Er_2FeC_4$  (197 pm).

There are 18 crystallographically different carbon atoms in the host structure. Only C4 and C6 are monoatomic species, and the remaining 16 carbon atoms form  $C_2$  pairs. In the host structure, the metal matrix contains two different kinds of voids which accommodate carbon atoms. As shown in *Figure 5.9 (10 to 12)*, the monoatomic carbon atoms and half of the  $C_2$  pairs occupy octahedral voids, whereas the remaining half of the  $C_2$  pairs accommodate distorted pentagonal bipyramidal voids. In all reported ternary and binary carbides, carbon atoms usually occupy octahedral or trigonal prismatic voids formed by metal atoms. The average C–C distances range between 129.66(1) and 135.13(1) pm. The average distances  $d(C-C)$  in the composite is close to 133 pm indicating the presence of  $C_2^{4-}$  species with double bonds.

The Dy atoms of the guest structure are forming linear modulated chains running along [001]. The average Dy–Dy distances in the guest structure are  $d(Dy-Dy) = 333.2$  pm and 389.8 pm.

The oxidation states for iron atoms within the complex anions can be assigned as follows. The average C–C distance in the composite is close to 133 pm indicating the presence of  $C_2^{4-}$  species with double bonds. Magnetic susceptibility measurements are consistent with the presence of  $Dy^{3+}$  species. Trigonal planar and tetrahedral coordinations around iron atoms by carbon atoms are known from the crystal structures of  $La_{3.67}[Fe(C_2)_3]$  and  $Y_2[Fe(C_2)_2]$  with  $Fe^{+1}$  and  $Fe^{+2}$ , respectively. The compound under consideration contains both types of environments of Fe atoms by mixed carbon ligands, monoatomic and diatomic. Thus, taking into account all the above mentioned informations a charge balanced ionic formula of the composite can be written as  $\{(Dy)^{3+}_{0.67}\}\{(Dy^{3+})_5[Fe^{2+}(C_2)_{4/2}][CFe^{1+}(C_2)_2]\}$ . Considering the two different coordinations of iron atoms, we expect oxidation states close to  $Fe^{+1}$  and  $Fe^{+2}$  for the trigonal planar and the tetrahedrally coordinated Fe atoms, respectively.

#### 5.4 Magnetic susceptibility

A SQUID magnetometer (MPMS XL-7, Quantum Design) was used for the measurement of the magnetic susceptibility in the temperature range of  $T = 1.8$  K to 400 K and in magnetic fields  $\mu_0H = 10$  mT to 7 T as described in *Section 3.11.1*.

From powder XRD it was known that the sample contains  $\sim 4$ -5 wt.% of Fe as a minority phase. Therefore, the Honda-Owen method was applied to correct the magnetic susceptibilities  $\chi = M/H$  for  $\mu_0H > 1$  T for the Fe impurity. *Figure 5.10* shows the corrected inverse



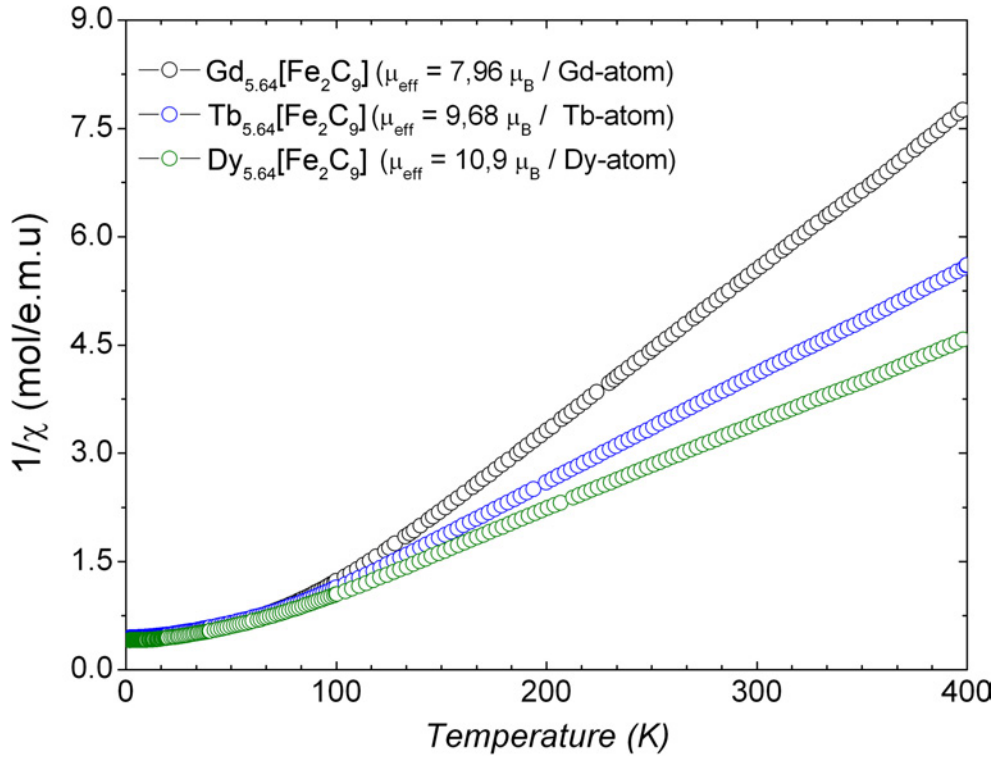


Figure 5.10: The corrected inverse magnetic susceptibility of  $RE_{5.64}[Fe_2C_9]$  ( $RE = Y, Gd, Tb, Dy$ ).

magnetic susceptibility of the compounds  $RE_{5.64}[Fe_2C_9]$  ( $RE = Gd, Tb, Dy$ ). The corrected data  $\chi_{corr}(T)$  are well described by the Curie-Weiss law for  $T > 100$  K. The effective magnetic moments  $\mu_{eff} = 7.96 \mu_B / Gd\text{-atom}$  ( $\theta_P \approx +51$  K),  $\mu_{eff} = 9.68 \mu_B / Tb\text{-atom}$  ( $\theta_P \approx +25$  K) and  $\mu_{eff} = 10.9 \mu_B / Dy\text{-atom}$  ( $\theta_P \approx +15$  K), respectively, corresponding to the values expected for the ground state multiplets ( $Gd^{3+}$ :  $^8S_{7/2}$ ,  $Tb^{3+}$ :  $^7F_6$ ,  $Dy^{3+}$ :  $^6H_{15/2}$ ) of the trivalent  $RE$  ions. Broad anomalies for  $T < 20$  K probably originate from magnetic ordering of the  $RE$  moments.  $Y_{5.64}[Fe_2C_9]$  shows Pauli-paramagnetic behavior. These results reveal a non-magnetic anionic structure for the compounds  $RE_{5.64}[Fe_2C_9]$  ( $RE = Y, Gd, Tb, Dy$ ).

## 5.5 Electrical resistivity

The electrical resistivity  $\rho(T)$  measured on compact pieces shows a metal-like temperature dependence for  $Y_{5.64}[Fe_2C_9]$  and  $Dy_{5.64}[Fe_2C_9]$ , and a semiconductor-like temperature dependence for  $Gd_{5.64}[Fe_2C_9]$  and  $Tb_{5.64}[Fe_2C_9]$  (Figure 5.11). In other words, there is a transition from semiconductor-like to metal-like behavior in the sequence from Gd to Dy. The resistivities at 300 K are 3.17 m $\Omega$ cm, 0.87 m $\Omega$ cm, 0.63 m $\Omega$ cm and 1.64 m $\Omega$ cm for  $Y_{5.64}[Fe_2C_9]$ ,  $Gd_{5.64}[Fe_2C_9]$ ,  $Tb_{5.64}[Fe_2C_9]$  and  $Dy_{5.64}[Fe_2C_9]$ , respectively. A broad hump at 25 K and a strong decrease of  $\rho(T)$  below this temperature is observed only for  $Dy_{5.64}[Fe_2C_9]$ , which indicates a magnetic ordering of the  $Dy^{3+}$  ions. A similar behavior is also observed for the compound  $Dy_{15}[Fe_8C_{25}]$  [224].

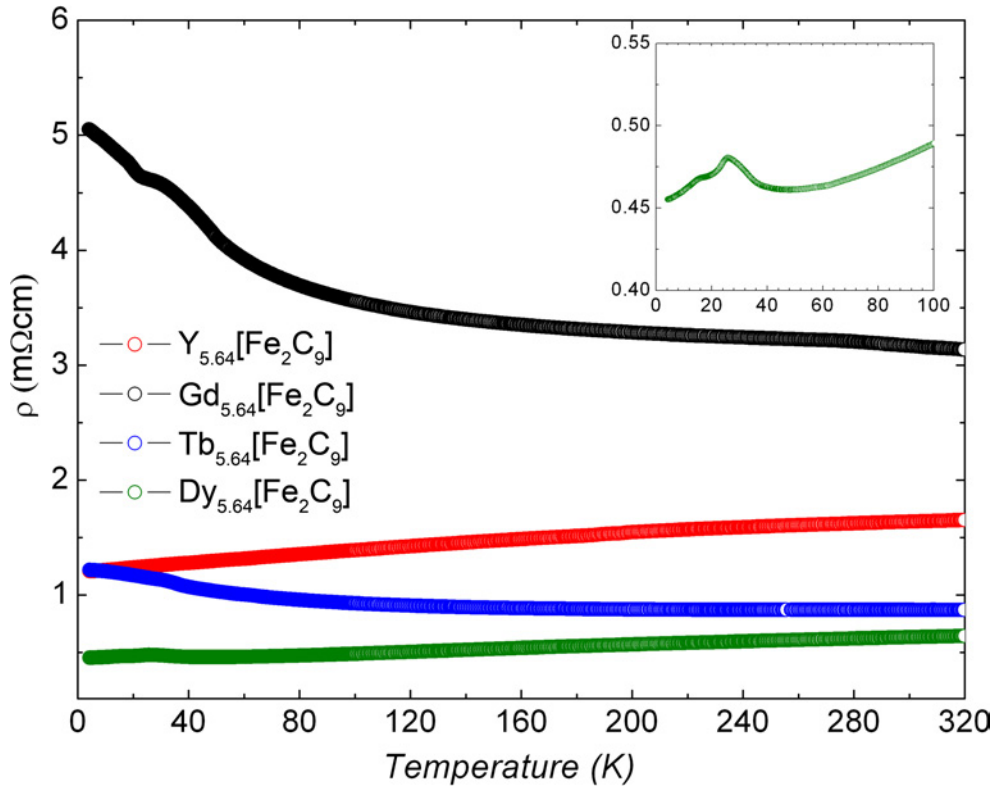


Figure 5.11: Electrical resistivity of compounds  $RE_{5.64}[Fe_2C_9]$  ( $RE = Y, Gd, Tb, Dy$ ). The broad hump observed for  $Dy_{5.64}[Fe_2C_9]$  is also shown in the inset.

## 5.6 Mössbauer spectroscopic studies

The samples were prepared and measured according to the procedure described in *Section 3.8*. *Figure 5.12* shows the Mössbauer spectrum of  $Gd_{5.64}[Fe_2C_9]$  measured at room temperature.

The crystal structure of  $Gd_{5.64}[Fe_2C_9]$  contains three crystallographically independent Fe positions. Both, Fe1 and Fe2 have trigonal coordination by  $C_2$  as well as monoatomic carbon ligands with an average bond length of Fe–C about 180 pm. Fe3 has a tetragonal coordination of carbon ligands with an average bond length of about 200 pm. In addition, the multiplicity of Fe1 and Fe2 is four whereas there are 8 Fe3 atoms in the unit cell. This means, that number of iron atoms on Fe3 sites is equal to that on Fe1 and Fe2 sites together. Since Fe1 and Fe2 have the same coordination polyhedra and similar distances, they can be assigned to the same Mössbauer subspectrum. Thus, the observed Mössbauer spectrum can be fitted with two subspectra associated with Fe3 on the one hand and (Fe1 + Fe2) atoms on the other hand. Because the multiplicity ratio of Fe3/(Fe1 + Fe2) is one, the area of the two subspectra should be the same. The hyperfine parameters obtained from the fit are listed in *Table 5.6*. Considering the coordination of the Fe atoms, in *Section 5.3*, the following oxidation states for Fe atoms in isotypic  $Dy_{5.64}[Fe_2C_9]$  were chosen:  $Fe^I$  (Fe1 and Fe2) and  $Fe^{II}$  (Fe3). In this sense, the Fe atom with the lower oxidation state should show a higher positive shift with respect to the Doppler zero velocity in the Mössbauer spectrum. However, experimental results show that the Fe3 atom have a higher IS value (*Table 5.6*). This, can be explained by



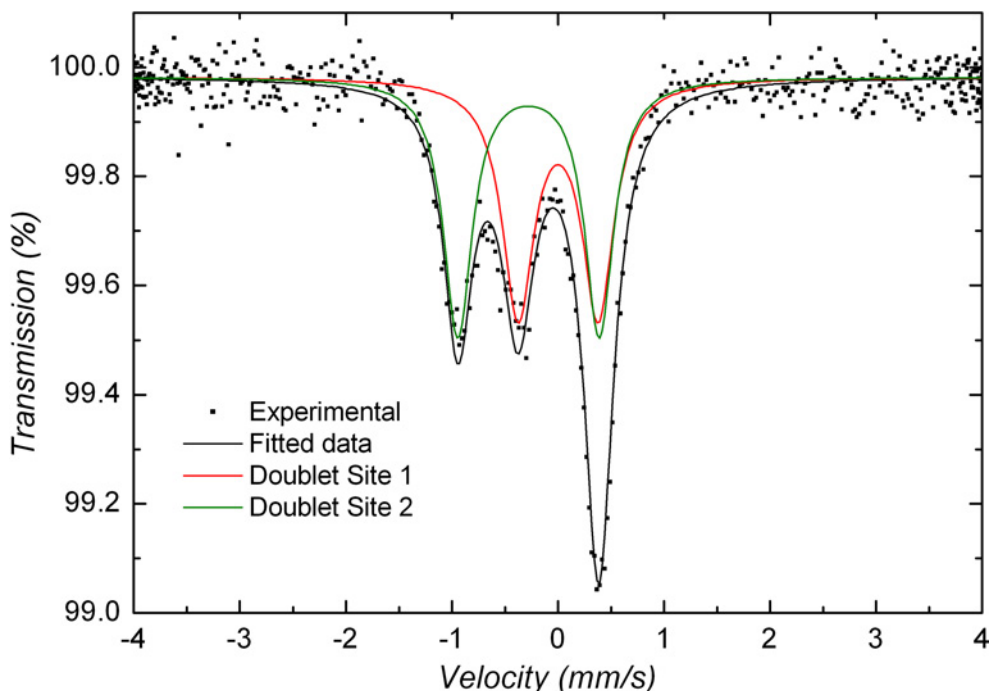


Figure 5.12: The Mössbauer spectrum of  $\text{Gd}_{5.64}[\text{Fe}_2\text{C}_9]$  measured at room temperature. The measured spectrum (dots) is fitted (black) with two subspectra (red and olive).

considering the average bond length of the Fe–C contacts in  $\text{Gd}_{5.64}[\text{Fe}_2\text{C}_9]$ . Because of the smaller average bond length the IS for the Fe1 and Fe2 polyhedra could be smaller than the IS of the subspectra of the Fe3 tetrahedron. Because of these arguments the subspectrum 1 can be associated with the Fe3 site, whereas subspectrum 2 can be associated with the Fe1 and Fe2 sites.

Table 5.6: Mössbauer parameters of  $\text{Gd}_{5.64}[\text{Fe}_2\text{C}_9]$ : Isomer shift (IS) relative to  $\alpha$ -Fe, half width ( $\Gamma/2$ ), quadrupole splitting ( $\Delta E_Q$ ), and relative area ( $A$ ) of the subspectra, estimated standard deviations are given in brackets.

Subspectra	Assignment	IS (mm/s)	$\Delta E_Q$ (mm/s)	$\Gamma/2$ (mm/s)	$A$ (%)
1 (red)	Fe3	0.11(5)	0.8(1)	0.18(2)	50(1)
2 (olive)	Fe1 + Fe2	-0.17(4)	1.34(9)	0.16(2)	49(3)

## 5.7 X-ray absorption spectroscopic studies

The samples for the XAS measurements were prepared and measured according to the procedure described in Section 3.7.2. Pure iron was used as a reference. Figure 5.13 shows the XAS spectrum of the phases  $\text{RE}_{5.64}[\text{Fe}_2\text{C}_9]$  ( $\text{RE} = \text{Y}, \text{Gd}, \text{Tb}, \text{Dy}$ ).

Data processing was done as described in Section 4.9. The XAS spectra of the phases  $\text{RE}_{5.64}[\text{Fe}_2\text{C}_9]$  are of similar shape indicating their isotypism. The XANES region contains main edge and pre-edge peaks. The electrical resistivity measurements of  $\text{Gd}_{5.64}[\text{Fe}_2\text{C}_9]$

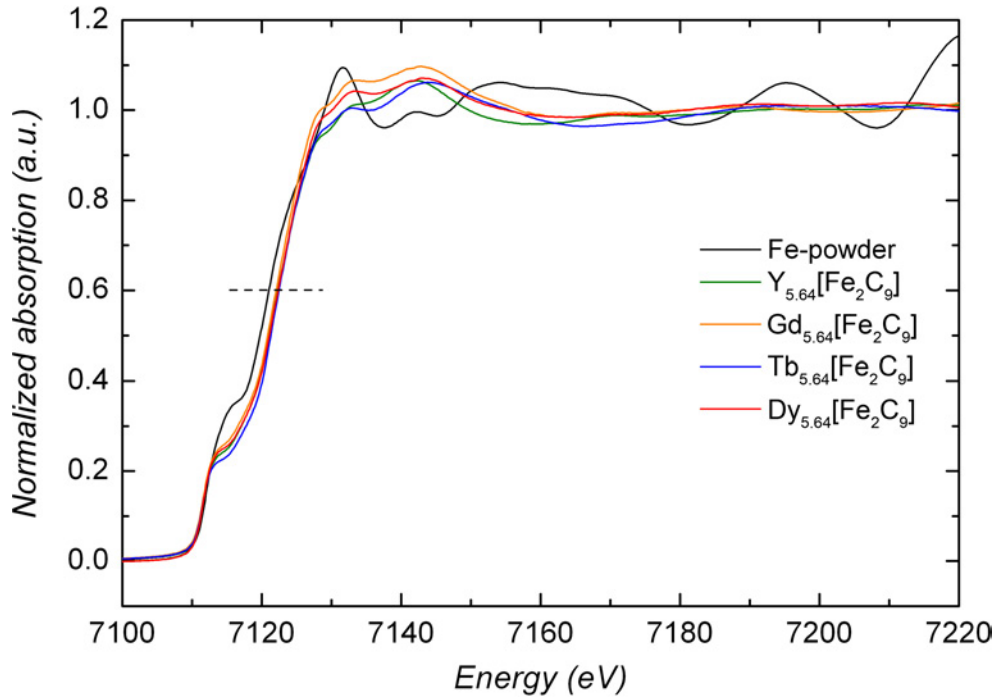


Figure 5.13: Normalized XAS spectra of the Fe- $K$  threshold of the ternary phases  $RE_{5.64}[Fe_2C_9]$  ( $RE = Y, Gd, Tb, Dy$ ) together with the spectrum of metallic iron.

and  $Tb_{5.64}[Fe_2C_9]$  show a semiconductor-like behavior and  $Y_{5.64}[Fe_2C_9]$  and  $Dy_{5.64}[Fe_2C_9]$  very weak and almost temperature independent resistivity. In this reason, the pre-edge peak is most probably associated with the local environment of Fe atoms [218–220]. From the crystal structure, we know that Fe is present in two different non-centrosymmetric coordinations: distorted tetrahedral and distorted trigonal planar (*Section 5.3*). As discussed in *Section 4.9*, the shape of the XAS spectra might indicate a higher filling of the  $3d$  states, which corresponds to a lower oxidation state of Fe [221]. The Fe  $K$  threshold of  $RE_{5.64}[Fe_2C_9]$  at 0.6 of the normalized absorption of the  $K$ -edge showed positive energy shifts with respect to elemental Fe indicating oxidation states larger than zero. Their values are listed in *Table 5.7*. All energy shift values are equal within estimated standard deviations (0.5 eV).

Table 5.7: X-ray absorption Fe  $K$ -edge threshold and energy shift ( $\Delta E$ ) observed for compounds  $RE_{5.64}[Fe_2C_9]$  ( $RE = Y, Gd, Tb, Dy$ ).

Compound	Energy at 0.6 (eV)	$\Delta E$ (eV)
Fe	7112.0	
$Y_{5.64}[Fe_2C_9]$	7122.3	10.3
$Gd_{5.64}[Fe_2C_9]$	7122.1	10.1
$Tb_{5.64}[Fe_2C_9]$	7122.5	10.5
$Dy_{5.64}[Fe_2C_9]$	7122.4	10.4

## 5.8 Summary

The new, complex rare-earth iron carbides  $RE_{5.64}[Fe_2C_9]$  ( $RE = Y, Gd, Tb, Dy$ ) were synthesized and structurally characterized. The materials are air and moisture sensitive and are the first representatives of a new structure type containing two different types of complex anions: discrete trigonal planar  $[FeC(C_2)_2]$  units and infinite chains of distorted edge sharing  $[Fe(C_2)_{4/2}]$  tetrahedra. The crystal structure was solved for  $Dy_{5.64}[Fe_2C_9]$  and treated as a composite of a host  $\{Dy_5[Fe_2C_9]\}$ - and a guest  $\{Dy_{0.64}\}$ - substructure sharing their  $a$  and  $b$  lattice parameters but, with mismatch concerning  $c$ . As mentioned in [178], the thermodynamic stability of incommensurate composite crystal structures is achieved through the bonding interactions between atoms of two subsystems in more than one direction. Thus, the host and guest substructures of  $Dy_{5.64}[Fe_2C_9]$  have a common  $ab$  plane in order to achieve thermodynamic stability. The composite approach clearly gives the building principles of the crystal structure. The charge of the fairly rigid host structure defines the number of guest atoms for electroneutrality reasons and can be considered as the driving force for the modulation. Since the C–C bond order is connected to the resulting oxidation states of the Fe atoms, it is important to investigate the bonding situation of the  $C_2^{n-}$  units in detail. The XAS investigations show that the oxidation state of the Fe atoms in  $RE_{5.64}[Fe_2C_9]$  is greater than zero. Considering the C–C bond length and magnetic susceptibility data ( $Dy^{3+}$ ), a charge balanced ionic formula of the composite can be written as  $\{(Dy)^{3+}_{0.67}\}\{(Dy^{3+})_5[Fe^{2+}(C_2)_{4/2}][CFe^{1+}(C_2)_2]\}$ , reflecting the general trend to low valence states in carboferrates. The Mössbauer spectra recorded at room temperature show non-magnetic iron species which is consistent with the results of the magnetic susceptibility measurement. The ternary compound can be used in the future as a reference material for Mössbauer investigations of binary and ternary iron carbides. The compounds  $RE_{5.64}[Fe_2C_9]$  ( $RE = Y, Gd, Tb, Dy$ ) show paramagnetic behavior. Metal-like temperature dependence was observed for  $Y_{5.64}[Fe_2C_9]$  and  $Dy_{5.64}[Fe_2C_9]$ , while  $Gd_{5.64}[Fe_2C_9]$  and  $Tb_{5.64}[Fe_2C_9]$  show a semiconductor-like temperature dependence.

## 6 $\text{La}_{3.67}[\text{T}(\text{C}_2)_3]$ ( $T = \text{Fe}, \text{Ru}$ )

The crystal structures of  $\text{La}_{3.67}[\text{T}(\text{C}_2)_3]$  ( $T = \text{Fe}, \text{Ru}$ ) were previously reported by Jeitschko *et al.* [30] and are briefly discussed in *Section 2.2.2 and 2.2.3*. In this work, threefold superstructures for  $\text{La}_{3.67}[\text{Fe}(\text{C}_2)_3]$  and  $\text{La}_{3.67}[\text{Ru}(\text{C}_2)_3]$  were experimentally observed, and reinvestigation of the crystal structure was performed by powder X-ray and single crystal diffraction methods. The crystal structure of  $\text{La}_{3.67}[\text{Fe}(\text{C}_2)_3]$  was treated using a split atom model, while the superspace approach was used to determine and to describe the crystal structure of  $\text{La}_{3.67}[\text{Ru}(\text{C}_2)_3]$ .

### 6.1 Synthesis and phase analysis

Mixtures of La (Ames, 99.99 %), Fe (Alfa Aesar, 99.99%) or Ru (Alfa Aesar, 99.99%) and graphitic carbon (Chempur, 99.9%) were prepared in the molar ratio  $\text{La} : T : \text{C} = 4 : 1 : 6$ . The mixtures were cold-pressed into pellets using a hydraulic press (PERKIN ELMER 20 kN) and a 6 mm stainless steel die. The pellets were arc melted several times to improve the homogeneity of the samples. As cast samples were crushed in an agate mortar and analyzed by powder X-ray diffraction. A remaining part of the sample was wrapped in Ta-foil, sealed in evacuated fused silica ampoules, annealed at different temperatures (1173 K, 1273 K, 1373 K or 1473 K) for one week in a horizontal tube furnace and finally quenched in water. The optimal annealing temperature (concerning highest yields of the main phase) was determined to be 1173 K for  $\text{La}_{3.67}[\text{FeC}_6]$  and 1373 K for  $\text{La}_{3.67}[\text{RuC}_6]$ . The reaction product was grey with good crystallinity and block shaped crystals could be isolated from the surface of the crushed specimens. Attempts to obtain single phase materials as well as large single crystals suitable for physical property measurements, using the metal flux method as described in *Section 3.2*, failed. The metals Ga, In, Sn and Bi were used as fluxes. Changes of the temperature program and the molar ratios of the educt materials to the flux resulted in binary phases only. Further experiments using other fluxes should be done.

Flat sample holders with vaseline-coated Mylar foil were charged with the crushed and ground samples. A small amount of  $\text{LaB}_6$  as internal standard (SRM660a,  $a = 415.6916$  pm) was added to the samples in order to determine the unit cell parameters of the phases precisely. X-ray powder diffraction patterns were recorded on a Huber-Guinier camera G670 in the range  $10^\circ < 2\theta < 85^\circ$  with a step width of  $0.005^\circ$  using monochromatic  $\text{Cu K}\alpha_1$  radiation ( $\lambda = 154.059(1)$  pm) for  $\text{La}_{3.67}[\text{RuC}_6]$  and  $\text{Co K}\alpha_1$  radiation ( $\lambda = 178.896(1)$  pm) for  $\text{La}_{3.67}[\text{FeC}_6]$ . The diffraction patterns of the as-cast samples did not show the presence of  $\text{La}_{3.67}[\text{TC}_6]$ , indicating that these phases may melt incongruently. Nearly single-phase bulk materials were obtained after annealing. According to powder X-ray diffraction analysis the title compounds were obtained as majority phases, with well developed superstructure

reflections. A small number of very weak reflections ( $< 5\%$  of max. intensity) could not be identified, and most probably originated from minor trace phases (Figure 6.1).

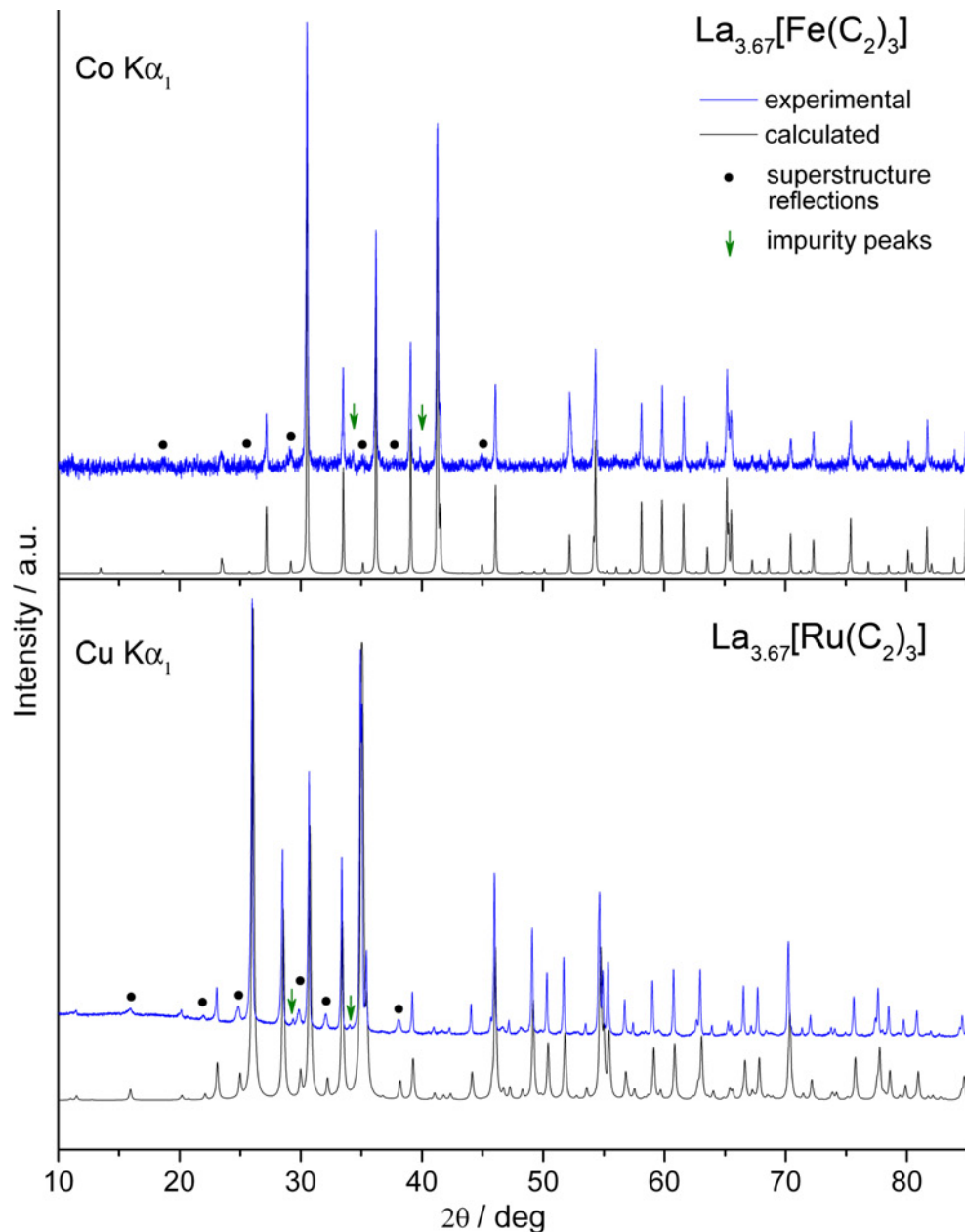
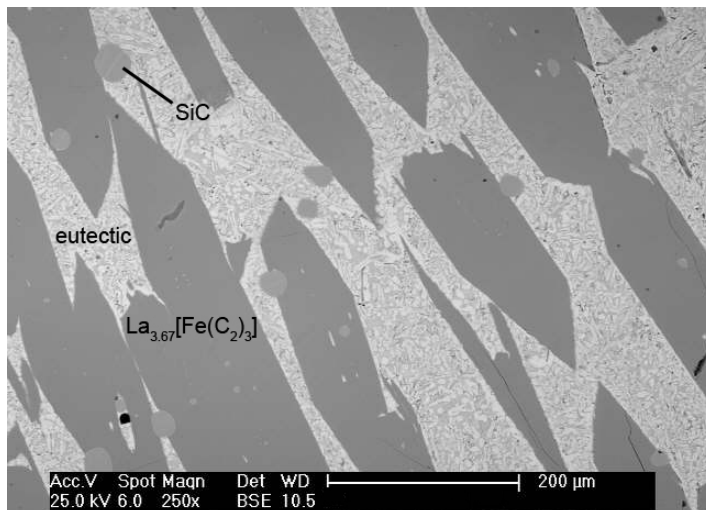


Figure 6.1: Experimental and calculated X-ray powder diffraction patterns of  $\text{La}_{3.67}[\text{T}(\text{C}_2)_3]$  ( $\text{T} = \text{Fe}, \text{Ru}$ ). The superstructure reflections are denoted by filled circles whereas the peaks of unidentified trace phases are marked with green arrows.

The unit cell parameters were determined by least-squares refinements of the peak positions obtained from powder X-ray diffraction pattern using the program WinCSD [157–159]. The lattice parameters are:  $a = 879.26(8)$  pm,  $c = 1604.59(15)$  pm for  $\text{La}_{3.67}[\text{FeC}_6]$  and  $a = 888.7(5)$  pm,  $c = 1612.7(4)$  pm for  $\text{La}_{3.67}[\text{RuC}_6]$ . These lattice parameters correspond to a 3-fold superstructure ( $c = 3c_0$ ) of the previously reported crystal structure [30].

Pieces of the bulk material with about 5 mm diameter were processed for metallographic

Figure 6.2: BSE image of a typical microstructure after prolonged heat treatment;  $\text{La}_{3.67}[\text{FeC}_6]$  is the primary phase and the fine matrix in between is composed of the title compound together with an unknown phase. After polishing some SiC particles were stick to the samples (marked on the image).



examinations as described in *Section 3.6*. *Figure 6.2* shows a BSE image of a typical microstructure containing large crystals of the  $\text{La}_{3.67}[\text{FeC}_6]$ . The space between the grains of the majority phase is filled by an unknown phase. The fine matrix is probably a remnant of a eutectic structure, which has partly survived even after prolonged heat treatments. The EDX analyses of the polished samples of  $\text{La}_{3.67}[\text{FeC}_6]$  as well as of single crystals of  $\text{La}_{3.67}[\text{RuC}_6]$  yielded the atomic ratio  $\text{La} : T = 3.6(1) : 1$ . No reliable determination of the chemical composition of the unknown phase was possible.

## 6.2 $\text{La}_{3.67}[\text{Fe}(\text{C}_2)_3]$

### 6.2.1 Crystal structure determination

Block-shaped single crystals were isolated from the surface of the samples under liquid paraffin in an Ar filled glove box. The selected specimens were mounted on  $\varnothing 0.1$  mm Lindemann glass capillaries and inserted into  $\varnothing 0.2$  mm glass capillaries which were then sealed using a hot Pt wire. Intensity data were collected on a Rigaku AFC7 diffractometer with Mercury CCD detector and graphite-monochromatized Mo  $\text{K}\alpha$  ( $\lambda = 71.069$  pm) radiation. The single crystal diffraction patterns clearly showed hexagonal symmetry with Laue group  $6/m$  with reasonable  $R(\text{int}) = 0.04$ . Indexing the diffraction spots gives a primitive hexagonal cell with weak superstructure reflections arising from a tripled  $c$ -axis, which is consistent with the lattice parameters obtained from powder diffraction patterns. The subcell parameters were the same as those reported in the reference [30]. After integration the data were corrected for Lorentz factor, polarization (LP) and absorption. Relevant crystallographic data and further details of data collection and structure refinements are listed in *Table 6.1*.

The crystal structure was solved by direct methods (SHELXS97) and refined by using the program package SHELXL97 [165]. Diffraction symmetry, Laue group and serial extinction conditions,  $l = 2n+1 \rightarrow 6_3$ -screw axes, give two possible space groups:  $P6_3$  (173) and  $P6_3/m$  (176). The E-statistics or the normalized structure factor statistics suggested that the structure

Table 6.1: Crystallographic data and details on data collection and structure refinement for La<sub>3.67</sub>[Fe(C<sub>2</sub>)<sub>3</sub>]<sup>†</sup>.

Chemical formula, <i>Z</i>	La <sub>3.67</sub> [Fe(C <sub>2</sub> ) <sub>3</sub> ], 6
Crystal system	hexagonal
Space group	<i>P</i> 6 <sub>3</sub> / <i>m</i> (no. 176)
Formula mass [g·mol <sup>-1</sup> ]	637.23
Radiation, $\lambda$ [pm]	Mo K $\alpha$ , 71.069
Temperature [K]	295
<i>a</i> [pm]	879.3(2)
<i>b</i> [pm]	1605.0(7)
<i>V</i> [pm <sup>3</sup> ·10 <sup>6</sup> ]	1074.5(6)
$\rho_{calc}$ [g·cm <sup>3</sup> ]	5.909
Crystal size [ $\mu$ m]	20 × 12 × 11
<i>T</i> <sub>min</sub> , <i>T</i> <sub>max</sub>	0.049, 0.077
<i>R</i> <sub>int</sub> .	0.0414
Scan	$\phi$ , $\omega$
$\theta$ -range [°]	2.54 - 33.79
<i>hkl</i> -range	-13 ≤ <i>h</i> ≤ 13 -13 ≤ <i>k</i> ≤ 12 -23 ≤ <i>l</i> ≤ 20
Extinction coefficient $\chi$ <sup>(a)</sup>	0.00030(9)
Absorption correction	multiscan
Absorption coefficient, $\mu$ [mm <sup>-1</sup> ]	23.28
Unique reflections / parameters	1387 / 60
<i>R</i> ( <i>F</i> <sub>o</sub> ) / <i>wR</i> ( <i>F</i> <sub>o</sub> <sup>2</sup> ) / <i>Goof</i> (all data)	0.044 / 0.075 / 1.19
max. / min. $\Delta\rho$ [e <sup>-</sup> / (10 <sup>6</sup> · pm <sup>3</sup> )]	5.42 / -7.45
<i>w</i> <sub>1</sub> / <i>w</i> <sub>2</sub> <sup>(b)</sup>	0 / 25.78

<sup>†</sup> Supplementary data are available from the FIZ, D-76344 Eggenstein-Leopoldshafen, Germany, e-mail crysdata@FIZ-karlsruhe.de, by quoting the depository number 419578

<sup>(a)</sup> *F*<sub>*c*</sub> is multiplied by  $k[1 + 0.001 \cdot x F_c^2 \cdot \lambda^3 / \sin(2\theta)]^{-1/4}$

<sup>(b)</sup>  $R = \Sigma(|F_o| - |F_c|) / \Sigma |F_o|$ ,  $wR = (\Sigma w(F_o^2 - F_c^2) / (\Sigma w(F_o^2)^2))^{1/2}$  with  $w = 1 / [\sigma^2(F_o^2) + (w_1 \cdot P)^2 + w_2 \cdot P]$  with  $P = (F_o^2 + 2F_c^2) / 3$

is centrosymmetric with 77% probability. Thus, the crystal structure of La<sub>3.67</sub>[Fe(C<sub>2</sub>)<sub>3</sub>] was refined in space group *P*6<sub>3</sub>/*m* (176) with residuals *R*1 = 0.044 and *wR*2 = 0.075 for 1387 unique reflections and 60 variables.

The unit cell contains 64 atoms distributed on 4 La, 2 Fe and 4 C crystallographic sites. The relationship between the subcell and the 3-fold superstructure is shown in *Figure 6.3*. In fact, the 4*e* site in the subcell should split into 3×4*e* sites in the maximal isomorphic subgroup *P*6<sub>3</sub>/*m* (*c* = 3*c*<sub>o</sub>) [226]. However, the refinement results only in two La positions at

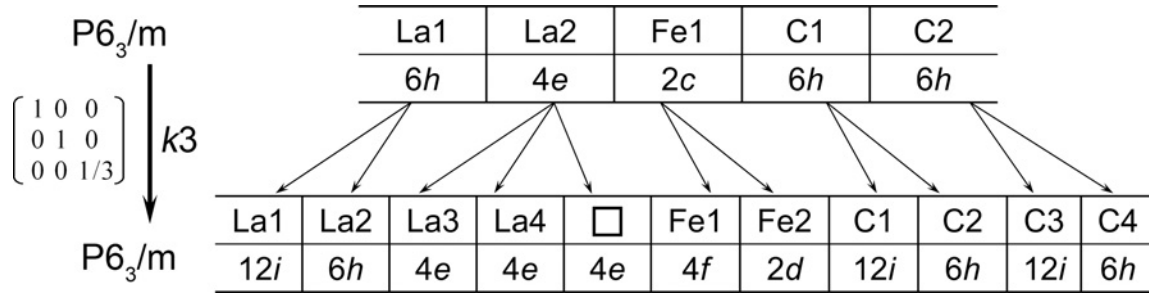


Figure 6.3: The substructure of  $\text{La}_{3.67}[\text{Fe}(\text{C}_2)_3]$  transforms to a 3-fold superstructure by a *klassen-gleiche* transformation of index 3. Splittings of the atomic sites during the  $k_3$  transformation are given.

$4e$  site, with nearly 50% occupancy. The third  $4e$  site is not occupied within the estimated standard deviations. The occupancy factors were refined in separate series of least-squares cycles for checking the correlation between partial occupancy and atomic displacement parameters. In the final cycles of the refinements all atoms were refined anisotropically with full site occupancy, except La3 and La4 whose occupancies were set to 0.5 and with the restriction to have equal atomic displacement parameters. The fractional atomic coordinates and anisotropic displacement parameters are given in *Tables 6.2* and *Tables 9.28*, respectively.

Table 6.2:  $\text{La}_{3.67}[\text{Fe}(\text{C}_2)_3]$ : Fractional atomic coordinates in the asymmetric unit and equivalent isotropic displacement parameters [ $10^4 \text{ pm}^2$ ]; estimated standard deviations are given in parentheses.

Atom	Site	Occ.	$x$	$y$	$z$	$U_{eq.}$
La1	12i	1	0.3935(1)	0.3344(1)	0.0845(1)	0.0088(1)
La2	6h	1	0.0632(1)	0.3988(1)	1/4	0.0087(1)
La3	4e	1/2	0	0	0.0223(1)	0.0102(3)
La4	4e	1/2	0	0	0.1900(1)	0.0105(3)
Fe1	4f	1	1/3	2/3	0.0826(1)	0.0075(3)
Fe2	2d	1	2/3	1/3	1/4	0.0086(5)
C1	12i	1	0.0240(13)	0.2771(13)	0.0849(5)	0.029(2)
C2	12i	1	0.1475(10)	0.4426(10)	0.0831(5)	0.0118(13)
C3	6h	1	0.2861(14)	0.2778(15)	1/4	0.0103(19)
C4	6h	1	0.4426(14)	0.2987(14)	1/4	0.0074(18)

## 6.2.2 Crystal chemistry

The crystal structure of  $\text{La}_{3.67}[\text{Fe}(\text{C}_2)_3]$  contains trigonal planar  $[\text{Fe}(\text{C}_2)_3]$  groups (*Figure 6.4a*) with  $\text{C}_2$  ligands bonded end-on to the iron atoms. The complex anions are surrounded by 9 La atoms located at the vertices of a tricapped trigonal prism (*Figure 6.4b*). The filled prisms are stacked along  $[001]$  sharing common triangular faces, thus forming an arrangement of infinite chains. Six chains around a sixfold axis are further connected via common faces to form a host framework containing hexagonal channels of carbon octahedra (*Figure*



6.5a). In total, the host framework contains two crystallographically independent Fe atoms at  $4f$  (Fe1) and  $2d$  (Fe2), two La atoms at  $12i$  (La1) and  $6h$  (La2) sites, and four C atoms at  $2 \times 12i$  (C1, C2) and  $2 \times 6h$  (C3, C4). All these sites are fully occupied and form a partial structure with chemical composition La<sub>3</sub>[Fe(C<sub>2</sub>)<sub>3</sub>]. This kind of host structure is also observed in closely related nitridometalates. In *Figure 6.5* the perspective view of a) La<sub>3.67</sub>[Fe(C<sub>2</sub>)<sub>3</sub>] and b) Ba<sub>3</sub>[FeN<sub>3</sub>] [197] along [001] is shown. Both structures contain trigonal planar Fe(L)<sub>3</sub> ( $L = \text{C}_2^{4-}, \text{N}^{3-}$ ) groups and form host frameworks containing hexagonal channels. In the case of La<sub>3.67</sub>[Fe(C<sub>2</sub>)<sub>3</sub>], the guest La atoms (La3 and La4) at the crystallographic  $4e$  sites are present in these channels while these channels are empty in case of Ba<sub>3</sub>[FeN<sub>3</sub>]. The total number of La atoms (La3 and La4) within the channel is four per supercell or  $4/3$  La per subcell. When comparing the host structure in the previously reported subcell [30] and the supercell of the present work, the only difference is given by minor atomic displacements. Therefore, the superstructure reflections mainly carry informations on the arrangement of the La atoms accommodated inside the channels.

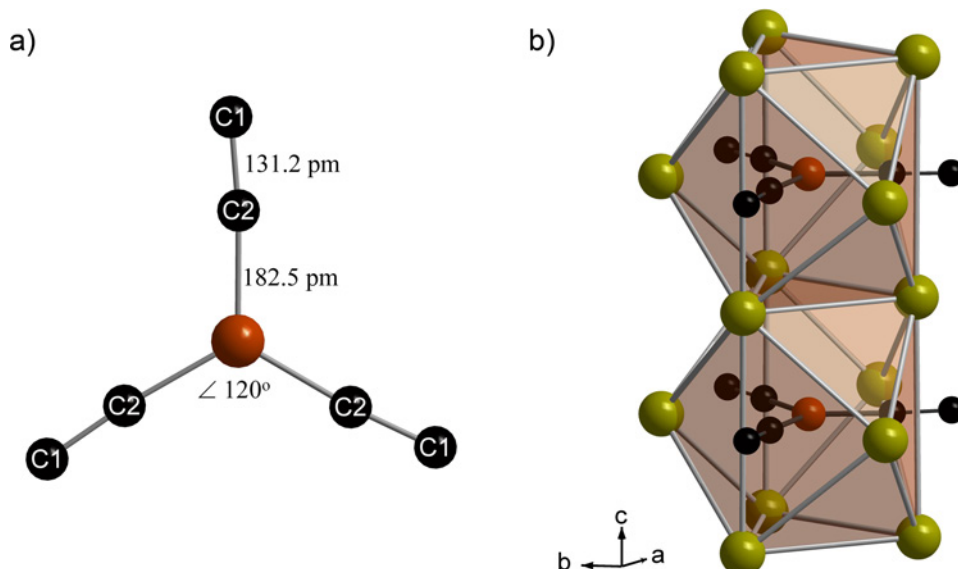


Figure 6.4: La<sub>3.67</sub>[Fe(C<sub>2</sub>)<sub>3</sub>]: Coordination around Fe, for Fe1 as a representative: a) the trigonal planar complex Fe(C<sub>2</sub>)<sub>3</sub>; b) two tricapped trigonal prisms (La) sharing common faces and enclosing the trigonal planar groups Fe(C<sub>2</sub>)<sub>3</sub>; the prisms form infinite chains along [001].

*Figure 6.6* shows different arrangements of La atoms at  $0, 0, z$  along [001]. With respect to the substructure, i.e., folding back the superstructure (*Figure 6.6a*), La3 and La4 atoms would occupy split positions with  $1/3$  probability at a  $4e$  site of the space group  $P6_3/m$  ( $a = a_0, c = 3c_0$ ). This is the highest possible site occupancy factor corresponding to maximum La content because only every third position at  $0, 0, z$  can be occupied due to distance constraints. Jeitschko *et al.* [30] obtained a site occupancy factor of  $0.32(3)$  from the refinement of the corresponding La position (La2 at  $4e$  in Table III of [30]). This occupancy yields the chemical composition La<sub>3.64</sub>[FeC<sub>6</sub>]. However, the authors decided to set the occupancy factor to the maximum value of  $1/3$ .

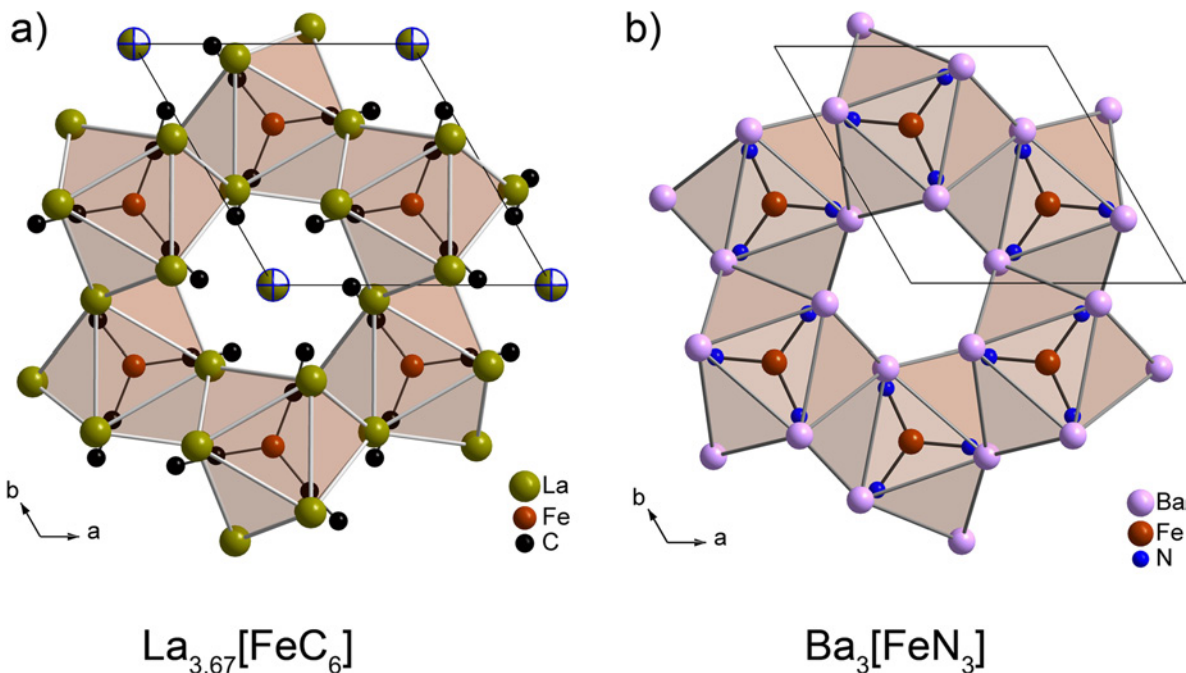


Figure 6.5: Comparison of the crystal structures of  $\text{La}_{3.67}[\text{Fe}(\text{C}_2)_3]$  with  $\text{Ba}_3[\text{FeN}_3]$ . a) Projection viewed along  $[001]$  showing the hexagonal channel stuffed by La atoms. b) Projection of the crystal structure viewed along  $[001]$  showing the empty hexagonal channel.

In the superstructure with the triple cell the two La sites, La3 and La4, are occupied with 50% probability each (Figure 6.6b), which again results in a maximum La content and the chemical formula  $\text{La}_{3.67}[\text{Fe}(\text{C}_2)_3]$ . Even in this supercell occupational disorder is still present. In case of a simultaneous occupation of neighboring sites the arrangement of La atoms along the chains would result in too short La–La distances. A chain of La atoms at maximum content is a priori determined by choosing a start atom and then extending the chain to infinity. Two different orientations with respect to the host structure are possible, denoted here as (+) and (-) (see Figure 6.6c). Both chains have the same local environment, thus interchain interactions will determine the orientation of all chains. Because the interchain distance of 879 pm is quite large, significant interactions between the chains are not expected. Therefore, one can assume that the orientations of the chains are uncorrelated, giving rise to the observed split atom density. In case that every second chain runs in opposite (-/+) directions (Figure 6.6c), the average electron density is consistent with the obtained superstructure model given in Figure 6.6b. Long range order of the chains would lead to a symmetry-break, which, however, has not been observed. For example, a ferromagnetic-like correlation (++++) would result in a simple ordered arrangement in space group  $P6_3$ , whereas antiferromagnetic-like correlations would give rise to a more complex problem. In case of the presence of long range order additional superstructure reflections must appear indicating even larger supercells. One can even anticipate complex domain structures. In general, the problem is similar as discussed for a triangular lattice Ising antiferromagnet. The ordered chain model as shown in Figure 6.6c indicates a Peierls-like distortion of the La-chains,

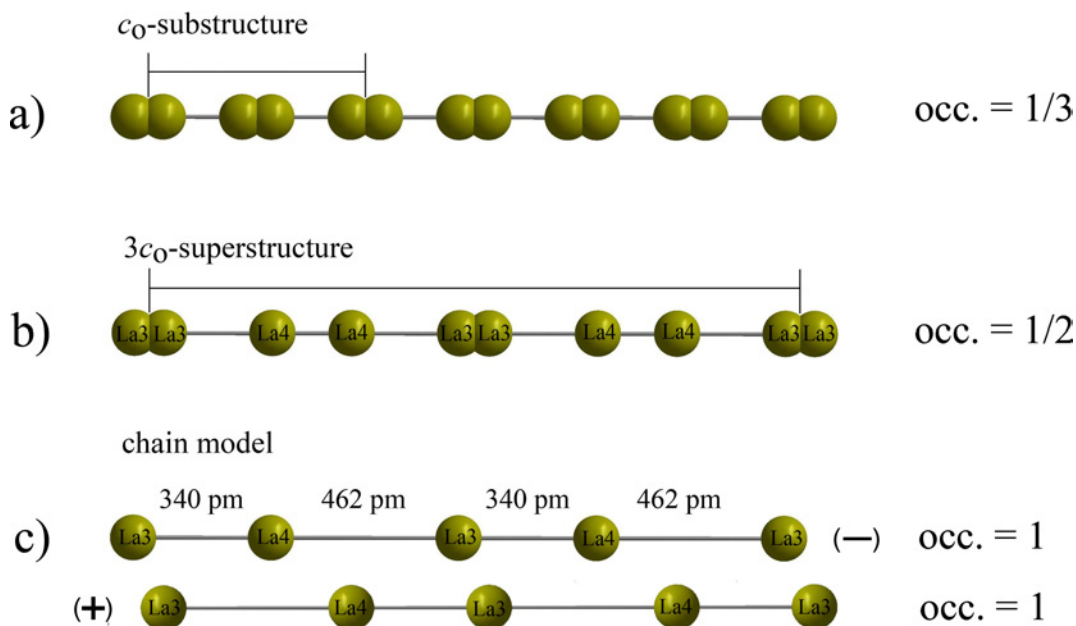


Figure 6.6: Different arrangements of La atoms in the hexagonal channels running along the  $c$  axis: a) split atom model of the substructure; b) split atom model of the superstructure; this model is interpreted as a superposition of ordered chains as shown in c): sequence of La atoms (La3, La4) with alternating short and long distances for two chains running in opposite (-/+) directions.

yielding physically favorable distances. This is more clearly shown in *Figure 6.7* with two La-chains running antiparallel and surrounded by carbon octahedra. Within each chain, pairs of La atoms occupy positions out of the centers of two neighboring carbon octahedra and alternate with one empty octahedron along [001].

As pointed out already, the chemical composition La<sub>3.67</sub>[Fe(C<sub>2</sub>)<sub>3</sub>] represents the La-rich border of a possible homogeneity range. Higher La contents would result in too short La–La distances. The volume per formula unit of La<sub>3.67</sub>[Fe(C<sub>2</sub>)<sub>3</sub>] of the triple cell is larger by about 1 Å<sup>3</sup> than the volume reported by Jeitschko *et al.* [30] for the subcell. This small volume discrepancy together with the slightly smaller occupancy factor and the not observed superstructure (triple cell) indicate a possible La deficiency in the crystal investigated by Jeitschko *et al.* Indeed, in the case of high quality crystals and at maximum La content one should observe the triple cell. However, a lower La content offers the possibility to arrange La atoms and vacancies in a disordered way within the chains, which then gives an additional contribution to the entropy of the system.

The coordination polyhedra around La are shown in (*Figure 6.8*). La1 and La2 are surrounded by six metal atoms (three La and three Fe; *Figure 6.8a*) forming a distorted mono-capped square pyramid. La3 and La4 are coordinated by seven La atoms in a form of a mono-capped distorted octahedron (*Figure 6.8b*). The La–La distances vary between 340.34 pm and 372.68 pm which is slightly smaller than 366 pm to 377 pm observed in the various modifications of the pure metal [227–230]. The La–Fe distances are quite large (321.9 pm to 358.47 pm) and slightly longer than observed in the crystal structure of La<sub>2</sub>Fe<sub>14</sub>C [231]

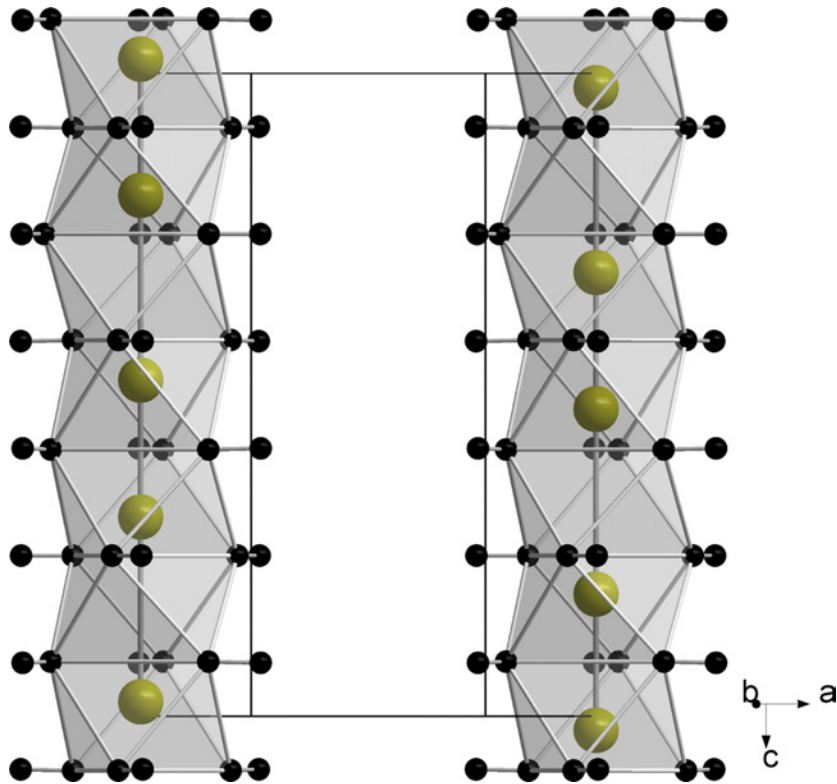


Figure 6.7:  $\text{La}_{3.67}[\text{Fe}(\text{C}_2)_3]$ : Two chains of face-sharing carbon octahedra enclosing the La chains (La at  $0, 0, z$ ) in + and - directions. Within each chain, pairs of La atoms occupy positions displaced relative to the centers of two neighboring carbon octahedra, and alternating with one empty octahedron.

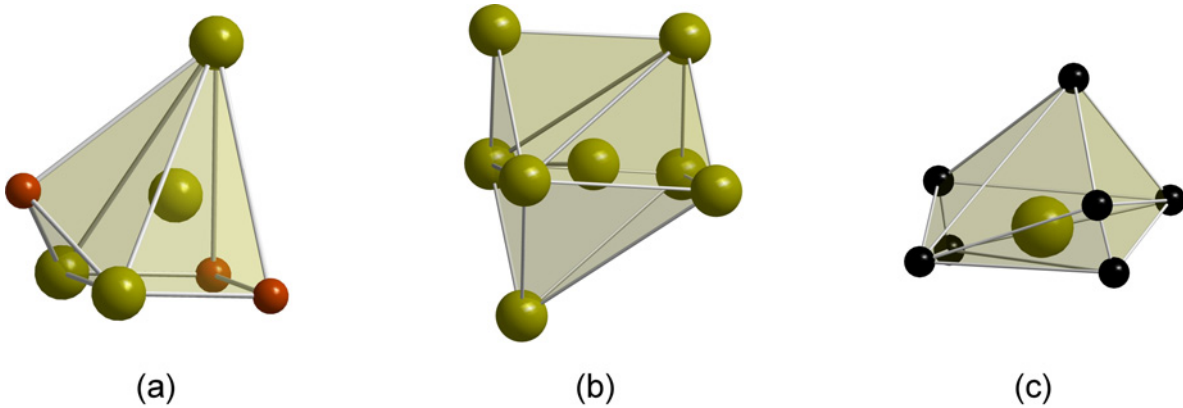


Figure 6.8:  $\text{La}_{3.67}[\text{Fe}(\text{C}_2)_3]$ : Coordination polyhedra around La: a) mono-capped square pyramid (coordination of La1 and La2) formed from three La and three Fe, b) mono-capped distorted octahedron (coordination of La3 and La4), c)  $\text{La}(\text{C}_2)_2\text{C}_3$  flattened monocapped octahedron (coordination of La1 and La2).

(306.4 pm to 339.5 pm). The La1 and La2 atoms have seven carbon neighbors, with  $d(\text{La1}-\text{C}) = 265.73$  pm to 281.53 pm and  $d(\text{La2}-\text{C}) = 273.45$  pm to 286.48 pm, respectively (Figure 6.8c). These distances are slightly shorter than the distances  $d(\text{La}-\text{C}) = 268.6$  pm to 297.3 pm in the crystal structure of  $\text{La}_2\text{C}_3$  [44]. The Fe–C distances at 182.47 pm to 183.65 pm are close to the respective values in the crystal structures of  $\text{Ho}_2\text{Fe}_{17}\text{C}_{3-x}$  [232] ( $d(\text{Fe}-\text{C}) = 175.7$  pm to 191.7 pm),  $\text{Th}_2\text{Fe}_{17}\text{C}_x$  [233] ( $d(\text{Fe}-\text{C}) = 191.4$  pm),  $\text{Er}_2\text{FeC}_4$  [29] ( $d(\text{Fe}-\text{C}) =$

196.8 pm), Lu<sub>2</sub>Fe<sub>14</sub>C [234] ( $d(\text{Fe}-\text{C}) = 198$  pm), and La<sub>2</sub>Fe<sub>14</sub>C [17] ( $d(\text{Fe}-\text{C}) = 203.5$  pm to 219.8 pm). The C–C distances (129.4 pm and 131.18 pm) are close to the double bond length in ethylene (134 pm). The interatomic distances in the crystal structure of La<sub>3.67</sub>[Fe(C<sub>2</sub>)<sub>3</sub>] are summarized in *Table 9.29*.

Assuming double bonds for the C<sub>2</sub>-pairs, the electropositive La donates all valence electrons to the [(FeC<sub>2</sub>)<sub>3</sub>] anions. Without significant metal–metal interactions one may assign the oxidation state +1 for Fe: (La<sup>3+</sup>)<sub>0.67</sub>La<sup>3+</sup><sub>3</sub>[Fe<sup>1+</sup>(C<sub>2</sub>)<sup>4-</sup><sub>3</sub>].

### 6.2.3 Phase stability and homogeneity range

Correlations between the occupancy of the La sites inside the channels on the 3-fold symmetry axes and the stability of these phases were studied by construction of various superstructure models (*Figure 6.9*), and by evaluation of their total energies using the DFT ab-initio code VASP [208, 209].

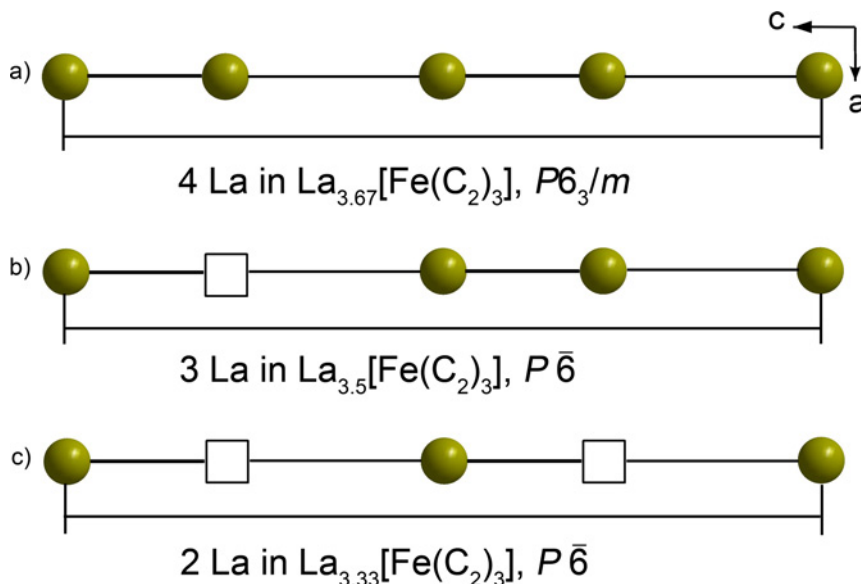


Figure 6.9: Different superstructure models for La arrangements within the channels of the crystal structure of La<sub>3.67</sub>[Fe(C<sub>2</sub>)<sub>3</sub>] used for total energy calculations. a) Structure model with fully occupied, La chains, b) superstructure with one vacancy and c) superstructure with two vacancies in the La chain.

We employed the projector-augmented wave generalization of the pseudo-potential approach with the Perdew-Wang generalized gradient approximation exchange-correlation functional [235]. The 5s, 5p, 5d and 6s orbitals for La, the 3d and 4s orbitals for Fe, and the 2s and 2p orbitals were treated as valence states. Each model was relaxed non-magnetically with respect to atom positions, cell shape and volume, until the maximal force on every atom in the cell was less than 0.05 eV/atom. The result of the calculations show: *i*) La<sub>22</sub>[Fe<sub>6</sub>C<sub>36</sub>] (La<sub>3.67</sub>[FeC<sub>6</sub>],  $Z = 6$ , *Figure 6.9a*) is the La-richest stable structure within the homogeneity range with fully occupied La atoms ordered as Peierls-like pairs inside the hexagonal channel, confirming the results of the crystal structure refinements. Neighboring chains are running

in the crystal structure either parallel or antiparallel, as already described in *Section 6.2.2*. Parallel orientation of the chains of La pairs is energetically more favorable than an antiparallel arrangement as shown in *Figure 6.7*. However, due to the minuscule difference in energy an equilibrium state should be difficult to obtain; *ii*)  $\text{La}_{21}[\text{Fe}_6\text{C}_{36}]$  (*Figure 6.9b*) is stable at 0 K while  $\text{La}_{20}[\text{Fe}_6\text{C}_{36}]$  (*Figure 6.9c*) with lower occupancy of the 4e site by La atoms becomes unstable with respect to the competing compounds in the ternary phase diagram. These results strongly support a small homogeneity range between  $\text{La}_{21}[\text{Fe}_6\text{C}_{36}]$  and  $\text{La}_{22}[\text{Fe}_6\text{C}_{36}]$  ( $\text{La}_x\text{La}_3[\text{FeC}_6]$ ,  $0.5 < x < 0.67$ ) at high temperature and extending down to low temperatures.

#### 6.2.4 Electronic band structure and chemical bonding analysis

The electronic structure of the  $\text{La}_{3.67}[\text{Fe}(\text{C}_2)_3]$  series was calculated using the self-consistent scalar relativistic TB-LMTO-ASA method [210] within the local (spin) density approximation (L(S)DA) [211] to the DFT. The chemical bonding was examined within the framework of crystal orbital Hamilton population (COHP) analysis [133].

The total and projected density of states (DOS) and the band structures without spin polarization are displayed in *Figure 6.10* and the crystal orbital interactions (COHP) in *Figure 6.11*. For the calculations we used two optimized superstructure models, which were relaxed using the VASP code as described above: 1)  $\text{La}_{22}[\text{Fe}_6\text{C}_{36}]$ , ( $P6_3/m$ ,  $a = 879.26(8)$  pm,  $c = 1604.59(15)$  pm), the La-richest composition within the homogeneity range with fully ordered La sites containing 4 La atoms within the hexagonal channel and 2)  $\text{La}_{20}[\text{Fe}_6\text{C}_{36}]$  ( $P\bar{6}$ ,  $a = 879.3$  pm,  $c = 1070$  pm), the La-poorest phase with 2 La atoms within the channel. We used the 5s, 5p, 5d and 6s orbitals of La, the 3d, 4s orbitals of Fe and the 2s and 2p orbitals of C as the basis set; the 6p orbital of La, the 4p of Fe, and the 3d of the C atoms were downfolded. For each model we kept the atomic radius and number of empty spheres similar. The calculations for  $\text{La}_{22}[\text{Fe}_6\text{C}_{36}]$  reveal that the compound is a metal with a sharp pseudo band gap of ca. 0.9 eV just below the Fermi level. The band structure along all directions display bands with relatively small dispersion up to  $E_F$ , indicating high localization of the orbitals. In the primitive cell there are 36 carbon atoms corresponding to 18  $\text{C}_2$ -dimers. The bands between -15 eV and -13 eV and between -9 eV and -7 eV can be assigned to bonding and antibonding C–C  $\sigma$  orbitals, respectively. These orbitals do not contribute to the higher valence band and contain  $36e^-$ . The states derived from the C 2p orbitals are also clearly separated; the bonding C–C  $\pi$  bands lie in the range of -7 eV to -3.3 eV. Antibonding  $\pi^*$  bands strongly hybridize with La 5d and Fe 3d orbitals and extend from -3.3 eV to the band gap below the Fermi energy. This region contains  $252e^-$ . The DOS at  $E_F$  is characterized by La 5d bands with small contributions of C–C  $\pi^*$  and Fe 3d states. Summing up to  $E_F$ , we can count  $258e^-$ , with  $6e^-$  predominantly belonging to the La 5d orbitals. In the case of  $\text{La}_{20}[\text{Fe}_6\text{C}_{36}]$ , the primitive unit cell contains a total of  $252e^-$ , however the compound still has metallic and not semiconducting character as expected. Instead of a shift of  $E_F$  down-



wards to the band gap, the sharp peaks around the Fermi level become broader leading to a more narrow pseudo gap. The band structure of this compound remains almost the same as that observed for La<sub>22</sub>[Fe<sub>6</sub>C<sub>36</sub>] up to the pseudo gap. The main difference is that the La 5*d* bands get broader around the Fermi level in the directions  $\Gamma \rightarrow K$  (1/3, 1/3, 0) and  $\Gamma \rightarrow M$  (1/2, 0, 0), representing the directions towards the surrounding La atoms of the host structure. The results show that slight deficiencies on the La sites within the homogeneity range do not significantly influence the transport properties.

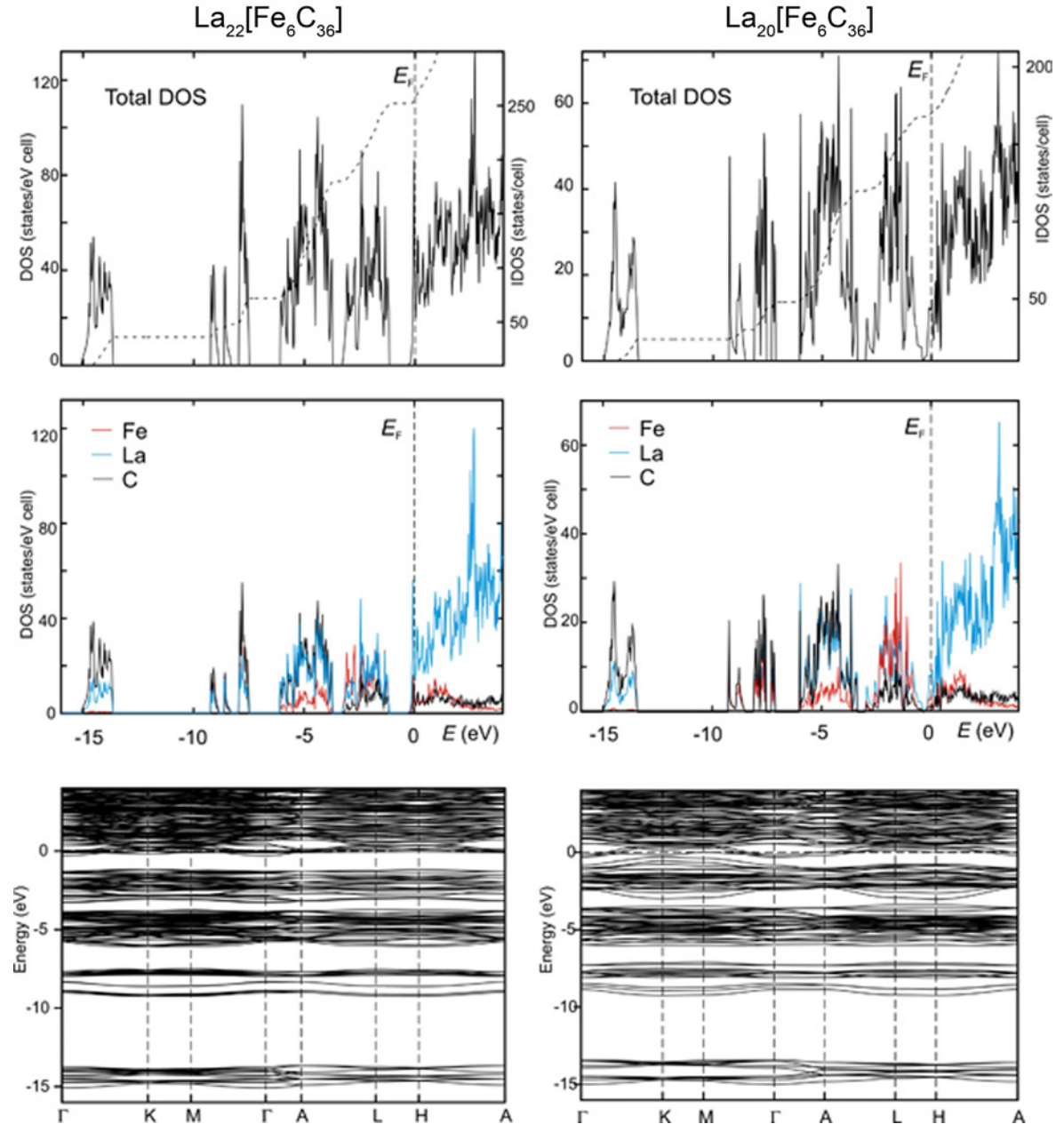


Figure 6.10: Total and atom-projected DOS and band structure for La<sub>22</sub>[Fe<sub>6</sub>C<sub>36</sub>] (left) and La<sub>20</sub>[Fe<sub>6</sub>C<sub>36</sub>] (right).

The chemical bonding situation is analyzed for the La-rich model La<sub>22</sub>[Fe<sub>6</sub>C<sub>36</sub>] by the COHP method. *Figure 6.11* shows five orbital interactions: Fe–C, La–C, C–C, La–Fe, and

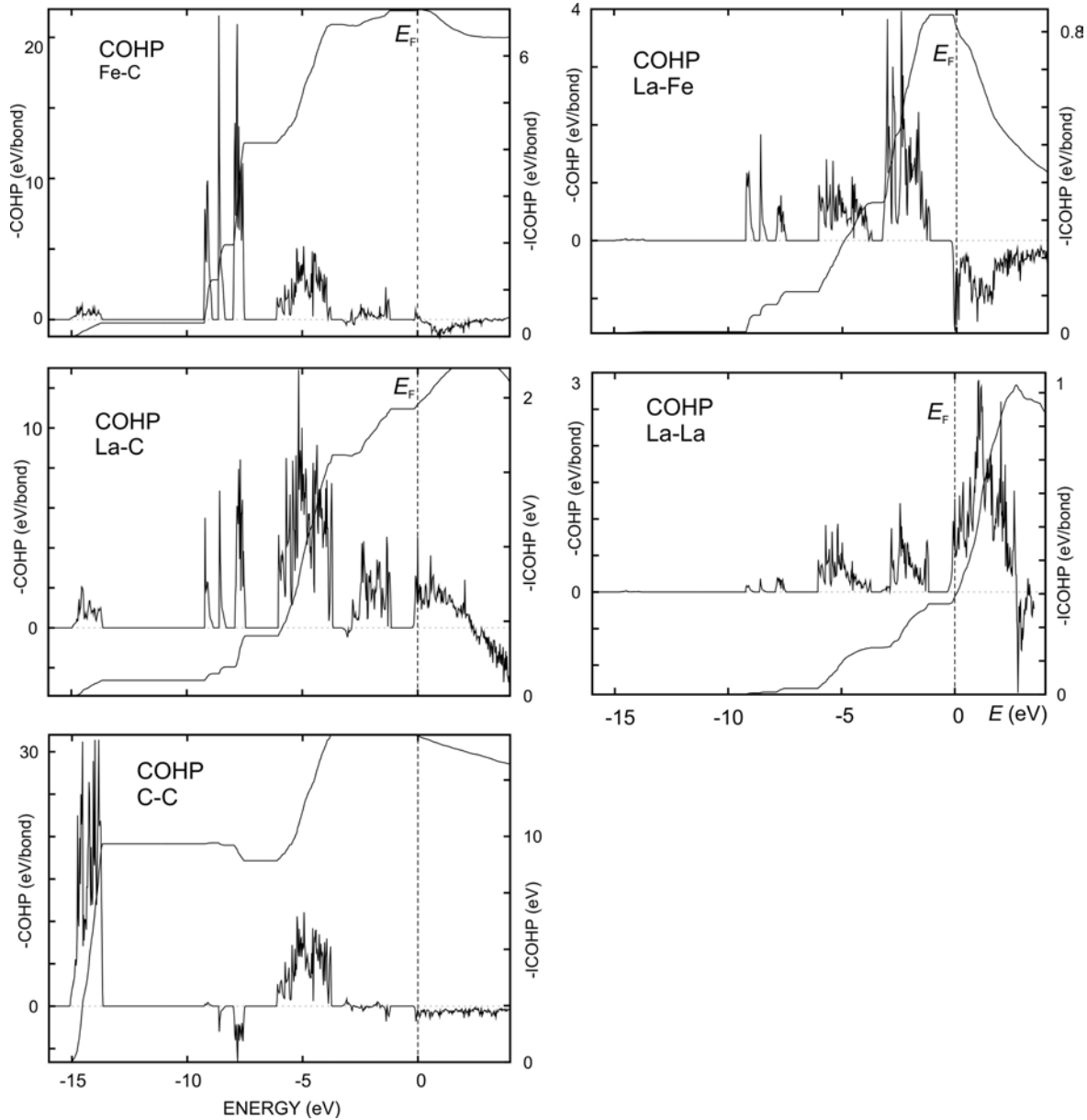


Figure 6.11: COHP and integrated COHP (ICOHP) diagrams for selected interactions in the crystal structure of  $\text{La}_{22}[\text{Fe}_6\text{C}_{36}]$ .

La—La. The integrated ICOHP values are given in *Table 6.3*. In order to find out which kind of interactions are important for the whole crystal structure, we not only considered the average ICOHP values per bond, but also the ICOHP values weighted by the bond multiplicities per unit cell.

The covalent bond in the  $\text{C}_2$  carbon pair with an  $-\text{ICOHP}_{\text{aver.}}$  value of 16.7 eV/bond is the strongest, followed by Fe—C bonds with  $-\text{ICOHP}_{\text{aver.}} = 7.2$  eV/bond. Both are completely exhausted at  $E_F$ . In contrast, the La—C bonds with  $-\text{ICOHP}_{\text{aver.}}$  value of 1.7 eV/bond display obviously weaker covalent bonding interactions compared to Fe—C bonds. They are not completely saturated and reveal a bonding character even above  $E_F$ . Metal-metal bonding interactions are significantly weaker but not negligible. La—Fe interactions with  $-\text{ICOHP}_{\text{aver.}}$



Table 6.3: La<sub>3.67</sub>[Fe(C<sub>2</sub>)<sub>3</sub>]: Selected interatomic distances (pm, denoted as  $d$ ), multiplicities per unit cell (denoted as  $n$ ) of the superstructure and integrated crystal orbital Hamilton populations per bond (-ICOHP [eV/bond]).

Bond	$n$	$d^\dagger$	-ICOHP	Bond	$n$	$d^\dagger$	-ICOHP	
La–C	x 12	265.0	2.32	Fe–C	x 12	177.0	7.50	
	x 12	273.4	1.20		x 6	181.3	6.46	
	x 12	275.6	1.47		-ICOHP <sub>aver.</sub> = 7.15			
	x 12	278.8	1.04		La–La	x 12	338.5	0.29
	x 12	280.1	1.14			x 2	365.6	0.45
	x 12	282.7	0.90			x 12	373.0	0.33
	x 12	290.2	1.05	x 12		361.5	0.18	
	x 12	269.5	1.22	x 2		334.1	0.18	
	x 12	274.9	1.16	-ICOHP <sub>aver.</sub> = 0.27				
	x 6	276.0	1.38	La–Fe		x 12	324.4	0.84
	x 6	278.5	1.14			x 6	317.5	0.66
	x 12	282.3	1.13		-ICOHP <sub>aver.</sub> = 0.77			
	x 6	288.7	1.65		C–C	x 12	133.5	17.72
	x 6	267.5	1.68	x 6		135.5	14.84	
x 12	274.4	1.46	-ICOHP <sub>aver.</sub> = 16.76					
-ICOHP <sub>aver.</sub> = 1.66								

<sup>†</sup> Note: Atomic coordinates were relaxed during the calculations. Thus, the interatomic distance given in this table have small differences compared with those from Table 9.29 (obtained from crystal structure refinement results).

value of 0.8 eV/bond are clearly more covalent than the very weak La–La interactions with -ICOHP<sub>aver.</sub> = 0.3 eV/bond. The La–Fe interactions, however, become strongly antibonding at the Fermi level. The COHP analyses tell us that the Fe–C covalent bonds are 4.2 times stronger than La–C bonds and the ratio of ICOHP's between total metal-carbon and metal-metal interaction is ca. 8.1 (ICOHP(M–C) / ICOHP(M–M) = (7.2 eV + 1.7 eV) / (0.8 eV + 0.3 eV) = 8.1). Two criteria for the presence of complex anions using the COHP method are discussed [9]: 1) ICOHP(*T*–C) should be much larger than ICOHP(*RE*–C), and 2) the ratio of ICOHP(*M*–C) / ICOHP(*M*–M) is larger than 3. According to these criteria, La<sub>22</sub>[Fe<sub>6</sub>C<sub>36</sub>] can be described as a compound containing complex anions, which are characterized by covalent Fe–C interactions together with Coulomb interactions to the La cations.

### 6.2.5 Mössbauer spectroscopic studies

The samples were prepared and measured according to the procedure described in Section 3.8. Figure 6.12 shows the Mössbauer spectrum of La<sub>3.67</sub>[Fe(C<sub>2</sub>)<sub>3</sub>] measured at room temperature.

The measured spectrum can be fitted with two doublets, which indicates two different Fe positions. From crystal structure refinement results we know that the multiplicity of the Fe1

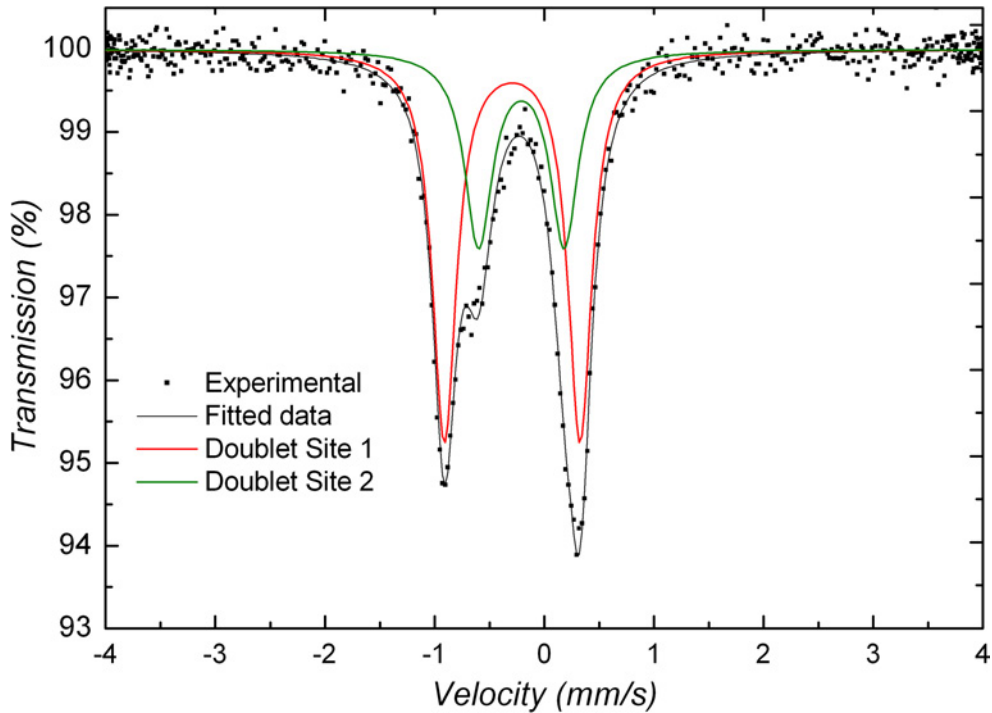


Figure 6.12: The Mössbauer spectrum of  $\text{La}_{3.67}[\text{Fe}(\text{C}_2)_3]$  measured at room temperature. The measured spectrum (dots) is fitted (black) with two subspectra (red and green).

is two and that of Fe2 is four. The ratio of the multiplicities is given by the area fraction of the respective subspectrum. The comparison of the multiplicity of the Fe1 and Fe2 sites in the crystal structure of  $\text{La}_{3.67}[\text{Fe}(\text{C}_2)_3]$  and the area fractions of the Mössbauer subspectra let us assume that doublet 1 (red) can be assigned to Fe2 and doublet 2 (green) to Fe1. The Mössbauer parameters obtained from the fit are listed in *Table 6.4*.

Table 6.4: Mössbauer parameters of  $\text{La}_{3.67}[\text{Fe}(\text{C}_2)_3]$ : Isomer shift (IS) [mm/s] relative to  $\alpha$ -Fe, quadrupole splitting ( $\Delta E_Q$ ) [mm/s], half width ( $\Gamma/2$ ) [mm/s], and relative area (A) [%] of the subspectra; estimated standard deviations are given in brackets.

Subspectra	Assignment	IS	$\Delta E_Q$	$\Gamma/2$	A
1 (red)	Fe2	0.1820(29)	1.2369(67)	0.1319(54)	63.4(31)
2 (green)	Fe1	0.0980(50)	0.781(16)	0.154(11)	36.6(30)

According to the crystal structure refinement results, both Fe1 and Fe2 have the same local environment,  $3 \text{C}_2 + 9 \text{La}$  atoms (see *Section 6.2.2*). However, all interatomic distances for Fe2 are slightly longer than those for Fe1,  $d(\text{Fe1}-\text{C}_2) = 182.47(1)$  pm,  $d(\text{Fe2}-\text{C}_4) = 183.65(1)$  pm and  $\text{Fe}-\text{La}$  ( $d(\text{Fe1}-\text{La}) = 346.72(1)$  pm,  $d(\text{Fe2}-\text{La}) = 346.89(1)$  pm). Because of differences in bond length, the nucleus of a Fe1 atom will experience a slightly different electric field than the nucleus of a Fe2 atom. This explains the appearance of two subspectra in the Mössbauer spectrum of  $\text{La}_{3.67}[\text{Fe}(\text{C}_2)_3]$ .

### 6.2.6 X-ray absorption spectroscopic studies

The Fe- $K$  threshold of  $\text{La}_{3.67}[\text{Fe}(\text{C}_2)_3]$  was measured at the synchrotron beamline  $E4$  at HASYLAB/DESY in Hamburg, with metallic iron as a reference material. *Figure 6.13* shows the XAS spectrum of  $\text{La}_{3.67}[\text{Fe}(\text{C}_2)_3]$ .

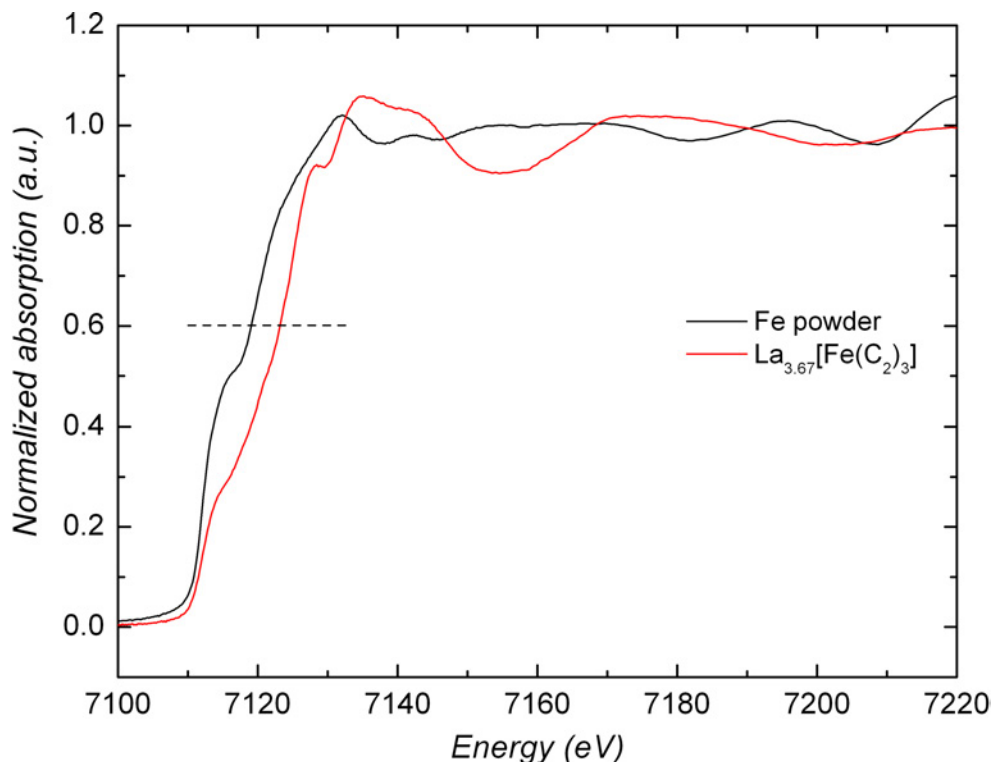


Figure 6.13: Normalized XAS spectrum of  $\text{La}_{3.67}[\text{Fe}(\text{C}_2)_3]$ . The spectrum is compared with the spectrum of metallic iron.

The data processing was done as described in *Section 4.9*. In this case, the XANES region again consists of main edge and pre-edge peaks. The lack of centrosymmetry in the coordination of Fe atoms in the complex anion could explain the appearance of the pre-edge peak. On the other hand,  $\text{La}_{3.67}[\text{Fe}(\text{C}_2)_3]$  is characterized as a bad-metal, which means that some  $d$ - $p$  mixing at the Fermi level occurs, thus the pre-edge peak can be assigned to the  $1s \rightarrow 3d$  transition [218–220]. As discussed in *Section 4.9*, the shape of the XAS spectra might indicate a higher filling of  $3d$  states, corresponding to a lower oxidation state of Fe atoms in  $\text{La}_{3.67}[\text{Fe}(\text{C}_2)_3]$ . The Fe  $K$ -edge threshold, determined at 0.6 of the full jump of the normalized curve, equals to 7123 eV, and again gives a positive energy shift,  $\Delta E = 7123 - 7112 = 11$  eV, with respect to the element Fe. This means that the Fe atoms in  $\text{La}_{3.67}[\text{Fe}(\text{C}_2)_3]$  are positively charged.

### 6.3 $\text{La}_{3.67}[\text{Ru}(\text{C}_2)_3]$

#### 6.3.1 Crystal structure determination

Prismatic single crystals of about  $20 \times 20 \times 80 \mu\text{m}$  in size were isolated from the annealed sample under liquid paraffin in an Ar filled glove box, mounted on glass fibres and sealed in Lindemann glass capillaries ( $\varnothing 0.2\text{mm}$ ) (Figure 6.14).

X-ray single crystal measurements were carried out on an image plate diffractometer IPDS-2 (Stoe Cie., Darmstadt, Germany) with Mo  $K\alpha$  ( $\lambda = 71.069 \text{ pm}$ ) radiation at room temperature. The diffraction symmetry revealed the Laue group  $6/m$ . Figure 6.15 shows the reciprocal layer  $2kl$ . The diffraction pattern clearly reveals a threefold superstructure of the previously reported unit cell of  $\text{La}_{3.67}[\text{Ru}(\text{C}_2)_3]$  [30]. As mentioned before, in this case the structure was treated as an one-dimensional modulated structure. The weak superstructure reflections along  $c^*$ , marked by green circles in Figure 6.15, were regarded as satellite reflections. Thus, the components of the modulation wave vector  $q$ , with respect to the reciprocal lattice of the average structure, are  $\sigma_1 = 0$ ,  $\sigma_2 = 0$  and  $\sigma_3 \neq 0$ . Details on data collection and structure refinements are given in Table 6.5.



Figure 6.14: A single crystal of  $\text{La}_{3.67}[\text{Ru}(\text{C}_2)_3]$  mounted on a glass capillary.

The determination and refinement of the modulation wave vector, as well as the data reduction including Lorentz and polarization factor correction was performed using the IPDS software package X-AREA [163]. The  $q$  vector was determined to be  $(0, 0, 0.323(1))$ . Since this value is close to  $1/3$ , it is difficult to decide within the resolution of the measurement whether the wave vector is commensurate (threefold superstructure) or incommensurate with the average crystal structure. For this reason, the data were integrated for both, the commensurate and incommensurate cases. In the commensurate case the modulation wave vector  $q$  was taken as  $q = 1/3 c^*$  and the data were integrated only with first order satellite reflections ( $m = \pm 1$ ) besides the main reflections. In the incommensurate case ( $q = 0.323c^*$ ), the second order satellites were also taken into account ( $m = \pm 1, \pm 2$ ). By using the refined crystal shape [236], absorption corrections for the main and satellite reflections were applied using the program XSHAPE [236]. The structure refinements of the modulated structure were carried out using JANA2006 [161]. The Laue group,  $6/m$ , and the reflection conditions  $(00lm, l + m = 2n)$  suggest the (3+1)D superspace group  $P6_3/m(00g)s_0$  [237], giving an internal residual value  $R_{int}$  of 2.2%. The structure solution was performed using the charge flipping algorithm SUPERFLIP [166] integrated in the program package JANA2006. The general strategy for the

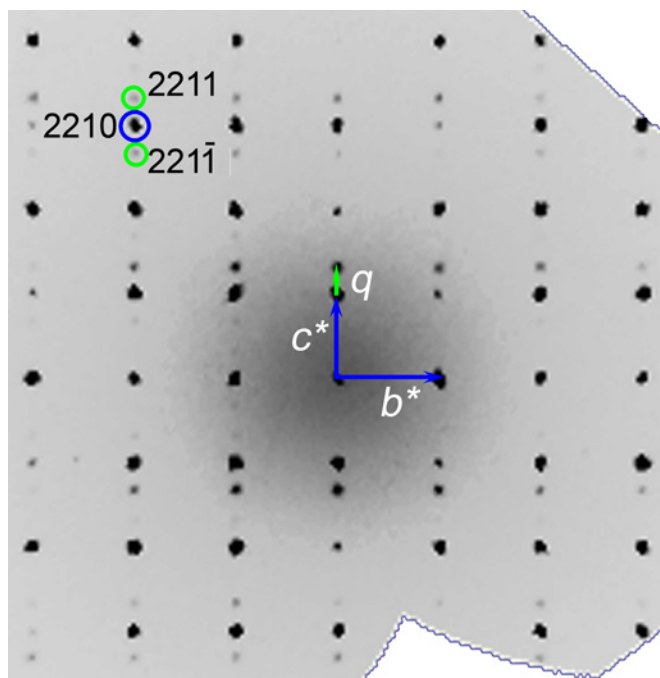


Figure 6.15:  $\text{La}_{3.67}[\text{Ru}(\text{C}_2)_3]$ : Reciprocal layer  $2kl$ . The blue arrows mark the reciprocal basis vectors of the average structure. The modulation wave vector  $q$  is denoted by the green arrow. The main reflection 2210 with its satellite reflections 2211 and  $221\bar{1}$  are marked with blue and green circles, respectively.

refinement was: *i*) to achieve a good fit for the average structure model using only the main reflections. As for  $\text{La}_{3.67}[\text{Fe}(\text{C}_2)_3]$ , the crystal structure contains one partially occupied La position at a  $4e$  site (La2); *ii*) to introduce the modulation functions to the crystal structure by using all reflections. The structure refinements started by introducing a modulation function for the occupational modulation of the La2 sites and were improved by adding one displacive modulation wave for each atom. The crystal structure of  $\text{La}_{3.65}[\text{Ru}(\text{C}_2)_3]$  shows both occupational and positional modulations. Finally, the modulations of the anisotropic displacement parameters (ADP) of all atoms were modeled by one harmonic wave. The refinement of the commensurately modulated structure converged to residuals of  $R1 = 4.9\%$  for all reflections ( $R1 = 2.6\%$  for the main reflections,  $R1 = 11.1\%$  for the first order satellites; only one modulation wave along  $q$  was implemented). Two different functions can be used to describe the occupational modulation : 1) a simple harmonic function or 2) a special modulation function such as Crenel and saw-tooth functions. The refinement using a Crenel function for the occupational modulation of the La2 sites resulted in a higher value of  $R_{obs} = 7.1\%$  for the observed reflections ( $R_{obs} = 3.9\%$  for main reflections and  $R_{obs} = 14.8\%$  for first order satellites). In addition, the remaining maximum electron density calculated from difference Fourier maps was about  $5.73 \text{ e}^-/\text{\AA}^3$ , which is rather high compared to the value of the harmonic refinement ( $1.78 \text{ e}^-/\text{\AA}^3$ ). Refinements using a saw-tooth function were unstable. Thus, the observed electron density is best described with simple harmonic functions. After each cycle of the refinements the contour map of the observed electron density was drawn in order to judge

Table 6.5: Crystallographic data and details on data collection and structure refinements of  $\text{La}_{3.65}[\text{Ru}(\text{C}_2)_3]^\dagger$ .

		Average structure data	
Chemical formula, $Z$	$\text{La}_{3.65}[\text{Ru}(\text{C}_2)_3], 2$		
Crystal system	hexagonal		
Space group	$P6_3/m$ (no. 176)		
Formula mass [ $\text{g}\cdot\text{mol}^{-1}$ ]	683		
Radiation, $\lambda$ [pm]	Mo $K\alpha$ , 71.069		
Temperature [K]	295		
$a$ [pm]	887.9(2)		
$b$ [pm]	535.6(2)		
$V$ [ $\text{pm}^3\cdot 10^6$ ]	365.7(6)		
$\rho_{\text{calc}}$ [ $\text{g}\cdot\text{cm}^3$ ]	7.31		
Crystal size [ $\mu\text{m}$ ]	$20 \times 20 \times 80$		
$T_{\text{min}}, T_{\text{max}}$	0.5577, 1.0		
$R_{\text{int}}$	0.0414		
$\theta$ -range [ $^\circ$ ]	2.57 - 32		
Scan	$\phi, \omega$		
$hkl$ -range	$-13 \leq h \leq 13$ $-13 \leq k \leq 12$ $-8 \leq l \leq 6$		
Absorption correction	multiscan		
Absorption coefficient, $\mu$ [ $\text{mm}^{-1}$ ]	22.9		
	Commensurate	Incommensurate	
Superspace group	$P6_3/m(00g)s0$		
Modulation wave vector	$q = 1/3 c^*$	$q = 0.323 c^*$	
Unique reflections / parameters	1098 / 63	1806 / 93	
$R1 / wR2 / \text{GooF}$ (all data)	0.0488 / 0.0635 / 1.71	0.0509 / 0.0675 / 1.72	
$R1 / wR2$ (all main)	0.0256 / 0.0454	0.0261 / 0.0493	
$R1 / wR2$ (all 1st order satellite)	0.1111 / 0.1027	0.0824 / 0.0858	
$R1 / wR2$ (all 2nd order satellite)		0.0860 / 0.0979	
max. / min. $\Delta\rho$ [ $\text{e}^- / (10^6 \cdot \text{pm}^3)$ ]	1.76 / -1.38	4.70 / -4.38	

<sup>†</sup> Further details of the crystal structure investigation are available from the Fachinformationszentrum Karlsruhe, 76344 Eggenstein-Leopoldshafen, Germany (fax: +49-7247-808-666; email: crysdata@fiz-karlsruhe.de) on quoting the depository number CSD-420969.

whether the selected modulation parameters properly describe the electron density or not. *Figure 6.16* shows that the discontinuous electron density corresponding to the La2 atoms can be well fitted by using commensurate harmonic functions.

In the final refinement step of the commensurate modulation, three different origins ( $T_0 =$

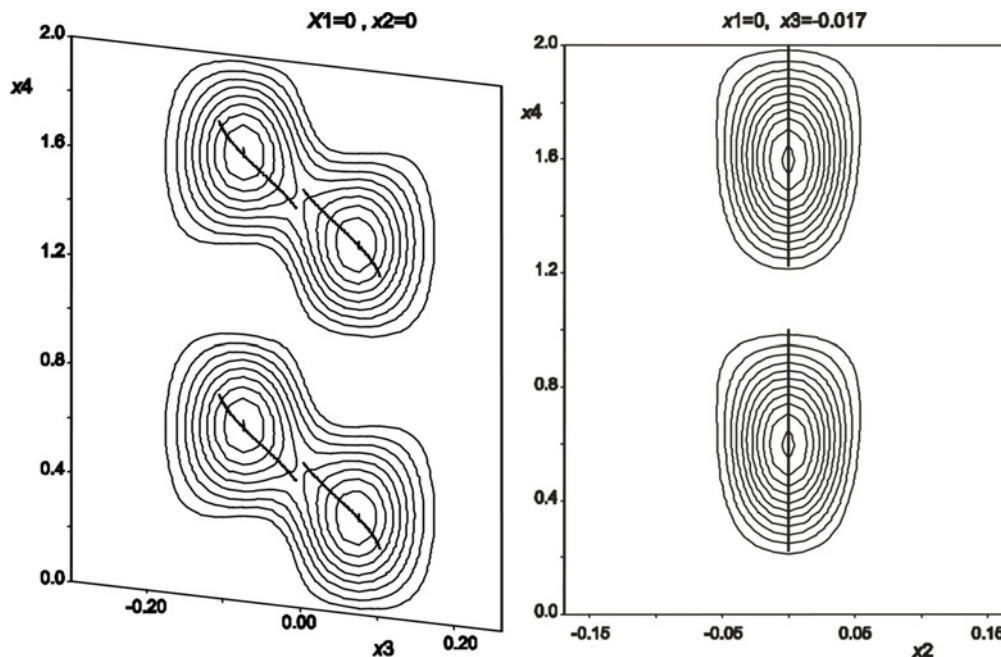


Figure 6.16: La<sub>3.67</sub>[Ru(C<sub>2</sub>)<sub>3</sub>]: Fourier maps of the commensurate structure:  $x_3 - x_4$  (left) and  $x_2 - x_4$  (right) sections for La2 atoms; the line on the contour shows the modulation function of La2. Contour lines represent constant electron density at intervals of 10% of the maximum density.

0, 1/3 and 2/3) of the modulation were tested and the best fit was achieved for a model with  $T_0 = 0$  associated with superspace group symmetry  $P6_3/m(00g)s0$ . In case of incommensurate modulation two modulation waves were used to better describe the electron density, which is related to the presence of second order satellite reflections. The refinement converged to residuals  $R1 = 5.1\%$  for all measured reflections,  $R1 = 2.6\%$  for main reflections,  $R1 = 8.2\%$  for first order satellites and  $R1 = 8.6\%$  for second order satellites. The incommensurate model shows lower  $R$  values for the satellite reflections, although the electron density is better fitted with the commensurate model, used for the further discussions. The atomic coordinates in the asymmetric unit and the equivalent atomic displacement parameters are given in Table 6.6. The anisotropic atomic displacement parameters of the atoms are listed in Table 9.30.

Table 6.6: La<sub>3.65</sub>[Ru(C<sub>2</sub>)<sub>3</sub>]: Fractional atomic coordinates in the subcell, site occupancies and equivalent isotropic displacement parameters [ $10^4 \text{ pm}^2$ ]; estimated standard deviations are given in parentheses.

Atom	Site	Occ.	$x$	$y$	$z$	$U_{eq.}$
La1	6 <i>h</i>	1	0.0647(1)	0.6658(1)	1/4	0.015(1)
La2	4 <i>e</i>	0.322(2)	0	0	-0.018(3)	0.055(3)
Ru1	2 <i>d</i>	1	2/3	1/3	1/4	0.012(1)
C1	6 <i>h</i>	1	0.2722(8)	0.0135(7)	1/4	0.026(2)
C2	6 <i>h</i>	1	0.4315(6)	0.1394(6)	1/4	0.015(2)

As clearly described in the literature [178] the superspace approach has the following advantages: *i*) all reflections are properly handled using the basic cell together with a modula-



tion vector; *ii*) since the modulation wave functions are independent from the basic structure, structural correlations are avoided which lead to a more stable refinement and *iii*) the quality of the fit is improved by an increased data-to-parameter ratio and by introducing partial  $R$  values for the satellite reflections. Only for the electronic structure calculations the data were integrated and refined using the threefold superstructure.

### 6.3.2 Crystal chemistry

The crystal structure of  $\text{La}_3[\text{Ru}(\text{C}_2)_3]$  comprises a partial structure consisting of planar  $[\text{Ru}(\text{C}_2)_3]$  groups surrounded by La atoms, which form a host framework containing hexagonal channels of carbon atoms. The remaining La atoms occupy the hexagonal channels forming modulated metal chains. By comparing the  $R$ -values only, the modulated metal chains can be described by the commensurate and the incommensurate models with the same quality. However, the electron density distribution within the channels and the modulated positions of the La2 atoms must be carefully examined in order to decide which structure model is the most suitable one. In *Figure 6.17* the occupancy (*Figure 6.17a*) and the equivalent atomic displacement parameters (*Figure 6.17b*) of the La2 atoms in the commensurate and incommensurate structure model are plotted as a function of the modulation phase  $t$ .

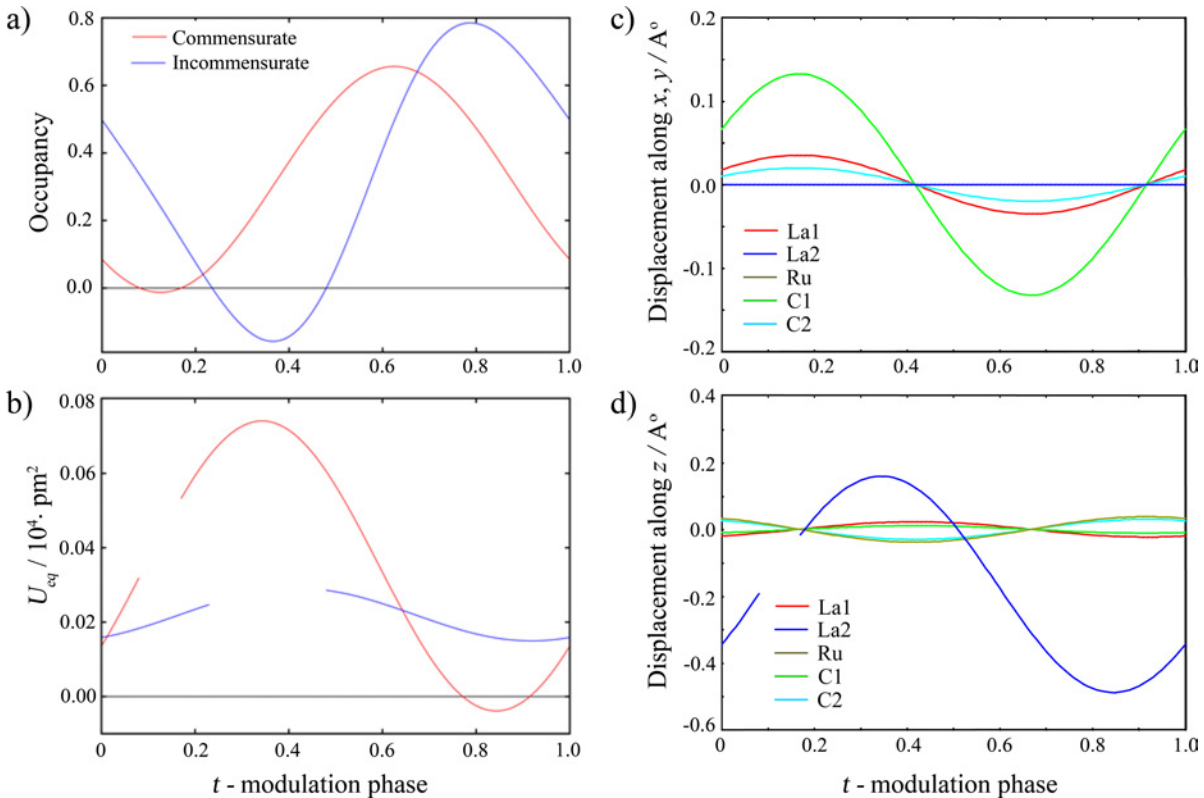


Figure 6.17:  $\text{La}_{3.65}[\text{Ru}(\text{C}_2)_3]$ : a) Modulation of the site occupancy factor for the commensurate and incommensurate case, b) temperature factors of La2 atoms as a function of the internal coordinate  $t$ . Red lines show the modulations in the commensurate and blue lines in the incommensurate case. The modulation functions of the deviations from the average positions are shown in c) along  $x$  and d) along  $z$  directions as a function of  $t$  for the commensurate model.



The highest occupancy for the commensurate model is obtained in the  $t$  range between 0.4 and 0.8, whereas the incommensurate model gives a range of  $t = 0.6$  to 1.0. In both cases the maximum occupancy of the site is less than 80%. A negative occupancy was observed in case of the incommensurate model in the range  $t = 0.22$  to 0.48, which is physically not reasonable (omitted regions in *Figure 6.17*). This observations strongly supports that the incommensurate model is not appropriate. The equivalent ADP increases with a decrease of the occupancy of the La2 site indicating a strongly smeared electron density at lower occupancies. The modulation wave function of the equivalent ADP shows a discontinuous character and the wave function of the commensurate model reveal a higher amplitude than the incommensurate model. The discontinuity range corresponds to 0 occupancies i.e., vacancies. The difference Fourier maps show residual electron densities of  $1.78 \text{ e}^-/\text{\AA}^3$  for the commensurate model and of  $4.7 \text{ e}^-/\text{\AA}^3$  for the incommensurate model, respectively. On the basis of the Fourier syntheses and the refinement results, it can be concluded that the commensurate model better describes the observed electron density than the incommensurate one. Thus, the structure analyses were further conducted using the commensurate structure model. A site occupancy factor of 0.322(2) for the La2 position was obtained from the refinements (see *Table 6.6*), which is slightly lower than the maximal occupancy of  $1/3$ , leading to the chemical composition La<sub>3.65</sub>[RuC<sub>6</sub>].

The main structural motif for both commensurate and incommensurate structures is a pair of La atoms (*Figure 6.18*). However, the symmetry allows vacancies and discrete La atoms within the chains only in the incommensurate model with the restriction of an appropriate occupancy cut off criterion.

a) Commensurate,  $z = 0 \dots 9$



b) Incommensurate,  $z = 0 \dots 9$



c) Incommensurate,  $z = -6 \dots 3$



*Figure 6.18*: La<sub>3.65</sub>[Ru(C<sub>2</sub>)<sub>3</sub>]: Three different variants of La chains running along [001]: a) commensurate modulation, b) and c) incommensurate modulations. The commensurate model exclusively contains atom pairs, while the incommensurate models show additional vacancies and discrete atoms, respectively.  $z$  represents the range taken along the  $c$  axis.

The modulations of atomic displacements and the interatomic distances in the crystal

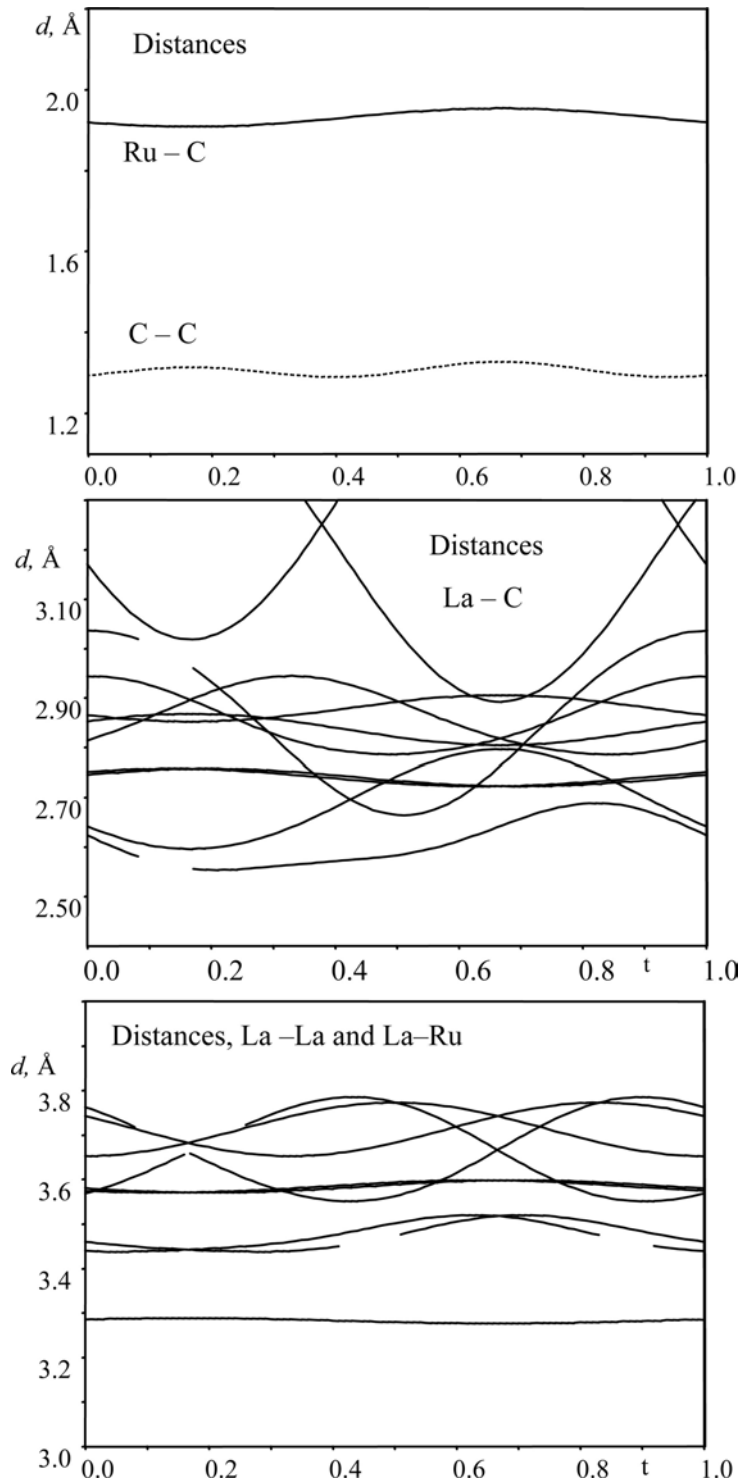


Figure 6.19:  $\text{La}_{3.65}[\text{Ru}(\text{C}_2)_3]$ :  $t$ -plots describing the modulation of distances: a) Ru-C and C-C, b) La-C and c) La-La and La-Ru.

structure are plotted as a function of  $t$  in *Figure 6.17c, d* and *Figure 6.19*. The La2 atom shows a strong positional modulation along the  $c$ -axis with an amplitude of  $\Delta z = 0.7 \text{ \AA}$  (for  $t = 0.35$  and  $t = 0.85$ ). One can conclude that the La2 atoms are embedded within the carbon octahedra; large displacements along  $[001]$  with respect to the centers of the octahedra are allowed. From a structural point of view the atomic arrangement of the La species to form

pairs within the chain is obviously stabilizing. This is possible, since two carbon octahedra are occupied and alternate with one empty octahedron (vacancy). Furthermore, it is obvious that the strong displacement of the La2 atoms along [001] will cause a positional shift of the carbon atoms on the *ab*-plane forming the octahedra, namely the C1 atoms. Thus, the C1 atoms have a displacement amplitude of  $\Delta x = 0.2 \text{ \AA}$  ( $t = 0.17$  and  $t = 0.67$ ). It is interesting to notice that the displacement of the C1 atom is associated with the occupancy of the La2 site (*Figure 6.17a* and *Figure 6.17c*). When the occupancy of the La2 site is increasing the C1 atoms have a negative shift along *x* or *y* and with decreasing occupancy of La2, the shift is flipping to a positive value. This regularity is probably associated with charge balancing of the negatively charged carbon octahedral channels with the positively charged La atoms. On the other hand, it could also indicate considerable La–C interactions. The other atoms exhibit deviations from their average positions less than  $0.1 \text{ \AA}$ . The displacement of the C1 atom along *x* affects the strongly bonded C2 atom, but has only little effect on the Ru atom. The Ru and C2 atoms are breathing together along the *c*-axis which supports the crystal structure refinement results. As a consequence of the positional modulation the interatomic distances are also shifting. The largest shifts are observed between the atoms which have the highest displacement modulation amplitude. The smallest changes in the interatomic distances occur for La1–Ru ( $\Delta d = 0.015 \text{ \AA}$ ) and for Ru1–C2 and C1–C2 ( $\Delta d = 0.04 \text{ \AA}$ ). The largest distance deviations are observed for La2–C1 ( $\Delta d = 0.35 \text{ \AA}$  for  $t = 0$  and  $t = 0.5$ ) and La1–La2 ( $\Delta d = 0.3 \text{ \AA}$  for  $t = 0.45$  and  $t = 0.9$ ) as shown in *Figure 6.19*. The modulation amplitudes of the distances C1–C2 and C2–Ru1, and especially Ru1–La1, are small. Interatomic distances in the crystal structure of  $\text{La}_{3.65}[\text{Ru}(\text{C}_2)_3]$  are listed in *Table 9.31*.

## 6.4 Phase stability

Phase stability and homogeneity range of  $\text{La}_{3.67}[\text{Ru}(\text{C}_2)_3]$  were examined by ab-initio calculations. The standard convex hull program QHULL [238] was used. Details of the calculations are described in *Section 6.2.3*.

In order to identify energetically stable phases structure models for  $\text{La}_x\text{La}_3[\text{Ru}(\text{C}_2)_3]$  were tested with  $0.5 \leq x \leq 0.67$  including known binary and plausible ternary compounds in our considerations. The enthalpies and total energies were calculated for every structure. For instance, the Gd atom in  $\text{Gd}_3\text{Ru}_2\text{C}_5$ , *hP50*, was replaced by La atoms and  $\Delta H$  and  $\Delta E$  of  $\text{La}_3\text{Ru}_2\text{C}_5$  were calculated. In a plot of the total energy over the composition, the given compounds form a scatter-plot over the triangle. Edges and facets of the convex hull represent two- and three-phase regions, respectively, of the phases at vertices. Their projections onto the composition (i.e.  $x_{\text{La}}$ ,  $x_{\text{Ru}}$ ,  $x_{\text{C}}$ ) plane correspond to tie lines and tie triangles, respectively, of the isothermal section at 0 K. High-temperature phases lie over the convex hull, but must be sufficiently close so that entropy contributions can stabilize them. Stable compounds are associated with a negative enthalpy of formation.  $\Delta E$  measures the thermodynamic dri-

ving force for decomposition to the appropriate combination of stable phases. For the stable phases these values are negative. In contrast to  $\Delta H$ , the value of  $\Delta E$  depends on the cohesive energies of other competing structures. As for  $\text{La}_{3.67}[\text{Fe}(\text{C}_2)_3]$ , the results show that the  $\text{La}_{22}[\text{Ru}_6\text{C}_{36}]$  and  $\text{La}_{21}[\text{Ru}_6\text{C}_{36}]$  are energetically stable, whereas  $\text{La}_{20}[\text{Ru}_6\text{C}_{36}]$  is unstable at 0 K. This result supports a small homogeneity range  $\text{La}_x\text{La}_3[\text{Ru}(\text{C}_2)_3]$  with  $0.5 \leq x \leq 0.67$  at high temperatures. The superstructure formation most probably depends on the annealing temperature, the molar ratio of the starting materials (La-rich or -deficient) and the annealing time which is necessary for ordering of the atoms within the channel.

### 6.5 Electronic structure and chemical bonding analysis

The electronic structure of  $\text{La}_{3.67}[\text{Ru}(\text{C}_2)_3]$  was calculated using the self-consistent scalar relativistic TB-LMTO-ASA method [210] within the local (spin) density approximation (L(S)DA) [211] to the DFT. The chemical bonding was examined within the framework of crystal orbital Hamilton population (COHP) analyses [133].

Structural parameters of the threefold superstructure were used for the band structure calculations. *Figure 6.20* shows the total and the partial DOS as well as COHP curves for selected orbital interactions. The total DOS reveals metallic behavior for  $\text{La}_{3.67}[\text{Ru}(\text{C}_2)_3]$ . The DOS can be divided into four ranges: Range **A** between -16 eV and -13 eV originates from the C 2s states with only small contributions of metal atoms. The ranges **B** (-9 eV and -7 eV) and **C** (-6.5 eV and -3 eV) are dominated by C 2p orbitals with considerable Ru 4d and La 5d contributions (*Figure 6.20, DOS*). The states just below the Fermi level in range **D** (-3 eV up to  $E_F$ ) consist of orbitals of metal atoms. The unit cell contains 6 formula units and a total of 258 valence electrons from 22 La, 6 Ru and 36 C atoms. These 258 valence electrons can be rationalized in the following way. Ranges **A**, **B** and **C** contain 180  $e^-$  which mostly originate from 36 C atoms. Range **D** contains 78  $e^-$  for Ru 4d, La 5d, 6s and small contributions of carbon  $\pi^*$  states. In order to assign the effective charges for the constituents QTAIM integration will be performed, a work which is not done up to now. For the chemical bonding analysis, each interaction is weighted by the respective bond multiplicities per formula unit, giving information about the relative importance of this interaction for the whole crystal structure (for the ICOHP values see *Table 6.7*). The Ru–C bond is the strongest, dominating interaction (*Figure 6.20, COHP*). Strong Ru–C bonds are fully exhausted at  $E_F$ , whereas the weak La–C bonds are not. The ratio of  $\text{ICOHP}(\text{Ru–C}) / \text{ICOHP}(\text{La–C})$  is 4.66, and the same findings have been reported for RE carbometalates containing only monoatomic carbon species [9]. Metal–metal bonding interactions La–Ru are weak but significant, and are situated at  $E_F$ . This can be taken as evidence for the fact that the complex entities  $\text{Ru}(\text{C}_2)_3$  are electronically not completely isolated from the metallic part of the structure. The orbital interactions La–La in total are smaller in extent but dominate at  $E_F$ , where a DOS peak of mostly La states is observed. At 0.5 eV below  $E_F$  a sharp

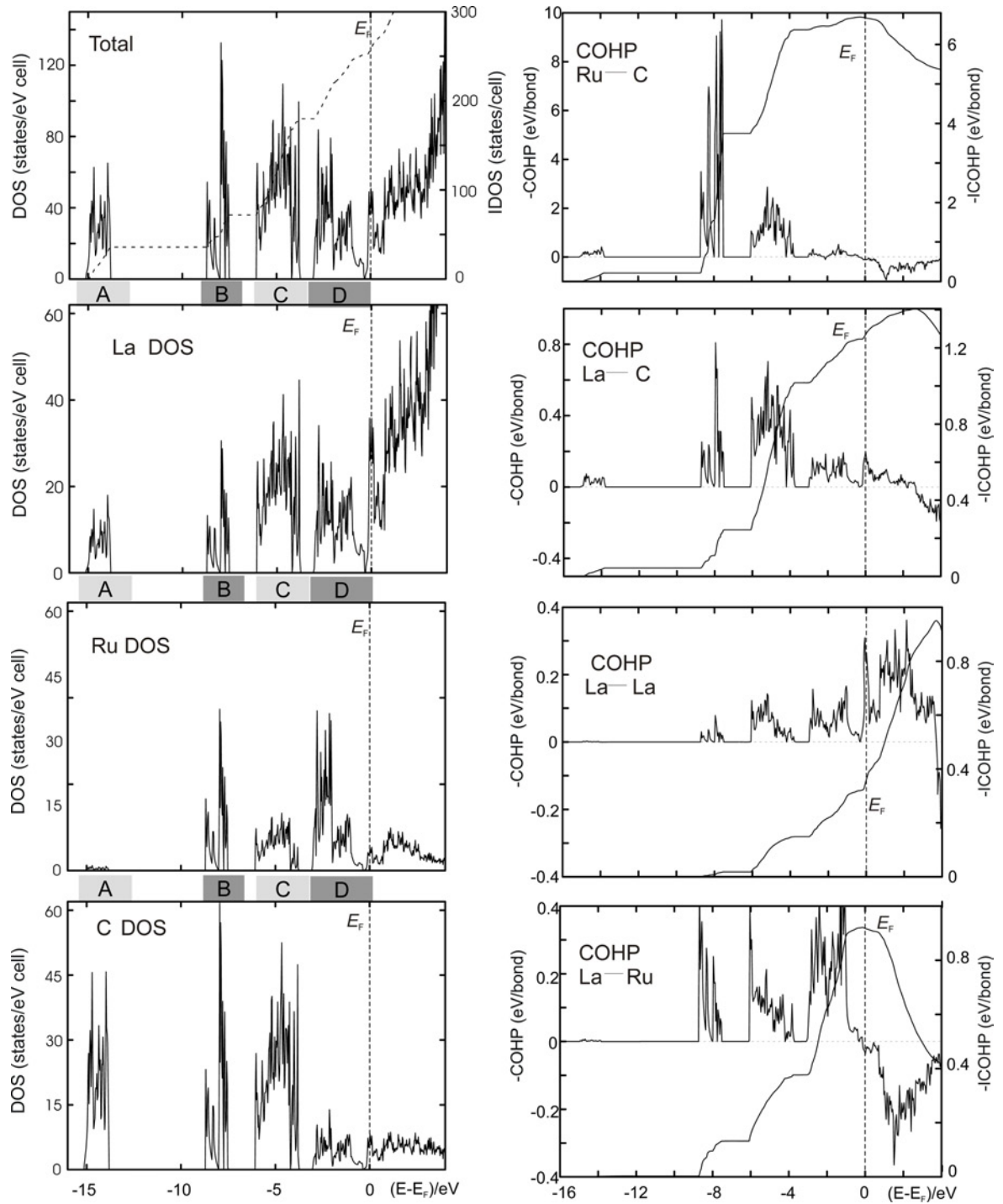


Figure 6.20: Total DOS and atom-projected DOS for  $\text{La}_{3.67}[\text{Ru}(\text{C}_2)_3]$  (left column). DOS regions are denoted by letters *A*, *B*, *C*, *D* (see text for details). COHP and integrated COHP (ICOHP) diagrams for selected interactions in the crystal structure of  $\text{La}_{3.67}[\text{Ru}(\text{C}_2)_3]$  are presented in the right column.

pseudogap is formed. The integrated DOS from the pseudogap up to  $E_F$  yields  $6 e^-$  ( $Z = 6$ ,  $1 e^-$  per formula unit), contributed by both La species. Band structure calculations of  $\text{La}_{20}[\text{Fe}_6\text{C}_{36}]$  revealed that the introduction of vacancies within the La-chains does not influence the electrical transport properties (Section 6.2.4).

Table 6.7:  $\text{La}_{3,67}[\text{Ru}(\text{C}_2)_3]$ : Selected interatomic distances [pm] (denoted as  $d$ ), multiplicities per unit cell (denoted as  $n$ ) of the superstructure and their integrated crystal orbital Hamilton populations per bond (-ICOHP [eV/bond]).

<b>La - C</b>		<b>Ru - C</b>		<b>La - La</b>		<b>La - Ru</b>		<b>C - C</b>						
$n$	$d$	-ICOHP	$n$	$d$	-ICOHP	$n$	$d$	-ICOHP	$n$	$d$	-ICOHP			
$\times 12$	263.56	2.54	$\times 12$	191.58	7.02	$\times 12$	346.78	0.45	$\times 12$	328.48	0.94	$\times 12$	130.42	15.23
$\times 12$	274.36	1.14	$\times 6$	194.00	6.50	$\times 2$	364.61	0.35	$\times 6$	327.55	0.87	$\times 6$	134.94	13.86
$\times 12$	275.41	1.19				$\times 12$	374.43	0.39						
$\times 12$	280.54	1.30				$\times 12$	365.26	0.24						
$\times 12$	285.33	1.11				$\times 2$	344.67	0.32						
$\times 12$	286.25	0.81												
$\times 12$	295.11	0.91												
$\times 12$	316.27	0.56												
$\times 12$	272.46	1.18												
$\times 6$	279.95	1.82												
$\times 6$	280.78	1.06												
$\times 12$	282.55	1.20												
$\times 6$	287.77	0.99												
$\times 6$	289.77	1.09												
$\times 12$	265.63	1.99												
$\times 12$	274.68	1.66												
<b>-ICOHP<sub>aver</sub> = 1.47</b>		<b>-ICOHP<sub>aver</sub> = 6.85</b>		<b>-ICOHP<sub>aver</sub> = 0.36</b>		<b>-ICOHP<sub>aver</sub> = 0.92</b>		<b>-ICOHP<sub>aver</sub> = 14.78</b>						

The total energy calculations support a narrow homogeneity range at high temperatures due to La deficiencies within the channels, however, a structure with large deficiencies is found to be unstable by total energy calculations. This result is corroborated by inspecting the La–La COHP, where the peak in the DOS is identified as a bonding interaction. For better understanding of the chemical bonding situation and for confirmation of the presence of excess electrons, measurements of the physical properties on single phase materials are necessary.

## 6.6 Magnetic susceptibility

Magnetization measurements in external fields  $\mu_0 H$  between 0.01 T and 7 T were performed in the temperature range 1.8 K to 400 K by use of a SQUID magnetometer (MPMS XL-7, Quantum Design). Polycrystalline samples were sealed in a quartz glass tube under 0.4 bar He. Corrections for the sample container were applied. An extrapolation of the high-field susceptibility data  $\chi(T, H)$  for  $1/H \rightarrow 0$  in order to correct for minor ferromagnetic impurities was performed (Honda-Owen method).

The experimental high-field magnetic susceptibility data  $\chi = M/H$  ( $\mu_0 H = 3.5$  T and 7.0 T) as well as the corrected data  $\chi_{\text{corr}}(T)$  for  $\text{La}_{3.67}[\text{Ru}(\text{C}_2)_3]$  are plotted in Figure 6.21.

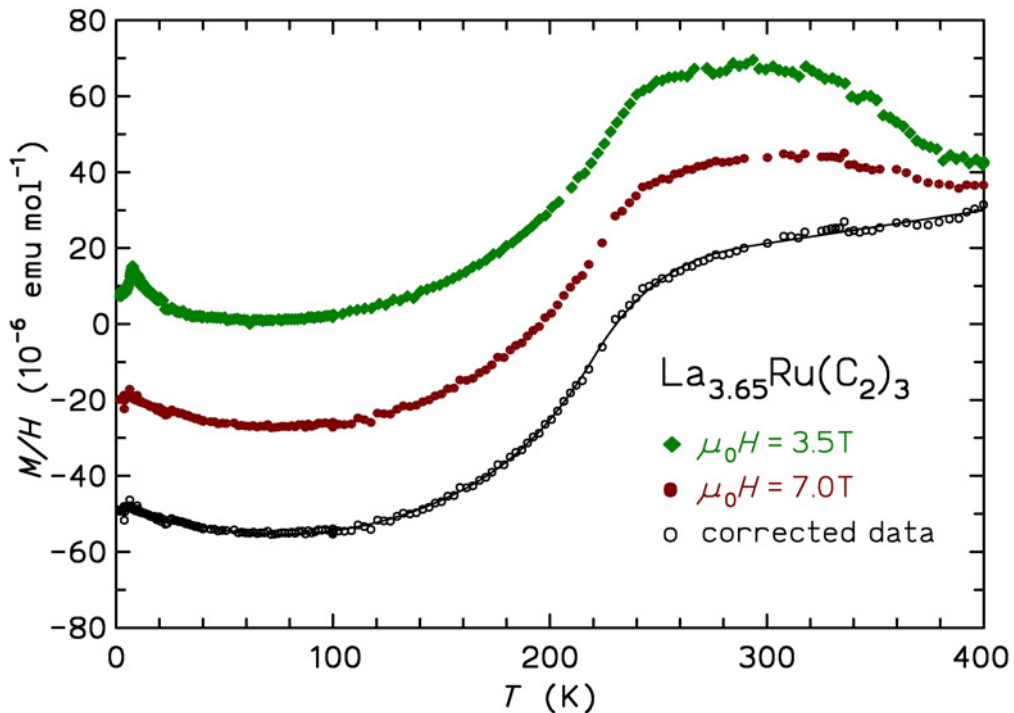


Figure 6.21: Experimental and corrected magnetic susceptibility data  $M(T)/H$  of  $\text{La}_{3.65}[\text{Ru}(\text{C}_2)_3]$ .

The magnetic susceptibility is weak and thus indicates the absence of localized paramagnetic moments. A broad phase transition is revealed at around 240 K, below which  $\chi_{\text{corr}}(T)$  decreases strongly and then approaches a value of  $-50 \times 10^{-6} \text{ emu/mol}$  at the lowest temperature. The upturn towards  $T = 0$  K is due to minor paramagnetic impurities. For low fields

a diamagnetic signal becomes dominant which is maybe caused by an unidentified superconducting phase with  $T_c \approx 8.4$  K and an upper critical field  $\mu_0 H_{c2} > 7$  T (possibly  $\text{La}_2\text{C}_{3-x}$ ). The maximum volume fraction of the phase as estimated from the shielding at  $\mu_0 H = 0.01$  T is about 1%. Similar observations were observed for  $\text{La}_2\text{C}_{3-x}$ : while  $\text{La}_2\text{C}_3$  has a  $T_C$  of 13.4 K [239, 240], in samples with lower C content a  $T_C$  between 6 K and 9 K was observed [239].

$\text{La}_{3.67}[\text{Fe}(\text{C}_2)_3]$  shows Pauli-paramagnetic behavior with  $\chi_0$  ca.  $1.54 \cdot 10^{-4}$  emu/mol. Traces ( $< 0.14$  vol%) of a superconducting phase with  $T_c = 8.4$  K, probably binary  $\text{La}_2\text{C}_3$  [239, 240], were observed as in case of  $\text{La}_{3.67}[\text{Ru}(\text{C}_2)_3]$ .

### 6.7 Electrical resistivity

The electrical resistivities  $\rho(T)$  of  $\text{La}_{3.67}[\text{T}(\text{C}_2)_3]$  ( $T = \text{Fe}, \text{Ru}$ ) show a temperature dependence typical for metals. The absolute values are large, thus the compounds are bad metals (Figure 6.22). A phase transition in  $\text{La}_{3.67}[\text{Ru}(\text{C}_2)_3]$  is visible in  $\rho(T)$  as a kink at  $\approx 240$  K and a broad hump around 215 K. Below the transition, the slope of  $\rho(T)$  is larger than at higher temperatures. From this characteristic the transition maybe classified as a kind of spin density wave state, however the paramagnetic susceptibility above the transition is quite small compared with other related systems. Further investigations on big single crystals must be conducted to explain the origin of this phase transition.

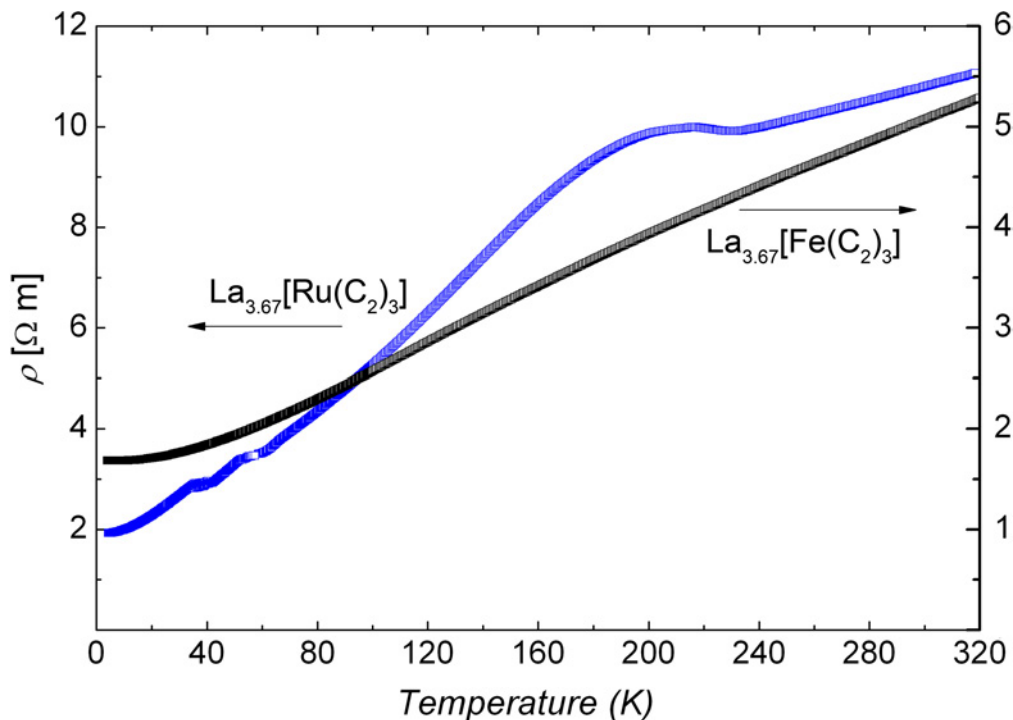


Figure 6.22: Electrical resistivity  $\rho(T)$  of  $\text{La}_{3.67}[\text{T}(\text{C}_2)_3]$  ( $T = \text{Fe}, \text{Ru}$ ). The anomalies around 40 K and 50 K are artefacts. For further details see text.



## 6.8 Summary

A threefold superstructure was observed during the re-investigation of the crystal structure of  $\text{La}_{3.67}[\text{Fe}(\text{C}_2)_3]$ . The structure was refined in the isomorphic subgroup of the aristotype in  $P6_3/m$  ( $P6_3/m$ ,  $a = 879.3(2)$  pm,  $c = 1605.0(7)$  pm,  $V = 1074.5(6) \cdot 10^6$  pm<sup>3</sup>). The electron density in the octahedral channels of the structure formed by carbon atoms was described by a split atom model (La3/La4) resulting in rather high residual electron density of  $5.42 \text{ e}^-/\text{\AA}^3$  near the La4 atom. The superstructure is caused by an ordered arrangement of La atoms, however, the alignment between the chains is still uncorrelated. The Mössbauer spectrum of  $\text{La}_{3.67}[\text{Fe}(\text{C}_2)_3]$  was fitted with two doublets, indicating two different Fe positions, which supports our observation of a 3-fold superstructure of  $\text{La}_{3.67}\text{Fe}[(\text{C}_2)_3]$ . The compound can be used as a reference in the future for Mössbauer investigations of binary and ternary iron carbides. XAS measurement results confirmed that the oxidation state of Fe atoms in  $\text{La}_{3.67}\text{Fe}[(\text{C}_2)_3]$  is positive.

The crystal structure of  $\text{La}_{3.67}[\text{Ru}(\text{C}_2)_3]$  was refined using the superspace approach in the limit of a commensurate modulated structure ( $P6_3/m(00g)s0$ ,  $a = 887.8(8)$  pm,  $c = 535.5(5)$  pm,  $V = 365.6(6) \cdot 10^6$  pm<sup>3</sup>,  $q = (0, 0, 1/3)$ ). The refinements reveal that the crystal structure is better described by a commensurate (superstructure) than by an incommensurate modulation. The best fit of the structure refinement was obtained using harmonic occupational and displacive modulation functions. The large displacive and occupational modulation amplitudes of the La atoms in the chains cause moderate shifts of the surrounding carbon atoms (C1) in the  $ab$  plane but have almost no effect on all other structure parameters. The final refinement for the single crystal under investigation resulted in the formula  $\text{La}_{3.65}[\text{Ru}(\text{C}_2)_3]$ .

Total energy calculations with the PAW method (VASP) predict stable structures for  $\text{La}_{22}[\text{T}_6\text{C}_{36}]$  ( $\text{La}_{3.67}[\text{T}(\text{C}_2)_3]$ ) and  $\text{La}_{21}[\text{T}_6\text{C}_{36}]$  ( $\text{La}_{3.5}[\text{T}(\text{C}_2)_3]$ ) at 0 K, indicating a small homogeneity range at high temperatures.

Assuming the absence of significant metal–metal interactions one may assign the oxidation state +1 for the  $T$  atoms:  $(\text{La}^{3+})_{0.67}\text{La}^{3+}_3[\text{T}^{1+}(\text{C}_2)^{4-}_3]$ . However, the COHP analyses indicate considerable contributions of La–C and La– $T$  interactions besides strong covalent C–C and  $T$ –C bonds. The compounds under investigation contain complex anions  $[\text{T}(\text{C}_2)_3]$  and La cations. Magnetic susceptibility measurements indicate the presence of  $\text{La}^{3+}$ . The compounds are bad metals.

## 7 Sm<sub>2</sub>[Cr<sub>2</sub>C<sub>3</sub>]

### 7.1 Synthesis and phase analysis

Sm<sub>2</sub>[Cr<sub>2</sub>C<sub>3</sub>] is a new member of the isotypic series of Ho<sub>2</sub>[Cr<sub>2</sub>C<sub>3</sub>] type compounds with RE = Y, Gd–Lu. Details about these compounds are discussed in *Section 2.2.1*.

Sm<sub>2</sub>[Cr<sub>2</sub>C<sub>3</sub>] was prepared by high temperature reaction in a tube furnace (HTM Reetz GmbH, Lora 1800) of cold-pressed pellets of the elements (Sm: 99.9%, *Alfa*, Cr: 99.9%, *Chempur* and graphitic carbon: 99.95%, *Chempur*) in the molar ratio Sm : Cr : C = 2 : 2 : 3.1. The starting materials and the reaction products are sensitive to air and moisture, and all handlings were performed under dry argon in a glove box. The choice of a suitable crucible material which is inert to the reaction mixtures is important for the high temperature synthesis. Different crucible materials, Ta, Mo, Nb and glassy carbon were tested using an induction furnace. All crucible materials, except Mo, react with the educt materials above 1373 K, which was confirmed by X-ray phase analyses. Thus, Mo was chosen as a reaction container. However, it was found that at high temperatures of about 1823 K Sm<sub>2</sub>Mo<sub>2</sub>C<sub>3</sub> is formed [241]. Considering the melting point of Sm (1345 K) and its vapor pressure the reaction temperature was chosen to be maximum 1673 K. The pellets were encapsulated in weld-sealed Mo ampoules and slowly heated to 1673 K with a rate of 5 K/min, annealed for 72h and finally cooled down to 1173 K under continuous argon flow, as described in *Section 3.1.2*. The reaction product was ground and annealed at 1473 K for several times in order to improve the homogeneity of the sample. After each cycle the phase content was checked by X-ray powder diffraction. The brittle reaction product is grey with a metallic luster.

Powder X-ray diffraction patterns were recorded in the range  $10^\circ < 2\theta < 90^\circ$  (Huber-Guinier-camera G670, Ge monochromator, Cu K $\alpha_1$  radiation ( $\lambda = 154.059$  pm), transmission geometry, flat sample holder with vaseline-coated mylar foil). LaB<sub>6</sub> (SRM660a,  $a = 415.6916$  pm) was used as internal standard to determine the unit cell parameters. The unit cell parameters were refined by the least squares method using the program PPLP of the NRCVAX suite [156]:  $a = 1051.2(3)$  pm,  $b = 347.1(1)$  pm,  $c = 569.2(1)$  pm and  $\beta = 105.55(1)^\circ$ ;  $V = 200.1(1) \cdot 10^6$  pm<sup>3</sup>. All X-ray powder diffraction investigations were carried out at ambient temperature. Metallographic examinations and powder diffraction analyses show that the title compound is the majority phase besides small amounts of Cr<sub>7</sub>C<sub>3</sub> (ca. 5 vol.%) as shown in *Figure 7.1*. Several samples with different carbon content in the starting mixture ( $\pm 10$  at.%) were prepared in order to check the existence of a homogeneity range. The powder diffraction patterns did not show any significant change of the lattice parameters, indicating no perceptible homogeneity range. The atomic ratio of metals was quantitatively determined by metallographic examinations combined with WDXS analyses as described in *Section 3.7.1* on polished samples (*Section 3.6*). WDXS (Cameca SX 100) analyses revealed a composi-

tion of the majority phase (95 vol.%) corresponding to the atomic ratio Sm : Cr = 2 : 1.9(1). The powder diffraction pattern, the lattice parameters and the atomic ratio Sm : Cr clearly indicate that the synthesized phase is isotypic to  $\text{Ho}_2[\text{Cr}_2\text{C}_3]$ .

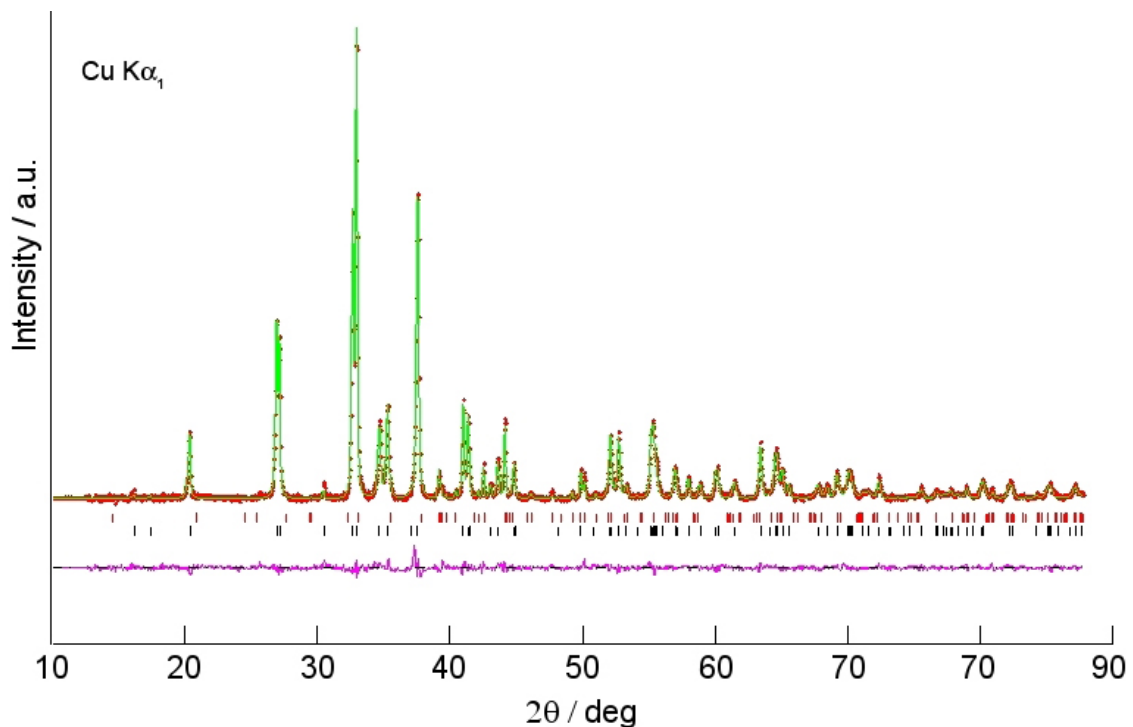


Figure 7.1: X-ray diffraction pattern of  $\text{Sm}_2[\text{Cr}_2\text{C}_3]$ : the observed profile is indicated by red dots and the calculated profile by the solid line. Bragg peak positions of  $\text{Sm}_2[\text{Cr}_2\text{C}_3]$  and  $\text{Cr}_7\text{C}_3$  are indicated by black and red tick marks, respectively. The difference curve is shown at the bottom.

## 7.2 Crystal structure determination

Crystals of  $\text{Sm}_2[\text{Cr}_2\text{C}_3]$  grow with a platy morphology. However, single crystals suitable for X-ray structure analysis were not obtained by the high temperature methods. The attempt to grow single crystals of  $\text{Sm}_2[\text{Cr}_2\text{C}_3]$  by changing the reaction temperature and the molar ratio of the starting materials failed. Thus, the crystal structure was refined using the powder X-ray diffraction data by the Rietveld method (program package GSAS [160]).  $\text{Sm}_2[\text{Cr}_2\text{C}_3]$  is isotypic to  $\text{Ho}_2[\text{Cr}_2\text{C}_3]$  [242]. The atomic coordinates of  $\text{Ho}_2[\text{Cr}_2\text{C}_3]$  were used as a starting model for the refinements. The unit cell parameters obtained from calibrated powder diffraction patterns were used and kept constant during the refinements. All atomic coordinates and atomic displacement parameters were refined step by step in separate refinement cycles. The reflection profiles were fitted with pseudo-Voigt functions while the background intensity was modeled by a series of shifted Chebyshev polynomials. The atomic displacement parameters were isotropically refined and the occupancies of the all atomic positions were fixed to full occupancy of the respective sites. Structural data of  $\text{Cr}_7\text{C}_3$  was taken from

the Inorganic Crystal Structures Database [11]. The unit cell parameters and site occupation factors of this minority phase (Cr<sub>7</sub>C<sub>3</sub>) were kept constant during the refinements. As there was no peak overlap between the binary carbide and the ternary majority phase, the presence of Cr<sub>7</sub>C<sub>3</sub> did not cause any difficulties in the refinement. After the final refinement cycle, the refinement converged to Bragg residuals ( $R_B$ ) of 7% and weighted profile residuals ( $R_{wp}$ ) of 11%, respectively. Intensity versus  $2\theta$  plots of the observed and calculated patterns, Bragg-reflection markers and a difference curve plot are shown in *Figure 7.1*. Crystallographic data and details for the two-phase Rietveld structure refinement of Sm<sub>2</sub>[Cr<sub>2</sub>C<sub>3</sub>], the atomic coordinates as well as the isotropic thermal displacement parameters are given in *Table 7.1* and *Table 7.2*, respectively.

Table 7.1: Crystallographic data and details on the Rietveld structure refinement of Sm<sub>2</sub>[Cr<sub>2</sub>C<sub>3</sub>]<sup>†</sup>.

Chemical formula, Z	Sm <sub>2</sub> [Cr <sub>2</sub> C <sub>3</sub> ], 2
Crystal system	monoclinic
Space group	<i>C2/m</i> (no. 12)
Formula mass [g·mol <sup>-1</sup> ]	881.65
Radiation, $\lambda$ [pm]	Cu K $\alpha_1$ , 154.093
Temperature [K]	295
$a^1$ [pm]	1051.2(3)
$b^1$ [pm]	347.1(1)
$c^1$ [pm]	569.2(1)
$\beta^*$ [°]	105.55(1)
$V$ [10 <sup>6</sup> pm <sup>3</sup> ]	200.1(1)
$\rho_{calc.}$ [g·cm <sup>-3</sup> ]	7.31
$2\theta$ - range [°]	$8.0^\circ < 2\theta < 90^\circ$
No. of data points / parameters	15053 / 71
$R_B^2 / R_{wp}^3$	0.07 / 0.11

<sup>†</sup> Supplementary data are available from the FIZ, D-76344 Eggenstein-Leopoldshafen, Germany, e-mail [crysdata@FIZ-karlsruhe.de](mailto:crysdata@FIZ-karlsruhe.de), by quoting the depository number CSD380337

<sup>1</sup> from calibrated X-ray powder diffraction data

<sup>2</sup>  $R_B = \sum |I_{ko} - I_{kc}| / \sum I_{ko}$  with  $I_k$  intensity assigned to  $k^{th}$  Bragg reflection

<sup>3</sup>  $R_{wp} = (\sum w_i (y_{oi} - y_{ci})^2 / \sum w_i (y_{oi}^2))^{1/2}$

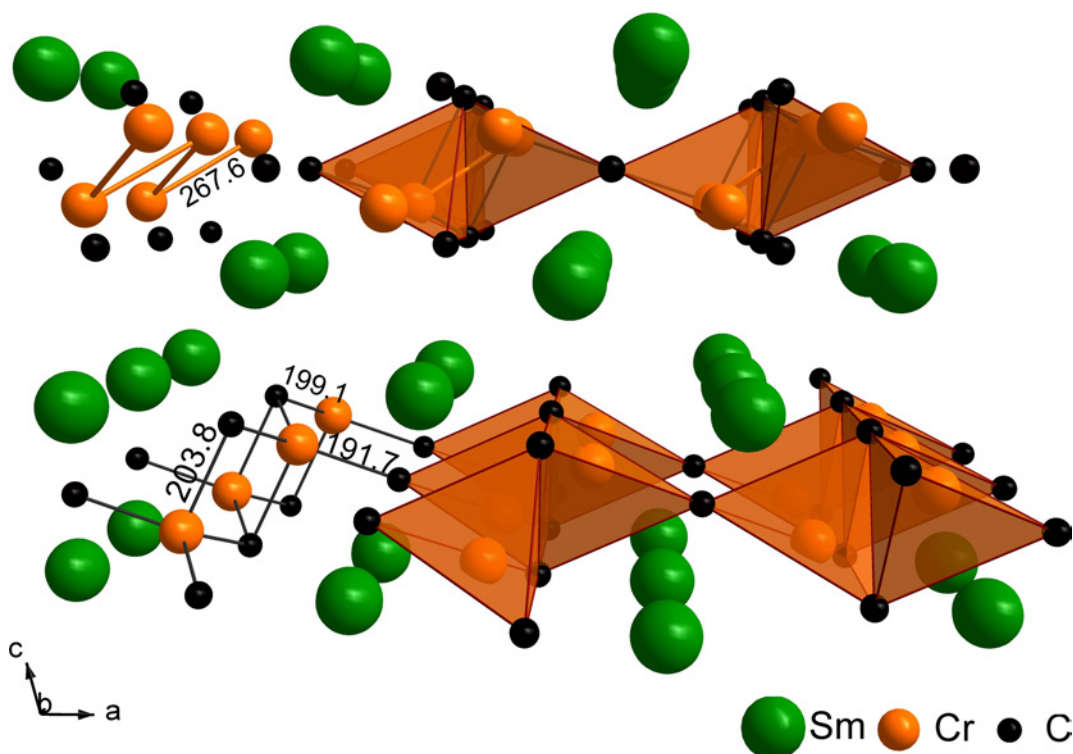
### 7.3 Crystal chemistry

The Cr atoms in the crystal structure of Sm<sub>2</sub>[Cr<sub>2</sub>C<sub>3</sub>] are tetrahedrally coordinated by four carbon ligands with distances  $d(\text{Cr}-\text{C})$  of  $2 \times 191.7(1)$  pm,  $199.1(4)$  pm and  $203.8(6)$  pm, and sharing common tetrahedral edges (C1...C1) *Figure 7.2*. Chromium atoms in the crystal structures of Ba<sub>5</sub>[CrN<sub>4</sub>]N [243] and Li<sub>4</sub>Sr<sub>2</sub>[Cr<sub>2</sub>N<sub>6</sub>] [244] are also tetrahedrally coordi-

Table 7.2: Fractional atomic coordinates and isotropic displacement parameters [ $10^4\text{pm}^2$ ] of  $\text{Sm}_2[\text{Cr}_2\text{C}_3]$ .

Atom	Site	$x$	$y$	$z$	$U_{iso}$
Sm	$4i$	0.3967(1)	0	0.1820(1)	0.0045(2)
Cr	$4i$	0.1564(1)	0	0.3908(2)	0.0042(2)
C1	$4i$	0.2884(6)	0	0.7245(11)	0.0071(2)
C2	$2a$	0	0	1/2	0.0041(2)

nated by four nitrogen ligands, thus pointing out the structural similarity between carbo- and nitridometalates (Figure 7.3). In the crystal structure of  $\text{Ba}_5[\text{CrN}_4]\text{N}$ , the Cr atoms form isolated, distorted  $\text{CrN}_4$  tetrahedra with angles ( $\text{N-Cr-N}$ ) =  $97.0^\circ$  to  $116.3^\circ$ , whereas  $\text{Li}_4\text{Sr}_2[\text{Cr}_2\text{N}_6]$  contains almost ideal  $\text{CrN}_4$  tetrahedra,  $\angle(\text{N-Cr-N}) = 106.8^\circ$  to  $110.3^\circ$ , forming edge-sharing tetrahedral dimers  $[\text{Cr}_2\text{N}_6]$  with  $d(\text{Cr-Cr}) = 249.7(1)$  pm. The angles ( $\text{C-Cr-C}$ ) in  $\text{Sm}_2[\text{Cr}_2\text{C}_3]$  range from  $97^\circ$  to  $121^\circ$ , showing a stronger distortion with the Cr atoms directed to one face of the tetrahedra. This displacements points towards the Sm atoms and may indicate a marginal Sm-Cr interaction. The interatomic distances and bond angles are listed in Table 7.3 and Table 9.32, respectively. The values are similar to those observed in the crystal structures of the binary carbides, for instance  $\text{Cr}_3\text{C}_2$  [64] and  $\text{Sm}_3\text{C}$  [44, 45].

Figure 7.2: The crystal structure of  $\text{Sm}_2[\text{Cr}_2\text{C}_3]$  viewed along  $[010]$ . The coordination of Cr by C atoms is illustrated by orange polyhedra; distances  $d(\text{Cr-C})$  and  $d(\text{Cr-Cr})$  are given in pm.

The connection of neighboring chains of distorted  $\text{CrC}_4$  tetrahedra via common C2 vertices leads to the formation of polyanionic layers  ${}_{\infty}^2[(\text{Cr}_2\text{C}_3)^{6-}]$  extending parallel to the  $ab$

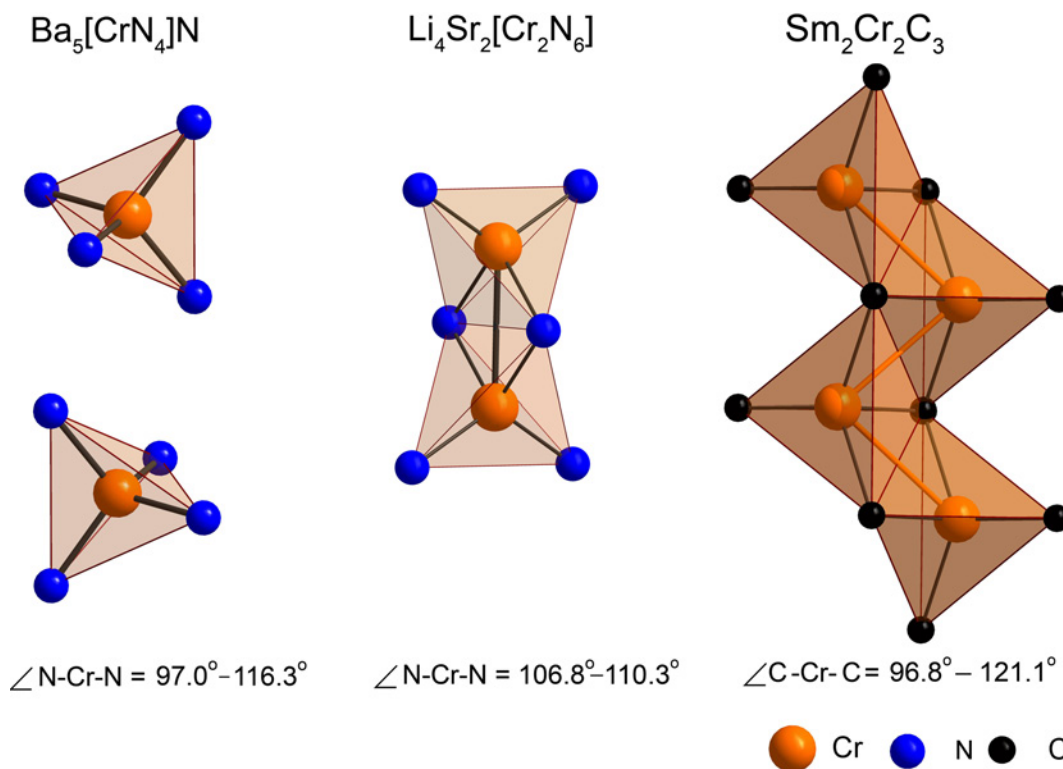


Figure 7.3: Comparison of Cr coordination polyhedra in the crystal structure of  $\text{Sm}_2[\text{Cr}_2\text{C}_3]$  (right)  $\text{Ba}_5[\text{CrN}_4]\text{N}$  (left) and  $\text{Li}_4\text{Sr}_2[\text{Cr}_2\text{N}_6]$  (middle).

plane (Figure 7.2). The Sm atoms are located between the layers, i.e., they are sandwiched between the  $\infty[(\text{Cr}_2\text{C}_3)^{6-}]$  layers. The metal atoms, Sm and Cr together form a distorted body-centered cubic arrangement with a total of 24 octahedral voids per unit cell. In the present structure type, the carbon atoms occupy only one quarter (= 6/24) of all octahedral voids in an ordered arrangement. The chemical formula can therefore be expressed as  $\text{Sm}_2\text{Cr}_2\text{C}_3\Box_3$ , where  $\Box$  denotes vacancies at the octahedral voids. The C2 atoms are in linear coordination by two Cr atoms, augmented by four Sm atoms (Figure 7.4e), thus forming an octahedron. The C1 atoms have three Cr and three Sm atoms as nearest neighbors forming the octahedral arrangement (Figure 7.4d).

The atoms in the crystal structure are distributed over one Sm, one Cr and two C positions (see Table 7.2). The Sm, Cr and C1 atoms lie on mirror planes perpendicular to the y axis, thus having the same site symmetry,  $m$ , whereas, the C2 atoms are located at the centers of symmetry given by the point group symmetry  $2/m$  of the space group  $C2/m$  [245]. The Sm atoms in the structure have 6 Sm nearest neighbors with Sm–Sm interatomic distances of  $d(\text{Sm}-\text{Sm}) = 338.3(1)$  pm,  $2 \times 346.8(1)$  pm,  $2 \times 366.5(1)$  pm and  $368.8(1)$  pm (Table 7.3 and Figure 7.4a), which are close to the respective values found in  $\text{Sm}_2\text{C}_3$  [246].

The closest two Sm–Sm distances are approximately 4-6% shorter than the covalent diameter of the Sm atom,  $d(\text{Sm}) \approx 360$  pm [165]. At a first glance, these short Sm–Sm contacts could be considered to reveal some bonding character. In addition to this, Sm atoms have 5 contacts to Cr atoms at  $306.8(2)$  pm,  $2 \times 316.4(1)$  pm and  $2 \times 318.7(1)$  pm. Similar interatomic

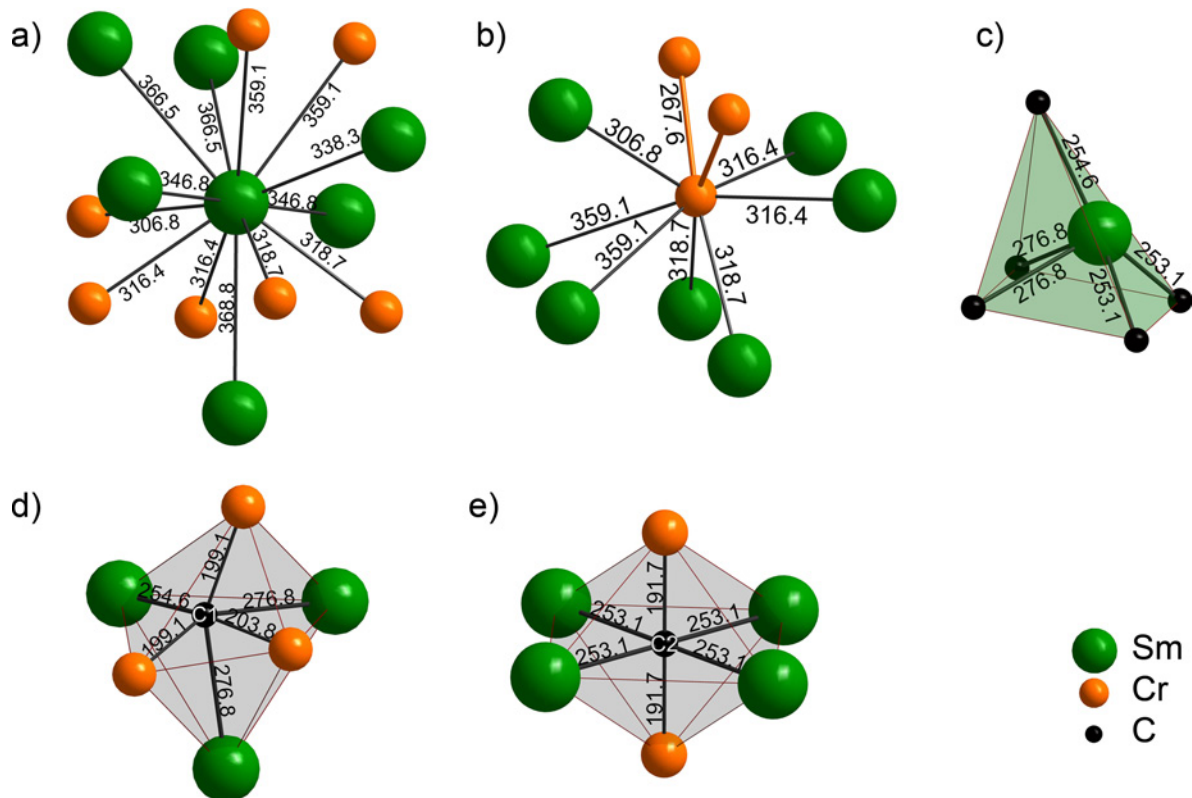


Figure 7.4: Coordination polyhedra in the crystal structure of  $\text{Sm}_2[\text{Cr}_2\text{C}_3]$ . a) Coordination of Sm atoms by metal atoms, c) by carbon atoms; b) nearest metal neighbors of Cr atoms; d) coordination polyhedron around C1 and e) around C2.

Table 7.3: Interatomic distances in the crystal structure of  $\text{Sm}_2[\text{Cr}_2\text{C}_3]$  (estimated standard deviations are given in parentheses).

Bond	Distances / pm	Bond	Distances / pm
Sm – C1	254.6(6)	Sm – Cr	306.8(3)
Sm – C1	$2 \times 276.8(6)$	Sm – Cr	$2 \times 316.4(1)$
Sm – C2	$2 \times 253.1(1)$	Sm – Cr	$2 \times 318.7(1)$
Cr – C1	$2 \times 199.1(4)$	Sm – Sm	338.3(1)
Cr – C1	203.8(6)	Sm – Sm	$2 \times 346.8(1)$
Cr – C2	191.7(1)	Sm – Sm	$2 \times 366.5(1)$
Cr – Cr	267.6(1)	Sm – Sm	368.8(1)

distances were observed in ternary samarium chromium borides, e.g.,  $\text{SmCrB}_4$  [247] which are slightly longer than the sum of covalent radii of Sm and Cr (304 pm) [165]. There are also two Sm–Cr contacts with distance  $d(\text{Sm–Cr}) = 359.1(1)$  pm. The first coordination sphere around Sm is formed by five C arranged in a distorted square pyramidal manner as shown in *Figure 7.4c*. The Sm–C interatomic distances are:  $d(\text{Sm–C}) = 2 \times 253.1(1)$  pm, 254.6(6) pm and  $2 \times 276.8(6)$  pm. The shortest Sm–C contact in the crystal structure of  $\text{Sm}_2[\text{Cr}_2\text{C}_3]$  is about 50 pm longer than the sum of the covalent radii of Sm and C, indicating weak Sm–C interactions. The Cr atoms are coordinated by 6 Sm and 2 Cr atoms forming monocapped

distorted square prisms (Figure 7.4b). The Cr atoms form one dimensional zig-zag chains running along [010], with distances  $d(\text{Cr}-\text{Cr}) = 267.6(1)$  pm, which is just between the Cr-Cr contacts found in W-type metallic Cr (250.1 pm and 288.8 pm) [11].

#### 7.4 Magnetic susceptibility

The magnetization behavior of  $\text{Sm}_2[\text{Cr}_2\text{C}_3]$  was measured within the temperature range 1.8 K to 400 K in external magnetic fields  $\mu_0 H$  of 10 mT to 7 T using a SQUID magnetometer (MPMS XL-7, Quantum Design). An irregular shaped bulk piece with a mass of 27.26 mg was weighted in an Ar filled glove box. A glass-quartz tube ( $\varnothing$  0.4 mm), corrected for magnetization, was charged with the sample which in turn was fixed with cotton wool. Afterwards, the sample was sealed in quartz tubes under 0.4 bar He atmosphere. Magnetic susceptibility measurements on polycrystalline samples indicate a small amount of ferromagnetic impurities. The compound displays a paramagnetic non-Curie-Weiss susceptibility with minimum  $\chi(T)$  at 320 K, typical for  $\text{Sm}^{3+}$  ions with  ${}^6\text{H}_{5/2}$  ground state and  ${}^6\text{H}_{7/2}$  thermally excited state, as well as several magnetic transitions which are most probably due to impurity phases (143 K ferromagnetic, 52 K antiferromagnetic, 30 K and 2.2 K). Two magnetic transitions at lowest temperatures might be intrinsic. Together with the result of the magnetic susceptibility measurement the ionic formula  $(\text{Sm}^{3+})_2[\text{Cr}_2\text{C}_3]^{6-}$  can be given for the compound under investigation.

#### 7.5 Total energy calculations and phase stability

In the family of carbometalates, three different structure types with the same chemical composition  $RE_2[T_2C_3]$  ( $RE$  = rare-earth metals,  $T$  = Cr, Mo) are reported up to now. These structure types are represented by  $\text{Er}_2[\text{Mo}_2\text{C}_3]$  [22],  $\text{Ho}_2[\text{Cr}_2\text{C}_3]$  [20] and  $\text{Pr}_2[\text{Mo}_2\text{C}_3]$  [248].  $\text{Er}_2[\text{Mo}_2\text{C}_3]$  and  $\text{Ho}_2[\text{Cr}_2\text{C}_3]$  crystallize with the same space group,  $C2/m$  (12), while  $\text{Pr}_2[\text{Mo}_2\text{C}_3]$  has space group symmetry  $P2_1/c$  (14). The atomic positions in  $\text{Er}_2[\text{Mo}_2\text{C}_3]$  and  $\text{Ho}_2[\text{Cr}_2\text{C}_3]$  are the same except for one carbon position, which occupies a  $2a$  site in the  $\text{Er}_2[\text{Mo}_2\text{C}_3]$  structure type and a  $2c$  site in the  $\text{Ho}_2[\text{Cr}_2\text{C}_3]$  structure type, resulting in different connection patterns of the polyanions as discussed in reference [241]. In the case of carbomolybdates, both, the  $\text{Er}_2[\text{Mo}_2\text{C}_3]$  and  $\text{Ho}_2[\text{Cr}_2\text{C}_3]$  structure types are formed depending on the size of the  $RE$  cation, whereas all carbochromates reported up to now crystallize in the  $\text{Ho}_2[\text{Cr}_2\text{C}_3]$  type structure. The total energies of the  $\text{Sm}_2[\text{Cr}_2\text{C}_3]$  with  $\text{Er}_2[\text{Mo}_2\text{C}_3]$  and  $\text{Ho}_2[\text{Cr}_2\text{C}_3]$  structure types have been calculated in order to unravel the different crystal chemical behavior of carbochromates compared to carbomolybdates.

The total energy of the  $\text{Sm}_2[\text{Cr}_2\text{C}_3]$  was calculated with *i*)  $\text{Ho}_2[\text{Cr}_2\text{C}_3]$  and *ii*)  $\text{Er}_2[\text{Mo}_2\text{C}_3]$  (hypothetical) structure type using the PAW method within the generalized gradient approximation (GGA) implemented in the DFT ab-initio code VASP [208, 209].



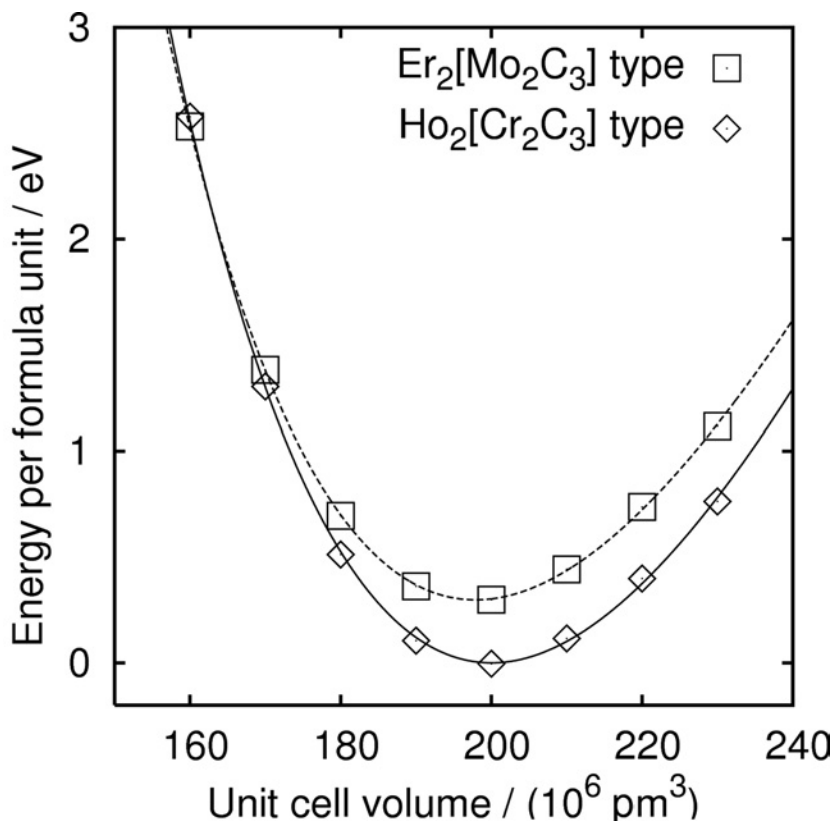


Figure 7.5: Normalized total energies of  $\text{Sm}_2[\text{Cr}_2\text{C}_3]$  with the *i*)  $\text{Ho}_2[\text{Cr}_2\text{C}_3]$  and the *ii*)  $\text{Er}_2[\text{Mo}_2\text{C}_3]$  structure type as a function of the unit cell volume.

Figure 7.5 shows the calculated total energy of  $\text{Sm}_2[\text{Cr}_2\text{C}_3]$  normalized to the minimum value as a function of the unit cell volumes. At the respective equilibrium volumes, the  $\text{Ho}_2[\text{Cr}_2\text{C}_3]$  type is more stable than the  $\text{Er}_2[\text{Mo}_2\text{C}_3]$  type by 0.30 eV/formula unit (29 kJ/mol). There are hints for a size effect: *i*) the  $\text{Er}_2[\text{Mo}_2\text{C}_3]$  type has only a marginally smaller equilibrium unit cell volume (approx. 1%) than the  $\text{Ho}_2[\text{Cr}_2\text{C}_3]$  type, *ii*) the  $\text{Er}_2[\text{Mo}_2\text{C}_3]$  type becomes more stable than the  $\text{Ho}_2[\text{Cr}_2\text{C}_3]$  type at a unit cell volume smaller than  $163.9 \cdot 10^6 \text{ pm}^3$ . However, this unit cell volume lies well outside the range observed for rare-earth carbochromates, the smallest one being that of  $\text{Lu}_2[\text{Cr}_2\text{C}_3]$  ( $V = 180.62(1) \cdot 10^6 \text{ pm}^3$ ), [242]. Therefore, the results of the total energy calculations confirm that  $\text{Sm}_2[\text{Cr}_2\text{C}_3]$  can adopt only the  $\text{Ho}_2[\text{Cr}_2\text{C}_3]$  structure type, which is consistent with the experimental observation.

## 7.6 Electronic structure and Chemical bonding analysis

Both, unpolarized and spin polarized calculations were carried out. The self-consistent TB-LMTO-ASA method [210] within the local (spin) density approximation (L(S)DA) [249] to the DFT was used to calculate the electronic structure in order to investigate the chemical bonding in  $\text{Sm}_2[\text{Cr}_2\text{C}_3]$ . Atomic sphere and empty sphere radii were determined according to the automatic procedure proposed in [250]. Chemical bonding was examined within the

framework of crystal orbital Hamilton population (COHP) analysis [133] and by analysis of the electron localizability indicator (ELI-D) [251–253].

Spin polarized (LSDA) calculations for  $\text{Sm}_2[\text{Cr}_2\text{C}_3]$  indicate a  $4f^5$  configuration for  $\text{Sm}^{3+}$  in agreement with the magnetization measurements. The calculated magnetic moment was  $12.55 \mu_B$  per unit cell, thereof  $5.51 \mu_B$  per Sm atom. Except for the Sm  $4f$  states, the electronic densities of states (DOS) of the majority and the minority spin channels are very similar. Therefore, it is adequate to consider the minority spin channel alone for the bonding analysis of  $\text{Sm}_2[\text{Cr}_2\text{C}_3]$ . The total and the partial DOS as well as COHP curves for selected orbital interactions for the minority spin channel of  $\text{Sm}_2[\text{Cr}_2\text{C}_3]$  are shown in *Figure 7.6*.

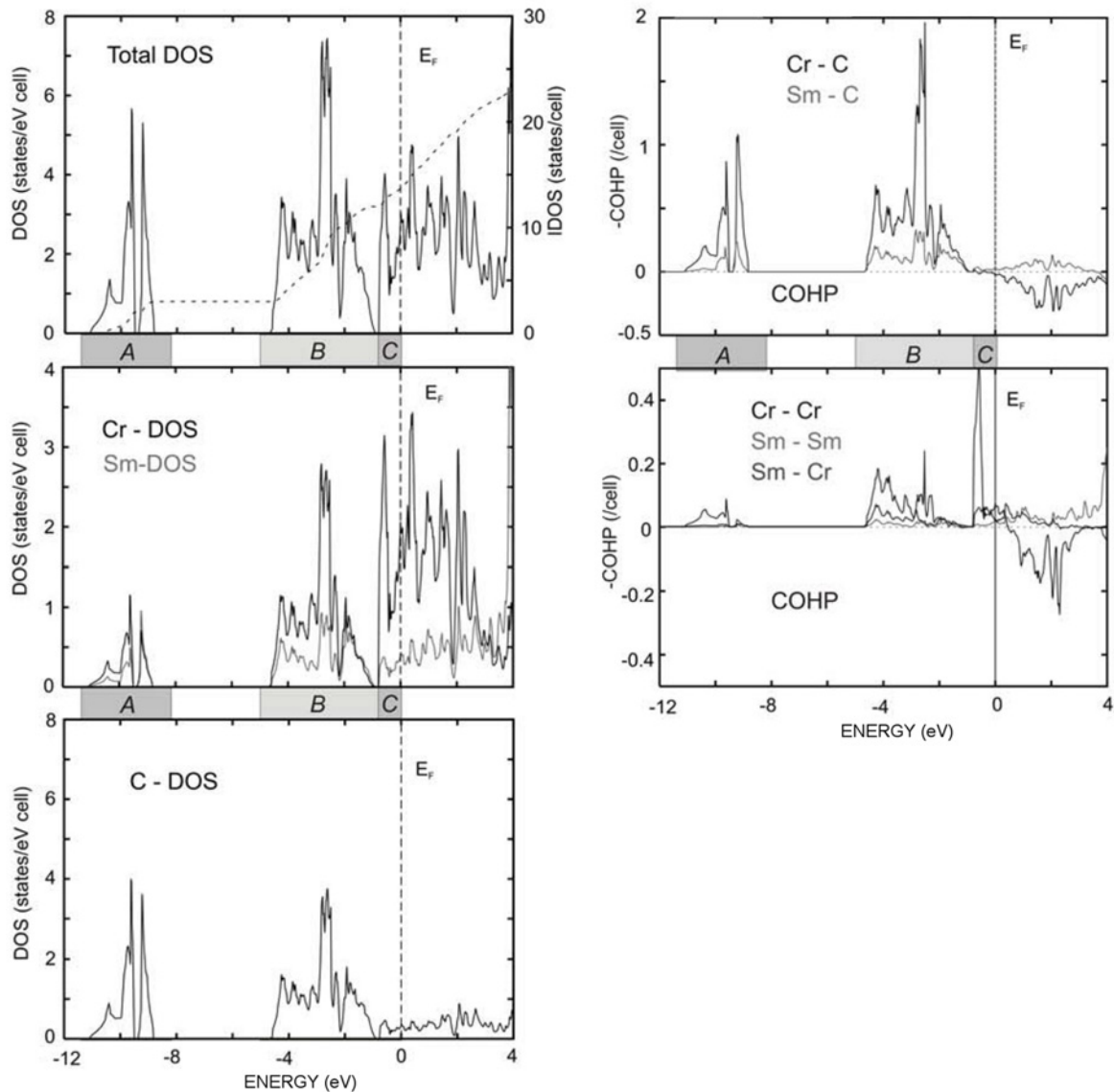


Figure 7.6: Total and projected DOS (left) and COHP (right) curves for selected orbital interactions for the minority spin direction of  $\text{Sm}_2[\text{Cr}_2\text{C}_3]$ . The total DOS of the valence electrons displays three different structures denoted **A**, **B** and **C** ranges.

$\text{Sm}_2[\text{Cr}_2\text{C}_3]$  shows metallic behavior. The states at the Fermi level are dominated by contributions from the metal atoms. One can divide the electronic density of states into three

ranges: Range **A** between -11 eV and -8 eV originates from the C 2s states with very small contributions of Cr 3d and Sm 6s, indicating a strongly localized character of these orbitals (*Figure 7.6.*, total DOS). In the range **B** between -5 eV and -1 eV, the C 2p orbitals dominate together with considerable Cr 3d and marginal Sm 5d contributions. The states just below the Fermi level in range **C** (between -1 eV up to  $E_F$ ) are dominated by Cr 3d with small contributions of Sm 5d states. Range **A** contains 3 e<sup>-</sup> and range **B** 9 e<sup>-</sup>, in total giving 12 e<sup>-</sup> per spin channel, i.e., 24 e<sup>-</sup> for both spin channels. Due to the weak contribution of Cr 3d, Sm 6s and 5d orbitals to the DOS in the ranges **A** and **B** all electrons in these ranges were counted on the carbon atoms. Thus, the 24 e<sup>-</sup> can be rationalized to three C atoms,  $24 e^- = 3 \times C 2s^2 2p^6$ , corresponding to C<sup>4-</sup> species. Range **C** contains 1.7 e<sup>-</sup> for the minority and 14.3 e<sup>-</sup> for the majority spin channels, respectively. In addition to the Cr 3d state, the majority spin channel contains the occupied 4f states of Sm. These 16 e<sup>-</sup> (= 1.7 e<sup>-</sup> + 14.3 e<sup>-</sup>) can be assigned to Cr<sup>3+</sup> (2 × Cr 3d<sup>3</sup> state) and Sm<sup>3+</sup> (2 × Sm 4f<sup>5</sup>), which are fully localized in the majority spin channel. From the analysis of the DOS it is concluded that the samarium atoms can conceptually be considered to transfer all valence electrons to the anionic part of the crystal structure. Thus, an idealized ionic formula can be written as: (Sm<sup>3+</sup>)<sub>2</sub>[(Cr<sup>3+</sup>)<sub>2</sub>(C<sup>4-</sup>)<sub>3</sub>].

Table 7.4: Sm<sub>2</sub>[Cr<sub>2</sub>C<sub>3</sub>]: Integrated crystal orbital Hamilton populations (-ICOHP [eV/bond]) for minority spin channel.

Interaction type	- ICOHP	Interaction type	- ICOHP
Sm – C1	0.768	Sm – Cr	0.153
Sm – C1	0.396	Sm – Cr	0.131
Sm – C2	0.685	Sm – Cr	0.094
Cr – C1	2.325	Sm – Sm	0.011
Cr – C1	1.810	Sm – Sm	0.028
Cr – C2	2.269	Cr – Cr	0.411

By analyzing the orbital interactions between the atoms with the COHP method, predominantly strong covalent Cr–C, weak Sm–C bonds and very weak metal–metal bonds are found. The ICOHP values are listed in *Table 7.4*. As shown in the right part of *Figure 7.6*, Cr–C bonds are completely exhausted even below range **C** indicating a strong covalent Cr–C bonding character. In contrast, Sm–C bonding states are still available above the Fermi level. Metal–metal interactions are weak, and the only significant contribution stems from Cr–Cr interactions which are exhausted approximately 1 eV above  $E_F$ . At this point, Sm–Sm and Sm–Cr contributions still have only weakly bonding character and are far away from bond saturation. By applying the classification criteria proposed in [9] to the results of the COHP analysis, Sm<sub>2</sub>[Cr<sub>2</sub>C<sub>3</sub>] is classified as a carbochromate: covalent Cr–C bonds dominate all other interactions and the ratio ICOHP(metal–C) : ICOHP(metal–metal) is equal to 10.

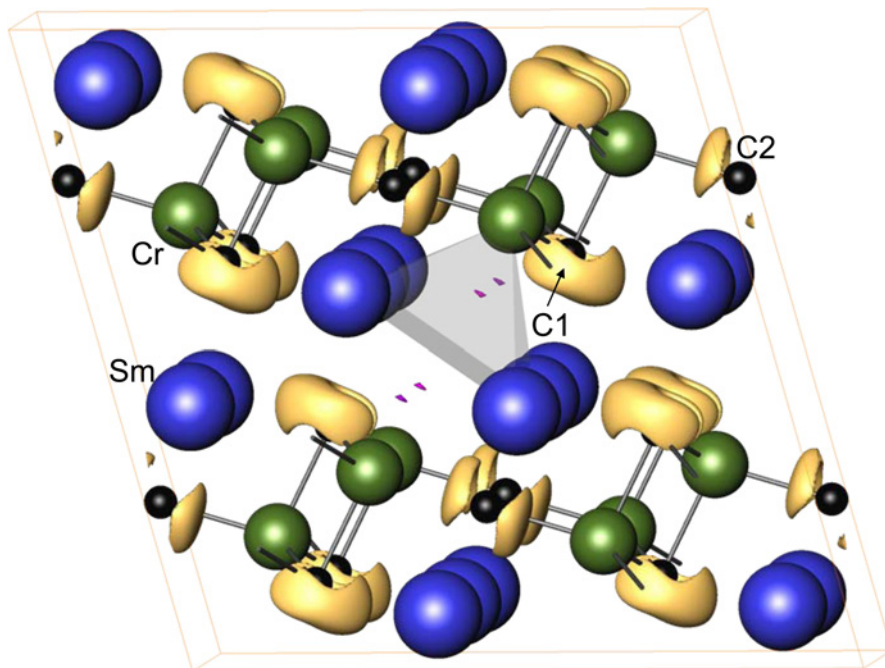


Figure 7.7: ELI-D picture of  $\text{Sm}_2[\text{Cr}_2\text{C}_3]$ : light brown domains at an isovalue  $Y_D = 1.41$  indicate covalent bonds Cr – C and lone pairs around C1 atoms; purple domains at an isovalue  $Y_D = 0.89$  close to the center of a square pyramid (1 Cr + 4 Sm) indicates a multi-center metal–metal bond situation.

Consistent with the COHP analysis, the ELI-analysis reveals two different attractor types in the anionic part of the structure (Figure 7.7). Light brown isosurfaces at  $Y_D = 1.41$  indicate covalent Cr–C bonds with both C1 and C2 atoms and lone pairs around C1. Additionally, at a lower isovalue ( $Y_D = 0.89$ ) small ELI maxima (small purple domains in Figure 7.7) are observed close to the center of the square pyramid formed by one Cr and four Sm atoms, indicating a multi-center metal–metal bond.

### 7.7 Summary

$\text{Sm}_2[\text{Cr}_2\text{C}_3]$  is a new member of the isotypic series  $RE_2[\text{Cr}_2\text{C}_3]$  ( $RE = \text{Y}, \text{Sm–Lu}$ ) crystallizing in the  $\text{Ho}_2[\text{Cr}_2\text{C}_3]$  structure type, and extending the series to larger  $RE$  cations. Up to now isotypic members with  $RE = \text{La–Nd}$  were not observed and the existence of these phases is still an open question. One of the possible reasons could be that the atoms ( $RE = \text{La–Nd}$ ) do not form a stable *bcc* metal matrix together with Cr because of the big size difference between rare earth and Cr atoms. In agreement with the experimental observations, the calculations confirm that the  $\text{Ho}_2[\text{Cr}_2\text{C}_3]$  structure type is preferred over the closely related  $\text{Er}_2[\text{Mo}_2\text{C}_3]$  structure type. A close inspection of the chemical bonding situation using both orbital based and real space analysis methods confirms that  $\text{Sm}_2[\text{Cr}_2\text{C}_3]$  is a carbochromate (III).

## 8 Summary

The main goal of this work was an explorative search for novel rare-earth transition metal compounds with special focus on compounds containing  $C_2^{n-}$ ,  $C_3^{m-}$  or mixed  $C^{4-}$  and  $C_2^{n-}$  as structural units in order to extend the recently established concept of carbometalates. In the scope of this work, eleven carbocompounds, crystallizing in four different structure types,  $Er_{15}[Fe_8C_{25}]$ ,  $Dy_{5.64}[Fe_2C_9]$ ,  $La_{3.67}[Fe(C_2)_3]$  and  $Ho_2[Cr_2C_3]$ , were successfully prepared and characterized using a wide spectrum of techniques.

The crystal structure of the isotypic ternary phases  $RE_{15}[Fe_8C_{25}]$  represents a new structure type, *hP48*. Four isotypic compounds were obtained with  $RE = Y, Dy, Ho, Er$ . The crystal structure contains two ligand types,  $C^{4-}$  and  $C_2^{4-}$ , and planar (magnetic)  $Fe_6$ -clusters which are characterized by covalent Fe–Fe bonds. This is the first example for a carbocompound containing trigonal and tetrahedral coordinated Fe atoms. The homonuclear  $Fe_6$  clusters represent a new structural unit in the crystal chemistry of iron compounds, which can be regarded as a fragment of the crystal structures of  $\gamma$ -Fe,  $\epsilon$ - $Fe_3C$  or  $\eta$ - $Fe_2C$ . The  $RE$  atoms between the clusters reveal significant contributions to Fe– $RE$  bonds in the sense of polar dative interactions. The integrated COHP analysis reveals strong covalent Fe–C bonds and weak metal–metal interactions. The ratio  $ICOHP(\text{metal–C}) / ICOHP(\text{metal–metal})$  is about 3 and  $ICOHP(\text{Fe–C})$  is much larger than  $ICOHP(\text{Y–C})$ . This is consistent with values observed for carbometalates [9]. Both, magnetic susceptibility measurements and the chemical bonding analysis shows that these compounds contain complex anions that are charge balanced by the rare-earth cations. The  $C_2$  units in the crystal structure of  $RE_{15}[Fe_8C_{25}]$ , are definitely not  $C_2^{2-}$ , but rather have  $C_2^{4-}$  character. Thus, altogether the (ionic) chemical formula of the cluster compounds can be written as  $(RE^{+3})_{15}[(Fe_6)^{5+}(Fe^{1+})_2(C_2^{4-})_{12}C^{4-}]$ . This results in a mean valence state of 0.83+ for the six iron atoms of the cluster unit, pointing out the general trend to low valence states of iron atoms in carbocompounds compared to nitridoferrates. Mössbauer investigations of  $Dy_{15}[Fe_8C_{25}]$  show the existence of three crystallographically different iron species, Fe1, Fe2 and Fe3, which is in agreement with the results of the crystal structure refinement. By considering the calculated electron densities at the nuclei of the Fe atoms, one expects that the valence state of the Fe atoms in  $RE_{15}[Fe_8C_{25}]$  would decrease in following sequence:  $Fe3 > Fe2 > Fe1$ . Low temperature Mössbauer studies confirm the local magnetic ordering of the Fe atoms.

The ternary rare-earth iron carbides  $RE_{5.64}[Fe_2C_9]$  ( $RE = Y, Gd, Tb, Dy$ ) also represent a new structure type. For the first time, two different types of complex anions, i.e., discrete trigonal planar  $[FeC(C_2)_2]$  units containing mixed carbo- ligands and infinite chains of distorted edge sharing  $[Fe(C_2)_{4/2}]$  tetrahedra, have been observed in one crystal structure. The crystal structure was treated as a composite of host  $\{Dy_5[Fe_2C_9]\}$ - and guest  $\{Dy_{0.64}\}$ - assembly sharing common (001) planes but with a mismatch along [001]. The

charge of the fairly rigid host structure seems to define the number of guest atoms and can be considered as the driving force for a modulation of infinite Dy-chains. Using the concept of the complex anions, a charge balanced ionic formula of the composite can be written as  $\{(\text{Dy})^{3+}_{0.67}\}\{(\text{Dy}^{3+})_5[\text{Fe}^{2+}(\text{C}_2)_{4/2}][\text{CFe}^{1+}(\text{C}_2)_2]\}$ , which reflects the general trend to low valence states. The compounds  $RE_{5.64}[\text{Fe}_2\text{C}_9]$  ( $RE = \text{Y, Gd, Tb, Dy}$ ) are bad-metals with paramagnetic behavior.

Additionally, a three-fold superstructure of the previously reported compound  $\text{La}_{3.67}[\text{T}(\text{C}_2)_3]$  ( $T = \text{Fe, Ru}$ ) [30] was experimentally observed and was studied by means of single crystal X-ray diffraction. It was found that even with a tripled unit cell, some disorder of the La guest atoms in the  $\text{La}_3[\text{T}(\text{C}_2)_3]$  host structure remains. Total energy calculations predict stable structures for  $\text{La}_{22}\text{T}_6\text{C}_{36}$  ( $\text{La}_{3.67}\text{T}(\text{C}_2)_3$ ) and  $\text{La}_{21}\text{T}_6\text{C}_{36}$  ( $\text{La}_{3.5}\text{T}(\text{C}_2)_3$ ) at 0 K, indicating a small homogeneity range at high temperatures. On the basis of electronic structure calculations and chemical bonding analyses using an ordered chain model, it is again possible to distinguish the anionic partial structure from the cations. Assuming the lack of metal–metal interactions the oxidation state +1 for  $T$  can be assigned which, again, shows the trend to form low oxidation states of transition metal in carbocompounds:  $(\text{La}^{3+})_{0.67}\text{La}^{3+}_3[\text{T}^{1+}(\text{C}_2)^{4-}_3]$ . However, in case of the isotypic phase  $\text{La}_{3.67}[\text{Ru}(\text{C}_2)_3]$ , La–C and La–Ru interactions become considerable. The Mössbauer parameters (isomer shift and quadrupole splitting) of  $\text{La}_{3.67}[\text{Fe}(\text{C}_2)_3]$  result in non-magnetic iron species on two crystallographically different sites, which is consistent with crystal structure refinements and the magnetic susceptibility measurements. The compounds can be used as a reference material for future Mössbauer investigations of binary and ternary iron carbides.

$\text{Sm}_2[\text{Cr}_2\text{C}_3]$  is a new member of the isotypic series  $RE_2[\text{Cr}_2\text{C}_3]$  ( $RE = \text{Y, Sm–Lu}$ ) with  $\text{Ho}_2[\text{Cr}_2\text{C}_3]$  structure type, which extends the isotypic series to larger  $RE$  cations. The structure contains polyanionic layers  ${}_{\infty}^2[(\text{Cr}_2\text{C}_3)^{6-}]$  which are charge balanced by  $\text{Sm}^{3+}$  cations. The polyanion consists of highly polarizable monoatomic  $\text{C}^{4-}$  ligands stabilizing lower valence state of chromium ( $\text{Cr}^{3+}$ ), compared to nitridochromates ( $\text{Cr}^{5+}$ ). A close inspection of the chemical bonding using orbital based and real space analysis methods reveals that  $\text{Sm}_2[\text{Cr}_2\text{C}_3]$  fully satisfies the criteria for carbometalates. Thus, according to IUPAC nomenclature rules,  $\text{Sm}_2[\text{Cr}_2\text{C}_3]$  is named a trisamarium carbochromate(III). The magnetic susceptibility and electrical resistivity data are consistent with the electronic structure and the chemical bonding analysis.

It seems that  $\text{C}_2$  units play an important role for the phase formation, phase stability and flexibility of ternary iron-rare-earth carbides with low valency Fe. Thus, theoretical and experimental investigations should be carried out on further examples in order to understand the nature of the chemical bonding in  $\text{C}_2$  units and to develop a classification scheme for the determination of the charges of  $\text{C}_2$  units.

All the compounds investigated in this work fulfill the following criteria which were originally defined for carbometalates [9]: *a*) the covalent  $T$ –C bonds are much stronger than the

*RE*-C bonds; *b*) the metal-carbon interactions are much stronger than metal-metal interaction; *c*) the crystal structures contain complex anions  $[(T_yC_2)^{n-}]$ ; *d*) the oxidation states of the *T*-atoms are low (e.g. Fe<sup>I</sup>, Fe<sup>II</sup>, Ru<sup>I</sup>). Based on these criteria the concept of carbometalates can be extended to compounds containing complex anions with mixed ligands, such as dicarbo ligands (C<sub>2</sub>) besides monoatomic C<sup>4-</sup>. Due to the high melting points, the synthesis and preparation of single phase materials of the compounds under investigation proved to be very challenging. However, satisfying quality materials could be prepared using conventional high temperature methods. Besides the conventional methods, high reactive-synthetic techniques, such as SPS (Spark Plasma Sintering) and metal flux (Ca, Ga, In, Sn, Bi) methods, should be tested for such systems in the future. Development of new methods and the optimization of the experimental conditions are very time consuming and need to receive more efforts in the future. It was shown that by means of ab-initio methods (VASP) not only the phase stability and homogeneity ranges can be examined, but also candidate phases could be predicted when appropriate models were included in the calculations. In the case of Y<sub>15</sub>[Fe<sub>8</sub>C<sub>25</sub>] it was shown that local ferromagnetism of planar Fe<sub>6</sub> clusters is energetically favored over a non magnetic phase, which later on could be confirmed experimentally. Furthermore, the calculated enthalpy of formation predicted the existence of La<sub>11</sub>Ru<sub>12</sub>C<sub>18</sub> and La<sub>7</sub>Ru<sub>4</sub>C<sub>9</sub> at 0 K. Such computational support will be considered in future works, since it is helpful not only for the explorative synthesis of novel materials, but will also contribute to fundamental understanding of structure-property-relationships. The compounds under investigations have shown significant metal-metal interactions combining low-dimensional anionic partial structures with low-valence states of transition metal atoms. The crystal structures of isotypic phases *RE*<sub>15</sub>[Fe<sub>8</sub>C<sub>25</sub>] contain planar (magnetic) Fe<sub>6</sub>-clusters whereas the ternary compounds of *RE*<sub>5.64</sub>[Fe<sub>2</sub>C<sub>9</sub>] and La<sub>3.67</sub>[Fe(C<sub>2</sub>)<sub>3</sub>] show low dimensional Fe-Fe and *RE*-Fe interactions. This opens a possibility to consider these compounds as structural derivatives of pure metallic iron and binary iron carbides, where metal-metal interactions are confined to lower-dimensional partial structures. An important focus will lie on the determination of the charge of the transition metal atoms and the carbon species. Experimental methods such as XPS (X-ray Photoelectron Spectroscopy), ARPES (Angle-Resolved Photoemission Spectroscopy) and EELS (Electron Energy Loss Spectroscopy), will give informations on the electronic structures of these materials in combination with DFT methods. Ternary rare-earth carbides are still only poorly explored. However, the present results show that these compounds reveal a large structural and chemical diversity, such as transition metal chains, cluster units, composite structures *etc.*, as well as interesting magnetic and chemical properties which have to be further studied systematically.

## 9 Appendix

### 9.1 Unit cell parameters of related binary compounds

Table 9.1: Unit cell parameters and unit cell volumes of compounds  $\beta$ - $RE_3C$  and  $\alpha$ - $RE_2C$ .

$\beta$ - $RE_3C$	$a / \text{pm}$	$V/10^6 \text{ pm}^3$	$\alpha$ - $RE_2C$	$a / \text{pm}$	$c / \text{pm}$	$V/10^6 \text{ pm}^3$
$Y_3C$	510.2(2)	132.8(1)	$Y_2C$	364.5(1)	1796.4(1)	204.4(1)
$Sm_3C$	517.2(1)	138.4(1)	$Gd_2C$	364.8(1)	1779.0(7)	205.0(1)
$Gd_3C$	512.6(5)	134.7(1)	$Tb_2C$	358.4(3)	1804.0(1)	200.7(1)
$Tb_3C$	510.7(2)	133.2(1)	$Dy_2C$	358.4(3)	1789.0(3)	199.0(2)
$Dy_3C$	507.9(5)	131.0(1)	$Ho_2C$	355.6(1)	1770.3(1)	193.9(1)
$Ho_3C$	506.1(2)	129.6(1)				
$Er_3C$	503.4(1)	127.6(1)				
$Tm_3C$	501.6(2)	126.2(1)				
$Yb_3C$	499.3(1)	124.5(1)				
$Lu_3C$	496.5(1)	122.4(1)				

Table 9.2: Unit cell parameters and unit cell volumes of the compounds  $RE_4C_3$ .

$RE_4C_3$	$a / \text{pm}$	$V/10^6 \text{ pm}^3$	$RE_4C_3$	$a / \text{pm}$	$V/10^6 \text{ pm}^3$
$Y_4C_3$	787.0(1)	487.4(1)	$Er_4C_3$	775.2(1)	465.9(1)
$Tb_4C_3$	782.0(1)	478.2(1)	$Tm_4C_3$	770.4(1)	457.3(1)
$Dy_4C_3$	784.0(1)	481.9(1)	$Yb_4C_3$	766.2(1)	449.8(1)
$Ho_4C_3$	780.0(1)	474.5(1)	$Lu_4C_3$	762.6(1)	443.4(1)

Table 9.3: Unit cell parameters and unit cell volumes of the compounds  $RE_3C_4$ .

$RE_3C_4$	$a / \text{pm}$	$c / \text{pm}$	$V/10^6 \text{ pm}^3$
$Ho_3C_4$	805.0(1)	1586.9(2)	1028.2(2)
$Er_3C_4$	798.8(1)	1578.5(3)	1007.3(2)
$Tm_3C_4$	793.0(1)	1573.0(4)	989.2(2)
$Yb_3C_4$	791.0(1)	1552.1(4)	970.7(2)
$Lu_3C_4$	785.0(1)	1563.3(2)	963.3(2)



Table 9.4: Unit cell parameters and unit cell volumes of the compounds  $RE_2C_3$ .

$RE_2C_3$	$a / \text{pm}$	$V/10^6 \text{ pm}^3$	$RE_2C_3$	$a / \text{pm}$	$V/10^6 \text{ pm}^3$
$Y_2C_3$	823.4(1)	558.2(1)	$Tb_2C_3$	825.3(1)	562.1(1)
$La_2C_3$	881.6(1)	685.2(1)	$Dy_2C_3$	820.6(1)	552.6(1)
$Ce_2C_3$	844.8(1)	602.8(1)	$Ho_2C_3$	816.3(2)	543.9(1)
$Pr_2C_3$	857.2(2)	629.9(1)	$Er_2C_3$	813.2(1)	537.8(1)
$Nd_2C_3$	853.4(5)	621.5(1)	$Tm_2C_3$	809.2(1)	529.8(1)
$Sm_2C_3$	842.5(1)	598.0(1)	$Yb_2C_3$	807.2(1)	526.0(1)
$Gd_2C_3$	833.2(1)	578.4(1)	$Lu_2C_3$	803.5(1)	518.8(1)

Table 9.5: Unit cell parameters and unit cell volumes of the compounds  $\alpha$ - $REC_2$ .

$\alpha$ - $REC_2$	$a / \text{pm}$	$c / \text{pm}$	$V/10^6 \text{ pm}^3$	$\alpha$ - $REC_2$	$a / \text{pm}$	$c / \text{pm}$	$V/10^6 \text{ pm}^3$
$YC_2$	366.4(1)	616.9(2)	82.8(1)	$GdC_2$	371.8(1)	627.5(4)	86.7(1)
$LaC_2$	393.5(1)	657.1(1)	101.8(1)	$TbC_2$	369.0(1)	621.6(4)	84.6(1)
$CeC_2$	387.7(1)	648.5(2)	97.5(1)	$DyC_2$	366.9(2)	617.1(4)	83.1(1)
$PrC_2$	384.7(3)	643.0(1)	95.2(1)	$HoC_2$	364.8(4)	614.4(4)	81.8(1)
$NdC_2$	381.7(2)	639.1(6)	93.1(1)	$ErC_2$	361.9(1)	609.7(1)	79.8(1)
$SmC_2$	376.7(1)	632.4(2)	89.7(1)	$TmC_2$	360.2(1)	604.0(1)	78.4(1)
$EuC_2$	408.2(4)	670.1(6)	111.7(1)	$YbC_2$	363.8(3)	611.2(5)	80.9(1)

Table 9.6: Unit cell parameters and unit cell volumes of the compounds  $\alpha$ - and  $\beta$ - $RE_4C_7$ .

$RE_4C_7$	$a / \text{pm}$	$b / \text{pm}$	$c / \text{pm}$	$\beta / ^\circ$	$V/10^6 \text{ pm}^3$
$\alpha$ - $Y_4C_7$	370.1(1)	1258.9(1)	1371.8(1)	96.6(1)	634.9(1)
$\alpha$ - $Ho_4C_7$	368.1(1)	1251.8(1)	1364.4(1)	96.6(1)	624.4(1)
$\beta$ - $Ho_4C_7$	371.1(1)	1363.6(2)	651.0(1)	102.8(1)	321.3(4)
$\beta$ - $Er_4C_7$	368.2(1)	1358.8(3)	644.9(1)	103.3(1)	314.0(3)
$\beta$ - $Tm_4C_7$	365.0(1)	1356.4(1)	636.1(1)	104.4(1)	305.1(4)
$\beta$ - $Lu_4C_7$	360.4(1)	1351.4(3)	629.0(2)	105.0(1)	296.0(5)

Table 9.7: Unit cell parameters and unit cell volumes of the phases  $RE_4C_5$ .

$RE_4C_5$	$a / \text{pm}$	$b / \text{pm}$	$c / \text{pm}$	$V/10^6 \text{ pm}^3$
$Y_4C_5$	657.6(1)	1191.8(1)	366.9(1)	287.5(2)
$Gd_4C_5$	666.7(1)	1208.4(2)	372.6(1)	300.2(4)
$Tb_4C_5$	660.8(1)	1197.3(2)	368.7(1)	291.7(1)
$Dy_4C_5$	657.4(1)	1190.5(1)	366.5(1)	286.9(3)
$Ho_4C_5$	653.0(1)	1184.6(1)	363.8(1)	281.4(4)

Table 9.8: Unit cell parameters and unit cell volumes of the rare-earth iron Laves phases.

C15	$a / \text{pm}$	$V/10^6 \text{ pm}^3$	C14	$a / \text{pm}$	$c / \text{pm}$	$V/10^6 \text{ pm}^3$
YFe <sub>2</sub>	735.6(1)	398.0(3)				
CeFe <sub>2</sub>	730.2(1)	389.3(1)				
PrFe <sub>2</sub>	746.7(4)	416.3(1)				
NdFe <sub>2</sub>	745.2(5)	413.8(1)				
SmFe <sub>2</sub>	741.5(4)	407.7(1)				
GdFe <sub>2</sub>	739.4(3)	404.2(1)				
TbFe <sub>2</sub>	734.5(6)	396.3(1)	TbFe <sub>2</sub>	527.0(2)	864.0(1)	207.8(1)
DyFe <sub>2</sub>	732.2(3)	392.6(1)				
HoFe <sub>2</sub>	730.3(6)	389.5(1)	HoFe <sub>2</sub>	530.0(2)	854.0(1)	207.8(1)
ErFe <sub>2</sub>	728.0(2)	385.8(1)	ErFe <sub>2</sub>	533.0(2)	857.0(1)	210.9(1)
TmFe <sub>2</sub>	724.7(5)	380.6(1)	TmFe <sub>2</sub>	529.0(2)	854.0(1)	207.0(1)
YbFe <sub>2</sub>	723.1(5)	378.1(1)	YbFe <sub>2</sub>	527.2(2)	848.7(5)	204.3(1)
LuFe <sub>2</sub>	722.9(2)	377.8(1)	LuFe <sub>2</sub>	527.0(2)	851.0(1)	204.7(1)

Table 9.9: Unit cell parameters and unit cell volumes of the compounds Th<sub>2</sub>Ni<sub>17</sub>- and Th<sub>2</sub>Zn<sub>17</sub>-type RE<sub>2</sub>Fe<sub>17</sub>.

Th <sub>2</sub> Ni <sub>17</sub>	$a / \text{pm}$	$c / \text{pm}$	$V/10^6 \text{ pm}^3$	Th <sub>2</sub> Zn <sub>17</sub>	$a / \text{pm}$	$c / \text{pm}$	$V/10^6 \text{ pm}^3$
Y <sub>2</sub> Fe <sub>17</sub>	846.3(1)	828.2(3)	513.7(1)	Y <sub>2</sub> Fe <sub>17</sub>	846.0(1)	1241.0(1)	769.2(1)
Ce <sub>2</sub> Fe <sub>17</sub>	849.0(1)	828.1(1)	516.9(1)	Ce <sub>2</sub> Fe <sub>17</sub>	849.2(1)	1243.2(1)	776.4(1)
Gd <sub>2</sub> Fe <sub>17</sub>	848.6(1)	834.9(1)	520.7(1)	Pr <sub>2</sub> Fe <sub>17</sub>	862.1(4)	1251.8(6)	805.0(1)
Tb <sub>2</sub> Fe <sub>17</sub>	846.7(1)	830.9(1)	515.9(1)	Nd <sub>2</sub> Fe <sub>17</sub>	858.1(1)	1246.5(1)	749.9(1)
Dy <sub>2</sub> Fe <sub>17</sub>	844.4(1)	831.0(1)	513.1(1)	Sm <sub>2</sub> Fe <sub>17</sub>	855.4(4)	1244.3(6)	788.5(2)
Ho <sub>2</sub> Fe <sub>17</sub>	843.4(1)	828.4(1)	510.3(1)	Gd <sub>2</sub> Fe <sub>17</sub>	853.8(1)	1243.4(1)	785.0(1)
Er <sub>2</sub> Fe <sub>17</sub>	842.3(1)	828.4(1)	509.0(1)	Tb <sub>2</sub> Fe <sub>17</sub>	849.0(1)	1242.0(1)	775.3(1)
Tm <sub>2</sub> Fe <sub>17</sub>	841.2(1)	827.8(1)	507.3(1)	Dy <sub>2</sub> Fe <sub>17</sub>	852.0(1)	1251.4(1)	786.4(1)
Yb <sub>2</sub> Fe <sub>17</sub>	840.6(1)	828.8(1)	507.2(1)				
Lu <sub>2</sub> Fe <sub>17</sub>	840.0(1)	826.2(1)	504.9(1)				

Table 9.10: Unit cell parameters and unit cell volumes of the compounds REFe<sub>7</sub>.

REC <sub>7</sub>	$a / \text{pm}$	$c / \text{pm}$	$V/10^6 \text{ pm}^3$
CeFe <sub>7</sub>	848.8(3)	1240.2(7)	773.8(1)
PrFe <sub>7</sub>	858.2(3)	1246.2(7)	794.9(1)
NdFe <sub>7</sub>	857.8(3)	1246.2(7)	794.1(1)
SmFe <sub>7</sub>	855.4(3)	1244.1(7)	788.4(1)

Table 9.11: Unit cell parameters and unit cell volumes of the compounds RE<sub>6</sub>Fe<sub>23</sub>.

RE <sub>6</sub> Fe <sub>23</sub>	$a / \text{pm}$	$V/10^6 \text{ pm}^3$	RE <sub>6</sub> Fe <sub>23</sub>	$a / \text{pm}$	$V/10^6 \text{ pm}^3$
Y <sub>6</sub> Fe <sub>23</sub>	1208.2(1)	1763.7(1)	Ho <sub>6</sub> Fe <sub>23</sub>	1202.9(1)	1740.6(1)
Sm <sub>6</sub> Fe <sub>23</sub>	1222.0(1)	1824.8(1)	Er <sub>6</sub> Fe <sub>23</sub>	1201.1(1)	1732.8(1)
Gd <sub>6</sub> Fe <sub>23</sub>	1208.7(1)	1765.9(1)	Tm <sub>6</sub> Fe <sub>23</sub>	1198.0(1)	1719.4(1)
Tb <sub>6</sub> Fe <sub>23</sub>	1207.0(1)	1758.4(1)	Yb <sub>6</sub> Fe <sub>23</sub>	1202.8(5)	1740.1(1)
Dy <sub>6</sub> Fe <sub>23</sub>	1205.6(1)	1752.5(1)	Lu <sub>6</sub> Fe <sub>23</sub>	1195.0(1)	1706.5(1)

Table 9.12: Unit cell parameters and unit cell volumes of the compounds  $REFe_5$ .

$REFe_5$	$a / \text{pm}$	$c / \text{pm}$	$V/10^6 \text{ pm}^3$
NdFe <sub>5</sub>	494.6(2)	417.0(3)	88.3(1)
SmFe <sub>5</sub>	496.0(1)	413.0(1)	88.0(1)
GdFe <sub>5</sub>	492.0(1)	411.0(1)	86.2(1)
HoFe <sub>5</sub>	493.3(1)	417.6(1)	88.0(1)

Table 9.13: Unit cell parameters and unit cell volumes of the  $PuNi_3$  type rare-earth iron binary phases.

$REFe_3$	$a / \text{pm}$	$c / \text{pm}$	$V/10^6 \text{ pm}^3$	$REFe_3$	$a / \text{pm}$	$c / \text{pm}$	$V/10^6 \text{ pm}^3$
YFe <sub>3</sub>	512.2(1)	2460.6(1)	559.1(1)	DyFe <sub>3</sub>	511.5(1)	2450.8(1)	555.3(1)
SmFe <sub>3</sub>	518.7(1)	2491.0(1)	580.4(1)	HoFe <sub>3</sub>	508.4(1)	2445.0(1)	547.3(1)
GdFe <sub>3</sub>	516.4(1)	2470.7(2)	570.9(1)	ErFe <sub>3</sub>	508.0(2)	2439.8(8)	545.3(1)
TbFe <sub>3</sub>	514.5(1)	2464.0(1)	564.9(1)	TmFe <sub>3</sub>	506.3(1)	2462.1(1)	546.6(1)

Table 9.14: Unit cell parameters and unit cell volumes of the  $RERu_2$  Laves phases.

C15	$a / \text{pm}$	$V/10^6 \text{ pm}^3$	C14	$a / \text{pm}$	$c / \text{pm}$	$V/10^6 \text{ pm}^3$
			YRu <sub>2</sub>	525.8(1)	882.4(1)	211.3(1)
LaRu <sub>2</sub>	770.3(1)	457.1(1)	NdRu <sub>2</sub>	529.3(1)	895.5(1)	217.3(1)
CeRu <sub>2</sub>	753.6(1)	428.0(1)	SmRu <sub>2</sub>	528.9(1)	894.6(1)	216.6(1)
PrRu <sub>2</sub>	762.4(1)	443.2(1)	GdRu <sub>2</sub>	527.5(1)	890.0(1)	214.5(1)
NdRu <sub>2</sub>	761.4(1)	441.4(1)	TbRu <sub>2</sub>	526.5(5)	885.3(8)	212.5(1)
SmRu <sub>2</sub>	758.0(1)	435.5(1)	DyRu <sub>2</sub>	525.5(1)	883.4(1)	211.3(1)
GdRu <sub>2</sub>	756.0(1)	432.1(1)	HoRu <sub>2</sub>	524.6(1)	882.0(1)	210.2(1)
			ErRu <sub>2</sub>	523.1(1)	878.5(1)	208.2(1)
			TmRu <sub>2</sub>	523.0(1)	874.0(8)	207.0(1)
			YbRu <sub>2</sub>	522.1(1)	874.6(8)	206.5(1)
			LuRu <sub>2</sub>	521.3(1)	873.2(1)	205.5(1)

Table 9.15: Unit cell parameters and unit cell volumes of the compounds  $RE_5Ru_2$ .

$RE_5Ru_2$	$a / \text{pm}$	$b / \text{pm}$	$c / \text{pm}$	$\beta / ^\circ$	$V/10^6 \text{ pm}^3$
Y <sub>5</sub> Ru <sub>2</sub>	1576.9(1)	634.1(1)	732.0(1)	97.2(1)	726.2(1)
La <sub>5</sub> Ru <sub>2</sub>	1679.0(1)	667.2(1)	742.2(1)	95.8(1)	827.2(1)
Pr <sub>5</sub> Ru <sub>2</sub>	1642.4(1)	654.5(1)	734.1(1)	96.5(1)	784.1(1)
Nd <sub>5</sub> Ru <sub>2</sub>	1629.5(1)	650.9(1)	734.2(1)	96.7(1)	773.5(1)
Sm <sub>5</sub> Ru <sub>2</sub>	1608.3(1)	643.8(1)	731.4(1)	96.9(1)	751.8(1)
Gd <sub>5</sub> Ru <sub>2</sub>	1593.9(1)	639.1(1)	732.4(1)	97.1(1)	740.4(1)
Tb <sub>5</sub> Ru <sub>2</sub>	1574.5(1)	631.8(1)	727.9(1)	97.2(1)	718.4(1)
Dy <sub>5</sub> Ru <sub>2</sub>	1567.6(1)	628.1(1)	727.8(1)	97.4(1)	710.7(1)
Ho <sub>5</sub> Ru <sub>2</sub>	1556.4(1)	625.1(1)	726.4(1)	97.3(1)	701.1(1)
Er <sub>5</sub> Ru <sub>2</sub>	1545.2(1)	620.7(1)	723.8(1)	97.4(1)	688.5(1)
Tm <sub>5</sub> Ru <sub>2</sub>	1536.2(1)	615.2(1)	722.9(1)	97.4(1)	677.4(1)
Lu <sub>5</sub> Ru <sub>2</sub>	1525.2(1)	610.9(1)	722.3(1)	97.4(1)	667.4(1)

Table 9.16: Unit cell parameters and unit cell volumes of the cementite type phases in the binary  $RE$ -Ru systems.

$RE_3Ru$	$a / \text{pm}$	$b / \text{pm}$	$c / \text{pm}$	$V/10^6 \text{ pm}^3$
$Y_3Ru$	731.3(1)	919.2(1)	632.3(1)	425.0(1)
$La_3Ru$	746.8(1)	1003.2(1)	655.5(1)	491.1(1)
$Ce_3Ru$	724.2(1)	986.3(1)	641.9(1)	458.5(1)
$Pr_3Ru$	737.9(8)	977.0(10)	643.5(9)	463.8(1)
$Nd_3Ru$	735.5(1)	967.5(1)	640.6(1)	455.9(1)
$Sm_3Ru$	733.0(1)	946.1(1)	633.4(1)	439.3(1)
$Gd_3Ru$	731.0(1)	935.0(1)	631.7(1)	431.8(1)
$Tb_3Ru$	725.5(2)	922.2(2)	627.1(2)	419.6(1)
$Dy_3Ru$	728.4(1)	915.1(1)	624.8(1)	416.5(1)
$Ho_3Ru$	727.7(1)	910.6(2)	623.5(2)	413.2(1)
$Er_3Ru$	726.2(1)	904.0(1)	620.0(1)	407.0(1)
$Tm_3Ru$	726.0(1)	898.6(1)	617.3(1)	402.7(1)
$Lu_3Ru$	724.7(1)	891.5(1)	613.1(1)	396.1(1)

Table 9.17: Unit cell parameters and unit cell volumes of the  $Er_3Ru_2$  type rare-earth iron binary compounds.

$RE_3Ru_2$	$a / \text{pm}$	$c / \text{pm}$	$V/10^6 \text{ pm}^3$	$RE_3Fe_2$	$a / \text{pm}$	$c / \text{pm}$	$V/10^6 \text{ pm}^3$
$Y_3Ru_2$	800.4(1)	399.8(1)	221.8(1)	$Er_3Ru_2$	787.5(2)	393.1(1)	211.1(1)
$Dy_3Ru_2$	795.3(1)	397.2(1)	217.6(1)	$Tm_3Ru_2$	784.4(1)	391.9(1)	208.8(1)
$Ho_3Ru_2$	791.9(1)	395.8(2)	215.0(1)	$Lu_3Ru_2$	778.8(2)	389.4(1)	204.5(1)

**9.2 Atomic coordinates, ADP, interatomic distances and bond angles for the crystal structure of  $RE_{15}[Fe_8C_{25}]$** Table 9.18:  $RE_{15}[Fe_8C_{25}]$  ( $RE = Dy$  and  $Ho$ ): Fractional atomic coordinates, equivalent isotropic displacement parameters [ $10^4 \text{ pm}^2$ ] and site occupancy; estimated standard deviations are given in parentheses.

Atom	Site	Occ.	x	y	z	$U_{eq.}$
<b>Dy<sub>15</sub>Fe<sub>8</sub>C<sub>25</sub></b>						
Dy1	6g	1	0.2878(1)	0.4037(1)	0.2539(2)	0.0066(1)
Dy2	6g	1	0.5123(1)	0.1439(1)	0.2454(1)	0.0064(1)
Dy3	3f	1	0.1694(1)	0	1/2	0.0091(2)
Fe1	3e	1	0.2496(1)	0	0	0.0105(5)
Fe2	3e	1	0.8681(2)	0	0	0.0079(5)
Fe3	2d	1	1/3	2/3	0.2628(9)	0.0059(5)
C1	6g	1	0.0796(12)	0.3974(11)	0.2404(32)	0.0105(19)
C2	6g	1	0.1662(10)	0.5243(11)	0.2594(30)	0.0053(17)
C3	6g	1	0.2975(12)	0.1918(13)	0.1887(21)	0.0086(24)
C4	6g	1	0.4184(10)	0.2956(9)	0.2371(31)	0.0065(19)
C5	2c	0.5	0	0	0.2348(92)	0.0106(71)
<b>Ho<sub>15</sub>Fe<sub>8</sub>C<sub>25</sub></b>						
Ho1	6g	1	0.2882(1)	0.4044(1)	0.2537(1)	0.0057(1)
Ho2	6g	1	0.5119(1)	0.1441(1)	0.2455(1)	0.0059(1)
Ho3	3f	1	0.1692(1)	0	1/2	0.0088(6)
Fe1	3e	1	0.2489(1)	0	0	0.0106(1)
Fe2	3e	1	0.8683(1)	0	0	0.0066(2)
Fe3	2d	1	1/3	2/3	0.2609(4)	0.0058(2)
C1	6g	1	0.0775(5)	0.3960(5)	0.2410(16)	0.0088(7)
C2	6g	1	0.1656(4)	0.5253(4)	0.2583(4)	0.0056(6)
C3	6g	1	0.3002(6)	0.1898(6)	0.1905(11)	0.0095(9)
C4	6g	1	0.4194(4)	0.2962(4)	0.2402(16)	0.0063(6)
C5	2c	0.5	0	0	0.2413(44)	0.0053(20)

Table 9.19:  $RE_{15}[\text{Fe}_8\text{C}_{25}]$  ( $RE = \text{Dy}, \text{Ho}, \text{Er}$ ): anisotropic displacement parameters  $U_{ij}$  [ $10^4 \text{ pm}^2$ ]; estimated standard deviations are given in parentheses.

Dy <sub>15</sub> [Fe <sub>8</sub> C <sub>25</sub> ]						
Atom	$U_{11}$	$U_{22}$	$U_{33}$	$U_{12}$	$U_{13}$	$U_{23}$
Dy1	0.0078(2)	0.0082(2)	0.0049(2)	-0.0009(3)	-0.0009(3)	0.0049(2)
Dy2	0.0077(3)	0.0075(2)	0.0045(2)	-0.0005(3)	-0.0001(3)	0.0041(2)
Dy3	0.0102(3)	0.0096(4)	0.0073(3)	0.0007(3)	0.0004(1)	0.0048(2)
Fe1	0.0100(1)	0.0152(13)	0.0083(9)	0.0051(11)	0.0026(5)	0.0076(7)
Fe2	0.0065(9)	0.0089(13)	0.0090(9)	-0.0006(1)	0	0.0045(6)
Fe3	0.0068(8)	0.0068(8)	0.0045(12)	0	0	0.0034(4)
C1	0.0105(2)					
C2	0.0053(17)					
C3	0.0086(24)					
C4	0.0065(19)					
C5	0.0106(71)					
Ho <sub>15</sub> [Fe <sub>8</sub> C <sub>25</sub> ]						
Atom	$U_{11}$	$U_{22}$	$U_{33}$	$U_{12}$	$U_{13}$	$U_{23}$
Ho1	0.0055(1)	0.0064(1)	0.0060(1)	-0.0006(1)	-0.0005(1)	0.0035(1)
Ho2	0.0060(1)	0.0065(1)	0.0056(1)	-0.0001(1)	-0.0003(1)	0.0034(1)
Ho3	0.0084(1)	0.0073(1)	0.0104(1)	0.0013(1)	0.0006(1)	0.0036(1)
Fe1	0.0088(3)	0.0140(5)	0.0106(4)	0.0037(5)	0.0018(2)	0.0070(2)
Fe2	0.0052(3)	0.0058(4)	0.0090(4)	0	0	0.0029(2)
Fe3	0.0050(3)	0.0050(3)	0.0075(5)	0	0	0.0025(1)
C1	0.0088(7)					
C2	0.0056(6)					
C3	0.0095(9)					
C4	0.0063(6)					
C5	0.0053(20)					
Er <sub>15</sub> [Fe <sub>8</sub> C <sub>25</sub> ]						
Atom	$U_{11}$	$U_{22}$	$U_{33}$	$U_{12}$	$U_{13}$	$U_{23}$
Er1	0.0046(1)	0.0054(1)	0.0049(1)	-0.0004(1)	-0.0004(1)	0.0030(1)
Er2	0.0048(1)	0.0054(1)	0.0047(1)	-0.0003(1)	-0.0002(1)	0.0028(1)
Er3	0.0068(3)	0.0061(1)	0.0076(1)	0.0010(4)	0.0005(1)	0.0030(1)
Fe1	0.0065(1)	0.0120(2)	0.0083(17)	0.0040(2)	0.0020(1)	0.0060(1)
Fe2	0.0043(1)	0.0045(1)	0.0077(15)	-0.0003(1)	-0.0002(1)	0.0023(1)
Fe3	0.0042(1)	0.0042(1)	0.0066(19)	0	0	0.0021(1)
C1	0.0061(5)	0.0072(5)	0.0093(7)	0.0006(8)	0.0009(8)	0.0035(4)
C2	0.0069(5)	0.0060(5)	0.0033(6)	-0.0005(6)	-0.0027(6)	0.0031(4)
C3	0.0072(6)	0.0072(6)	0.0087(8)	0.0033(6)	0.0022(6)	0.0016(5)
C4	0.0048(4)	0.0077(5)	0.0056(6)	0.0018(7)	0.0014(6)	0.0039(4)
C5	0.0063(10)	0.0063(10)	0.0080(20)	0	0	0.0031(5)

Table 9.20:  $Dy_{15}[Fe_8C_{25}]$ : interatomic distances, [pm]; estimated standard deviations are given in parentheses and  $n$  is the multiplicity.

Atom 1	Atom 2	$n$	Distance	Atom 1	Atom 2	$n$	Distance	
Dy1	C1	6×	244.91(1)	Dy1	Dy3	6×	340.62(1)	
	C4	6×	246.97(0)		Dy1	3×	348.38(1)	
	C2	6×	250.16(0)		Dy1	3×	354.22(1)	
	C4	6×	253.06(1)		Dy2	6×	363.14(1)	
	C3	6×	257.83(1)		Dy2	6×	363.65(1)	
	C2	6×	259.42(1)		Dy2	6×	366.66(1)	
	C3	6×	260.98(1)		Dy2	6×	367.15(1)	
	C4	6×	262.17(1)		Dy2	6×	370.24(1)	
Dy2	C4	6×	242.93(1)	Dy2	Dy2	6×	360.54(1)	
	C1	6×	250.97(0)		Dy3	6×	379.02(1)	
	C2	6×	255.84(1)		Dy2	3×	390.06(1)	
	C4	6×	255.99(0)		Dy2	3×	396.21(1)	
	C2	6×	260.59(1)	Dy3	Dy3	3×	349.95(1)	
	C1	6×	276.49(1)		Dy1	Fe3	6×	290.38(1)
	C1	6×	290.40(1)		Fe2	6×	310.50(1)	
	C3	6×	290.55(1)		Fe1	6×	324.93(1)	
Dy3	C5	6×	243.95(1)	Dy2	Fe1	6×	299.67(1)	
	C3	6×	257.47(1)		Fe3	6×	327.56(1)	
	C1	6×	273.87(1)		Fe3	6×	334.19(1)	
Fe1	C1	6×	196.23(0)	Dy3	Fe1	6×	274.38(1)	
	C3	6×	227.65(0)		Fe2	6×	316.11(1)	
Fe2	C5	6×	198.15(0)	Fe1	Fe2	6×	257.92(1)	
	C3	6×	198.3(1)		Fe2	Fe2	6×	272.49(1)
Fe3	C2	6×	186.3(1)					
C1	C2	6×	134.48(3)					
C3	C4	6×	137.52(3)					

Table 9.21:  $\text{Ho}_{15}[\text{Fe}_8\text{C}_{25}]$ : interatomic distances, [pm]; estimated standard deviations are given in parentheses and  $n$  is the multiplicity.

Atom 1	Atom 2	$n$	Distance	Atom 1	Atom 2	$n$	Distance	
Ho1	C1	6×	246.00(1)	Ho1	Ho3	6×	340.37(1)	
	C4	6×	247.23(0)		Ho1	3×	347.41(0)	
	C2	6×	251.1(1)		Ho1	3×	352.86(0)	
	C4	6×	252.76(0)		Ho2	6×	361.45(0)	
	C2	6×	256.57(1)		Ho2	6×	362.06(0)	
	C3	6×	256.98(0)		Ho2	6×	364.42(0)	
	C4	6×	258.99(0)		Ho2	6×	365.03(0)	
	C3	6×	264.76(1)		Ho2	6×	369.85(1)	
Ho2	C4	6×	241.81(1)	Ho2	Ho2	6×	360.01(1)	
	C1	6×	248.74(0)		Ho3	6×	377.86(1)	
	C2	6×	254.44(0)		Ho2	3×	388.72(1)	
	C4	6×	254.71(0)		Ho2	3×	394.73(1)	
	C2	6×	258.32(0)		Ho3	3×	348.80(1)	
	C1	6×	275.94(0)		Ho1	Fe3	6×	289.18(1)
	C3	6×	284.63(1)			Fe2	6×	310.44(1)
	C1	6×	288.41(0)			Fe1	6×	324.40(1)
Ho3	C5	6×	241.08(0)	Ho2	Fe1	6×	299.08(1)	
	C3	6×	255.21(0)		Fe3	6×	326.78(0)	
	C1	6×	271.99(0)		Fe3	6×	331.81(0)	
Fe1	C1	6×	195.35(0)	Ho3	Fe1	6×	272.46(0)	
	C3	6×	224.63(0)		Fe2	6×	314.31(0)	
Fe2	C5	6×	199.18(0)	Fe1	Fe2	6×	256.74(1)	
	C3	6×	201.48(0)		Fe2	Fe2	6×	271.52(1)
Fe3	C2	6×	186.03(0)					
C1	C2	6×	136.46(3)					
C3	C4	6×	137.34(3)					



Table 9.22:  $Er_{15}[Fe_8C_{25}]$ : interatomic distances, [pm]; estimated standard deviations are given in parentheses and  $n$  is the multiplicity.

Atom 1	Atom 2	$n$	Distance	Atom 1	Atom 2	$n$	Distance	
Er1	C1	6×	245.3(2)	Er1	Er3	6×	339.5(1)	
	C4	6×	245.5(2)		Er1	3×	346.1(1)	
	C2	6×	250.6(2)		Er1	3×	347.1(1)	
	C4	6×	251.4(3)		Er2	6×	358.2(1)	
	C2	6×	255.5(2)		Er2	6×	360.9(1)	
	C3	6×	257.6(2)		Er2	6×	363.4(1)	
	C4	6×	258.4(3)		Er2	6×	368.8(1)	
	C3	6×	263.6(2)		Er2	6×	376.6(0)	
	Er2	C4	6×		240.6(2)	Er2	Er2	6×
C1		6×	248.1(2)	Er3	6×		379.1(1)	
C2		6×	252.7(3)	Er2	3×		390.1(1)	
C4		6×	254.1(2)	Er2	3×		396.2(1)	
C2		6×	257.8(3)	Er3	3×		349.8(1)	
C1		6×	275.4(3)	Er1	Fe3		6×	288.0(1)
C3		6×	283.5(2)		Fe2		6×	309.3(1)
C1		6×	286.5(3)		Fe1		6×	323.4(1)
Er3		C5	6×	240.0(6)	Er2		Fe1	6×
	C3	6×	253.1(2)	Fe3		6×	325.2(1)	
	C1	6×	271.0(2)	Fe3		6×	330.6(1)	
Fe1	C1	6×	195.4(3)	Er3	Fe1	6×	271.5(1)	
	C3	6×	224.3(3)		Fe2	6×	313.0(1)	
Fe2	C5	6×	198.5(6)	Fe1	Fe2	6×	255.7(1)	
	C3	6×	200.7(2)		Fe2	Fe2	6×	270.9(1)
Fe3	C2	6×	186.6(2)					
C1	C2	6×	134.7(3)					
C3	C4	6×	137.8(3)					

Table 9.23:  $RE_{15}[Fe_8C_{25}]$  ( $RE = Dy, Ho, Er$ ): bond angles in the polyanionic partial structure; estimated standard deviations are given in parentheses and  $A1, A2, A3$  denote the atoms defining the angle

Dy <sub>15</sub> Fe <sub>8</sub> C <sub>25</sub>				Ho <sub>15</sub> Fe <sub>8</sub> C <sub>25</sub>				Er <sub>15</sub> Fe <sub>8</sub> C <sub>25</sub>			
A1	A2	A3	Angle [°]	A1	A2	A3	Angle [°]	A1	A2	A3	Angle [°]
Fe1	C1	C1	97.98(1)	Fe1	C1	C1	97.43(0)	Fe1	C1	C1	97.5(1)
	C1	C3	93.98(1)		C1	C3	103.66(1)		C1	C3	103.32(9)
	C1	C3	105.14(1)		C1	C3	93.97(0)		C1	C3	94.39(9)
	C1	Fe2	141.08(1)		C1	Fe2	110.10(1)		C1	Fe2	110.07(7)
	C1	Fe2	109.65(1)		C1	Fe2	140.93(0)		C1	Fe2	140.83(7)
	C3	C3	150.82(1)		C3	C3	153.25(0)		C3	C3	153.07(8)
	C3	Fe2	104.20(1)		C3	Fe2	105.32(0)		C3	Fe2	105.21(6)
	C3	Fe2	47.70(1)		C3	Fe2	48.93(0)		C3	Fe2	48.91(6)
	Fe2	Fe2	63.78(1)		Fe2	Fe2	63.85(1)		Fe2	Fe2	63.97(1)
Fe2	C5	C5	74.89(1)	Fe2	C5	C5	76.18(0)	Fe2	C5	C5	75.98(1)
	C5	C3	146.55(1)		C5	C3	145.56(0)		C5	C3	145.71(7)
	C5	C3	103.89(1)		C5	C3	103.23(1)		C5	C3	102.89(8)
	C5	Fe1	88.50(1)		C5	Fe1	88.49(0)		C5	Fe1	88.44(0)
	C5	Fe2	46.56(1)		C5	Fe2	47.03(0)		C5	Fe2	46.96(1)
	C5	C3	103.89(1)		C5	C3	103.23(1)		C5	C3	102.89(8)
	C5	C3	146.55(1)		C5	C3	145.56(0)		C5	C3	145.71(7)
	C3	C3	94.84(1)		C3	C3	95.96(0)		C3	C3	96.54(9)
	C3	Fe1	124.94(1)		C3	Fe1	125.93(0)		C3	Fe1	125.85(6)
	C3	Fe1	58.12(1)		C3	Fe1	57.19(0)		C3	Fe1	57.35(6)
	C3	Fe2	108.10(1)		C3	Fe2	107.30(0)		C3	Fe2	107.16(7)
	C3	Fe2	149.47(1)		C3	Fe2	149.54(0)		C3	Fe2	149.08(7)
	Fe1	Fe1	176.22(1)		Fe1	Fe1	176.15(1)		Fe1	Fe1	176.03(1)
	Fe1	Fe2	118.11(1)		Fe1	Fe2	118.08(1)		Fe1	Fe2	118.02(1)
	Fe1	Fe2	58.11(1)		Fe1	Fe2	58.08(1)		Fe1	Fe2	58.02(1)
Fe2	Fe2	60.00(1)	Fe2	Fe2	60.00(1)	Fe2	Fe2	60.00(1)			
Fe3	C2	C2	119.99(1)	Fe3	C2	C2	119.20(1)	Fe3	C2	C2	120.03(8)
	C1	C2	144.32(1)		C1	C2	143.50(2)		C1	C2	143.43(2)
	C2	C1	153.86(2)		C2	C1	153.19(1)		C2	C1	152.90(1)
	C3	C4	145.03(2)		C3	C4	142.99(0)		C3	C4	142.07(2)
	C4	Fe1	127.23(1)		C4	Fe1	130.05(0)		C4	Fe1	129.72(2)
	Fe2	Fe1	74.17(1)		Fe2	Fe1	73.88(1)		Fe2	Fe1	73.74(8)
C5	Fe2	Fe2	86.88(1)	C5	Fe2	Fe2	85.94(1)	C5	Fe2	Fe2	86.09(0)
	Fe2	C5	52.56(1)		Fe2	C5	51.91(0)		Fe2	C5	52.01(1)
	Fe2	C5	127.44(1)		Fe2	C5	128.09(0)		Fe2	C5	127.99(1)
	Fe2	Fe2	86.88(1)		Fe2	Fe2	85.94(1)		Fe2	Fe2	86.09(1)
	C5	C5	180		C5	C5	180		C5	C5	180

### 9.3 Modulation functions, ADP and interatomic distances in the crystal structure of Dy<sub>5.64</sub>[Fe<sub>2</sub>C<sub>9</sub>]

Table 9.24: Dy<sub>5.64</sub>[Fe<sub>2</sub>C<sub>9</sub>]: anisotropic displacement parameters  $U_{ij}$  [ $10^4$  pm<sup>2</sup>]; estimated standard deviations are given in parentheses.

Atom	$U_{11}$	$U_{22}$	$U_{33}$	$U_{12}$	$U_{13}$	$U_{23}$
Host structure: {Dy <sub>5</sub> [Fe <sub>2</sub> C <sub>9</sub> ]}						
Dy1	0.0073(2)	0.0104(2)	0.0080(3)	0.0001(2)	0	0
Dy2	0.0085(2)	0.0086(2)	0.0084(3)	0.0003(2)	0	0
Dy3	0.0086(2)	0.0077(2)	0.0088(3)	-0.0013(2)	0	0
Dy4	0.0083(2)	0.0083(2)	0.0077(3)	0.0008(2)	0	0
Dy5	0.0100(2)	0.0093(2)	0.0086(3)	0.0003(2)	0	0
Dy6	0.0070(2)	0.0087(2)	0.0097(3)	0.0017(2)	0	0
Dy7	0.0120(2)	0.0088(2)	0.0096(3)	0.0016(2)	0	0
Dy8	0.0095(2)	0.0068(2)	0.0081(3)	0.0012(2)	0	0
Dy9	0.0071(2)	0.0064(2)	0.0091(3)	0.0005(2)	0	0
Dy10	0.0085(2)	0.0103(3)	0.0081(3)	0.0012(2)	0	0
Fe1	0.0071(6)	0.0058(7)	0.0066(8)	0.0005(5)	0	0
Fe2	0.0035(6)	0.0057(7)	0.0055(8)	-0.0018(5)	0	0
Fe3	0.0090(4)	0.0082(6)	0.0079(6)	0.0004(4)	-0.002(1)	-0.002(1)
C1	0.012(4)	0.012(4)	0.012(5)	0.000(3)	0	0
C2	0.024(5)	0.015(5)	0.011(6)	-0.004(4)	0	0
C3	0.015(4)	0.011(4)	0.014(5)	-0.001(3)	0	0
C4	0.007(4)	0.013(4)	0.013(5)	-0.000(3)	0	0
C5	0.017(4)	0.008(4)	0.014(6)	-0.001(3)	0	0
C6	0.012(4)	0.008(4)	0.016(5)	0.000(3)	0	0
C7	0.014(4)	0.012(4)	0.012(5)	0.004(3)	0	0
C8	0.018(4)	0.010(4)	0.012(6)	0.004(3)	0	0
C9	0.011(4)	0.015(5)	0.014(5)	0.001(3)	0	0
C10	0.018(4)	0.012(4)	0.012(5)	0.006(3)	0	0
C11	0.010(4)	0.019(5)	0.010(5)	0.000(3)	0	0
C12	0.015(4)	0.015(5)	0.011(5)	0.003(3)	0	0
C13	0.016(4)	0.011(4)	0.012(6)	0.003(3)	0	0
C14	0.020(4)	0.013(5)	0.009(5)	0.001(3)	0	0
C15	0.013(4)	0.016(5)	0.017(6)	0.001(3)	0	0
C16	0.014(4)	0.029(6)	0.014(6)	0.001(4)	0	0
C17	0.022(5)	0.013(5)	0.015(6)	-0.006(4)	0	0
C18	0.026(5)	0.021(6)	0.016(6)	0.010(4)	0	0
Guest structure: {Dy <sub>0.64</sub> }						
Dy11	0.0036(3)	0.0046(3)	0.0033(8)	-0.0005(3)	0	0
Dy12	0.0037(5)	0.0035(5)	0.0030(7)	-0.0004(4)	0	0

Table 9.25: Dy<sub>5.64</sub>[Fe<sub>2</sub>C<sub>9</sub>]: interatomic distances, [pm]; estimated standard deviations are given in parentheses and *n* is the multiplicity.

Atom 1	Atom 2	<i>n</i>	Distance	Atom 1	Atom 2	<i>n</i>	Distance
Host structure: {Dy <sub>5</sub> [Fe <sub>2</sub> C <sub>9</sub> ]}							
Dy1	Dy4	2×	349.47(1)	Dy3	C2	1×	250.49(1)
	Dy7	2×	353.32(1)		C11	1×	252.12(1)
	Dy3	2×	358.52(1)		C4	1×	252.35(1)
	Dy5	1×	359.97(1)		C10	2×	257.71(1)
	Dy10	1×	375.89(1)		C16	2×	272.44(1)
	Dy8	1×	383.61(1)		C18	1×	277.80(1)
Dy2	Dy4	1×	359.85(1)	Dy4	C3	1×	246.94(1)
	Dy9	2×	369.97(1)		C4	1×	248.98(1)
	Dy2	2×	377.43(1)		C1	1×	250.46(1)
	Dy3	2×	385.32(1)		C6	2×	252.07(1)
Dy3	Dy4	1×	351.28(1)	Dy5	C7	1×	239.27(1)
	Dy1	2×	358.52(1)		C8	2×	255.24(1)
	Dy10	2×	383.14(1)		C18	1×	255.82(1)
	Dy2	2×	385.32(1)		C5	1×	271.13(1)
Dy4	Dy1	2×	349.47(1)	Dy6	C17	2×	271.22(1)
	Dy8	2×	350.92(1)		C12	1×	248.39(1)
	Dy3	1×	351.28(1)		C8	1×	251.29(1)
	Dy9	2×	351.72(1)		C5	2×	252.23(1)
	Dy2	1×	359.85(1)		C7	1×	257.76(1)
	Dy8	1×	370.12(1)		C11	1×	265.98(1)
Dy5	Dy7	1×	399.07(1)	Dy7	C17	1×	266.47(1)
	Dy1	1×	359.97(1)		C13	2×	282.00(1)
	Dy7	2×	368.05(1)		C4	1×	247.97(1)
	Dy6	2×	369.50(1)		C7	2×	254.28(1)
	Dy10	1×	383.14(1)		C13	1×	262.75(1)
	Dy6	1×	389.93(1)		C8	1×	268.77(1)
Dy6	Dy10	2×	394.17(1)	Dy8	C5	1×	271.28(1)
	Dy10	2×	354.96(1)		C12	2×	275.24(1)
	Dy5	2×	369.50(1)		C9	1×	295.34(1)
	Dy7	2×	369.75(1)		C3	1×	245.51(1)
Dy7	Dy5	1×	389.93(1)	Dy9	C6	1×	245.60(1)
	Dy1	2×	353.32(1)		C3	2×	252.53(1)
	Dy5	2×	368.05(1)		C15	1×	258.97(1)
	Dy6	2×	369.75(1)		C1	1×	275.94(1)
	Dy10	1×	382.06(1)		C9	2×	279.53(1)
Dy8	Dy4	1×	399.07(1)	Dy9	C14	1×	245.14(1)
	Dy9	1×	345.53(1)		C6	1×	245.82(1)
	Dy4	2×	350.92(1)		C9	1×	251.40(1)
	Dy8	2×	362.63(1)		C1	2×	252.46(1)
	Dy9	2×	364.34(1)		C2	1×	253.11(1)
	Dy4	1×	370.12(1)		C3	1×	260.31(1)
	Dy1	1×	383.61(1)		C15	2×	283.94(1)

9.3 Modulation functions, ADP and interatomic distances in the crystal structure of Dy<sub>5.64</sub>[Fe<sub>2</sub>C<sub>9</sub>]65

Dy9	Dy8	1×	345.53(1)	Dy10	C5	1×	240.99(1)
	Dy4	2×	351.72(1)		C16	1×	255.97(1)
	Dy8	2×	364.34(1)		C11	2×	257.27(1)
	Dy2	2×	369.97(1)		C17	1×	258.03(1)
Dy10	Dy6	2×	354.96(1)		C18	2×	271.25(1)
	Dy1	1×	375.89(1)			×	
	Dy7	1×	382.06(1)	Fe3	Fe3	2×	252.07(2)
	Dy3	2×	383.14(1)			×	
	Dy5	1×	383.14(1)			×	
	Dy5	2×	394.17(1)	Fe1	C11	1×	181.85(1)
Dy1	Fe2	1×	295.35(1)		C8	1×	184.4(1)
	Fe1	2×	319.86(1)		C4	1×	189.62(1)
Dy2	Fe2	1×	294.61(1)	Fe2	C10	1×	182.92(0)
	Fe2	2×	336.49(1)		C14	1×	185.68(1)
Dy3	Fe1	1×	292.55(1)		C6	1×	193.24(1)
	Fe2	2×	341.82(1)	Fe3	C9	1×	198.16(1)
Dy4	Fe2	2×	318.45(1)		C12	1×	199.53(1)
Dy5	Fe1	2×	336.58(1)		C13	1×	202.44(1)
Dy6	Fe1	1×	293.42(1)		C15	1×	204.38(1)
	Fe3	2×	304.35(1)			×	
Dy7	Fe1	1×	292.23(1)	C1	C15	1×	129.66(0)
	Fe3	2×	293.15(1)	C2	C14	1×	130.96(0)
Dy8	Fe3	2×	299.92(1)	C3	C9	1×	134.12(0)
Dy9	Fe2	1×	290.05(1)	C5	C13	1×	135.13(0)
	Fe3	2×	310.97(1)	C7	C12	1×	134.86(0)
Dy10	Fe1	2×	338.77(1)	C8	C17	1×	131.66(0)
Dy1	C6	1×	241.20(1)	C9	C3	1×	134.12(0)
	C4	2×	252.18(1)	C10	C16	1×	133.78(0)
	C7	1×	264.41(1)	C11	C18	1×	130.60(1)
	C10	1×	267.86(1)	C12	C7	1×	134.86(0)
Dy2	C14	2×	255.43(1)	C13	C5	1×	135.13(0)
	C10	1×	255.64(1)	C14	C2	1×	130.96(0)
	C1	1×	257.89(1)	C15	C1	1×	129.66(0)
	C16	1×	271.98(1)	C16	C10	1×	133.78(0)
	C2	2×	273.80(1)	C17	C8	1×	131.66(0)
	C14	1×	286.53(1)	C18	C11	1×	130.60(1)
Guest structure: {Dy <sub>0.64</sub> }							
Dy11	Dy12	1×	333.21(2)				
	Dy11	1×	389.75(2)				
Dy12	Dy11	2×	333.21(2)				

Table 9.26: Dy<sub>5.64</sub>[Fe<sub>2</sub>C<sub>9</sub>]: Modulation functions for the atomic positions ( $u(\bar{x}_4)$ ) and site occupancy ( $p(\bar{x}_4)$ ). Here,  $n$  is the order of the satellite reflections, and A, B are Fourier coefficients.

Host structure: {Dy <sub>5</sub> [Fe <sub>2</sub> C <sub>9</sub> ]}		
Site	Modulation functions along $x, y, z$	
4c: (x,y,1/4)	$u(\bar{x}_4)_{x,y} = \sum_n A_{x,y} \cos(2n\pi\bar{x}_4), u(\bar{x}_4)_z = \sum_n B_z \sin(2n\pi\bar{x}_4)$	
8d: (x,y,z)	$u(\bar{x}_4)_{x,y,z} = \sum_n (A_{x,y,z} \cos(2n\pi\bar{x}_4) + B_{x,y,z} \sin(2n\pi\bar{x}_4))$	
Guest structure: {Dy <sub>0.64</sub> }		
Site	Even order ( $n$ )	Odd order ( $n$ )
4g: (x,y,0)	$u(\bar{x}_4)_{x,y} = \sum_n A_{x,y} \cos(2n\pi\bar{x}_4)$	$u(\bar{x}_4)_{x,y} = \sum_n A_{x,y} \sin(2n\pi\bar{x}_4)$
	$u(\bar{x}_4)_z = \sum_n B_z \sin(2n\pi\bar{x}_4)$	$u(\bar{x}_4)_z = \sum_n B_z \cos(2n\pi\bar{x}_4)$
	$p(\bar{x}_4) = \sum_n A_p \cos(2n\pi\bar{x}_4)$	$p(\bar{x}_4) = \sum_n B_p \sin(2n\pi\bar{x}_4)$
8i: (x,y,z)	$u(\bar{x}_4)_{x,y,z} = \sum_n (A_{x,y,z} \cos(2n\pi\bar{x}_4) + B_{x,y,z} \sin(2n\pi\bar{x}_4))$	

Table 9.27: Dy<sub>5.64</sub>[Fe<sub>2</sub>C<sub>9</sub>]: modulation amplitudes for displacement and occupational modulation functions.

Displacement amplitudes of host structure atoms: {Dy <sub>5</sub> [Fe <sub>2</sub> C <sub>9</sub> ]}							
Atom	n	A <sub>x</sub>	A <sub>y</sub>	A <sub>z</sub>	B <sub>x</sub>	B <sub>y</sub>	B <sub>z</sub>
Dy1	1	0.0018(0)	-0.0028(1)				
	2	0.0013(1)	-0.0005(1)				-0.0057
Dy2	1	0.0022(1)	0.0030(1)				0.0072(2)
	2	0.0033(1)	0.0013(1)				0.0042(3)
Dy3	1	-0.0010(1)	-0.0059(1)				-0.0027(2)
	2	0.0019(1)	0.0022(1)				0.0050(3)
Dy4	1	0.0001(1)	-0.0010(1)				0.0001(2)
	2	0.0019(1)	0.0014(1)				-0.0003(3)
Dy5	1	-0.0010(1)	0.0004(1)				-0.0023(2)
	2	0.0013(1)	-0.0012(2)				0.0050(3)
Dy6	1	0.0000(1)	0.0029(1)				0.0066(2)
	2	0.0021(1)	-0.0018(1)				-0.0059(3)
Dy7	1	0.0018(1)	0.0018(1)				-0.0063(2)
	2	0.0019(1)	-0.0009(1)				0.0007(3)
Dy8	1	-0.0007(1)	-0.0002(1)				0.0030(2)
	2	0.0016(1)	-0.0026(1)				0.0009(3)
Dy9	1	0.0012(1)	-0.0043(1)				-0.0087(2)
	2	0.0021(1)	0.0003(1)				-0.0028(3)
Dy10	1	-0.0018(1)	0.0058(1)				0.0037(2)
	2	0.0010(1)	0.0016(1)				0.0071(3)
Fe1	1	-0.0016(1)	-0.0097(2)				0.0057(6)
Fe2	1	0.0051(1)	0.0030(2)				-0.0051(6)
Fe3	1	-0.0002(1)	-0.0027(2)	-0.0033(4)	-0.0008(1)	-0.0084(1)	-0.0066(5)
	2	-0.0004(1)	0.0022(2)	0.0068(8)	0.0006(1)	-0.0053(3)	0.0004(5)

9.3 Modulation functions, ADP and interatomic distances in the crystal structure of Dy<sub>5.64</sub>[Fe<sub>2</sub>C<sub>9</sub>]67

C1	1	-0.0011(9)	-0.002(2)		-0.015(6)		
	2	0.003(1)	0.001(4)		0.029(7)		
C2	1	0.002(1)	0.001(2)		-0.009(6)		
	2	0.006(1)	0.000(4)		0.008(9)		
C3	1	-0.0027(9)	0.001(2)		0.016(6)		
	2	0.003(1)	-0.004(4)		0.011(8)		
C4	1	-0.0052(7)	-0.009(2)		0.000(6)		
	2	0.001(1)	0.004(4)		0.001(8)		
C5	1	-0.0015(9)	0.007(2)		0.006(6)		
	2	-0.001(2)	0.005(4)		0.020(8)		
C6	1	0.0002(9)	0.005(2)		0.007(6)		
	2	0.003(1)	-0.003(4)		0.015(8)		
C7	1	-0.0020(8)	0.003(2)		0.000(6)		
	2	0.003(1)	-0.002(4)		-0.004(8)		
C8	1	-0.0017(9)	-0.005(2)		0.011(6)		
	2	0.003(1)	0.009(3)		-0.022(8)		
C9	1	-0.0050(8)	-0.009(2)		-0.008(6)		
	2	0.000(1)	0.006(4)		0.003(8)		
C10	1	0.0045(8)	0.005(2)		0.006(6)		
	2	-0.002(1)	-0.008(3)		-0.010(8)		
C11	1	-0.0005(8)	-0.003(2)		-0.001(6)		
	2	0.001(1)	-0.004(4)		0.004(8)		
C12	1	0.0013(8)	0.008(2)		0.020(6)		
	2	0.001(1)	-0.005(4)		-0.008(8)		
C13	1	-0.0047(8)	0.002(2)		0.005(6)		
	2	-0.002(1)	-0.002(4)		0.001(8)		
C14	1	-0.0040(9)	-0.005(2)		-0.016(6)		
	2	0.006(1)	-0.003(3)		-0.012(8)		
C15	1	0.0008(9)	-0.010(2)		0.011(6)		
	2	0.004(1)	-0.004(4)		0.007(8)		
C16	1	-0.0015(8)	-0.021(2)		0.001(6)		
	2	-0.003(1)	0.001(4)		-0.010(8)		
C17	1	-0.0076(8)	0.006(2)		0.014(6)		
	2	0.001(2)	0.002(4)		0.000(8)		
C18	1	-0.0078(9)	-0.009(2)		0.018(7)		
	2	0.004(1)	-0.004(4)		-0.005(9)		
Displacement amplitudes of guest structure atoms: {Dy <sub>0.64</sub> }							
Dy11	1	0.0006(1)	0.0057(1)	0.0286(2)	-0.0009(1)	0.0044(1)	0.0982(1)
	2	-0.0009(1)	-0.0022(2)	0.0305(2)	-0.0003(1)	-0.0011(3)	0.0437(3)
	3	-0.0004(1)	0.0004(4)	0.0193(3)	0.0001(2)	0.0008(4)	0.0263(4)
	4	0.0001(2)	0.0003(4)	0.0182(3)	-0.0001(2)	-0.0002(4)	0.0111(4)
Dy12	1			-0.0719(3)	-0.0008(2)	-0.0010(3)	
	2	0.0017(2)	-0.0006(5)				-0.0686(5)
	3			0.0148(9)	0.0006(3)	-0.0001(8)	
	4	-0.0009(3)	0.0016(7)				0.021(2)
Occupational amplitudes of Dy12							
Atom	n	A <sub>p</sub>	B <sub>p</sub>				
Dy12	1		-0.2547(5)				
	2	0.1891(4)					
	3		0.0990(4)				
	4	-0.0375(4)					

#### 9.4 ADP and interatomic distances for the crystal structure of $\text{La}_{3.67}[\text{Fe}(\text{C}_2)_3]$

Table 9.28:  $\text{La}_{3.67}[\text{Fe}(\text{C}_2)_3]$ : Anisotropic displacement parameters  $U_{ij}$  [ $10^4 \text{ pm}^2$ ]; estimated standard deviations are given in parentheses.

Atom	$U_{11}$	$U_{22}$	$U_{33}$	$U_{12}$	$U_{13}$	$U_{23}$
La1	0.0108(2)	0.0078(1)	0.0081(1)	0.0048(1)	0.0003(2)	0
La2	0.0089(3)	0.0108(3)	0.0083(3)	0.0062(2)	0	0
La3	0.0073(3)	0.0073(3)	0.0161(7)	0.0037(1)	0	0
La4	0.0094(4)	0.0094(4)	0.0127(6)	0.0047(1)	0	0
Fe1	0.0067(4)	0.0067(4)	0.0091(7)	0.0034(2)	0	0
Fe2	0.0065(7)	0.0065(7)	0.0130(10)	0.0032(3)	0	0
C1	0.0230(40)	0.0270(50)	0.0040(30)	-0.0120(40)	0	0
C2	0.0080(30)	0.0120(30)	0.0140(30)	0	-0.0090(30)	0
C3	0.0070(40)	0.0090(40)	0.0120(50)	0	0	0
C4	0.0060(40)	0.0070(40)	0.0050(40)	0	0	0

Table 9.29:  $\text{La}_{3.67}[\text{Fe}(\text{C}_2)_3]$ : interatomic distances, [pm]; estimated standard deviations are given in parentheses and  $n$  is the multiplicity.

Atom 1	Atom 2	$n$	Distance	Atom 1	Atom 2	$n$	Distance	
La1	La3	1×	338.19(8)	La1	C1	1×	286.65(8)	
	La4	1×	364.80(1)		C1	1×	302.85(2)	
	La3	1×	365.80(1)		C1	1×	332.28(8)	
	La2	1×	367.63(1)		La2	C3	1×	265.68(5)
La1	1×	372.71(1)	C2	2×		275.47(8)		
La2	La4	2×	340.36(1)	C4	1×	279.30(5)		
	La1	2×	367.63(2)	C1	2×	281.36(5)		
La3	La3	1×	71.68(2)	C4	1×	283.13(9)		
	La4	1×	269.03(2)	C3	1×	313.28(5)		
	La1	3×	338.19(1)	C3	1×	323.78(9)		
	La4	1×	340.71(3)	La3	C1	3×	254.47(8)	
La1	3×	365.80(1)	C1		3×	290.33(8)		
La4	La4	1×	192.76(2)	La4	C3	3×	266.07(5)	
	La3	1×	269.03(2)		C1	3×	288.27(2)	
	La2	3×	340.36(1)	Fe1	C2	1×	182.50(3)	
	La3	1×	340.71(3)		C2	1×	182.56(6)	
La1	La1	3×	364.80(1)	Fe2	C2	1×	182.59(9)	
	C4	1×	273.46(4)		C4	1×	183.65(4)	
	C1	1×	275.02(7)	C4	1×	183.71(9)		
	C2	1×	276.45(6)	C4	1×	183.74(3)		
	C2	1×	277.30(8)	C1	C2	1×	131.05(8)	
	C3	1×	277.97(3)		C3	C4	1×	129.40(7)
	C2	1×	282.79(8)					



**9.5 Anisotropic displacement parameters (ADP) and interatomic distances for the crystal structure of  $\text{La}_{3.67}\text{[Ru(C}_2)_3]$**

Table 9.30: Subcell of  $\text{La}_{3.65}\text{[Ru(C}_2)_3]$  ( $a = 887.9(2)$  pm,  $c = 535.6(2)$  pm): anisotropic displacement parameters  $U_{ij}$  [ $10^4$  pm<sup>2</sup>]; estimated standard deviations are given in parentheses.

Atom	$U_{11}$	$U_{22}$	$U_{33}$	$U_{12}$	$U_{13}$	$U_{23}$
La1	0.0141(2)	0.0146(2)	0.0119(2)	0.0044(10)	0	0
La2	0.0121(10)	0.0121(10)	0.1410(80)	0.0061(5)	0	0
Ru1	0.0110(2)	0.0110(2)	0.0141(3)	0.0055(1)	0	0
C1	0.0170(20)	0.0150(20)	0.0150(20)	0	0	0
C2	0.0240(30)	0.0220(30)	0.0180(30)	0	0	0

Table 9.31: Average structure of  $\text{La}_{3.65}\text{[Ru(C}_2)_3]$ : interatomic distances, [pm]; estimated standard deviations are given in parentheses and  $n$  is the multiplicity.

Atom 1	Atom 2	$n$	Distance	Atom 1	Atom 2	$n$	Distance
La1	C1	18×	264.17(5)	La2	C1	12×	264.44(5)
	C2	18×	274.53(3)		C1	12×	276.61(4)
	C2	18×	275.12(3)		La1	12×	345.98(5)
	C1	18×	281.40(3)		La2	4×	348.29(4)
	C2	18×	285.23(7)	C2	12×	351.34(6)	
	C2	18×	286.52(6)	La1	12×	366.59(5)	
	C1	18×	294.41(3)	C2	12×	379.66(5)	
	C1	18×	317.02(8)	Ru1	C2	18×	191.95(4)
	Ru1	18×	328.55(6)		C1	18×	321.35(7)
	C1	18×	332.86(7)	La1	18×	328.55(8)	
	La2	18×	345.98(6)	La1	18×	357.47(4)	
	Ru1	18×	357.47(4)	La1	18×	359.82(4)	
	Ru1	18×	357.97(4)	C1	C2	18×	129.66(2)
	La1	18×	365.23(5)				
La1	18×	374.23(5)					
C2	18×	384.35(7)					

## 9.6 Bond angles for the crystal structure of $\text{Sm}_2\text{Cr}_2\text{C}_3$

Table 9.32: Bond angles in the crystal structure of  $\text{Sm}_2\text{Cr}_2\text{C}_3$ .

Atom 1	Atom 2	Atom 3	Angle [°]	Atom 1	Atom 2	Atom 3	Angle [°]
Sm	C2	C2	86.5(1)	C2	Cr	C1	137.0(1)
	C2	C1	136.0(1)		Cr	Sm	89.6(1)
	C2	C1	67.9(1)		Cr	Sm	89.6(1)
	C2	C1	118.8(1)		Cr	Sm	90.4(1)
	C2	C1	136.0(1)		Cr	Sm	90.4(1)
	C2	C1	118.8(1)		Cr	C1	137.0(1)
	C2	C1	67.9(1)		Cr	C1	43.0(1)
	C1	C1	92.9(1)		Sm	Sm	86.5(1)
	C1	C1	92.9(1)		Sm	Sm	93.5(1)
	C1	C1	77.6(1)		Sm	Sm	180
C1	Cr	Cr	121.1(2)	Sm	C1	120.2(1)	
	Cr	Cr	83.2(2)	Sm	C1	59.8(1)	
	Cr	Sm	104.0(2)	Sm	Sm	180	
	Cr	Sm	152.9(2)	Sm	Sm	93.5(1)	
	Cr	Sm	78.4(1)	Sm	C1	120.2(1)	
	Cr	C2	102.4(2)	Sm	C1	59.8(1)	
	Cr	Cr	83.2(2)	Sm	Sm	86.4(1)	
	Cr	Sm	104.0(2)	Sm	C1	59.8(1)	
	Cr	Sm	78.4(2)	Sm	C1	120.2(1)	
	Cr	Sm	152.9(2)	Sm	C1	59.8(1)	
	Cr	C2	102.4(2)	Sm	C1	120.2(1)	
	Cr	Sm	164.4(2)	C1	C1	180	
	Cr	Sm	80.8(1)	Cr	C2	C1	117.3(1)
	Cr	Sm	80.8(1)		C2	C1	117.3(1)
	Cr	C2	39.9(1)		C2	C1	97.1(1)
	Sm	Sm	87.1(1)		C2	Cr	115.8(1)
	Sm	Sm	87.1(1)		C2	Cr	115.8(1)
	Sm	C2	124.5(2)		C1	C1	121.1(2)
	Sm	Sm	77.6(1)		C1	C1	96.8(2)
	Sm	C2	52.3(1)		C1	Cr	49.2(1)
Sm	C2	52.3(1)	C1		Cr	118.3(1)	
Sm	C2	52.3(1)	C1		Cr	118.3(1)	
C2	Cr	Cr	180	C1	C1	96.8(2)	
	Cr	Sm	90.4(1)	C1	Cr	118.3(1)	
	Cr	Sm	90.4(1)	C1	Cr	49.2(1)	
	Cr	Sm	89.6(1)	C1	Cr	47.6(1)	
	Cr	Sm	89.6(1)	C1	Cr	47.6(1)	
	Cr	C1	43.0(1)	Cr	Cr	80.8(1)	

## Bibliography

- [1] N. N. Greenwood, A. Earnshaw, *Chemistry of the elements (2nd Edition)*, Elsevier **1997**.
- [2] J. Wang, Y. Zhou, Recent Progress in Theoretical Prediction, Preparation, and Characterization of Layered Ternary Transition-Metal Carbides, *Annu. Rev. Mater. Res.* **2009**, *39*, 415–443.
- [3] P. Friedrichs, T. Kimoto, L. Ley, G. Pensl, *Silicon Carbide. Volume 2: Power Devices and Sensors*, Wiley-VCH Verlag GmbH **2009**.
- [4] Holleman-Wiberg, *Lehrbuch der Anorganischen Chemie*, Walter de Gruyter **1995**.
- [5] F. A. Cotton, G. Wilkinson, P. L. Gaus, *Basic Inorg. Chem. (3rd edition)*, John Wiley and Sons **1995**.
- [6] F. A. Cotton, G. Wilkinson, C. A. Murillo, M. Bochmann, *Advanced Inorg. Chem. (6th edition)*, John Wiley and Sons **1999**.
- [7] U. Ruschewitz, Binary and ternary carbides of alkali and alkaline-earth metals, *Coord. Chem. Rev.* **2003**, *244*, 115–136.
- [8] D. Enkhsetseg, Carbometalates: Synthesis, Crystal Structures, Physical Properties and Chemical Bonding, *Science Doctoral Thesis, National University of Mongolia, Ulaanbaatar, Mongolia* **2008**.
- [9] E. Dashjav, F. R. Wagner, G. Kreiner, W. Jeitschko, R. Kniep, Ternary rare earth and actinoid transition metal carbides viewed as carbometalates, *J. Solid State Chem.* **2007**, *180*, 636–653.
- [10] CRYSTMET - The Metals Database (Version 4.2.0) **2009**.
- [11] P. Villars, K. Cenzual, Pearson's Crystal Data: Crystal Structure Database for Inorganic Compounds **2010**.
- [12] A. L. Bowman, G. P. Arnold, N. H. Krikorian, W. H. Zachariasen, The crystal structure of  $U_2IrC_2$ , *Acta Crystallogr. B* **1971**, *27*, 1067–1068.
- [13] M. A. Moss, W. Jeitschko, Kristallstrukturen und Eigenschaften der Thorium-Nickel-Carbide  $Th_3Ni_5C_5$  und  $Th_2NiC_2$ , *Z. Anor. Allg. Chem.* **1991**, *603*, 57–67.
- [14] M. H. Gerss, W. Jeitschko, YCoC and Isotypic Carbides with New, Very simple structure type, *Z. Naturforsch. B: Chem. Sci.* **1986**, *41*, 946–950.
- [15] M. E. Danebrock, W. Jeitschko, A. M. Witte, R. Pöttgen, Magnetic properties of the carbides  $RCoC$  ( $R = Y, Gd-Er, Lu$ ) with YCoC-type structure, *J. Phys. Chem. Solids* **1995**, *56*, 807–811.
- [16] W. Jeitschko, G. Block, G. E. Kahnert, R. K. Behrens,  $Pr_2ReC_2$  and other ternary rare earth metal rhenium carbides with filled  $PbCl_2$  ( $Co_2Si$ ) structure, *J. Solid State Chem.* **1990**, *89*, 191–201.

- [17] M. H. Gerdes, W. Jeitschko, K. H. Wachtmann, M. E. Danebrock,  $\text{Gd}_2\text{OsC}_2$ , a soft ferromagnet with a surprisingly high Curie temperature and other rare-earth osmium and rhenium carbides with  $\text{Pr}_2\text{ReC}_2$  type structure, *J. Mater. Chem.* **1997**, 7, 2427–2431.
- [18] E. Dashjav, G. Kreiner, W. Schnelle, F. R. Wagner, R. Kniep, Carbometalates: Complex Anions  ${}_{\infty}^2[\text{MoC}_{4/2}{}^{6-}]$  in the Crystal Structure of  $\text{Pr}^{\text{III}}_2[\text{Mo}^{\text{II}}\text{C}_2]$ , *Z. Anorg. Allg. Chem.* **2004**, 630, 689–696.
- [19] E. Dashjav, G. Kreiner, W. Schnelle, F. R. Wagner, R. Kniep, Neue Carbometallate im  $\text{Pr}_2[\text{MoC}_2]$ -Strukturtyp, *Z. Anorg. Allg. Chem.* **2004**, 630, 1716.
- [20] W. Jeitschko, R. K. Behrens, Ternary carbides with  $\text{Ho}_2\text{Cr}_2\text{C}_3$  and  $\text{UMoC}_2$  Type-Structure, *Z. Metallkd.* **1986**, 77, 788–793.
- [21] M. Reehuis, K. Zeppenfeld, W. Jeitschko, N. Stüsser, B. Ouladdiaf, A. Loidl, Magnetic phase transitions in the ternary carbides  $\text{Ln}_2\text{Cr}_2\text{C}_3$  ( $\text{Ln} = \text{Tb}, \text{Ho}, \text{Er}$ ), *J. Magn. Magn. Mater.* **2002**, 251, 260–270.
- [22] M. Reehuis, M. Gerdes, W. Jeitschko, B. Ouladdiaf, N. Stüsser, Crystal and magnetic structures of the ternary carbides  $\text{Ho}_2\text{Mo}_2\text{C}_3$  and  $\text{Er}_2\text{Mo}_2\text{C}_3$ , *J. Magn. Magn. Mater.* **1999**, 195, 657–666.
- [23] E. Dashjav, G. Kreiner, W. Schnelle, R. Kniep, Crystal structure of digadolinium tricarbomolybdate(III),  $\text{Gd}_2[\text{Mo}_2\text{C}_3]$ , *Z. Kristallogr. NCS* **2005**, 220, 129–130.
- [24] E. Dashjav, G. Kreiner, W. Schnelle, F. R. Wagner, R. Kniep, Carbomolybdate(III): Zur Kenntnis von  $\text{Pr}_2[\text{Mo}_2\text{C}_3]$  sowie Strukturbeziehungen zu  $\text{Er}_2\text{Mo}_2\text{C}_3$ , *Z. Anorg. Allg. Chem.* **2004**, 630, 2277–2286.
- [25] R. K. Behrens, W. Jeitschko,  $\text{UCr}_4\text{C}_4$ , A Distorted Structure Derived from  $\text{UCr}_4\text{C}_4$  and the Ternary U-W-C System, *J. Less-Common Met.* **1990**, 160(1), 185–192.
- [26] R. K. Behrens, W. Jeitschko,  $\text{UCr}_4\text{C}_4$  with Filled  $\text{MoNi}_4$  Type-Structure, *Monatsh. Chem.* **1987**, 118(1), 43–50.
- [27] G. Block, W. Jeitschko, The Crystal-Structure of  $\text{U}_5\text{Re}_3\text{C}_8$ , *Monatsh. Chem.* **1988**, 119(3), 319–326.
- [28] D. T. Cromer, A. C. Larson, R. B. R. Jr., The crystal structure of  $\text{UMoC}_2$ , *Acta Crystallogr.* **1964**, 17, 272–276.
- [29] M. H. Gerdes, W. Jeitschko, L. Boonk, J. Nienstedt, J. Grobe, E. Mörsen, A. Leson, Preparation and Crystal Structure of Superconducting  $\text{Y}_2\text{FeC}_4$  and Isotypic Lanthanoid Iron Carbides, *J. Solid State Chem.* **1987**, 70, 19–28.
- [30] A. M. Witte, W. Jeitschko, Preparation and Crystal Structure of the Isotypic Carbides  $\text{Ln}_{3.67}\text{TC}_6$  ( $\text{Ln} = \text{rare earth elements}$ ;  $\text{T} = \text{Mn}, \text{Fe}, \text{Ru}$ ) and  $\text{Eu}_{3.16}\text{NiC}_6$ , *Z. Naturforsch.* **1996**, 51b, 249–255.

- [31] M. H. Gerss, W. Jeitschko, The crystal structure of  $U_2NiC_3$ , *Z. Kristallogr.* **1986**, *175*, 203–210.
- [32] M. W. Pohlkamp, R.-D. Hoffmann, G. Kotzyba, W. Jeitschko, Preparation, Properties, and Crystal Structure of the Rare Earth Ruthenium Carbides  $R_3Ru_2C_5$  ( $R = Y, Gd-Er$ ), *J. Solid State Chem.* **2001**, *160*, 77–87.
- [33] R.-D. Hoffmann, K. H. Wachtmann, T. Ebel, W. Jeitschko,  $GdRuC_2$ , a ternary carbide with filled NiAs structure, *J. Solid State Chem.* **1995**, *118*, 158–162.
- [34] U. E. Musanke, W. Jeitschko, R.-D. Hoffmann, The lanthanoid ruthenium carbides  $Ln_7Ru_2C_{11}$  ( $Ln = Dy-Tm$ ) with a superstructure caused by differences in ruthenium carbon interactions, *J. Solid State Chem.* **1995**, *118*, 158–162.
- [35] R.-D. Hoffmann, W. Jeitschko, Carbides  $Ln_{10}Ru_{10}C_{19}$  ( $Ln = Y, Gd-Lu$ ): crystal structure of their subcells and the superstructures of  $Er_{10}Ru_{10}C_{19}$ , *Acta Crystallogr. B* **1998**, *54*, 834–850.
- [36] U. E. Musanke, W. Jeitschko, M. E. Danebrock, Preparation and Crystal Structure of the Isotypic Carbides  $Ln_4Ni_2C_5$  ( $Ln = Er, Tm, Yb$  and  $Lu$ ), *Z. Anorg. Allg. Chem.* **1993**, *619*, 321–326.
- [37] G. E. Kahnert, W. Jeitschko, The carbides  $Gd_3Mn_2C_6$  and  $Tb_3Mn_2C_6$ , *Z. Anorg. Allg. Chem.* **1993**, *619*, 93–97.
- [38] E. Dashjav, Y. Prots, G. Kreiner, W. Schnelle, F. R. Wagner, R. Kniep, Chemical bonding analysis and properties of  $La_7Os_4C_9$ —A new structure type containing C- and  $C_2$ -units as Os-coordinating ligands, *J. Solid State Chem.* **2008**, *181*(11), 3121–3130.
- [39] N. G. Connelly, T. Damhus, R. M. Hartshorn, A. T. Hutton, *IUPAC: Nomenclature of Inorg. Chem.*, RSC Publishing **2005**.
- [40] W. Scherer, C. Hauf, M. Presnitz, E.-W. Scheidt, G. Eickerling, V. Eyert, R.-D. Hoffmann, U. C. Rodewald, A. Hammerschmidt, C. Vogt, R. Pöttgen, Superconductivity in Quasi One-Dimensional Carbides, *Angew. Chem. Int. Ed.* **2010**, *49*, 1578–1582.
- [41] L. Wang, Q. Lin, J. Ji, D. Lan, New study concerning development of application of rare earth metals in steels, *J. Alloys Compd.* **2006**, *408-412*, 384–386.
- [42] S. K. Samanta, S. K. Mitra, T. Pal, Effect of rare earth elements on microstructure and oxidation behaviour in TIG weldments of AISI 316L stainless steel, *Mater. Sci. Eng. A* **2006**, *430*(1-2), 242 – 247.
- [43] N. Lin, F. Xei, T. Zhong, X. Wu, W. Tian, Influence of adding various rare earths on microstructures and corrosion resistance of chromizing coatings prepared via pack cementation on P110 steel, *J. Rare Earths* **2010**, *28*(2), 301 – 304.
- [44] H. Gmelin, *Inorganic and Organometallic Chemistry: Rare-earth elements: compounds with carbon, C 12a*, Springer-Verlag **1995**.

- [45] F. H. Spedding, K. J. Gschneidner, A. H. Daane, The Crystal Structures of Some of the Rare Earth Carbides, *J. Am. Chem. Soc.* **1958**, *80*, 4499–4503.
- [46] R. Pöttgen, W. Jeitschko, Scandium carbide  $\text{Sc}_3\text{C}_4$ , a carbide with  $\text{C}_3$  units derived from propadiene, *Inorg. Chem.* **1991**, *30*, 427–431.
- [47] H. Jedlicka, H. Nowotny, F. Benesovsky, Zum System Scandium-Kohlenstoff, 2. Mitt.: Kristallstruktur des C-reichen Carbids, *Monatsh. Chem.* **1971**, *102*, 389–403.
- [48] CRS, *Handbook of Chemistry and Physics*, Taylor and Francis Group **2010**.
- [49] The Landolt-Börnstein Database **Springer Materials**.
- [50] T. Sakai, G. Adachi, T. Yoshida, S. Ueno, J. Shiokawa, Preparation and physical properties of  $\text{EuC}_2$ , and its solid solutions  $R_x\text{Eu}_{1-x}\text{C}_2$  ( $R = \text{La}$  and  $\text{Gd}$ ), *Bull. Chem. Soc. Jpn.* **1982**, *55*, 699–703.
- [51] H. Mattausch, T. Gulden, R. K. Kremer, J. Horakh, A. Simon,  $\text{Ho}_4\text{C}_7$ ,  $\text{Y}_4\text{C}_7$ : Carbide mit  $\text{C}_3^{4-}$  und  $\text{C}^{4-}$  Ionen, *Z. Naturforsch. B* **1994**, *49*, 1439–1443.
- [52] R. Czekalla, T. Hüfken, W. Jeitschko, R. Hoffmann, H. Rabeneck, Preparation and crystal structure, and properties of the Lanthanoid carbides  $\text{Ln}_4\text{C}_7$  with  $\text{Ln} = \text{Ho-Tm}$  and  $\text{Lu}$ , *Z. Naturforsch. B* **1995**, *51*, 646–654.
- [53] R. Czekalla, T. Hüfken, W. Jeitschko, R. Hoffmann, R. Pöttgen, The Rare Earth Carbides  $\text{R}_4\text{C}_5$  with  $R = \text{Y, Gd, Tb, Dy, and Ho}$ , *J. Solid State Chem.* **1997**, *132*, 294–299.
- [54] T. R. Ohno, G. H. Kroll, J. H. Weaver, Yb and Yb-K fulleride formation, bonding, and electrical character, *Phys. Rev. B* **1992**, *46*, 10437–10441.
- [55] X. Chen, D. Chi, Z. Sun, T. Takenobu, Z. Liu, Y. Iwasa, Synthesis, Structure, and Transport Properties of Novel Fullerides  $\text{A}_3\text{C}_{70}$  ( $A = \text{Ba}$  and  $\text{Sm}$ ), *J. Am. Chem. Soc.* **2000**, *122*, 5729–5732.
- [56] A. F. Hebard, M. J. Rosseinsky, R. C. Haddon, D. W. Murphy, S. H. Glarum, T. T. M. Palstra, A. P. Ramirez, A. R. Kortan, Superconductivity at 18 K in potassium doped  $\text{C}_{60}$ , *Nature* **1991**, *350*, 600–601.
- [57] T. B. Massalski, *Binary Alloy Phase Diagrams, Second Edition, Vol 1*, ASM International, Materials Park, Ohio **1990**.
- [58] Pauling File Binaries Edition, Version 1.0 **2002**.
- [59] A. Westgren, Crystal structure and composition of cubic chromium carbide, *Jernk. Ann.* **1933**, *117*, 501–512.
- [60] K. Hirota, K. Mitani, M. Yoshinaka, O. Yamaguchi, Simultaneous synthesis and consolidation of chromium carbides ( $\text{Cr}_3\text{C}_2$ ,  $\text{Cr}_7\text{C}_3$  and  $\text{Cr}_{23}\text{C}_6$ ) by pulsed electric-current pressure sintering, *Mater. Sci. Eng.* **2005**, *399*, 154–160.

- [61] A. L. Bowman, G. P. Arnold, E. K. Storms, N. G. Nereson, The crystal structure of  $\text{Cr}_{23}\text{C}_6$ , *Acta Crystallogr. B* **1972**, 28, 3102–3103.
- [62] H. L. Yakel, Atom Distributions in Tau-Carbide Phases: Fe and Cr Distributions in  $(\text{Cr}_{23-x}\text{Fe}_x)\text{C}_6$  with  $x = 0, 0.7_4, 1.7_0, 4.1_3$  and  $7.3_6$ , *Acta Crystallogr. B* **1987**, 43, 230–238.
- [63] A. V. dos Santos, Comparative study between LMTO and FPLAPW into the calculation of the electronic structure of carbide  $\text{Cr}_{23}\text{C}_6$ , *Phys. B* **2007**, 387, 136–142.
- [64] J. Glaser, R. Schmitt, H. J. Meyer, Structure Refinement and Properties of  $\text{Cr}_3\text{C}_2$ , *Z. Naturforsch.* **2003**, 58b, 929–933.
- [65] A. Westgren, G. Phragmen, T. Negresco, Structure of iron-chromium-carbon system, *J. Iron and Steel Inst.* **1928**, Seiten 383–400.
- [66] M. A. Rouault, P. Herpin, M. R. Fruchart, Crystallographic study of carbides  $\text{Cr}_7\text{C}_3$  and  $\text{Mn}_7\text{C}_3$ , *Annales de Chimie France* **1970**, 5, 461–470.
- [67] C. Jiang, First-principles study of structural, elastic, and electronic properties of chromium carbides, *Appl. Phys. Lett.* **2008**, 92, 041909.
- [68] H. Gmelin, *Anorganische Chemie: Chromverbindungen, Auflage 8, Teil B*, Verlag Chemie **1962**.
- [69] P. Karen, H. Fjellvag, A. Kjekshus, A. F. Andresen, On the phase relations and structural and magnetic properties of the stable manganese carbides  $\text{Mn}_{23}\text{C}_6$ ,  $\text{Mn}_5\text{C}_2$  and  $\text{Mn}_7\text{C}_3$ , *Acta Chem. Scand.* **1991**, 45, 549–557.
- [70] M. A. Konyaeva, N. I. Medvedeva, Electronic Structure, Magnetic Properties, and Stability of the Binary and Ternary Carbides  $(\text{Fe,Cr})_3\text{C}$  and  $(\text{Fe,Cr})_7\text{C}_3$ , *Phys. Solid State* **2009**, 51, 2084–2089.
- [71] D. Music, U. Kreissig, R. Mertens, J. Schneider, Electronic structure and mechanical properties of  $\text{Cr}_7\text{C}_3$ , *Phys. Lett. A* **2004**, 326, 473–476.
- [72] A. Inoue, T. Masumoto, Formation of nonequilibrium  $\text{Cr}_3\text{C}$  carbide in Cr-C binary alloys quenched rapidly from the melt, *Scr. Metall.* **1979**, 13, 711–715.
- [73] B. X. Liu, X. Y. Cheng, A metastable Cr carbide of NaCl structure formed by carbon-ion implantation into chromium films, *J. Phys.: Condens. Matter* **1992**, 4, L265.
- [74] H. L. Yakel, Crystal structures of stable and metastable iron-containing carbides, *Int. Mater. Rev.* **1985**, 30, 17–40.
- [75] *Pandat 8.1*, CompuTherm **2009**.
- [76] Z. G. Yang, H. S. Fang, An overview on bainite formation in steels, *Curr. Opin. Solid State Mater. Sci.* **2005**, 9, 277–286.

- [77] Z. Q. Lv, S. H. Sun, P. Jiang, B. Z. Wang, W. T. Fu, First-principles study on the structural stability, electronic and magnetic properties of  $\text{Fe}_2\text{C}$ , *Comput. Mater. Sci* **2008**, *42*, 692–697.
- [78] J. J. Retief, Powder diffraction data and Rietveld refinement of Hägg-carbide,  $\chi\text{-Fe}_5\text{C}_2$ , *Powder Diffr.* **1999**, *14*, 130–132.
- [79] H. I. Faraoun, Y. D. Zhang, C. Esling, H. Aourag, Crystalline, electronic and magnetic structures of  $\theta\text{-Fe}_3\text{C}$ ,  $\chi\text{-Fe}_5\text{C}_2$  and  $\eta\text{-Fe}_2\text{C}$  from first principles calculation, *J. Appl. Phys.* **2006**, *19*, 093508.
- [80] B. Landolt, *Numerical Data and Functional Relationships in Science and Technology, Group III: Crystal and Solid State Physics, Vol 19c, p. 24*, Springer Verlag, Berlin **1988**.
- [81] S. I. Hirano, S. Tajima, Synthesis and magnetic properties of  $\text{Fe}_5\text{C}_2$  by reaction of iron oxide and carbon monoxide, *J. Mater. Sci.* **1990**, *25*, 4457–4461.
- [82] E. J. Fasiska, G. A. Jeffrey, On the cementite structure, *Acta Crystallogr.* **1965**, *19*, 463–471.
- [83] I. R. Shein, N. I. Medvedeva, A. L. Ivanovskii, Electronic and structural properties of cementite-type  $\text{M}_3\text{X}$  ( $\text{M} = \text{Fe}, \text{Co}, \text{Ni}$ ;  $\text{X} = \text{C}$  or  $\text{B}$ ) by first principles calculations, *Phys. B (Amsterdam)* **2006**, *371*, 126–132.
- [84] S. Nagakura, Study of Metallic Carbides by Electron Diffraction. Part III. Iron Carbides, *J. Phys. Soc. Jpn.* **1959**, *14*, 186–195.
- [85] Z. Q. Lv, F. C. Zhang, S. H. Sun, P. Jiang, B. Z. Wang, W. H. Zhang, W. T. Fu, First-principles study on the mechanical, electronic and magnetic properties of  $\text{Fe}_3\text{C}$ , *Comput. Mater. Sci* **2008**, *44*, 690–694.
- [86] C. M. Fang, M. A. van Huis, H. W. Zandbergen, Structural, electronic, and magnetic properties of iron carbide  $\text{Fe}_7\text{C}_3$  phases from first-principles theory, *Phys. Rev. B* **2009**, *80*, 224108.
- [87] F. H. Herbstein, J. A. Snyman, Identification of Eckstrom-Adcock Iron Carbide as  $\text{Fe}_7\text{C}_3$ , *Inorg. Chem.* **1964**, *3*, 894–896.
- [88] J. M. Morniroli, H. Ayatti, K. M. Knowles, W. M. Stobbs, M. Gantois, Transmission electron microscopy of  $\text{Ru}_7\text{B}_3$  borides, *J. Less-Common Met.* **1989**, *155*, 215–227.
- [89] R. J. P. Fruchart, J. P. Senateur, J. P. Bouchaud, A. Michel, A propos de la structure exacte du carbure de fer  $\text{Fe}_7\text{C}_3$ , *Bull. Soc. Chim. Fr.* **1965**, *2*, 392.
- [90] R. J. Fruchart, A. Rouault, Twin crystals of orthorhombic isomorphous  $\text{Cr}_7\text{C}_3$ ,  $\text{Mn}_7\text{C}_3$ ,  $\text{Fe}_7\text{C}_3$  carbides, *Ann. Chim. (Paris)* **1969**, *4*, 143.
- [91] R. C. Mansey, G. V. Raynor, I. R. Harris, Rare-earth intermediate phases V. The cubic Laves phases formed by rare earth metals with iron and nickel, *J. Less-Common Met.* **1968**, *14*, 329–336.



- [92] K. Hardman-Rhyne, J. J. Rhyne, Short- and long-range magnetic ordering of  $Y_6(Fe_{1-x}Mn_x)_{23}$  compounds using neutron scattering techniques, *J. Less-Common Met.* **1983**, *94*, 23–36.
- [93] R. Marazza, P. Riani, G. Cacciamani, Critical assessment of iron binary systems with light rare earths La, Ce, Pr, and Nd, *Inorg. Chim. Acta* **2008**, *361*, 3800–3806.
- [94] H. Fujii, M. Akayama, K. Nakao, K. Tatami, Effect of interstitial hydrogen and nitrogen on magnetic and structural properties of  $R_2T_{17}$  (R = Y, Ce and Sm; T = Fe, Co and Ni), *J. Alloys Compd.* **1995**, *219*, 10–15.
- [95] O. Mao, J. Yang, Z. Altounian, J. O. Ström-Olsen, Metastable  $RFe_7$  compounds (R=rare earths) and their nitrides with  $TbCu_7$  structure, *J. Appl. Phys.* **1996**, *79*, 4605–4607.
- [96] J. Gao, T. Volkmann, S. Yang, S. Reutzel, D. M. Herlach, X. P. Song, Crystallization of  $Nd_2Fe_{17}B_x$  from stoichiometric melt composition, *J. Alloys Compd.* **2007**, *433*, 356–362.
- [97] Y. G. Xiao, G. H. Rao, Q. Zhang, G. Y. Liu, Y. Zhang, J. K. Liang, Influence of rare earth mixing on structural and magnetic properties of  $Nd_{2-x}Er_xFe_{17}$  compounds, *J. Alloys Compd.* **2006**, *419*, 15–20.
- [98] E. Burzo, Magnetic and Crystallographic Properties of Rare-earth and Yttrium-Iron Laves Phases, *Z. Angew. Phys.* **1971**, *32*, 127–132.
- [99] H. Guo, H. Yang, H. Gong, L. Yang, B. Shen, R. Li, Magnetic and magnetorestrictive properties of  $Sm_{1-x}Dy_xFe_2$  compounds and its Mössbauer effect studies, *J. Appl. Phys.* **1994**, *75*, 7429–7432.
- [100] A. A. Sorokin, G. K. Ryasnyi, B. A. Komissarova, L. G. Shpinkova, A. V. Tsvyashchenko, L. N. Fomicheva, E. N. Shirani, PAC studies of hyperfine interactions of  $^{181}Ta$  in  $NdFe_2$ , *Solid State Commun.* **1993**, *88*, 529–531.
- [101] A. V. Tsvyashchenko, S. V. Popova, New phases melt quenched under high pressure in R-Fe systems (R = Pr, Sm, Dy, Tb, Ho, Er, Tm, Yb, Lu), *J. Less-Common Met.* **1985**, *108*, 115–121.
- [102] A. E. Ray, The crystal structure of  $CeFe_7$ ,  $PrFe_7$ ,  $NdFe_7$  and  $SmFe_7$ , *Acta Crystallogr.* **1966**, *21*, 426–430.
- [103] J. M. Moreau, L. Paccard, J. P. Nozieres, A new phase in the Nd-Fe system: crystal structure of  $Nd_5Fe_{17}$ , *J. Less-Common Met.* **1990**, *163*, 245–251.
- [104] R. K. Murakami, V. Villas-Boas, J. M. Filho, H. R. Rechenberg, F. Missell, Substitutional and interstitial modification of  $Nd_5Fe_{17}$ , *J. Alloys Compd.* **2007**, *443*, 1–6.
- [105] T. Saito, M. Ichihara, Synthesis and magnetic properties of  $Sm_5Fe_{17}$  hard magnetic phase, *Scripta. Mater.* **2007**, *57*, 457–460.
- [106] A. T. Pedziwiatr, E. B. Boltich, W. E. Wallace, R. S. Graig, Magnetic and structural properties of  $Y_{6-x}Er_xFe_{23}$  alloys and their hydrides, *J. Solid State Chem.* **1983**, *46*, 342–348.

- [107] J. J. Rhyne, K. H. Rhyne, Short and long-range magnetic ordering of  $Y_6(Fe_{1-x}Mn_x)_{23}$  compounds using neutron scattering technique, *J. Less-Common Met.* **1983**, *94*, 23–36.
- [108] J. J. Rhyne, K. H. Rhyne, Deuterium site occupation and magnetism in  $Ho_6Fe_{23}D_x$  compounds, *J. Less-Common Met.* **1983**, *94*, 95–105.
- [109] W. Zarek, M. P. Horvath, Z. Obuszko, Magnetic behaviour of  $Sm_6Mn_{23-x}Fe_x$  compounds, *J. Magn. Magn. Mater.* **1980**, *21*, 47–50.
- [110] J. J. Bara, A. T. Pedziwiatr, W. Zarek, Investigation of crystal and magnetic properties of Dy-Fe intermetallic compounds, *J. Magn. Magn. Mater.* **1982**, *27*, 168–174.
- [111] H. H. Stadelmaier, G. Schneider, M. Ellner, A  $CaCu_5$ -type iron-neodymium phase stabilized by rapid solidification, *J. Less-Common Met.* **1986**, *115*, L11–L14.
- [112] T. Miyazaki, M. Takahashi, Y. Xingbo, H. Saito, M. Takahashi, Formation and magnetic properties of metastable  $(TM)_5Sm$  and  $(TM)_7Sm_2$  ( $TM = Fe, Co$ ) compounds, *J. Magn. Magn. Mater.* **1988**, *75*, 123–129.
- [113] V. F. Novy, R. C. Vickery, E. V. Kleber, The Gadolinium-Iron System, *Trans. Metall. Soc. AIME* **1961**, *221*, 580–585.
- [114] J. F. Smith, D. A. Hansen, The structures of  $YNi_3$ ,  $YCo_3$ ,  $ThFe_3$  and  $GdFe_3$ , *Acta crystallogr.* **1965**, *19*, 1019–1024.
- [115] D. T. Cromer, C. E. Olsen, The crystal structure of  $PuNi_3$  and  $CeNi_3$ , *Acta Crystallogr.* **1959**, *12(9)*, 689–694.
- [116] S. K. Malik, F. Pourarian, W. E. Wallace, Magnetization behavior of  $RFe_3$ -hydrides ( $R = Tb, Er$  and  $Tm$ ), *J. Magn. Magn. Mater.* **1983**, *40*, 27–31.
- [117] N. M. Hong, J. J. M. Franse, N. P. Thuy, Magnetic anisotropy of the  $Y(Co_{1-x}Fe_x)$  pseudobinary compounds, *J. Magn. Magn. Mater.* **1989**, *80*, 159–164.
- [118] P. Sharifrazi, R. C. Mohanty, A. Raman, Intermediate phases in some rare earth-ruthenium systems, *Z. Metallkd.* **1984**, *75*, 801–805.
- [119] B. Hillenbrand, M. Wilhelm, Superconductivity in rare earth-ruthenium Laves phases, *Phys. Lett. A* **1970**, *33*, 61–62.
- [120] S. Roth, K. Ibel, W. Just, Neutron scattering experiment on the coexistence of superconductivity and ferromagnetism, *J. Phys. C: Solid State Phys.* **1973**, *6*, 3465–3468.
- [121] J. Chaboy, J. Garcia, A. Marcelli, The effect of hydrogen absorption on the structural, electronic and magnetic properties of the C15 Friauf-Laves phase compounds  $CeFe_2$ ,  $CeRu_2$  and  $LaRu_2$ : an X-ray absorption spectroscopy study, *J. Magn. Magn. Mater.* **1997**, *166*, 149–164.

- [122] K. Cenzual, A. Palenzona, E. Parthe, Dy<sub>5</sub>Ru<sub>2</sub> and Y<sub>5</sub>Ru<sub>2</sub> with Mn<sub>5</sub>C<sub>2</sub>-type structure, *Acta Crystallogr. B* **1980**, *36*, 1631–1634.
- [123] O. J. Loebich, E. Raub, Die Legierungen des Rutheniums mit Gd und Dy und ihre magnetischen Eigenschaften, *J. Less-Common Met.* **1976**, *46*, 7–15.
- [124] A. Palenzona, The phase diagram of Ce-Ru system, *J. Alloys Compd.* **1991**, *176*, 241–246.
- [125] E. Canepa, A. Palenzona, R. Eggenhoffner, Evidence of the strong correlations between anomalous lattice parameters and transport properties in Ce<sub>16</sub>Ru<sub>9</sub>, *J. Alloys Compd.* **1994**, *215*, 105–109.
- [126] M. L. Fornasini, A. Palenzona, The crystal structure of Ce<sub>4</sub>Ru<sub>3</sub>, *Z. Kristallogr.* **1992**, *200*, 57–61.
- [127] M. L. Fornasini, A. Mugnoli, A. Palenzona, Crystal structure of Y<sub>44</sub>Ru<sub>25</sub>, *J. Less-Common Met.* **1989**, *154*, 149–156.
- [128] M. L. Fornasini, A. Palenzona, The crystal structure of Er<sub>3</sub>Ru<sub>2</sub>, *Z. Kristallogr.* **1990**, *192*, 249–254.
- [129] A. Palenzona, F. Canepa, The phase diagram of the La-Ru and Nd-Ru systems, *J. Less-Common Met.* **1990**, *157*, 307–313.
- [130] A. Palenzona, F. Canepa, New compounds in the 30-40 at. percent Ru range of the rare earth-ruthenium (R-Ru) systems, *J. Less-Common Met.* **1990**, *162*, 267–272.
- [131] K. Zeppenfeld, R. Pöttgen, M. Reehius, W. Jeitschko, R. K. Behrens, Preparation of Yb<sub>2</sub>Cr<sub>2</sub>C<sub>3</sub> and magnetic properties of the carbides R<sub>2</sub>Cr<sub>2</sub>C<sub>3</sub> (R = Y, Gd - Lu) with Ho<sub>2</sub>Cr<sub>2</sub>C<sub>3</sub> - type structure, *J. Phys. Chem. Solids* **1993**, *54*, 257–261.
- [132] B. Davaasuren, E. Dashjav, A. Kerkau, G. Kreiner, W. Schnelle, F. R. Wagner, R. Kniep, Synthesis, crystal and electronic structure of a samarium carbochromate(III), Sm<sub>2</sub>[Cr<sub>2</sub>C<sub>3</sub>], *Z. Anorg. Allg. Chem.* **2009**, *635*, 1741–1745.
- [133] R. Dronskowski, P. E. Blöchl, Crystal orbital Hamilton populations (COHP): energy-resolved visualization of chemical bonding in solids based on density-functional calculations, *J. Phys. Chem.* **1993**, *97*(8617–8624).
- [134] M. Kohout, F. R. Wagner, Y. Grin, Electron localizability indicator for correlated wavefunctions. I. Parallel-spin pairs, *Theor. Chem. Acc.* **2004**, *112*, 453–459.
- [135] F. R. Wagner, V. Bezugly, M. Kohout, Y. Grin, Charge Decomposition Analysis of the Electron Localizability Indicator: A Bridge between the Orbital and Direct Space Representation of the Chemical Bond, *Chem.-Eur. J.* **2007**, *13*, 5724–5741.
- [136] A. Raman, Uses of rare earth metals in alloys in metallurgy, Part I. Applications in Ferrous materials, *Z. Metallkd.* **1976**, *67*, 780–789.

- [137] A. Raman, Uses of rare earth metals in alloys in metallurgy, Part II. Applications in Nonferrous materials, *Z. Metallkd.* **1977**, *68*, 163–172.
- [138] A. S. Zavyalov, M. M. Sandormirskiy, The effect of rare earth elements on the structure of steel, *Russian Metallurgy and Mining* **1964**, *3*, 77–84.
- [139] H. K. Park, H. H. Stadelmaier, L. T. Jordan, The ternary system Iron-Cerium-Carbon, *Z. Metallkd.* **1982**, *73*, 399–402.
- [140] T. Y. Hsu, Effects of rare earth elements on isothermal and martensitic transformations in low carbon steels, *ISIJ International* **1998**, *38*, 1153–1164.
- [141] H. H. Stadelmaier, H. K. Park, The system Iron-Gadolinium-Carbon and its ternary carbides, *Z. Metallkd.* **1981**, *72*, 417–422.
- [142] N. A. El-Masry, H. H. Stadelmaier, The ternary system Iron-Yttrium-Carbon, *Z. Metallkd.* **1989**, *80*, 723–725.
- [143] E. P. Marusin, O. I. Bodak, A. O. Tsokol, V. S. Fundamenskii, Crystal structure of  $\text{La}_2\text{Fe}_{14}\text{C}$ , *Soviet Physics - Crystallography* **1985**, *30*, 338–339.
- [144] W. G. Haije, T. H. Jacobs, K. H. J. Buschow, Magnetic structure of ternary rare earth carbides of the type  $\text{R}_2\text{Fe}_{17}\text{C}$ , *J. Less-Common Met.* **1990**, *163*, 353–359.
- [145] B. Davaasuren, E. Dashjav, G. Kreiner, H. Borrmann, R. Kniep, Reinvestigation and superstructure of  $\text{La}_{3.67}[\text{Fe}(\text{C}_2)_3]$ , *J. Solid State Chem.* **2009**, *182*, 1331–1335.
- [146] D. G. Parnell, N. H. Brett, P. E. Potter, Phase relationships in the Ce-Ru-C system, *J. Less-Common Met.* **1985**, *114*, 161–173.
- [147] K. H. Wachtmann, M. A. Moss, R.-D. Hoffmann, W. Jeitschko, Crystal structure of several ternary lanthanoid and actinoid ruthenium carbides, *J. Alloys Compd.* **1995**, *219*, 279–284.
- [148] H. Haschke, H. Nowotny, F. Benesovsky, Neodym-Perowskitcarbide und -nitride, *Monatsh. Chem.* **1967**, *98*, 2157–2163.
- [149] H. H. Stadelmaier, Über ternäre Verbindungen von Übergangsmetall, B-Metall und Metalloid, *Z. Metallkd.* **1961**, *52*, 758–762.
- [150] M. G. Kanatzidis, R. Pöttgen, W. Jeitschko, The Metal Flux: A Preparative Tool for the Exploration of Intermetallic Compounds, *Angew. Chem. Int. Ed.* **2005**, *44*, 6996–7023.
- [151] M. Boström, S. Hovmöller, Preparation and crystal structure of the novel decagonal approximant  $\text{Mn}_{123}\text{Ga}_{137}$ , *J. Alloys Compd.* **2001**, *314*, 154–159.
- [152] M. Boström, Y. Prots, Y. Grin, Preparation, crystal structure and chemical bonding analysis of the new binary compounds  $\text{Rh}_4\text{Ga}_{21}$  and  $\text{Rh}_3\text{Ga}_{16}$ , *J. Solid State Chem.* **2006**, *179*, 2472–2478.

- [153] S. S. INC., *What is SPS?* **2005**, [http://www.scm-sps.com/e\\_htm/whatsps\\_e\\_htm/whatsps1\\_e.htm](http://www.scm-sps.com/e_htm/whatsps_e_htm/whatsps1_e.htm).
- [154] C. Recknagel, N. Reinfried, P. Höhn, W. Schnelle, H. Rosner, Y. Grin, A. Leithe-Jasper, Application of spark plasma sintering to the fabrication of binary and ternary skutterudites, *Sci. Technol. Adv. Mater.* **2007**, *8*, 357–363.
- [155] STOE Win XPOW, Version 1.2, *STOE and Cie.*, Darmstadt **2001**.
- [156] E. J. Gabe, Y. L. Page, J. Charland, F. L. Lee, P. S. White, NRCVAX - an interactive program system for structure analysis, *J. Appl. Crystallogr.* **1989**, *22*, 384–387.
- [157] L. G. Akselrud, Y. Grin, P. Y. Zavalij, V. K. Pecharsky, V. S. Fundamenskii, CSD - Universal program package for single crystal and/or powder structure data treatment **1989**.
- [158] L. G. Akselrud, Y. Grin, P. Y. Zavalij, V. K. Pecharsky, Determination of atomic structure from powder full profile diffraction data using crystallographic program system CSD **1992**.
- [159] L. G. Akselrud, Y. Grin, P. Y. Zavalij, V. K. Pecharsky, B. Baumgartner, E. Wolfel, Use of the CSD program package for structure determination from powder data **1993**.
- [160] A. L. und R.B. Von Dreele, General Structure Analysis System (GSAS), *Los Alamos National Laboratory Report LAUR 86-748* **2000**.
- [161] V. Petricek, M. Dusek, L. Palatinus, Jana2006. The crystallographic computing system **2006**.
- [162] Software, CrystalClear-SM Expert 2.0 r4 **2009**.
- [163] X-AREA, *IPDS software*, *STOE and Cie.*, **2006**.
- [164] A. M. M. Schreurs, X. Xian, L. M. J. Kroon-Batenburg, *EVAL15*: a diffraction data integration method based on ab initio predicted profiles, *J. Appl. Crystallogr.* **2010**, *43*, 70–82.
- [165] G. M. Sheldrick, A short history of *SHELX*, *Acta Crystallogr. A* **2008**, *64*(1), 112–122.
- [166] L. Palatinus, G. Chapuis, *SUPERFLIP* – a computer program for the solution of crystal structures by charge flipping in arbitrary dimensions, *J. Appl. Crystallogr.* **2007**, *40*(4), 786–790.
- [167] L. M. Gelato, E. Parthé, *STRUCTURE TIDY* – a computer program to standardize crystal structure data, *J. Appl. Crystallogr.* **1987**, *20*(2), 139–143.
- [168] A. L. Spek, PLATON: A multipurpose crystallographic tool. [Version. 240108] **1980–2008**.
- [169] P. M. de Wolff, The pseudo-symmetry of modulated crystal structures, *Acta Crystallogr. A* **1974**, *30*, 777–785.
- [170] P. M. de Wolff, Symmetry operations for displacively modulated structures, *Acta Crystallogr. A* **1977**, *33*, 493–497.

- [171] A. Janner, T. Janssen, Symmetry of incommensurate crystal phases. I. Commensurate basic structures, *Acta Crystallogr. A* **1981**, *36*, 399–408.
- [172] A. Janner, T. Janssen, Symmetry of incommensurate crystal phases. I. Incommensurate basic structures, *Acta Crystallogr. A* **1981**, *36*, 408–415.
- [173] P. M. de Wolff, T. Janssen, A. Janner, The superspace groups for incommensurate crystal structures with One-dimensional modulation, *Acta Crystallogr. A* **1981**, *37*, 625–636.
- [174] A. Janner, T. Janssen, P. M. de Wolff, Bravais classes for Incommensurate crystal phases, *Acta Crystallogr. A* **1983**, *39*, 658–666.
- [175] A. Janner, T. Janssen, P. M. de Wolff, Determination of Bravais class for a number of incommensurate crystals, *Acta Crystallogr. A* **1983**, *39*, 671–678.
- [176] T. Wagner, A. Schönleber, A non-mathematical introduction to superspace description of modulated structures, *Acta Crystallogr. B* **2009**, *65*, 249–268.
- [177] S. van Smaalen, An elementary introduction to superspace crystallography, *Z. Kristallogr.* **2004**, *219*, 681–691.
- [178] S. van Smaalen, *Incommensurate crystallography*, Oxford University Press **2007**.
- [179] V. Petricek, A. van der Lee, M. Evain, On the use of crenel functions for occupationally modulated structures, *Acta Crystallogr. A* **1995**, *51*, 529–535.
- [180] V. Petricek, Y. Gao, P. Lee, P. Coppens, X-ray analysis of the incommensurate modulation in the 2:2:1:2 Bi-Sr-Ca-Cu-O superconductor including the oxygen atoms, *Phys. Rev. B* **1990**, *42*, 387–392.
- [181] K. Brandenburg, *Diamond Version 3.0c*, Crystal Impact GbR, Bonn, Germany **2005**.
- [182] K. V. Klementiev, XAFSmass, freeware **2003**.
- [183] B. Ravel, M. Newville, *ATHENA, ARTEMIS, HEPHAESTUS*: data analysis for X-ray absorption spectroscopy using *IFEFFIT*, *J. Synchrotron Rad.* **2005**, *12*(4), 537–541.
- [184] T. E. Cranshaw, B. W. Dale, G. O. Longworth, C. E. Johnson, *Mössbauer Spectroscopy and its Applications*, Cambridge Univ. Press **1985**.
- [185] T. C. Gibb, *Principles of Mössbauer Spectroscopy*, Chapman and Hall **1977**.
- [186] M. Cardona, *Albert Einstein as the father of solid state physics* **2005**, <http://www.citebase.org/abstract?id=oai:arXiv.org:physics/0508237>.
- [187] R. Mössbauer, *Nobel lecture: Recoilless Nuclear Resonance Absorption of Gamma Radiation* **1961**, [http://nobelprize.org/nobel\\_prizes/physics/laureates/1961/mossbauer-lecture.html](http://nobelprize.org/nobel_prizes/physics/laureates/1961/mossbauer-lecture.html).

- [188] K. Lagerec, D. G. Rancourt, Recoil: Mössbauer Spectral Analysis Software for Windows. [Version 1.0] **1998**.
- [189] N. Proteus, *Thermal Analysis, Version 4.0 beta and Version 4.3*, Netzsch-Geraetebau GmbH **1999**.
- [190] S. Cottenier, *Density Functional Theory and the family of (L)APW-methods: a step-by-step introduction*, Instituut voor Kern- en Stralingsfysica, K. U. Leuven, Belgium **2002**.
- [191] G. Krier, O. Jepsen, A. Burkhardt, O. K. Andersen, , A Tight Binding LMTO-ASA Program, Version 4.7 **1998**.
- [192] F. Boucher, O. Jepsen, O. K. Andersen, Supplement to the LMTO-ASA Program. Version 4.7 **1998**.
- [193] R. F. W. Bader, *Atoms in Molecules: A Quantum Theory*, Oxford University Press **1994**.
- [194] G. Jansen, M. Schubart, B. Findeis, L. H. Gade, I. J. Scowen, M. McPartlin, Unsupported Ti-Co and Zr-Co Bonds in Heterobimetallic Complexes: A Theoretical Description of Metal-Metal Bond Polarity, *J. Am. Chem. Soc.* **1998**, *120*, 7239–7251.
- [195] P. Muller, R. Herbst-Irmer, A. L. Spek, *Crystal Structure Refinement: A Crystallographer's Guide to SHELXL*, Oxford University Press **2006**.
- [196] L. J. Farrugia, WinGX, An integrated System of Windows Programs for the Solution and Refinement and Analysis of Single Crystal X-ray Diffraction Data **2005**.
- [197] P. Höhn, R. Kniep, A. Rabenau, Ba<sub>3</sub>[FeN<sub>3</sub>]: Ein neues Nitridoferrat(III) mit [CO<sub>3</sub>]<sup>2-</sup>-isosteren Anionen [FeN<sub>3</sub>]<sup>6-</sup>, *Z. Kristallogr.* **1991**, *196*, 153–158.
- [198] C. F. Putnik, J. J. Welter, G. D. Stucky, M. J. D. Jr., B. A. Sosinsky, J. F. Kirner, E. L. Muetterties, Metal clusters in catalysis. 15. A structural and chemical study of a dinuclear metal complex, hexacarbonylbis(eta.3-2-propenyl)diiron(Fe-Fe), *J. Am. Chem. Soc.* **1978**, *100*, 4107–4116.
- [199] H. Deng, S. G. Shore, Crystal structure, infrared, and NMR spectra of tetrakis(pyridine-N)sodium octacarbonyldiiron [(C<sub>5</sub>H<sub>5</sub>N)<sub>4</sub>Na]<sub>2</sub>[Fe<sub>2</sub>(CO)<sub>8</sub>].infin.: a two-dimensional extended structure due to sodium-isocarbonyl interactions, *Inorg. Chem.* **1992**, *31*, 2289–2291.
- [200] D. Luart, M. Sellin, P. Laurent, J.-Y. Salauen, R. Pichon, L. Toupet, H. D. Abbayes, Synthesis and Crystal Structure of a New Binuclear Organoiron Nonbridged Complex: Bis(tert-butoxycarbonyl)octacarbonyldiiron, [Fe(CO<sub>2</sub>tBu)(CO)<sub>4</sub>]<sub>2</sub>, *Organometallics* **1995**, *14*, 4989–4991.
- [201] T. M. Bockman, H.-C. Cho, J. K. Kochi, Charge-Transfer Crystals of Octacarbonyldiferrate. Solid-State Structure and Oxidation-Reduction of an Iron-Iron-Bonded Electron Donor, *Organometallics* **1995**, *14*, 5221–5231.

- [202] C. R. Hess, T. Weyhermüller, E. Bill, K. Wieghardt, [Fe(tim)<sub>2</sub>]: ein Fe-Fe-Dimer mit einer unverbrückten Metall-Metall-Bindung und redoxaktiven N<sub>4</sub>-makrocyclischen Liganden, *Angew. Chem.* **2009**, *121*, 3758–3761.
- [203] J. F. Herbst, J. J. Croat, B. van Laar, W. B. Yelon, Magnetic structure of Er<sub>6</sub>Fe<sub>23</sub>, *J. Appl. Phys.* **1984**, *56*(4), 1224–1226.
- [204] U. Müller, *Inorganic Structural Chemistry*, Wiley **2007**.
- [205] M. Atoji, Magnetic and Crystal Structures of ErC<sub>2</sub> at 297–2 K, *The J. Chem. Phys.* **1972**, *57*(6), 2410–2413.
- [206] A. V. Morozkin, Er-Fe-Sb system at 1170 K, *J. Alloys Compd.* **2004**, *373*, L3–L4.
- [207] J. Häglund, A. F. Guillermet, G. Grimvall, M. Körling, Theory of bonding in transition-metal carbides and nitrides, *Phys. Rev. B* **1993**, *48*, 11685–11691.
- [208] G. Kresse, J. Furthmüller, Efficient iterative schemes for ab initio total-energy calculations using a plane-wave basis set, *Phys. Rev. B* **1996**, *54*, 11169–11186.
- [209] G. Kresse, J. Hafner, Ab initio molecular-dynamics for liquid-metals, *Phys. Rev. B* **1993**, *47*, 558–561.
- [210] O. Jepsen, A. Burkhard, O. K. Andersen, The Program TB-LMTO-ASA, version 4.7 **1999**.
- [211] U. Barth, L. Hedin, Local exchange-correlation potential for spin polarized case. i, *J. Phys. C: Solid State Phys.* **1972**, *5*, 1629.
- [212] G. A. Landrum, R. Dronskowski, The Orbital Origins of Magnetism: From Atoms to Molecules to Ferromagnetic Alloys, *Angew. Chem. Int. Ed.* **2000**, *39*(1560–1585).
- [213] J. S. Kim, W. Xie, R. K. Kremer, V. Babizhetskyy, O. Jepsen, A. Simon, K. S. Ahn, B. Raquet, H. Rakoto, J.-M. Broto, B. Ouladdiaf, Strong electron-phonon coupling in the rare-earth carbide superconductor La<sub>2</sub>C<sub>3</sub>, *Phys. Rev. B* **2007**, *76*(1), 014516.
- [214] M. V. Butovskii, O. L. Tok, F. R. Wagner, R. Kempe, Bismetallocenes: Lanthanoid-Transition-Metal Bonds through Alkane Elimination, *Angew. Chem. Int. Ed.* **2008**, *47*, 6469–6472.
- [215] M. Kohout, F. R. Wagner, Y. Grin, Electron localization function for transition-metal compounds, *Theor. Chem. Acc.* **2002**, *108*, 150–156.
- [216] P. Blaha, K. Schwarz, G. K. H. Madsen, D. Kvanicka, J. Luitz, WIEN2K, An Augmented Plane Wave+Local Orbital Program for Calculating Crystal Properties Karlheinz Schwarz **2001**.
- [217] P. Gütlich, C. Schröder, Mössbauer spectroscopy, *Bunsen-Mag.* **2010**, *1*, 4–22.
- [218] R. Niewa, Y. Hu, R. Knip, Mn and Fe K-edge XAS Spectra of Manganese and Iron Nitrido Compounds, *Eur. J. Inorg. Chem.* **2003**, *2003*, 1632–1634.



- [219] D. C. Konigsberger, R. Prins, *X-ray Absorption: Principles, Applications, Techniques of EXAFS, SEXAFS and XANES, in Chemical Analysis 92*, John Wiley and Sons **1988**.
- [220] F. Patrick, D. Anthony, H. Britt, H. K. O., A New Structural Motif for Biological Iron: Iron K-Edge XAS Reveals a [Fe<sub>4</sub>-μ-(OR)<sub>5</sub>(OR)<sub>9-10</sub>] Cluster in the Ascidian *Perophora annectens*, *Inorg. Chem.* **2006**, *45*(10), 3920–3931, pMID: 16676950.
- [221] G. Meitzner, G. H. Via, F. W. Lytle, J. H. Sinfelt, Analysis of x-ray absorption edge data on metal catalysts, *The J. Phys. Chem.* **1992**, *96*(12), 4960–4964.
- [222] K. H. Wachtmann, T. H. The Rare Earth Osmium Carbides Ln<sub>5</sub>Os<sub>3</sub>C<sub>4-x</sub> (Ln = La-Nd, Sm) with a New Type of Filled Mn<sub>3</sub>Si<sub>3</sub>-Structure, *J. Solid State Chem.* **1997**, *131*(1), 49 – 53.
- [223] H. Lind, *Modulations in intermetallic family of compounds*, Dissertation, Stockholm University **2004**.
- [224] B. Davaasuren, E. Dashjav, G. Kreiner, H. Borrmann, W. Schnelle, F. R. Wagner, M. Widom, R. Kniep, Planar Fe<sub>6</sub>-cluster units in the crystal structure of RE<sub>15</sub>Fe<sub>8</sub>C<sub>25</sub> (RE = Y, Dy, Ho, Er), *Angew. Chem.* **2010**, *122*, 5824–5828.
- [225] T. Sakai, G. Adachi, T. Yoshida, J. Shiokawa, Magnetic and electrical properties of rare earth dicarbides and their solid solutions, *J. Less-Common Met.* **1981**, *81*, 91–102.
- [226] H. Wondratschek, U. Müller, *International Tables for Crystallography*, Symmetry relations between space groups, Volume A1, Springer **2006**.
- [227] B. J. Beaudry, P. E. Palmer, The lattice parameters of La-Eu and Yb, *J. Less-Common Met.* **1974**, *34*, 225–231.
- [228] K. W. Herrmann, , *Iowa State College J. Science* **1956**, *31*, 439–440.
- [229] F. H. Spedding, J. J. Hanak, A. H. Daane, High temperature allotropy and thermal expansion of rare-earth metals, *J. Less-Common Met.* **1961**, *3*, 110–124.
- [230] G. J. Piermarini, C. E. Weir, Allotropy in Some Rare-Earth Metals at High Pressures, *Science* **1964**, *144*, 69–71.
- [231] E. P. Marusin, O. I. Bodak, A. O. Tsokol, V. S. Fundamenskii, , *Kristallografiya* **1985**, *30*, 581–583.
- [232] G. Bocelli, G. Calestani, F. Leccabue, B. E. Watts, L. J. L. Sanchez, Structural properties of a holmium iron carbide interstitial compound, Ho<sub>2</sub>Fe<sub>17</sub>C<sub>3-x</sub>, *Chem. Mater.* **1993**, *5*, 129–131.
- [233] O. Isnard, J. L. Soubeyroux, D. Fruchart, T. H. Jacobs, K. H. J. Buschow, Structural and magnetic behaviour of the series Th<sub>2</sub>Fe<sub>17</sub>C<sub>x</sub> (x = 0 to 1.25), *J. Alloys Compd.* **1992**, *186*, 135–145.
- [234] C. J. M. Denissen, B. D. de Mooij, K. H. J. Buschow, Structure and <sup>57</sup>Fe Mössbauer effect in R<sub>2</sub>Fe<sub>14</sub>C compounds, *J. Less-Common Met.* **1988**, *139*, 291–298.

- [235] L. P. Perdew, Y. Wang, Accurate and simple analytic representation of the electron-gas correlation-energy, *Phys. Rev. B* **1992**, *45*, 13244–13249.
- [236] STOE and Cie., *Crystal optimization for numerical absorption correction*, Darmstadt **1999**.
- [237] T. Janssen, A. Janner, A. Looijenga-Vos, P. M. de Wolff, *International Tables for Crystallography Vol. C*, International series in pure and applied physics, Springer **1992**.
- [238] C. B. Barber, D. P. Dobkin, H. T. Huhdanpaa, The Quickhull algorithm for convex hulls, *ACM Trans. on Mathematical Software* **1996**, *22*, 469–483.
- [239] J. S. Kim, W. Xie, R. K. Kremer, V. Babizhetskyy, O. Jepsen, A. Simon, K. S. Ahn, B. Raquet, H. Rakoto, J.-M. Broto, B. Ouladdiaf, Strong electron-phonon coupling in the rare-earth carbide superconductor  $\text{La}_2\text{C}_3$ , *Phys. Rev. B* **2007**, *76*, 014516.
- [240] J. S. Kim, R. K. Kremer, O. Jepsen, A. Simon, Electronic and superconducting properties of the binary carbide  $\text{La}_2\text{C}_3$ , *Curr. Appl. Phys.* **2006**, *6*, 897–902.
- [241] E. Dashjav, F. R. Wagner, G. Kreiner, W. Schnelle, R. Kniep, Crystal and Electronic Structures of the New Carbomolybdates(III),  $\text{RE}_2[\text{Mo}_2\text{C}_3]$  with  $\text{RE} = \text{Ce}, \text{Sm}, \text{Tb}, \text{and Dy}$ , *Z. Anorg. Allg. Chem.* **2007**, *633*, 1349–1358.
- [242] W. Jeitschko, R. K. Behrens, Refractory metals und intermetallic precipitates in cobalt-chromium alloys, *Z. Metallkd.* **1986**, *70*, 788–793.
- [243] A. Tennstedt, R. Kniep,  $\text{Ba}_5[\text{CrN}_4]\text{N}$ : The First Nitridochromate(V), *Z. Anorg. Allg. Chem.* **1995**, *621*, 511–515.
- [244] O. Hochrein, M. Kohout, W. Schnelle, R. Kniep,  $\text{Li}_4\text{Sr}_2[\text{Cr}_2\text{N}_6]$ : Ein Hexanitridodichromat(V), *Z. Anorg. Allg. Chem.* **2002**, *628*, 2738–2743.
- [245] T. Hahn, *International Tables for Crystallography*, Space group symmetry, Volume A, Springer **2005**.
- [246] A. S. Bolgar, V. B. Muratov, A. V. Blinder, A. I. Kryklya, A. P. Suodis, Thermodynamic properties of the rare earth borides and carbides in a wide temperature range, *J. Alloys Compd.* **1993**, *201*, 127–128.
- [247] S. I. Mikhalenko, Y. B. Kuzma, The (Pr,Nd,Sm)-Cr-B ternary systems, *Dopov. Akad. Nauk Ukr. RSR (Ser. A)* **1977**, Seiten –951.
- [248] E. Dashjav, F. R. Wagner, G. Kreiner, W. Schnelle, R. Kniep, Carbomolybdate(III): Zur Kenntnis von  $\text{Pr}_2[\text{Mo}_2\text{C}_3]$  sowie Strukturbeziehungen zu  $\text{Er}_2\text{Mo}_2\text{C}_3$ , *Z. Anorg. Allg. Chem.* **2007**, *630*, 2277–2286.
- [249] U. Barth, L. Hedin, A local exchange-correlation potential for the spin polarized case. i, *J. Phys. C* **1972**, *5(13)*, 1629–1642.

- [250] O. Jepsen, O. K. Andersen, Calculated electronic structure of the sandwich d1 metals  $\text{LaI}_2$  and  $\text{CeI}_2$ : Application of new LMTO techniques, *Z. Phys.* **1995**, *B97*, 35–47.
- [251] M. Kohout, F. R. Wagner, Y. Grin, Atomic Shells From the Electron Localizability in Momentum Space, *Int. J. Quant. Chem.* **2006**, *106*, 1499–1507.
- [252] M. Kohout, Bonding indicators from electron pair density functionals, *Faraday Discuss.* **2007**, *135*, 43–54.
- [253] E. Dashjav, Y. Prots, F. R. Wagner, G. Kreiner, R. Kniep, Chemical bonding analysis and properties of  $\text{La}_7\text{Os}_4\text{C}_9$ : A new structure type containing C- and  $\text{C}_2$ -units as Os-coordinating ligands, *J. Solid State Chem.* **2008**, *181*, 3121–3130.

## List of Figures

1.1	Oxidation states and coordination numbers of <i>3d</i> , <i>4d</i> , <i>5d</i> -metals in carbo-, nitrido-, oxo-, and fluorometalates [9]. . . . .	3
1.2	Ionic formulae and building units of complex carbometalate anions. Oxidation states of the transition metal atoms are indicated. . . . .	4
2.1	Sequence of close packed layers in the crystal structure of a) $\beta$ - <i>RE</i> <sub>3</sub> C and b) $\alpha$ - <i>RE</i> <sub>2</sub> C. . . . .	9
2.2	The binary phase diagram of the system Cr–C (50 to 100 at%). The local environments of the carbon atoms in the respective carbides are also shown. Redrawn from Pauling file [58]. . . . .	12
2.3	The Fe-rich part of the metastable Fe–C phase diagram. Drawn by the program Pandat [75]. . . . .	15
2.4	The pleated layers of Fe <sub>3</sub> C viewed along [100]. The carbon atoms are arranged in different manner on the <i>A</i> and <i>B</i> pleated layers [82]. . . . .	16
2.5	<i>hcp</i> layers of Fe atoms in the crystal structure of $\eta$ -Fe <sub>2</sub> C and $\epsilon$ -Fe <sub>3</sub> C. Carbon atoms occupy the octahedral voids; the lower layer is shaded. . . . .	17
2.6	Isothermal section of the ternary phase diagram Gd–Cr–C at 1173 K [20]. . . . .	24
2.7	Ho <sub>2</sub> Cr <sub>2</sub> C <sub>3</sub> : unit cell projection along [001]. The chromium atoms are forming zig-zag chains running along [010]. The overall interconnection of coordination tetrahedron results in $\frac{2}{\infty}[(\text{Cr}_2\text{C}_3)^{6-}]$ . . . . .	25
2.8	The crystal structure of <i>RE</i> <sub>2</sub> FeC <sub>4</sub> exemplarily shown for Er <sub>2</sub> FeC <sub>4</sub> . a) Unit cell projection viewed along [001] and coordination of Fe atoms by C and Er atoms, b) polyanionic part of the structure. Interatomic distances Fe–Fe, Fe–C and C–C are given in pm. . . . .	28
2.9	The Fe(C <sub>2</sub> ) <sub>3</sub> anionic unit in the crystal structure of <i>RE</i> <sub>3,67-x</sub> FeC <sub>6</sub> . . . . .	29
2.10	The crystal structure of <i>RE</i> FeC <sub>2</sub> viewed along [100]. The 2D planar polyanionic part of the structure is $\frac{2}{\infty}[(\text{FeC}_2)^{3-}]$ . . . . .	30
2.11	The crystal structure of GdRuC <sub>2</sub> contains polyanionic layers $\frac{2}{\infty}[(\text{RuC}_2)^{3-}]$ , in which the ruthenium atoms are tetrahedrally coordinated by C <sub>2</sub> units, and Gd atoms being sandwiched between the layers. . . . .	33
2.12	Electron counts for the representative units in the crystal structure of <i>RE</i> <sub>3</sub> Ru <sub>2</sub> C <sub>5</sub> a) trigonal Ru <sub>3</sub> C <sub>10</sub> cluster and valence electron distribution using the Lewis formalism, b) Chain model consisting of linear Ru <sub>3</sub> units. The open circle with number 2 in the center represents the partially occupied Ru atom (Ru2). The linear units carry large negative charges [32]. . . . .	34
2.13	The two different, discrete polyanions in the crystal structure of Er <sub>7</sub> Ru <sub>2</sub> C <sub>11</sub> , [Ru(C <sub>2</sub> ) <sub>4</sub> ] (on the left) and [Ru(C <sub>2</sub> )C] (on the right). All interatomic distances are shown on picture. The Ru–C bond with <i>d</i> (Ru–C) = 264 pm is designated by dashed lines indicating only a marginal Ru–C bonding. . . . .	36

3.1	A typical temperature program for high temperature reactions. . . . .	40
3.2	Schematic representation of the equipment used for reactions and crystal growth supported by the flux method. . . . .	41
3.3	Beryllium cells used for the XAS measurements of air and moisture sensitive polycrystalline samples. . . . .	46
3.4	Mössbauer spectrum of resonance absorption. . . . .	47
4.1	Experimental and calculated powder X-ray diffraction patterns for compounds $RE_{15}[Fe_8C_{25}]$ . The peaks corresponding to $\alpha$ -Fe are marked by solid green triangles, the Bragg peak positions of $Y_{5.64}[Fe_2C_9]$ phase are marked with red vertical bars and the dark-red arrows represent the peaks of an unidentified impurity/trace phase, respectively. . . . .	54
4.2	DTA curves (heating and cooling) of nearly single phase $Dy_{15}[Fe_8C_{25}]$ . . . . .	55
4.3	Back scattered electron (BSE) image of a $Er_{15}[Fe_8C_{25}]$ single crystal and its diffraction pattern (reconstructed Laue image, $hk2$ -layer). . . . .	57
4.4	Planar $Fe_6$ -clusters surrounded by twelve $C_2$ -pairs, six of them serving as bridging ligands to trigonal planar $[Fe(C_2)_3]$ -units. A monoatomic carbon ligand takes a position either above or below the $Fe_2$ triangle. . . . .	60
4.5	Crystal structure of $Er_{15}[Fe_8C_{25}]$ : a) Primitive stacking of layers in the crystal structure viewed along $[010]$ and b) Crystal structure viewed along $[001]$ . . . . .	61
4.6	Crystal structure of $Er_{15}[Fe_8C_{25}]$ : $Fe_6$ -clusters lying on a common $(001)$ plane (grey), and interconnected via trigonal planar $[Fe(C_2)_3]$ -units. . . . .	62
4.7	Structural fragments in the crystal structures of $RE_{15}[Fe_8C_{25}]$ , $\gamma$ -Fe, $\eta$ - $Fe_2C$ and $\epsilon$ - $Fe_3C$ . The $Fe_6$ cluster can be formally considered as part of the crystal structure of iron and binary carbides. . . . .	64
4.8	Comparison of the structural arrangements of Fe atoms in the hexagonal structure of $\gamma$ -Fe (top) with the arrangement of $Fe_6$ clusters in the crystal structure of $RE_{15}[Fe_8C_{25}]$ (bottom). . . . .	65
4.9	Coordination shells of all atomic types in the crystal structure of $Er_{15}[Fe_8C_{25}]$ . Coordination around a) Er atoms, c) Fe atoms and e) carbon atoms by metal atoms. Nearest carbon neighbors for b) Er atoms, and d) the Fe atoms, respectively. . . . .	66
4.10	Total and projected DOS for the majority ( $\beta$ ) and minority ( $\alpha$ ) spin channels of $Y_{15}[Fe_8C_{25}]$ . The total DOS of the valence electrons displays five different structures denoted <b>A</b> , <b>B</b> , <b>C</b> , <b>D</b> and <b>E</b> ranges. . . . .	70
4.11	COHP diagrams of selected interatomic interactions for the majority and minority spin channels of $Y_{15}[Fe_8C_{25}]$ . The energy shift in the $\beta$ -channel with respect to the $\alpha$ -channel is highlighted with red ellipses. . . . .	71
4.12	Partial DOS and COHP diagrams for the $C_2$ units of $Y_{15}[Fe_8C_{25}]$ (in the $\alpha$ -channel). The types of the two center interactions are shown on the respective peak maxima (right). COHP clearly reveal a partially filled $\pi_p^*$ states near the $E_F$ indicating the $C_2^{4-}$ character of the $C_2$ units. . . . .	72

4.13	Y <sub>15</sub> [Fe <sub>8</sub> C <sub>25</sub> ]: a) Fe <sub>6</sub> -cluster and nearest neighbors, b) Fe <sub>6</sub> -cluster superbasin of ELI-D (grey) and Fe 3rd shell basins (red), c) Fe <sub>6</sub> -cluster superbasin of ELI-D intersected by QTAIM atoms: red parts belong to Fe, green parts to Y atoms. . . . .	74
4.14	Corrected inverse magnetic susceptibility of RE <sub>15</sub> [Fe <sub>8</sub> C <sub>25</sub> ] (RE = Dy, Ho, Er) (top) and magnetization curve of Y <sub>15</sub> [Fe <sub>8</sub> C <sub>25</sub> ] at different magnetic fields (bottom). . . . .	76
4.15	Electrical resistivity ρ(T) of the isotypic phases RE <sub>15</sub> [Fe <sub>8</sub> C <sub>25</sub> ] (RE = Dy, Ho, Er). . . . .	77
4.16	The Mössbauer spectrum of Dy <sub>15</sub> [Fe <sub>8</sub> C <sub>25</sub> ] measured at temperatures between 10 K and 290 K. The measured spectra (dots) are fitted (black) with three subspectrum (red, green and blue) between 290 K and 50 K. . . . .	78
4.17	The Mössbauer spectrum of Y <sub>15</sub> [Fe <sub>8</sub> C <sub>25</sub> ] measured at temperatures between 5 K and 290 K. Due to the presence of trace phase signals the fit is not shown. . . . .	81
4.18	Normalized XAS spectra of the isotypic phases RE <sub>15</sub> [Fe <sub>8</sub> C <sub>25</sub> ] (RE = Y, Dy, Ho, Er) and of pure Fe as a reference material. . . . .	84
5.1	Experimental and calculated X-ray powder diffraction patterns of RE <sub>5,64</sub> [Fe <sub>2</sub> C <sub>9</sub> ] (RE = Y, Gd, Tb and Dy). The peaks corresponding to α-Fe are denoted by solid green triangles and the dark red arrows represent unidentified peaks. . . . .	88
5.2	Back scattering electron (BSE) image of a crystal Dy <sub>5,64</sub> [Fe <sub>2</sub> C <sub>9</sub> ]. . . . .	89
5.3	Oscillation photograph of a single crystal Dy <sub>5,64</sub> [Fe <sub>2</sub> C <sub>9</sub> ] along b*. Two possible choices for indexing the diffraction pattern are shown. The first choice corresponds to a modulated structure (blue), and the second choice corresponds to a composite with two sets of reciprocal basis vectors (orange). . . . .	90
5.4	Crenel function of width Δ and center x <sub>4</sub> <sup>0</sup> . . . . .	93
5.5	a) Host structure {Dy <sub>5</sub> [Fe <sub>2</sub> C <sub>9</sub> ]} viewed along [001], Pnam, a = 2934.63(9) pm, b = 1263.63(5) pm, c <sub>H</sub> = 504.14 (3) pm; the blue circles mark the empty channels and black crosses the positions of the guest atoms in the host substructure, i.e, the guest chain {Dy <sub>0,64</sub> } running along [100], Pbam, a = 2934.63(9) pm, b = 1263.63(5) pm, c <sub>G</sub> = 1056.01(5) pm; the dashed lines mark the length c <sub>H</sub> of the first subcell indicating the misfit of two subcells; b) the host structure {Dy <sub>5</sub> [Fe <sub>2</sub> C <sub>9</sub> ]} viewed along [001]. Building blocks <b>A</b> and <b>B</b> are shown. Linkage of <b>A</b> and <b>B</b> creates two different kinds of irregular shaped channels, labeled <b>1</b> and <b>2</b> . Zoom of channel <b>1</b> (left). The face sharing octahedral chain is depicted by grey polyhedra. . . . .	96
5.6	Polyanionic partial structures in the host structure {Dy <sub>5</sub> [Fe <sub>2</sub> C <sub>9</sub> ]}. . . . .	97
5.7	a) La atoms inside a channel of face-sharing octahedra together with trigonal planar Fe(C <sub>2</sub> ) <sub>3</sub> groups in the crystal structure of La <sub>3,67</sub> [Fe(C <sub>2</sub> ) <sub>3</sub> ]; La atoms occupy pairs of neighboring carbon octahedra. This pair alternates with one empty octahedron; b) Dy atoms within an octahedral channel of the modulated composite structure together with a tetrahedral string of Fe(C <sub>2</sub> ) <sub>4/2</sub> and trigonal planar FeC(C <sub>2</sub> ) <sub>2</sub> groups. . . . .	98
5.8	Dy <sub>5,64</sub> [Fe <sub>2</sub> C <sub>9</sub> ]: t-plots of the modulation for selected distances: a-b) Fe–C and C–C in the tetrahedral chains as well as in trigonal planar units, c) Dy–C connected to trigonal planar Fe–C units and d) Dy–Dy distances within the guest chain. . . . .	99

5.9	Coordination polyhedra of all atomic sites in the host structure $\{\text{Dy}_5[\text{Fe}_2\text{C}_9]\}$ . Local coordination of Dy by metal atoms: Dy1 - fourcapped square prism (1), Dy2 - tricapped square prism (2) and Dy3 - bicapped square prism (3). Coordination of Dy by carbon ligands: Dy1 - distorted square pyramid (4), Dy2 - tricapped distorted square pyramid (5), Dy5 - bicapped square pyramid (6), Dy6 - monocapped square prism (7). Metal coordination of Fe atoms: Fe1 - tricapped trigonal prism (8), Fe3 - unusual coordination polyhedra formed by 4 Dy and 2 Fe3 atoms (9). Coordination polyhedra around carbon atoms: monoatomic carbon C4 - occupies the octahedral void (10); C <sub>2</sub> pairs have two different local environments: octahedral (11) and distorted pentagonal bipyramidal (12). . . . .	101
5.10	The corrected inverse magnetic susceptibility of $RE_{5,64}[\text{Fe}_2\text{C}_9]$ ( $RE = \text{Y, Gd, Tb, Dy}$ ). . . . .	103
5.11	Electrical resistivity of compounds $RE_{5,64}[\text{Fe}_2\text{C}_9]$ ( $RE = \text{Y, Gd, Tb, Dy}$ ). The broad hump observed for $\text{Dy}_{5,64}[\text{Fe}_2\text{C}_9]$ is also shown in the inset. . . . .	104
5.12	The Mössbauer spectrum of $\text{Gd}_{5,64}[\text{Fe}_2\text{C}_9]$ measured at room temperature. The measured spectrum (dots) is fitted (black) with two subspectra (red and olive). . . . .	105
5.13	Normalized XAS spectra of the Fe-K threshold of the ternary phases $RE_{5,64}[\text{Fe}_2\text{C}_9]$ ( $RE = \text{Y, Gd, Tb, Dy}$ ) together with the spectrum of metallic iron. . . . .	106
6.1	Experimental and calculated X-ray powder diffraction patterns of $\text{La}_{3,67}[\text{T}(\text{C}_2)_3]$ ( $T = \text{Fe, Ru}$ ). The superstructure reflections are denoted by filled circles whereas the peaks of unidentified trace phases are marked with green arrows. . . . .	109
6.2	BSE image of a typical microstructure after prolonged heat treatment; $\text{La}_{3,67}[\text{FeC}_6]$ is the primary phase and the fine matrix in between is composed of the title compound together with an unknown phase. After polishing some SiC particles were stick to the samples (marked on the image). . . . .	110
6.3	The substructure of $\text{La}_{3,67}[\text{Fe}(\text{C}_2)_3]$ transforms to a 3-fold superstructure by a <i>klas-sengleiche</i> transformation of index 3. Splittings of the atomic sites during the $k3$ transformation are given. . . . .	112
6.4	$\text{La}_{3,67}[\text{Fe}(\text{C}_2)_3]$ : Coordination around Fe, for Fe1 as a representative: a) the trigonal planar complex $\text{Fe}(\text{C}_2)_3$ ; b) two tricapped trigonal prisms (La) sharing common faces and enclosing the trigonal planar groups $\text{Fe}(\text{C}_2)_3$ ; the prisms form infinite chains along [001]. . . . .	113
6.5	Comparison of the crystal structures of $\text{La}_{3,67}[\text{Fe}(\text{C}_2)_3]$ with $\text{Ba}_3[\text{FeN}_3]$ . a) Projection viewed along [001] showing the hexagonal channel stuffed by La atoms. b) Projection of the crystal structure viewed along [001] showing the empty hexagonal channel. . . . .	114
6.6	Different arrangements of La atoms in the hexagonal channels running along the $c$ axis: a) split atom model of the substructure; b) split atom model of the superstructure; this model is interpreted as a superposition of ordered chains as shown in c): sequence of La atoms (La3, La4) with alternating short and long distances for two chains running in opposite (-/+) directions. . . . .	115

6.7	La <sub>3.67</sub> [Fe(C <sub>2</sub> ) <sub>3</sub> ]: Two chains of face-sharing carbon octahedra enclosing the La chains (La at 0, 0, z) in + and - directions. Within each chain, pairs of La atoms occupy positions displaced relative to the centers of two neighboring carbon octahedra, and alternating with one empty octahedron. . . . .	116
6.8	La <sub>3.67</sub> [Fe(C <sub>2</sub> ) <sub>3</sub> ]: Coordination polyhedra around La: a) mono-capped square pyramid (coordination of La1 and La2) formed from three La and three Fe, b) mono-capped distorted octahedron (coordination of La3 and La4), c) La(C <sub>2</sub> ) <sub>2</sub> C <sub>3</sub> flattened monocapped octahedron (coordination of La1 and La2). . . . .	116
6.9	Different superstructure models for La arrangements within the channels of the crystal structure of La <sub>3.67</sub> [Fe(C <sub>2</sub> ) <sub>3</sub> ] used for total energy calculations. a) Structure model with fully occupied, La chains, b) superstructure with one vacancy and c) superstructure with two vacancies in the La chain. . . . .	117
6.10	Total and atom-projected DOS and band structure for La <sub>22</sub> [Fe <sub>6</sub> C <sub>36</sub> ] (left) and La <sub>20</sub> [Fe <sub>6</sub> C <sub>36</sub> ] (right). . . . .	119
6.11	COHP and integrated COHP (ICOHP) diagrams for selected interactions in the crystal structure of La <sub>22</sub> [Fe <sub>6</sub> C <sub>36</sub> ]. . . . .	120
6.12	The Mössbauer spectrum of La <sub>3.67</sub> [Fe(C <sub>2</sub> ) <sub>3</sub> ] measured at room temperature. The measured spectrum (dots) is fitted (black) with two subspectra (red and green). . . .	122
6.13	Normalized XAS spectrum of La <sub>3.67</sub> [Fe(C <sub>2</sub> ) <sub>3</sub> ]. The spectrum is compared with the spectrum of metallic iron. . . . .	123
6.14	A single crystal of La <sub>3.67</sub> [Ru(C <sub>2</sub> ) <sub>3</sub> ] mounted on a glass capillary. . . . .	124
6.15	La <sub>3.67</sub> [Ru(C <sub>2</sub> ) <sub>3</sub> ]: Reciprocal layer <i>2kl</i> . The blue arrows mark the reciprocal basis vectors of the average structure. The modulation wave vector <i>q</i> is denoted by the green arrow. The main reflection 2210 with its satellite reflections 2211 and 221 $\bar{1}$ are marked with blue and green circles, respectively. . . . .	125
6.16	La <sub>3.67</sub> [Ru(C <sub>2</sub> ) <sub>3</sub> ]: Fourier maps of the commensurate structure: <i>x</i> <sub>3</sub> - <i>x</i> <sub>4</sub> (left) and <i>x</i> <sub>2</sub> - <i>x</i> <sub>4</sub> (right) sections for La <sub>2</sub> atoms; the line on the contour shows the modulation function of La <sub>2</sub> . Contour lines represent constant electron density at intervals of 10% of the maximum density. . . . .	127
6.17	La <sub>3.65</sub> [Ru(C <sub>2</sub> ) <sub>3</sub> ]: a) Modulation of the site occupancy factor for the commensurate and incommensurate case, b) temperature factors of La <sub>2</sub> atoms as a function of the internal coordinate <i>t</i> . Red lines show the modulations in the commensurate and blue lines in the incommensurate case. The modulation functions of the deviations from the average positions are shown in c) along <i>x</i> and d) along <i>z</i> directions as a function of <i>t</i> for the commensurate model. . . . .	128
6.18	La <sub>3.65</sub> [Ru(C <sub>2</sub> ) <sub>3</sub> ]: Three different variants of La chains running along [001]: a) commensurate modulation, b) and c) incommensurate modulations. The commensurate model exclusively contains atom pairs, while the incommensurate models show additional vacancies and discrete atoms, respectively. <i>z</i> represents the range taken along the <i>c</i> axis. . . . .	129



6.19	La <sub>3.65</sub> [Ru(C <sub>2</sub> ) <sub>3</sub> ]: <i>t</i> -plots describing the modulation of distances: a) Ru–C and C–C, b) La–C and c) La–La and La–Ru. . . . .	130
6.20	Total DOS and atom-projected DOS for La <sub>3.67</sub> [Ru(C <sub>2</sub> ) <sub>3</sub> ] (left column). DOS regions are denoted by letters <i>A</i> , <i>B</i> , <i>C</i> , <i>D</i> (see text for details). COHP and integrated COHP (ICOHP) diagrams for selected interactions in the crystal structure of La <sub>3.67</sub> [Ru(C <sub>2</sub> ) <sub>3</sub> ] are presented in the right column. . . . .	133
6.21	Experimental and corrected magnetic susceptibility data $M(T)/H$ of La <sub>3.65</sub> [Ru(C <sub>2</sub> ) <sub>3</sub> ].	135
6.22	Electrical resistivity $\rho(T)$ of La <sub>3.67</sub> [T(C <sub>2</sub> ) <sub>3</sub> ] ( <i>T</i> = Fe, Ru). The anomalies around 40 K and 50 K are artefacts. For further details see text. . . . .	136
7.1	X-ray diffraction pattern of Sm <sub>2</sub> [Cr <sub>2</sub> C <sub>3</sub> ]: the observed profile is indicated by red dots and the calculated profile by the solid line. Bragg peak positions of Sm <sub>2</sub> [Cr <sub>2</sub> C <sub>3</sub> ] and Cr <sub>7</sub> C <sub>3</sub> are indicated by black and red tick marks, respectively. The difference curve is shown at the bottom. . . . .	139
7.2	The crystal structure of Sm <sub>2</sub> [Cr <sub>2</sub> C <sub>3</sub> ] viewed along [010]. The coordination of Cr by C atoms is illustrated by orange polyhedra; distances $d(\text{Cr–C})$ and $d(\text{Cr–Cr})$ are given in pm. . . . .	141
7.3	Comparison of Cr coordination polyhedra in the crystal structure of Sm <sub>2</sub> [Cr <sub>2</sub> C <sub>3</sub> ] (right) Ba <sub>5</sub> [CrN <sub>4</sub> ]N (left) and Li <sub>4</sub> Sr <sub>2</sub> [Cr <sub>2</sub> N <sub>6</sub> ] (middle). . . . .	142
7.4	Coordination polyhedra in the crystal structure of Sm <sub>2</sub> [Cr <sub>2</sub> C <sub>3</sub> ]. a) Coordination of Sm atoms by metal atoms, c) by carbon atoms; b) nearest metal neighbors of Cr atoms; d) coordination polyhedron around C1 and e) around C2. . . . .	143
7.5	Normalized total energies of Sm <sub>2</sub> [Cr <sub>2</sub> C <sub>3</sub> ] with the <i>i</i> ) Ho <sub>2</sub> [Cr <sub>2</sub> C <sub>3</sub> ] and the <i>ii</i> ) Er <sub>2</sub> [Mo <sub>2</sub> C <sub>3</sub> ] structure type as a function of the unit cell volume. . . . .	145
7.6	Total and projected DOS (left) and COHP (right) curves for selected orbital interactions for the minority spin direction of Sm <sub>2</sub> [Cr <sub>2</sub> C <sub>3</sub> ]. The total DOS of the valence electrons displays three different structures denoted <b>A</b> , <b>B</b> and <b>C</b> ranges. . . . .	146
7.7	ELI-D picture of Sm <sub>2</sub> [Cr <sub>2</sub> C <sub>3</sub> ]: light brown domains at an isovalue $Y_D = 1.41$ indicate covalent bonds Cr–C and lone pairs around C1 atoms; purple domains at an isovalue $Y_D = 0.89$ close to the center of a square pyramid (1 Cr + 4 Sm) indicates a multi-center metal–metal bond situation. . . . .	148

## List of Tables

2.1	Summary of binary rare-earth carbides. . . . .	8
2.2	Summary of binary chromium carbides . . . . .	14
2.3	Summary of binary iron carbides . . . . .	18
2.4	Unit cell parameters and unit cell volumes of the ternary phases $RE_2Cr_2C_3$ . . . . .	25
2.5	Unit cell parameters and Bravais lattice types of intermediate ternary phases reported during phase diagram studies in systems $RE-Fe-C$ . . . . .	27
2.6	Unit cell parameters and unit cell volumes of ternary carbides $RE_2FeC_4$ . . . . .	27
2.7	Unit cell parameters and unit cell volumes of ternary phases representing the $RE_{3.67-x}FeC_6$ -type structure. . . . .	29
2.8	Unit cell parameters and unit cell volumes of the isotypic ternary carbides $REFeC_2$ . . . . .	30
2.9	Unit cell parameters and unit cell volumes of $RE_{3.67-x}FeC_6$ -type compounds (left) and perovskite type ( $RERu_3C$ ) compounds (right). . . . .	32
2.10	Unit cell parameters and unit cell volumes of the isotypic carbides $RE_3Ru_2C_5$ . . . . .	33
2.11	Lattice parameters and unit cell volumes of the isotypic carbides $RE_7Ru_2C_{11}$ . The lattice parameters correspond to the <i>Amma</i> and <i>Pnma</i> settings of the subcell and the superstructure, respectively. . . . .	35
2.12	Lattice parameters and unit cell volumes of the subcell of the isotypic carbides $RE_{10}Ru_{10}C_{19}$ . . . . .	36
2.13	Survey of ternary compounds reported in the ternary systems $RE-T-C$ ( $T = Cr, Fe, Ru$ ). . . . .	38
3.1	Chemicals and materials used for synthesis and crucible/ampoule materials. . . . .	42
4.1	Unit cell parameters and the Bravais lattice types of compounds $RE_{15}[Fe_8C_{25}]$ ( $RE = Y, Dy, Ho$ and $Er$ ). . . . .	55
4.2	Possible space groups with extinction symbol $P- - -$ for Laue classes $\bar{3}m, \bar{3}, 6/m$ and $6/mmm$ . . . . .	57
4.3	Crystallographic data and details on data collection and structure refinements for compounds $RE_{15}[Fe_8C_{25}]$ ( $RE = Dy, Ho, Er$ ). . . . .	58
4.4	$Er_{15}[Fe_8C_{25}]$ : Fractional atomic coordinates, equivalent isotropic displacement parameters [ $10^4 \text{ pm}^2$ ] and site occupancies; estimated standard deviations are given in parentheses. . . . .	59
4.5	Fitted hyperfine parameters of $Dy_{15}[Fe_8C_{25}]$ : Temperature [K], Isomer shift (IS) [mm/s] relative to $\alpha$ -Fe, half width ( $\Gamma/2$ ) [mm/s], quadrupole splitting ( $\Delta E_Q$ ) [mm/s], hyperfine field H[T], and relative area (A) [%] of the subspectra, estimated standard deviations are given in brackets. . . . .	79
4.6	Calculated electric field gradient $V_{zz}$ [ $\text{V/m}^2$ ], asymmetry parameter $\eta$ , quadrupole splitting ( $\Delta E_Q$ ) [mm/s], hyperfine field H[T] and electron density at the Fe nucleus $\rho(0)$ [ $\text{au}^{-3}$ ] for $Y_{15}[Fe_8C_{25}]$ . . . . .	80

4.7	Fitted hyperfine parameters of $Y_{15}[Fe_8C_{25}]$ : Temperature [K], Isomer shift (IS) [mm/s] relative to $\alpha$ -Fe, half width ( $\Gamma/2$ ) [mm/s], quadrupole splitting ( $\Delta E_Q$ ) [mm/s], hyperfine field H[T], and relative area (A) [%] of the subspectra, estimated standard deviations are given in brackets. . . . .	82
4.8	X-ray absorption threshold of Fe $K$ -edge and energy shift ( $\Delta E$ ) of Fe observed for the isotypic phases $RE_{15}[Fe_8C_{25}]$ ( $RE = Y, Dy, Ho, Er$ ). . . . .	84
5.1	Unit cell parameters of the isotypic phases $RE_{5.64}[Fe_2C_9]$ ( $RE = Y, Gd, Tb$ and $Dy$ ) determined from X-ray powder data. . . . .	87
5.2	Reflection conditions for the average crystal structure of $Dy_{5.64}[Fe_2C_9]$ . . . . .	90
5.3	Crystallographic data and details on data collection and crystal structure refinements for the composite structure $Dy_{5.64}[Fe_2C_9]$ . . . . .	92
5.4	Unit cell parameters, modulation vectors and $W$ matrixes of host and guest structures of the composite structure $Dy_{5.64}[Fe_2C_9]$ . . . . .	93
5.5	$\{Dy_{0.64}\}\{Dy_5[Fe_2C_9]\}$ : Fractional atomic coordinates, equivalent isotropic displacement parameters [ $10^4 \text{ pm}^2$ ] of the atoms in the host-guest crystal structure; estimated standard deviations are given in parentheses. . . . .	94
5.6	Mössbauer parameters of $Gd_{5.64}[Fe_2C_9]$ : Isomer shift (IS) relative to $\alpha$ -Fe, half width ( $\Gamma/2$ ), quadrupole splitting ( $\Delta E_Q$ ), and relative area (A) of the subspectra, estimated standard deviations are given in brackets. . . . .	105
5.7	X-ray absorption Fe $K$ -edge threshold and energy shift ( $\Delta E$ ) observed for compounds $RE_{5.64}[Fe_2C_9]$ ( $RE = Y, Gd, Tb, Dy$ ). . . . .	106
6.1	Crystallographic data and details on data collection and structure refinement for $La_{3.67}[Fe(C_2)_3]$ . . . . .	111
6.2	$La_{3.67}[Fe(C_2)_3]$ : Fractional atomic coordinates in the asymmetric unit and equivalent isotropic displacement parameters [ $10^4 \text{ pm}^2$ ]; estimated standard deviations are given in parentheses. . . . .	112
6.3	$La_{3.67}[Fe(C_2)_3]$ : Selected interatomic distances (pm, denoted as $d$ ), multiplicities per unit cell (denoted as $n$ ) of the superstructure and integrated crystal orbital Hamilton populations per bond (-ICOHP [eV/bond]). . . . .	121
6.4	Mössbauer parameters of $La_{3.67}[Fe(C_2)_3]$ : Isomer shift (IS) [mm/s] relative to $\alpha$ -Fe, quadrupole splitting ( $\Delta E_Q$ ) [mm/s], half width ( $\Gamma/2$ ) [mm/s], and relative area (A) [%] of the subspectra; estimated standard deviations are given in brackets. . . . .	122
6.5	Crystallographic data and details on data collection and structure refinements of $La_{3.65}[Ru(C_2)_3]$ . . . . .	126
6.6	$La_{3.65}[Ru(C_2)_3]$ : Fractional atomic coordinates in the subcell, site occupancies and equivalent isotropic displacement parameters [ $10^4 \text{ pm}^2$ ]; estimated standard deviations are given in parentheses. . . . .	127
6.7	$La_{3.67}[Ru(C_2)_3]$ : Selected interatomic distances [pm] (denoted as $d$ ), multiplicities per unit cell (denoted as $n$ ) of the superstructure and their integrated crystal orbital Hamilton populations per bond (-ICOHP [eV/bond]). . . . .	134

7.1	Crystallographic data and details on the Rietveld structure refinement of $\text{Sm}_2[\text{Cr}_2\text{C}_3]$ .	140
7.2	Fractional atomic coordinates and isotropic displacement parameters [ $10^4\text{pm}^2$ ] of $\text{Sm}_2[\text{Cr}_2\text{C}_3]$ .	141
7.3	Interatomic distances in the crystal structure of $\text{Sm}_2[\text{Cr}_2\text{C}_3]$ (estimated standard deviations are given in parentheses).	143
7.4	$\text{Sm}_2[\text{Cr}_2\text{C}_3]$ : Integrated crystal orbital Hamilton populations (-ICOHP [eV/bond]) for minority spin channel.	147
9.1	Unit cell parameters and unit cell volumes of compounds $\beta\text{-RE}_3\text{C}$ and $\alpha\text{-RE}_2\text{C}$ .	152
9.2	Unit cell parameters and unit cell volumes of the compounds $\text{RE}_4\text{C}_3$ .	152
9.3	Unit cell parameters and unit cell volumes of the compounds $\text{RE}_3\text{C}_4$ .	152
9.4	Unit cell parameters and unit cell volumes of the compounds $\text{RE}_2\text{C}_3$ .	153
9.5	Unit cell parameters and unit cell volumes of the compounds $\alpha\text{-REC}_2$ .	153
9.6	Unit cell parameters and unit cell volumes of the compounds $\alpha$ - and $\beta\text{-RE}_4\text{C}_7$ .	153
9.7	Unit cell parameters and unit cell volumes of the phases $\text{RE}_4\text{C}_5$ .	153
9.8	Unit cell parameters and unit cell volumes of the rare-earth iron Laves phases.	154
9.9	Unit cell parameters and unit cell volumes of the compounds $\text{Th}_2\text{Ni}_{17}$ - and $\text{Th}_2\text{Zn}_{17}$ -type $\text{RE}_2\text{Fe}_{17}$ .	154
9.10	Unit cell parameters and unit cell volumes of the compounds $\text{REFe}_7$ .	154
9.11	Unit cell parameters and unit cell volumes of the compounds $\text{RE}_6\text{Fe}_{23}$ .	154
9.12	Unit cell parameters and unit cell volumes of the compounds $\text{REFe}_5$ .	155
9.13	Unit cell parameters and unit cell volumes of the $\text{PuNi}_3$ type rare-earth iron binary phases.	155
9.14	Unit cell parameters and unit cell volumes of the $\text{RERu}_2$ Laves phases.	155
9.15	Unit cell parameters and unit cell volumes of the compounds $\text{RE}_5\text{Ru}_2$ .	155
9.16	Unit cell parameters and unit cell volumes of the cementite type phases in the binary $\text{RE-Ru}$ systems.	156
9.17	Unit cell parameters and unit cell volumes of the $\text{Er}_3\text{Ru}_2$ type rare-earth iron binary compounds.	156
9.18	$\text{RE}_{15}[\text{Fe}_8\text{C}_{25}]$ ( $\text{RE} = \text{Dy}$ and $\text{Ho}$ ): Fractional atomic coordinates, equivalent isotropic displacement parameters [ $10^4 \text{pm}^2$ ] and site occupancy; estimated standard deviations are given in parentheses.	157
9.19	$\text{RE}_{15}[\text{Fe}_8\text{C}_{25}]$ ( $\text{RE} = \text{Dy}$ , $\text{Ho}$ , $\text{Er}$ ): anisotropic displacement parameters $U_{ij}$ [ $10^4 \text{pm}^2$ ]; estimated standard deviations are given in parentheses.	158
9.20	$\text{Dy}_{15}[\text{Fe}_8\text{C}_{25}]$ : interatomic distances, [pm]; estimated standard deviations are given in parentheses and $n$ is the multiplicity.	159
9.21	$\text{Ho}_{15}[\text{Fe}_8\text{C}_{25}]$ : interatomic distances, [pm]; estimated standard deviations are given in parentheses and $n$ is the multiplicity.	160
9.22	$\text{Er}_{15}[\text{Fe}_8\text{C}_{25}]$ : interatomic distances, [pm]; estimated standard deviations are given in parentheses and $n$ is the multiplicity.	161

9.23	$RE_{15}[Fe_8C_{25}]$ ( $RE = Dy, Ho, Er$ ): bond angles in the polyanionic partial structure; estimated standard deviations are given in parentheses and A1, A2, A3 denote the atoms defining the angle . . . . .	162
9.24	$Dy_{5.64}[Fe_2C_9]$ : anisotropic displacement parameters $U_{ij}$ [ $10^4 \text{ pm}^2$ ]; estimated standard deviations are given in parentheses. . . . .	163
9.25	$Dy_{5.64}[Fe_2C_9]$ : interatomic distances, [pm]; estimated standard deviations are given in parentheses and $n$ is the multiplicity. . . . .	164
9.26	$Dy_{5.64}[Fe_2C_9]$ : Modulation functions for the atomic positions ( $u(\bar{x}_4)$ ) and site occupancy ( $p(\bar{x}_4)$ ). Here, $n$ is the order of the satellite reflections, and A, B are Fourier coefficients. . . . .	166
9.27	$Dy_{5.64}[Fe_2C_9]$ : modulation amplitudes for displacement and occupational modulation functions. . . . .	166
9.28	$La_{3.67}[Fe(C_2)_3]$ : Anisotropic displacement parameters $U_{ij}$ [ $10^4 \text{ pm}^2$ ]; estimated standard deviations are given in parentheses. . . . .	168
9.29	$La_{3.67}[Fe(C_2)_3]$ : interatomic distances, [pm]; estimated standard deviations are given in parentheses and $n$ is the multiplicity. . . . .	168
9.30	Subcell of $La_{3.65}[Ru(C_2)_3]$ ( $a = 887.9(2) \text{ pm}$ , $c = 535.6(2) \text{ pm}$ ): anisotropic displacement parameters $U_{ij}$ [ $10^4 \text{ pm}^2$ ]; estimated standard deviations are given in parentheses. . . . .	169
9.31	Average structure of $La_{3.65}[Ru(C_2)_3]$ : interatomic distances, [pm]; estimated standard deviations are given in parentheses and $n$ is the multiplicity. . . . .	169
9.32	Bond angles in the crystal structure of $Sm_2Cr_2C_3$ . . . . .	170

## Curriculum Vitae

### PERSONAL DATA

Name: Bambar Davaasuren  
Data of birth: May 03. 1979  
Place of birth: Ulaanbaatar, Mongolia  
Marital Status: Married

### EDUCATION

Sept. 1997 – June 2001 Department of General and Analytical Chemistry, Faculty of Chemistry, National University of Mongolia, Mongolia; B.S. Degree  
Oct. 2002 – March 2005 Graduate School of Environmental Studies, Tohoku University, Japan; M.S. Degree  
March 2007 – present Max Planck Institute for Chemical Physics of Solids, Dresden, Germany; candidate for Dr. rer. nat.

### RESEARCH EXPERIENCE

March 2006 – March 2007 Lecturer, Department of General and Analytical Chemistry, Faculty of Chemistry, National University of Mongolia, Mongolia

## **Versicherung**

Hiermit versichere ich, dass ich die vorliegende Arbeit ohne unzulässige Hilfe Dritter und ohne Benutzung anderer als der angegebenen Hilfsmittel angefertigt habe; die aus fremden Quellen direkt oder indirekt übernommenen Gedanken sind als solche kenntlich gemacht. Die Arbeit wurde bisher weder im Inland noch im Ausland in gleicher oder ähnlicher Form einer anderen Prüfungsbehörde vorgelegt.

Die vorliegende Dissertation wurde unter Betreuung von Herrn Prof. Dr. Rüdiger Kniep in der Zeit von März 2007 bis November 2010 am Max-Planck-Institut für Chemische Physik fester Stoffe in Dresden angefertigt.

Es haben keine früheren erfolglosen Promotionsverfahren stattgefunden.

Ich erkenne die Promotionsordnung der Fakultät Mathematik und Naturwissenschaften der TU Dresden vom 19. August 2008 in vollem Umfang an.

Dresden, den

(Bambar Davaasuren)